Università degli studi di Pisa

DIPARTIMENTO DI FISICA "E. FERMI"

PhD thesis in Physics

Search for the visible $\tau\tau$ decay of a Z' dark boson in $\mu\mu\tau\tau$ final state with *Belle II*

Supervisor:
Prof. Francesco Forti

Co-supervisor:
Dr. Katsuro Nakamura

Author:
Luigi Corona

XXXIV cycle

This project has received the support of the JENNIFER2 PhD secondment programme under the EU grant n.822070.

Contents

Introduction

This thesis work concerns the search for the process $e^+e^- \to \mu^+\mu^- Z', Z' \to \tau^+\tau^-$ with 54.7 fb^{-1} of data collected in the first half of 2020 at the *Belle II* experiment. The results obtained from the analysis are shown for a data sample of 5.47 fb^{-1}, corresponding to the 10% unhided data. Additionally, the extrapolation to 80 fb^{-1} based on simulation is also shown. The *Belle II* experiment is installed on the SuperKEKB accelerator, which is an asymmetric electron-positron collider, located at KEK laboratory, Tsukuba, Japan.

The Standard Model of particle physics is the theory that currently describes with remarkable accuracy the known particles and their interactions. Recently some tensions between the theoretical predictions of the Standard Model and the experimental measurements have been observed. For example: the measurement of the anomalous magnetic moment of the muon $(g-2)_\mu$ deviates from the Standard Model prediction by 4.2σ, as recently confirmed by the Muon $g-2$ experiment at Fermilab. Other anomalies in rare B meson decays are observed by LHCb, *Belle* and *BABAR*, like the deviation of 3.7σ in the angular distributions of the final state particles in the rare decay $B \to K^*\mu^+\mu^-$. Moreover, the Standard Model does not include the description of dark matter, whose gravitational effects are observed and that constitutes the 26% of the matter in the Universe.
The observed deviations can be explained by introducing new physics in the theory through extensions of the Standard Model, and one class of such extensions predict a collection of hypothetical hidden particles interacting with the Standard Model particles, although very weakly, through new dark gauge bosons. Similarly, it is also possible to introduce the description of dark matter in the theory.
The experiments that search for new physics produced at colliders are based on two different approaches. The first consists in the search for new physics at the energy frontier, examples that employ this approach are ATLAS and CMS experiments at LHC that aim at searching new physics in the direct production of new particles in proton-proton collisions, while the second consists in the search for new physics at the precision frontier. The *Belle II* experiment is based on this approach, which aim at doing high precision measurements in flavor physics that highlight deviations between the Standard Model and the experimental observations, which could be interpreted through new physics models. The sensitivity of the experiments on new physics depends on the model parameters, luminosity of accelerators and performance of the detectors.

The purpose of this thesis is to investigate the production of a light dark gauge boson Z' in association with a $\mu\mu$-pair in electron-positron annihilation at the center of mass energy of 10.58 GeV. Through this analysis it is possible to limit the $L_\mu - L_\tau$ model, which introduces the boson Z' by extending the symmetry group of the Standard Model, $U(1)_Y \otimes SU(2)_L \otimes SU(3)_C$, with the abelian group $U(1)_{L_\mu - L_\tau}$. This new symmetry leads to an interaction term of the Z' boson with muons, tauons and their neutrino counterparts, while preserving the difference between the μ-leptonic number and the τ-leptonic number in the processes. The $L_\mu - L_\tau$ model is theoretically very well motivated and could explain some of the observed experimental anomalies. Moreover, this particular analysis is a first time search and can be considered a benchmark for other models that foresee a $\tau\tau$

resonance in $\mu\mu\tau\tau$ final state.

The process analyzed is $e^+e^- \to \mu^+\mu^- Z', Z' \to \tau^+\tau^-$, where the muon pair is produced at the $\Upsilon(4S)$ energy peak and the Z' boson is radiatively emitted by one of the two muons and decays to a $\tau\tau$-pair, of which we reconstruct only 1-prong τ decays. The signature of the process consists of two well identified muon tracks and two additional tracks coming from the interaction point. The signal yield is extracted by fitting the distribution of the recoil mass against the muon pair with respect to the center of mass momentum, which is expected to peak at the Z' mass for signal events. Many Standard Model processes with four charged tracks in the final state contribute to the background, such as $e^+e^- \to \tau^+\tau^-(\gamma)$, $e^+e^- \to q\bar{q}$, $e^+e^- \to \mu^+\mu^-(\gamma)$, $e^+e^- \to e^+e^-\mu^+\mu^-$, $e^+e^- \to e^+e^-\tau^+\tau^-$ and $e^+e^- \to \mu^+\mu^-\tau^+\tau^-$.

We apply a neural network based background rejection: we use the Multilayer Perceptron (MLP) method of the Multivariate Analysis (MVA) package of ROOT. The MLP is trained with 14 discriminating variables that can be classified in two groups: variables sensitive to the presence of a resonance in the recoil system and variables sensitive to the presence of a $\tau\tau$-pair in the recoil system, where the recoil system is calculated with respect to the $\mu\mu$-pair in the final state. Before applying the MLP-based background rejection, we select events with 4 tracks coming from the interaction point, two of them identified as muons, while the remaining two (τ-daughters) are required to have at least one of the particle identification variables, electron-ID (eID), muon-ID (μID) or hadron-ID ($1 - eID - \mu ID$), larger than 0.5, and with an invariant mass of the four tracks $M < 9.5$ GeV/c^2, to reduce the impact of background components with a kinematics that closes at the $\Upsilon(4S)$. As an example, for $M_{Z'} = 3.6$ GeV/c^2, the signal efficiency of the preselection is $\sim$33%, while it becomes $\sim$13% after the MLP selection. From simulation, we estimate the sensitivity to the coupling constant of Z' to leptons, g', and the cross section of the process as a function of the Z' mass, assuming an integrated luminosity of 80 fb^{-1}, at 90% confidence level (CL).

We perform data validation using control samples: the first named $\pi^+\pi^-\tau^+\tau^-$ (CS1) and the second named $\mu^+\mu^-\tau^+\tau^-$ with $M_{recoil} < 3.4$ GeV/c^2 (CS2). In the first, we select events with two well identified opposite charged pions in the final state (instead of muons), so we are not sensitive to signal at all, and it allows to test the MLP selection on data for a wide region of the recoil mass distribution. With the second, we are completely out from the M_{recoil} region where we expect to find signal; however, it has limitations due to the fact that the MVA is trained in range 3.6-10 GeV/c^2 and does not perform a reliable data-MC comparison outside of that region of recoil mass distribution (MVA is trained in range 3.6-10 GeV/c^2). In general, we obtain a reasonable data-MC agreement, where differences could be explained by the missing models in MC. To perform data validation we also measure the trigger efficiency for one of the trigger lines used in the analysis (*fff*) on data. It has been necessary to re-weight events in simulation, since trigger simulation is currently missing in MC.

Finally, we perform a 10% data unhiding, corresponding to 5.47 fb^{-1} from which we got the following upper limits at 90% CL: $\sigma_{90\%CL} \sim 2.72$ fb and $g' \sim 4.5 \times 10^{-2}$. The analysis has not yet been approved by the *Belle II* collaboration, so the result obtained with the 10% data unhided is not public and it can not be shown out of the context of this thesis.

Below, we report the list of Chapters with the topic covered within each of them:

- Chapter 1 is dedicated to the physics motivations for the analysis. It contains a brief introduction of the Standard Model of particle physics, a brief description of dark matter and the possibility to include new physics in the theory, with the focus on the $L_\mu - L_\tau$ model. Finally, a brief description of the existing experimental limits on different dark sector models, with a focus on the searches performed at e^+e^- colliders, is presented.

- Chapter 2 is dedicated to the detailed description of the *Belle II* experiment, both the detector and the SuperKEKB accelerator, with a general introduction to *B*-factories, in particular for what concerns the physics that can be investigated by these experiments and the analysis methods used. Finally, a brief description of the *Belle II* dark sector dedicated triggers, software and computing is provided.

- Chapter 3 is dedicated to an overview of the analysis of the process $e^+e^- \to \mu^+\mu^- Z'$, $Z' \to \tau^+\tau^-$ describing the characteristics of the signal events and of the background processes, as well as the discriminating variables, that are described in detail. The concept of Multivariate analysis is briefly introduced, as well as a brief description of MLP and BDT methods, that has been tested during the analysis, and the Multivariate Analysis strategy applied is discussed. Finally, checks of model independence using leptophilic dark scalars and axion-like particles models are presented.

- Chapter 4 is dedicated to the signal modeling and the description of the fit procedure designed to extract the signal yield.

- Chapter 5 is dedicated to the description of the control samples, data validation and the estimate of systematic uncertainties.

- Chapter 6 is dedicated to the sensitivity estimate based on simulation, to the implementation of the Look-elsewhere effect and a preliminary measurement based on 10% data unhiding.

Finally, this thesis will conclude with the discussion about the results obtained from the analysis presented, and its future perspectives at *Belle II*.
In addition to the analysis work, during the three years of Ph.D I actively took part in the operation of the Silicon Vertex Detector in particular taking the role of SVD operation coordinator during the 2020 and 2021 data taking periods.

1. Physics Motivations

The Standard Model of particle physics describes successfully the phenomenology of the constituent particles of matter and their interactions, but it is an incomplete theory. It is known that the 26% of the matter of the Universe is composed by dark matter of which gravitational effects are observed. However, the Standard Model does not contain a description of dark matter. Furthermore, experiments observed some tensions between the Standard Model predictions and experimental results that suggest the possibility to include new physics through a more extended theory than current Standard Model. A possibility to include new physics that could explain discrepancies and describe dark matter is what is called the dark sector. It foresees a new group of particles that interact with Standard Model particles, although very weakly, and hence it is possible in principle to observe them in precision experiments. In this chapter the Standard Model and dark matter are briefly introduced and some possible extension of the Standard Model are described, emphasizing the $L_\mu - L_\tau$ model that is of particular interest for this thesis work. The possibility to investigate the dark sector in accelerators will also be covered, in particular for what concerns the searches at e^+e^- colliders.

1.1 Introduction to the Standard Model of particle physics

The Standard Model of fundamental interactions is the theory that describes the constituent particles of matter and three of the four fundamental physics interactions between particles: the electromagnetic interaction, the weak interaction and the strong interaction. Elementary particles are divided in two categories: fermions, with half-integer spin, following the Fermi-Dirac statistics and bosons, with integer spin and following the Bose-Einstein statistics. Matter is composed of fermions grouped in three generations of quarks and leptons.

Leptons are sensitive to electromagnetic and weak interactions while quarks are sensitive to all three kinds of interactions. The three generations of leptons are organized in doublets composed by a charged leptons (e, μ, τ) with charge $-e$, which interact electromagnetically and weakly, and by neutral leptons, the neutrinos $(\nu_e, \nu_\mu, \nu_\tau)$, which interact only weakly. A different lepton number, $L_{e,\mu,\tau}$, is associated to each generation: generally it is a conserved quantum number in interactions, however violations to the conservation of lepton number are possible, neutrinos in fact can oscillate, changing family. An anti-lepton with the same mass of the respective lepton and opposite quantum numbers is associated to each lepton.

The three generations of quarks are organized in doublets of u-type quarks, characterized by a charge of $+2/3e$, and d-type quarks, characterized by a charge of $-1/3e$. Each of six quarks has a different flavour. An anti-quark with the same mass of the respective quark and opposite quantum numbers is associated to each quark. Quarks have an additional quantum number connected to strong interactions called *color*. Differently from leptons, it is not possible to observe isolated quarks because of the phenomenon called *confinement*, derived in the theory of strong interactions, implying that only color singlets can

be observed. Two kinds of color singlets are known, bound states of two quarks, mesons, or three quarks, baryons. The three generations of leptons and quarks have very different masses as shown in Table 1.1 [1], called a mass hierarchy.

Leptons				Quarks			
Charge	$L_e = 1$	$L_\mu = 1$	$L_\tau = 1$	Charge			
0	$\begin{pmatrix}\nu_e\\ e\end{pmatrix}$	$\begin{pmatrix}\nu_\mu\\ \mu\end{pmatrix}$	$\begin{pmatrix}\nu_\tau\\ \tau\end{pmatrix}$	$+\ 2/3$	$\begin{pmatrix}u\\ d\end{pmatrix}_i$	$\begin{pmatrix}c\\ s\end{pmatrix}_i$	$\begin{pmatrix}t\\ b\end{pmatrix}_i$
$-$ 1				$-\ 1/3$			
$M_e = 0.511\ \mathrm{MeV}/c^2$				$M_u = 2.2\ \mathrm{MeV}/c^2$			
$M_\mu = 105.7\ \mathrm{MeV}/c^2$				$M_d = 4.7\ \mathrm{MeV}/c^2$			
$M_\tau = 1777\ \mathrm{MeV}/c^2$				$M_c = 1.28\ \mathrm{GeV}/c^2$			
$M_\nu \sim \mathrm{eV}/c^2$				$M_s = 96\ \mathrm{MeV}/c^2$			
				$M_t = 173.1\ \mathrm{GeV}/c^2$			
				$M_b = 4.18\ \mathrm{GeV}/c^2$			

Table 1.1 Elementary fermions of Standard Model. The $i = 1,2,3$ subscript in quarks generations is the number of colors. Each quark exists in three different colors and in the SM there are six leptons and eighteen quarks. To each of these particles is associated an anti-particle. The value of masses reported in this table are taken from the Particle Data Group (PDG) [2].

The Standard Model is a quantum gauge theory based on the symmetry group $U(1)_Y \otimes SU(2)_L \otimes SU(3)_C$. The electroweak theory (EW) (the unified theory of electromagnetic interaction (QED) and weak interaction) is described by the gauge group $U(1)_Y \otimes SU(2)_L$. It introduces the vectorial gauge fields B_μ, relative to $U(1)_Y$, and W^a_μ where $a = 1,2,3$, relative to $SU(2)_L$. After spontaneous symmetry breaking $U(1)_Y \otimes SU(2)_L \to U(1)_{e.m.}$ and diagonalization of the gauge boson mass terms, the photon A_μ and the weak interaction bosons, $W^\pm_\mu$ and Z_μ, become explicit fields in the theory. There is no mass term associated to the gauge field of the photon because of the residual symmetry of the Lagrangian under the group $U(1)_{e.m.}$, while the mass terms of the gauge fields $W^\pm_\mu$ and Z_μ appear explicitly in the theory. The spontaneous Lagrangian gauge symmetry breaking is possible through the introduction of the complex scalar field doublet of $SU(2)$ ϕ, known as Higgs field, and its potential $V(\phi^\dagger\phi)$ of the form

$$V(\phi^\dagger\phi) = \lambda[\phi^\dagger\phi - \frac{v^2}{2}]^2 \tag{1.1}$$

where λ is adimensional and v is the vacuum expectation value that has the dimension of a mass. This potential allows the spontaneous symmetry breaking because its ground state is not invariant under the symmetry. This mechanism is known as Higgs mechanism and it explains how fermions take mass interacting with the Higgs field.
The strong interaction theory is described by quantum chromodynamics (QCD) and it is based on the gauge group $SU(3)_C$ that introduces the vectorial gauge fields of the gluons,

G^A_μ where $A = 1, ..., 8$.
From this theoretical framework it is derived that interactions are mediated by spin-1 gauge bosons. The photon γ is the non-massive mediator of electromagnetic interactions, the $W^\pm$ bosons are the massive mediators of the charged current weak interaction, the Z^0 boson is the massive mediator of the neutral current weak interaction and finally the eight gluons g are the non-massive mediators of the strong interaction between quarks.
The theory is completed by the massive scalar Higgs boson that is introduced in the Standard Model through the Higgs mechanism. Standard Model bosons are shown in Table 1.2
[1]. The Lagrangian of the Standard Model is [1]:

Weak ($s=1$)	Electromagnetic ($s=1$)	Strong ($s=1$)	Higgs ($s=0$)
$W^\pm, Z^0$	γ	g_A	H
$M_{W^\pm} = 80.4\ \mathrm{GeV}/c^2$ $M_{Z^0} = 91.2\ \mathrm{GeV}/c^2$	$M_\gamma = 0\ \mathrm{GeV}/c^2$	$M_g = 0\ \mathrm{GeV}/c^2$	$M_H = 125\ \mathrm{GeV}/c^2$

Table 1.2 Elementary bosons of Standard Model. The photons, the Z^0 boson and gluons are electromagnetically discharged and they have no anti-particles associated to them. Gluon carry the color charge, the quantum number connected to strong interaction. The $A = 1, ..., 8$ subscript denotes the eight gluons. W^- and W^+ bosons are electromagnetically charged and W^- is the anti-particle of W^+.

$$
\begin{aligned}
&\mathscr{L} = \mathscr{L}_{kin} + \mathscr{L}_{EW} + \mathscr{L}_{QCD} + \mathscr{L}_{Higgs} + \mathscr{L}_Y \\
&\mathscr{L}_{kin} = -\frac{1}{4} B_{\mu\nu} B^{\mu\nu} - \frac{1}{4} W^a_{\mu\nu} W^{\mu\nu}_a - \frac{1}{4} G^A_{\mu\nu} G^{\mu\nu}_A \\
&\mathscr{L}_{EW} = \bar{Q}_i i\gamma^\mu D_\mu Q_i + \bar{u}_i i\gamma^\mu D_\mu u_i + \bar{d}_i i\gamma^\mu D_\mu d_i + \\
&\qquad + \bar{L}_i i\gamma^\mu D_\mu L_i + \bar{e}_i i\gamma^\mu D_\mu e_i \\
&\mathscr{L}_{Higgs} = |D_\mu \phi|^2 - V(\phi^\dagger \phi) \\
&\mathscr{L}_Y = -\Lambda'_{ij} \tilde{\phi} \bar{Q}_i u_j - \Lambda_{ij} \phi \bar{Q}_i d_j - \lambda_{e,ij} \phi \bar{L}_i e_j + h.c. \\
&\mathscr{L}_{QCD} = \bar{\psi}_i \gamma^\mu g_S T_{A,ij} G^A_\mu \psi_j
\end{aligned}
\tag{1.2}
$$

where

$$
\begin{aligned}
&G^A_{\mu\nu} \equiv \partial_\mu G^A_\nu - \partial_\nu G^A_\mu + g_S f^{ABC} G^B_\mu G^C_\nu \\
&D_\mu \equiv \partial_\mu - i\frac{g'}{2} Y B_\mu - i\frac{g}{2} \tau_a W^a_\mu
\end{aligned}
\tag{1.3}
$$

The couplings g and g' are associated with B_μ and W^a_μ. Y is the value of the weak hypercharge of fields interacting with the B_μ field, and τ_a are the Pauli matrices whose eigenvalues are the weak isospin of particles interacting with the W^a_μ fields; $\lambda_{e,ij}$, Λ_{ij} and Λ'_{ij} are

the matrix of Yukawa coupling, respectively between leptons, d-type quarks and u-type quarks with the Higgs field.
$\mathscr{L}_{kin}$ is the kinetic term of gauge bosons, containing also the self-interaction terms of gauge bosons; f^{ABC}, that appear in the definition of $G^{A}_{\mu\nu}$, are the structure constants of $SU(3)$.
$\mathscr{L}_{EW}$ is the part of the electroweak theory describing the interaction between fermions and $U(1)_Y \otimes SU(2)_L$ gauge bosons; i sums over the three generations of fermions; Q, u, and d are the left-handed doublet, right-handed singlet up, and right handed singlet down quark fields; and L and e are the left-handed doublet and right-handed singlet electron fields.
$\mathscr{L}_{QCD}$ is the quark-gluons interaction term, g_S is the coupling of strong interaction, ψ_i is the quark field in the fundamental representation of the $SU(3)$ gauge group, indexed by $i, j = 1,2,3$, $T_{A,ij}$ are the infinitesimal $SU(3)$ generators in the fundamental representation.
$\mathscr{L}_{Higgs}$ describes the interactions of the Higgs boson with the gauge bosons of electroweak theory, its self-interactions and its kinetic term.
$\mathscr{L}_{Y}$ describes the interactions between fermions and Higgs field; as for $\mathscr{L}_{EW}$, Q and L are respectively the left-handed doublet quark and lepton fields, while u, d and e are respectively the right-handed singlet up, the right handed singlet down quark fields and the right-handed singlet electron fields, where i and j sum over the three generations of fermions; $\tilde{\phi}$ is the charge conjugated Higgs field.
The Higgs field ϕ is a doublet of $SU(2)_L$, hence the gauge invariance of $\mathscr{L}_{Y}$ is preserved [1].

The flavour changing transitions between quarks are mediated by charged current weak interactions. Nicola Cabibbo explained for the first time that the transitions between up-type and down-type quarks are possible in weak interactions, although the transitions between quarks that belong to different generations are suppressed with respect to transitions between quarks belonging to the same generation [3]. In order to explain the suppression, he introduced the eigenstates of weak interactions (d', s') as a linear combination of the eigenstates of mass (d, s) that can be expressed through the mixing matrix in Equation 1.4, where θ_C is called Cabibbo angle and from experimental observations Cabibbo estimated that $\theta_C \simeq 0.23$.

$$\begin{pmatrix} d' \\ s' \end{pmatrix} = \begin{pmatrix} cos\theta_C & sin\theta_C \\ -sin\theta_C & cos\theta_C \end{pmatrix} \begin{pmatrix} d \\ s \end{pmatrix} \tag{1.4}$$

The Cabibbo theory explains the flavour changing transitions if only two quark families are considered. The extension to three quark families is provided by the Cabibbo-Kobayashi-Maskawa (CKM) mixing matrix of quarks. The CKM matrix have four free parameters: three real angles θ_{ij} and a complex term $e^{i\delta}$ that is responsible for the CP violation in weak interactions as shown in the following equation that shows the CKM matrix in the standard parametrization [1].

$$V_{ij} = \begin{pmatrix} V_{ud} & V_{us} & V_{ub} \\ V_{cd} & V_{cs} & V_{cb} \\ V_{td} & V_{ts} & V_{tb} \end{pmatrix} = \\ = \begin{pmatrix} c_{12}c_{13} & s_{12}c_{13} & s_{13}e^{i\delta} \\ -s_{12}c_{13} - c_{12}s_{13}s_{23}e^{i\delta} & c_{12}c_{23} - s_{12}s_{13}s_{23}e^{i\delta} & c_{13}s_{23} \\ s_{12}s_{23} - c_{12}s_{13}c_{23}e^{i\delta} & -c_{12}s_{23} - s_{12}s_{13}c_{23}e^{i\delta} & c_{13}c_{23} \end{pmatrix} \tag{1.5}$$

The c_{ij} and s_{ij} terms are respectively defined as $c_{ij} = cos\theta_{ij}$ and $s_{ij} = sin\theta_{ij}$. The complex phase $i\delta$ is responsible for the *CP* violation.
The CKM matrix can be expressed in the basis of the independent parameters (A, λ, ρ, η) through the Wolfenstein parametrization:

$$V_{ij} = \begin{pmatrix} V_{ud} & V_{us} & V_{ub} \\ V_{cd} & V_{cs} & V_{cb} \\ V_{td} & V_{ts} & V_{tb} \end{pmatrix} = \begin{pmatrix} 1 - \frac{1}{2}\lambda^2 & \lambda & A\lambda^3(\rho - i\eta) \\ -\lambda & 1 - \frac{1}{2}\lambda^2 & A\lambda^2 \\ A\lambda^3(1 - \rho - i\eta) & -A\lambda^2 & 1 \end{pmatrix} + \\ + o\left(\lambda^4\right) \tag{1.6}$$

In this parametrization, the imaginary part η is connected with the complex phase δ, hence it gives rise to the *CP* violation in weak interactions. This parametrization highlights that transitions between quarks of the same generations are favored, indeed diagonal terms are close to 1, while transitions between quarks of different generations are suppressed, indeed off-diagonal terms are proportional to increasing powers of the small parameter λ, which corresponds to the sine of the Cabibbo angle.

CKM is a unitary matrix, i.e. $\Sigma_i V_{ij} {V_{ik}}^* = \mathbb{1}$. This property defines some relations between the CKM matrix elements: for example, the relation $V_{ud}{V_{ud}}^* + V_{us}{V_{us}}^* + V_{ub}{V_{ub}}^* = 1$ means that the total probability of transition of the quark u in a down-type quark is 1, while the relations $V_{ud}{V_{ub}}^* + V_{cd}{V_{cb}}^* + V_{td}{V_{tb}}^* = 0$ means that the quark d and the quark b are orthogonal states, hence a transition between them is not possible.
The relations defined by $\Sigma_{i,j,k} V_{ij} {V_{ik}}^* = 0$ for $j \neq k$ can be represented through unitarity triangles. For example, the relation $V_{ud}{V_{ub}}^* + V_{cd}{V_{cb}}^* + V_{td}{V_{tb}}^* = 0$ can be represented by the unitarity triangle in the (ρ, η) plane shown in Figure 1.1, where the sides of the triangle have been normalized respect to the quantity $V_{cd}{V_{cb}}^*$. The top vertex of the triangle has coordinates $(\bar{\rho}, \bar{\eta})$, where $\bar{\rho} = \rho\left(1 - \lambda^2/2\right)$ and $\bar{\eta} = \eta\left(1 - \lambda^2/2\right)$. The angles α, β and γ are associated to the CKM matrix elements by the following relations:
$\alpha = arg\left[\frac{V_{ud}{V_{ub}}^*}{V_{td}{V_{tb}}^*}\right]$, $\beta = arg\left[\frac{V_{td}{V_{tb}}^*}{V_{cd}{V_{cb}}^*}\right]$ and $\gamma = arg\left[\frac{V_{cd}{V_{cb}}^*}{V_{ud}{V_{ub}}^*}\right]$. An overview of the most recent experimental limits on the unitarity triangle parameters are shown in Figure 1.2 [4].

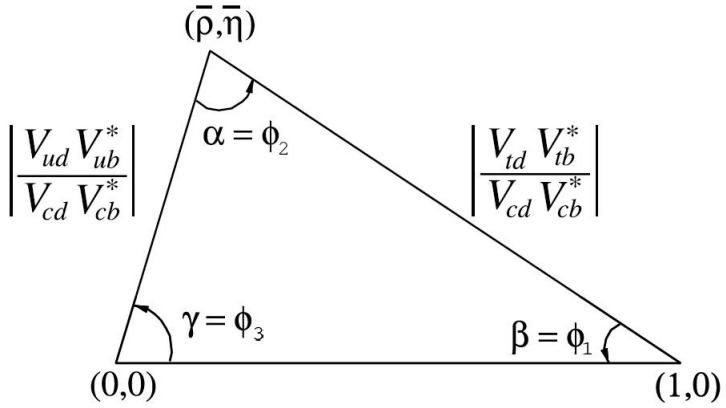

Figure 1.1 The unitarity triangle associated with the relation $V_{ud}V_{ub}^* + V_{cd}V_{cb}^* + V_{td}V_{tb}^* = 0$. The sides of the triangle have been normalized respect to the quantity $V_{cd}V_{cb}^*$.

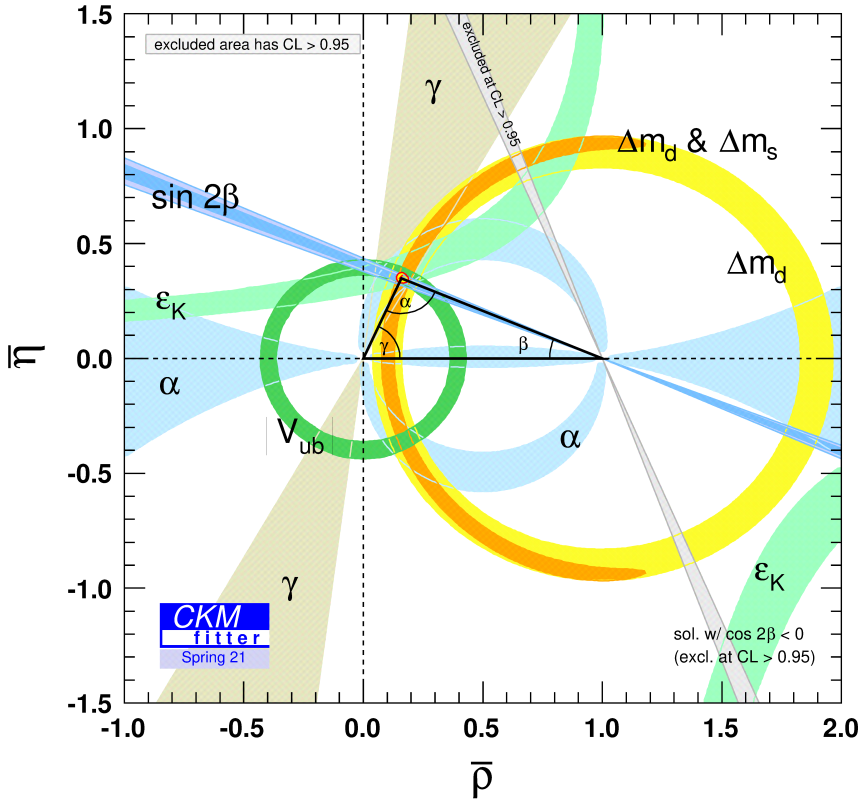

Figure 1.2 Constraints on the CKM matrix parameters in the $(\bar{\rho}, \bar{\eta})$ plane obtained from all the experimental measurements. The most probable position of the unitarity triangle vertex is into the red circle.

1.2 Introduction to dark matter

The first evidence of dark matter was attributed to the Swiss physicist F. Zwicky, who measured the rotational velocity of galaxies in the Coma cluster in 1933. Galaxies are composed of a spherical bulk of radius R_b, in the central region, and of a galactic disk of radius R_G. From the Newton's law, the rotational velocity v of an object rotating on a stable Keplerian orbit of radius r is $v(r) = \sqrt{M(r)G/r}$, where $M(r)$ is the mass of the galaxy contained inside the radius r. If $r \geq R_G$ then $M(r) = M_G$, where M_G is the mass of the galaxy, and $v(r) \propto r^{-1/2}$. The experimental measurement performed by Zwicky and confirmed by subsequent experiments shows that for $r > R_G$ the rotational velocity is $v(r) = \text{const}$, as shown in Figure 1.3, which suggests the presence of a dark halo with mass density of $\rho \propto 1/r^2$, i.e $M(r) \propto r$ [5].

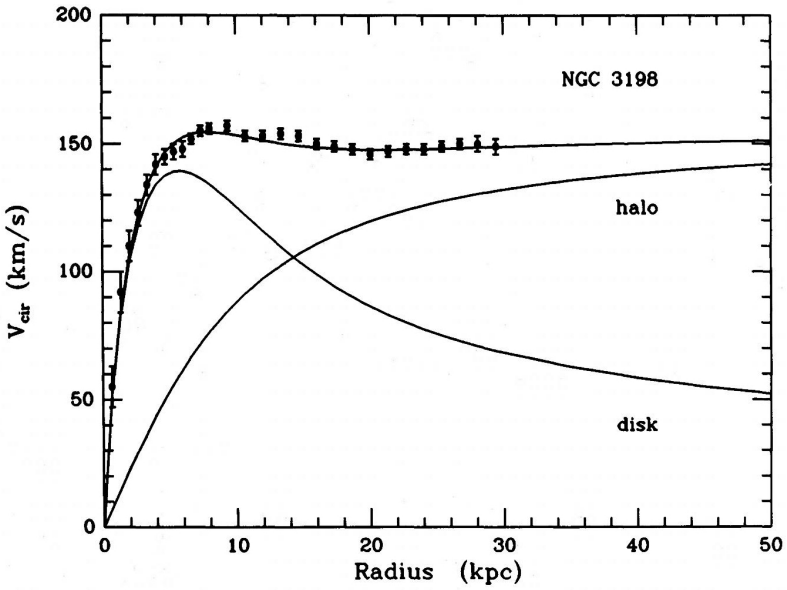

Figure 1.3 Rotational velocity curves of the NGC 3198 galaxy. Dots with error bars show the experimental data. Halo curve is based on a mass model assuming $a = 8.5$ kpc, $\gamma = 2.1$, $\rho(R_0) = 0.0040\ M_0\ \text{pc}^{-3}$: a is linked to the bulk radius, R_0 is the fiducial radius of the halo, γ is an appropriate parameter of the mass model and $\rho(R_0)$ is the mass density of the halo. The image was taken from the article by Albada et al. (1985) [6].

Other observations based on the mass distribution in the Universe, suggest the presence of dark matter in galaxies. For example: elliptical galaxies show evidence for dark matter through gravitational lensing effects; observations of X-rays from hot gas in hydrostatic equilibrium, filling the dark halo of elliptical galaxies, provides evidence of dark matter; the velocity dispersion of spiral galaxy satellites suggest the presence of dark halos characterized by radii ≥ 200 kpc; the velocity dispersion of dwarf spheroidal galaxies suggest the presence of higher mass compared to the mass of visible matter, and so on. Furthermore, some estimates of dark matter mass density in the Universe, consistent with the Big Bang cosmological model, are provided by precise measurements of the cosmological parameters through the study of Cosmic Microwave Background Radiation (CMBR)

fluctuations [5].
A simple explanation for the presence of dark matter is provided by the hypothesis of cold dark matter that consists of non-relativistic massive particles. Possible candidates of cold dark matter are the Weakly Interactive Massive Particles (WIMPs), briefly introduced below, however there is not a verified explanation for dark matter, and many other possible models exist.

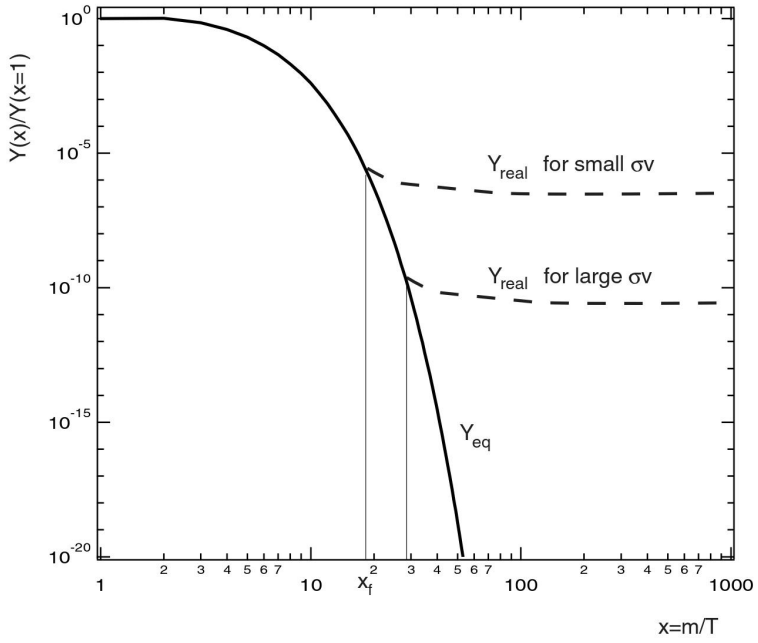

Figure 1.4 Freeze-out of a massive particle species derived from the Boltzmann equation. The variable $Y(x)$ is the numerical density of a particular particle species χ normalized to the entropy density s of the particle system in a volume a^3, where a is the scale factor of the Universe. The x_f parameter is defined as $x_f = m_\chi/T_f$, where m is the mass of the χ particles and T_f is the temperature at the freeze-out. The solid line is the value of Y at thermal equilibrium, Y_{eq}. For a certain value of x_f, χ particles leave the thermal equilibrium, Y becomes constant (dashed lines) and it represents the current abundance, Y_{real}. In the plot the ratio $Y(x)/Y(x=1)$ as a function of x is shown. At higher values of the annihilation rate σv, corresponds a smaller relic abundance. For WIMPs $x_f \approx 20$. The plot is taken from [7].

WIMPs They are hypothetical massive particles that interact with a self-annihilation cross section of $\sim 3 \cdot 10^{-36}$ cm^2. A non-relativistic particle that interacts weakly comes out from thermal equilibrium since its annihilation rate differs from its production rate. This can occur for two reasons in particular: lighter particles have not sufficient kinetic energy to produce heavier particles through interactions, and the rate of expansion of the Universe becomes higher than the interaction rate. At a certain time, the numerical density of heavier particles of a particular species becomes too small and those particles can't interact anymore, so the conditions of thermal equilibrium fail. This particular process is called freeze-out and the density of those heavier particles, since it does not change anymore, is called relic density. The Boltzmann equation describes the coming out of

particles from thermal equilibrium [8], in terms of the numerical density normalized to the entropy density of the particle system, Y. Figure 1.4 shows the freeze-out of a massive particle species derived by the Boltzmann equation.
The relic density is inversely proportional to the annihilation rate. Assuming $x = m/T \approx 20$, where m is the mass of the DM particle and T is the temperature at the freeze-out, and $\Omega_{0,DM} = 0.3$, a cross section of $\sigma \simeq 3 \cdot 10^{-36}$ cm^2, which is a typical cross section of weak interaction, is obtained for WIMPS. Assuming WIMPs interacting *via* weak interaction, a mass of the magnitude of the TeV/c^2 is estimated. Supersymmetric (SUSY) extensions of the Standard Model predict new particles with the same characteristics of WIMPs: this is known as WIMP Miracle [9].
The limit to the minimum mass of WIMPs was calculated by B. Lee and S. Weinberg to be a few GeV/c^2, assuming the annihilation cross section of weak interaction [5]. The Lee-Weinberg bound can be avoided if the mediator responsible for WIMP annihilation is something else than the Standard Model gauge bosons (Z,W and H). in that case, dark matter masses below a few GeV/c^2 are possible. Dark matter characterized by sub-GeV/c^2 mass is called light dark matter and it is well motivated by several theoretical models [5, 10–14].

Experiments sensitive to WIMPs with masses in the range GeV/c^2-TeV/c^2 have not found interesting signals yet, for this reason theoretically well-motivated models that introduce light dark matter candidates with a mass in the range keV/c^2-GeV/c^2 and consistent with the observed history of the Universe have been developed. Light dark matter particles could be part of a dark sector that could interact with Standard Model particles through a dark mediator that is charged under both sectors, Standard Model and dark sector. Figure 1.5 shows the 90% confidence level upper limit on the WIMP-nucleon cross section from the XENON1T experiment [15]. A large region above a WIMP mass of 6 GeV/c^2 has been excluded, leaving access to masses above few GeV/c^2, called light dark matter, assuming that dark matter is part of a wider dark sector that also include mediators of interactions.

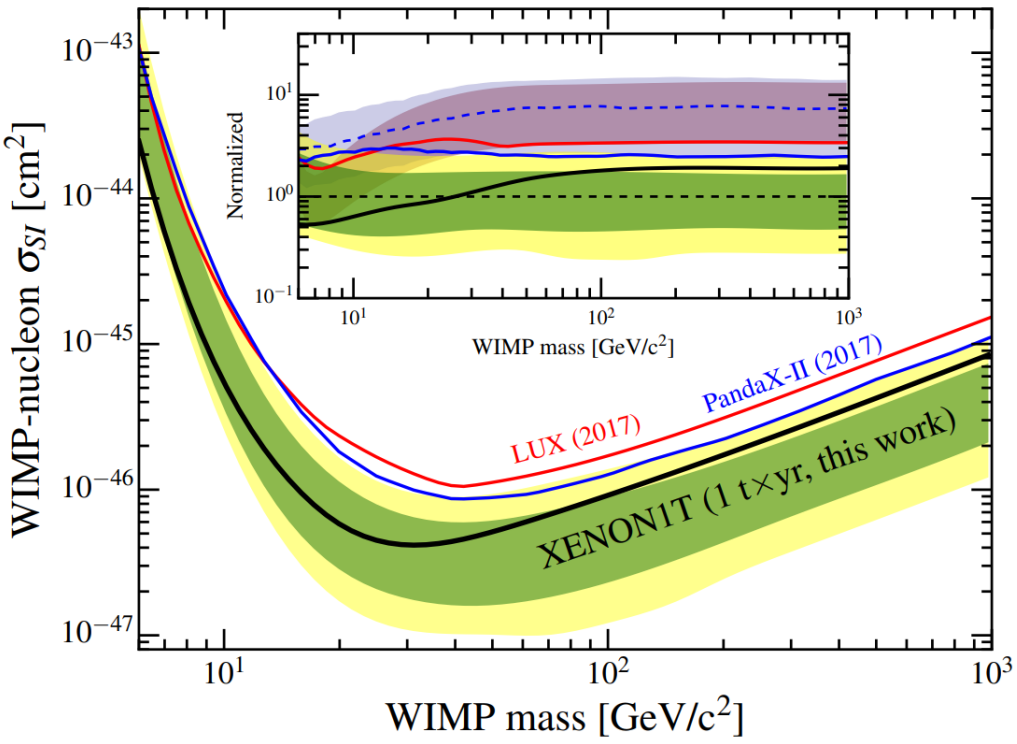

Figure 1.5 90% confidence level upper limit on the WIMP-nucleon spin independent elastic cross section σ_{SI} from the XENON1T experiment (thick black line) with the 1σ (green) and 2σ (yellow) sensitivity bands. Previous results from LUX [16] and PandaX-II [17] are shown for comparison. The inset shows these limits and corresponding $\pm 1\sigma$ bands normalized to the median of the XENON1T sensitivity band. The normalized median of the PandaX-II sensitivity band is shown as a dotted line.

1.3 Standard Model extensions

Several mechanisms for dark matter production suggest the existence of light dark matter with masses in the range keV/c^2-GeV/c^2. Limits on dark matter mass depends on the dark matter production mechanism. As example, the freeze-out, briefly described above, admits sub-GeV/c^2 light dark matter, assuming that dark matter is part of a wider dark sector that also include mediators of interactions [18].
Several theoretical scenarios introduce light dark matter weakly coupled with the Standard Model through different possible light dark sector mediators by extending the Standard Model through new gauge symmetries. The interactions between Standard Model and dark matter are classified by different portals, which depend on the spin and the parity of the dark sector mediator itself, requiring gauge and Lorentz symmetries of the Lagrangian. Portals are listed below:

The Vector Portal $\mathscr{L} \supset -\frac{\varepsilon}{2} B_{\mu\nu} F'^{\mu\nu}$, where $B_{\mu\nu} = \partial_\mu B_\nu - \partial_\nu B_\mu$ is the tensor field of $U(1)_Y$ and $F'^{\mu\nu} = \partial^\mu A'^\nu - \partial^\nu A'^\mu$ is the tensor field of an additional $U'(1)$ that extends

the gauge group of the Standard Model. The A' field represents the vector mediator introduced by the vector portal through the kinetic mixing.
Considering a model with a gauge symmetry with respect to the group $U(1) \otimes U'(1)$, the kinetic mixing term can be naturally introduced in the Lagrangian. The kinetic mixing process can only take place between two abelian gauge groups since the resulting mixing term is gauge invariant under the symmetry $U(1) \otimes U'(1)$, in fact the individual tensor fields are gauge invariant under the respective gauge group [19, 20]. The introduction of the kinetic mixing term makes the ordinary kinetic term no more diagonal. Being B_μ and X_μ the fields associated respectively to $U(1)$ and $U'(1)$, it is easy to verify that the kinetic term can be returned to its canonical form by redefining the field associated to the $U(1)$ group as $B_\mu \to B_\mu - \varepsilon X_\mu$. In the minimal model [18], the dark photon A' is a vector boson introduced extending the Standard Model with a dark $U'(1)$ gauge symmetry that mixes with the hypercharge group $U(1) = U(1)_Y$. After the spontaneous breaking symmetry from a Higgs field of the dark sector, the dark photon acquires mass and it mixes with the Standard Model photon thorugh the kinetic mixing mechanism. The kinetic mixing matrix can be diagonalized and renormalized by redefining the fields. The physics gauge fields are those for which the kinetic term assumes its canonical form. The interaction term between the dark photon and the electromagnetic current $\mathscr{L}_{int} \supset \varepsilon {A'}_\mu {J_{SM}}^\mu$ arises spontaneously in the theory, where ε is the strenght of the interaction, which makes explicit the coupling between the Standard Model and the dark sector particle. Depending on its mass, the dark photon can decay to Standard Model particles, $A' \to l^+l^-, h^+h^-$ (l =lepton, h =hadrons), or in dark matter particles χ if kinematically accessible.

The Higgs Portal $\mathscr{L} \supset (\mu\phi + \lambda\phi^2)H^\dagger H$, where ϕ is the dark sector scalar mediator that interacts with the Standard Model Higgs boson H, and μ and λ are appropriate parameters. A scalar dark sector mediator can interact with Standard Model through this portal.

The Axion Portal $\mathscr{L} \supset \frac{a}{f_a} F_{\mu\nu}\tilde{F}^{\mu\nu}$, where $F_{\mu\nu} = \partial_\mu A_\nu - \partial_\nu A_\mu$ is the tensor field of the Standard Model photon, $\tilde{F}_{\mu\nu}$ is the dual tensor field of $F_{\mu\nu}$ and a is the dark sector pseudoscalar mediator. The axion portal is suppressed by the mass scale f_a. The axion, introduced by R. Peccei and H. Quinn to solve the strong CP problem, can be a dark sector pseudoscalar mediator. Axion-like-particles (ALPs) are a generalized form of the axion.

The Neutrino Portal $\mathscr{L} \supset y_n LHN$, where y_n is a Yukawa coupling, N is a fermionic mediator that belongs to the dark sector, H is the Standard Model Higgs boson and L is a lepton doublet of $SU(2)$. N is a fermionic mediator analogous to a right-handed neutrino with a Yukawa coupling y_n.

1.3.1 The $L_\mu - L_\tau$ model

It is possible to consider another extension of the Standard Model, exploiting the kinetic mixing mechanism, which introduces a dark vector boson Z' with mass of $\mathscr{O}$(MeV)$-\mathscr{O}$(GeV) that can be copiously produced in e^+e^- colliders. The Z' boson could be a mediator of

a new kind of interaction between the Standard Model and the dark sector. Of particular interest is the search for a Z' introduced by a theoretically well motivated model called $L_\mu - L_\tau$ [21]. In this model the Z' has a coupling only to the second and third generation of leptons through the lagrangian term $\mathscr{L} = \sum_l \theta g' \bar{l} \gamma^\mu Z'_\mu l$, where $\theta = +1$ if $l = \mu, \nu_\mu$, $\theta = -1$ if $l = \tau, \nu_\tau$, and $g' \sim 10^{-6} - 10^{-2}$, where g' is the coupling constant of the Z' to leptons. Such a Z' does not couple with e and ν_e. The equations for the partial widths are,

$$\begin{aligned} \Gamma_{Z' \to l^+ l^-} &= \frac{(g')^2 M_{Z'}}{12\pi} \left(1 + \frac{2m_l^2}{M_{Z'}^2}\right) \sqrt{1 - \frac{4m_l^2}{M_{Z'}^2}} \theta(M_{Z'} - 2M_l) \\ \Gamma_{Z' \to \nu\bar{\nu}} &= \frac{(g')^2 M_{Z'}}{24\pi} \end{aligned} \tag{1.7}$$

Note that for $M_{Z'} \gg m_l$, the branching ratio (BR) to one neutrino species is half of the branching ratio to one charged lepton flavour. The reason is that the Z' only couples to left-handed neutrino chiralities whereas it couples to both left- and right-handed charged leptons. Figure 1.6 shows the value of the $BR(Z' \to ff)$ as a function of the Z' mass.

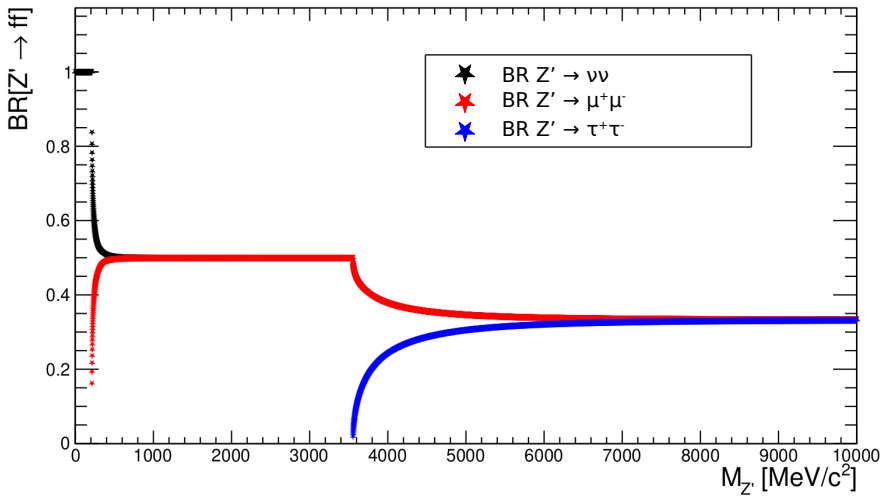

Figure 1.6 $BR(Z' \to ff)$ as a function of the Z' mass. The $\nu\bar{\nu}$ BR includes both ν_μ and ν_τ.

$Z' \to \tau\tau$ decay The topic of this thesis is the search for a visible Z' boson of the $L_\mu - L_\tau$ through the process $e^+e^- \to \mu^+\mu^- Z', Z' \to \tau^+\tau^-$, where the Z' is radiatively emitted by one of the two muons, produced in the electron-positron collision at the center-of-mass energy of 10.58 GeV, and decays in a $\tau\tau$ pair. The Feynman diagram of the process is shown in Figure 1.7. The $L_\mu - L_\tau$ model is theoretically very well motivated [22]. In this section we will discuss theoretical and experimental motivations.

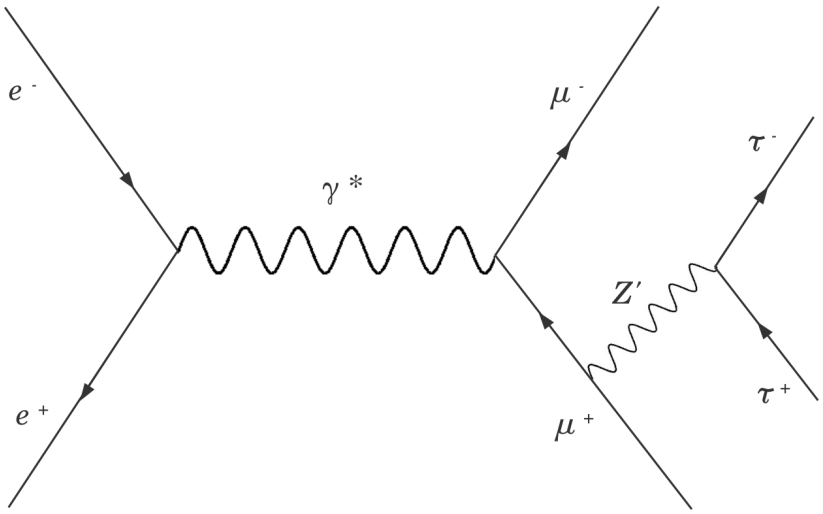

Figure 1.7 Feynman diagram of the process $e^+e^- \to \mu^+\mu^- Z', Z' \to \tau^+\tau^-$.

Theoretical motivations

- Solution to the anomalous magnetic moment of the muon. In models dealing with a dark photon candidate in the mass range of $\mathcal{O}$(MeV–GeV), like the Z' boson is, one of the most important constraint on the coupling of the dark sector with the Standard Model derives from the anomalous magnetic moment of the muon, $a_\mu = (g_\mu - 2)/2$. The gyromagnetic moment of the muon g_μ is one of the best known quantities in physics, both experimentally and theoretically, and very sensitive to New Physics through loop corrections. Currently, the experimental results deviates from Standard Model prediction of 4.2σ, as recently confirmed by Fermilab [23]. The contribution arising from the additional exchange term due to the dark photon or a dark Z' would go in the right direction to explain the observed deviation [24]. For the sake of completeness, the recent calculation performed by the BMW collaboration reduces the discrepancy of the Muon $(g_\mu - 2)$ experiment to 1.56σ [25].

- Neutral-current B-meson decays: decays involving $b \to sll$ transitions, where l represents a lepton, are suppressed in the Standard Model and sensitive to virtual contributions from new particles. Recent measurements by LHCb [26, 27] and *Belle* [28] on the branching ratio

$$R_{K^{(*)}} = \frac{B \to K^{(*)}\mu^+\mu^-}{B \to K^{(*)}e^+e^-} \tag{1.8}$$

  observed a deviation of 2.5σ from the Standard Model predictions. The measured $R_{K^{(*)}} < 1$ indicate Lepton Flavour Universality Violation (LFUV) that can be realized through neutral vector bosons. Moreover,LHCb collaboration observed a deviation of around 3.7σ from theoretical predictions in angular distributions of the final state particles in the rare decay $B \to K^*\mu^+\mu^-$, which can lead to a viable way

to search for new physics. Therefore, of special interest are the new physics models that generate the vector coupling to muons. The Z' boson of the anomaly-free $L_\mu - L_\tau$ model is one of the most promising candidate explanation for the discrepancy observed by LHCb collaboration [29].

- Charged-current B-meson decays: in addition to neutral-current B-meson decays anomalies, differences between the expected branching fraction and the measured one are observed also in the charged-current B-meson decays. In particular, the experimental measurements of $R_{D^{(*)}}$, defined as

$$R_{D^{(*)}} = \frac{B \to D^{(*)}\tau\nu}{B \to D^{(*)}l\nu} \tag{1.9}$$

where $l = e, \mu$, differ from Standard Model prediction of 3σ [30, 31]. Also in this case the $L_\mu - L_\tau$ model is one of the most promising models that can explain the observed deviations.

- In addition, the model $L_\mu - L_\tau$ can easily explain the observed dark matter relic abundance through the decay of the Z' boson in the early universe that produces a sufficient quantity of sterile neutrinos [32].

Experimental motivations Currently no experimental results for the search for a Z' resonance recoiling against a muon pair in $\mu^+\mu^-\tau^+\tau^-$ final state exists, and it can be considered a benchmark model with the possibility to reinterpret the results found for the Z' boson of the $L_\mu - L_\tau$ in other models, and in particular those with $\tau^+\tau^-$ resonance in a $\mu^+\mu^-\tau^+\tau^-$ final state, like axion-like particles and leptophilic dark scalars. In particular: for what concerns the leptophilic dark scalar model, with our seach we could probe the region of parameters for masses above 7 GeV/c^2 that it is not covered from the *BABAR* search in a leptophilic dark scalar produced in the process $e^+e^- \to \tau^+\tau^-\phi_L, \phi_L \to l^+l^-$, where ($l = e, \mu$). The lagrangian of interaction od the darkscalar with leptons is [33–36]:

$$\mathscr{L} = -\xi \sum_{l=e,\mu,\tau} \frac{m_l}{v} \bar{l}\phi_L l \tag{1.10}$$

where ξ denotes the flavor-independent coupling strength to leptons, m_l is the lepton mass and $v = 246$ GeV is the Standard Model Higgs vacuum expectation value; for what concerns axion-like particles (ALPs), in particular for models where ALP-photon coupling is negligible, the process we are searching for is favored by the fact that the coupling to leptons is Yukawa-like and if the ALP is heavy enough to decay into τs, the branching ratios for decays into lighter leptons will be disfavoured, and it will only be possible to reconstruct the decay in the heaviest lepton that is kinematically allowed [37, 38]. The decay rate of ALP to leptons is

$$\Gamma(ALP \to l^+l^-) = \frac{m_{ALP} m_l^2}{8\pi\Lambda^2} |c_{ll}^{eff}|^2 \sqrt{1 - \frac{4m_l^2}{m_{ALP}^2}} \tag{1.11}$$

where m_{ALP} is the mass of the axion-like particle, m_l is the mass of the lepton and $|c_{ll}^{eff}|$ is the effective ALP-lepton coupling

The analysis is challenging because of the very high background expected for this process. In particular selecting 1-prong τ decays the analysis is favored by the high branching ratio of 84%, but the expected background could be very hard to reject, while selecting 3-prong τ decays the statistics is reduced because of the 15% branching ratio. Moreover, the presence of neutrinos in the final state makes it impossible to exploit the kinematic constraint that the energy of the reconstructed final state in the center-of-mass frame is at the $\Upsilon(4S)$ resonance. Still, the B-factory clean environment should allow obtaining interesting results from this analysis as discussed in the following sections.

1.4 Detection of dark matter

There are three possible detection methods to investigate dark matter: direct detection, indirect detection and the direct production in laboratories. The first search for the scattering of dark matter particles on ordinary matter particles, the second search for products of annihilation or decay of dark matter in Standard Model particles, the third search for dark matter candidates can be produced in Standard Model particle annihilations resulting in several signatures which involve dark matter mediators.

Direct detection Experiments are based on the idea that our galaxy is filled with WIMPs that should cross the Earth, because of the motion of the solar system. This kind of experiments search for low-energy signals due to the recoil of nuclei, after the interaction between WIMPs and nuclei. The recoil energy, often producing scintillation light, is measured by sophisticated detection systems. Clearly many sources of background such as cosmic neutrino interactions and natural radioactivity can mimic the WIMP signal and must be carefully controlled. Because of the motion of the Earth around the Sun, the signal due to the recoil of nuclei is expected to be modulated with a period of one year. The sensitivity of direct detection experiments depends on the cross section of WIMP-nuclei interaction, and on the density and the velocity distributions of WIMPs in the galaxy, [5]. Many experiments searching for WIMP-nuclei interactions exist. The DAMA experiment, located at INFN laboratories under the Gran Sasso, claims the discovery of WIMPs because it observes an annual modulation of the signal consistent with the detection of a WIMP with a mass of 60 GeV/c^2 and a WIMP-nuclei scattering cross section of $\sim 10^{-41}$ cm^2 [39]. The DAMA experiment results have not been confirmed by other experiments yet.

Indirect detection Experiments search for the products of annihilation or decay of dark matter particles. In regions of the space in which there is high density of dark matter particles, they can annihilate producing Standard Model particle pairs. In addition dark matter particles could be unstable and decay in Standard Model particles that can be detected.
Some important results in Indirect detection have been provided by PAMELA, FERMI and AMS experiments. PAMELA experiment measured the fraction of positrons in cosmic rays, $\phi(e^+)/(\phi(e^+)+\phi(e^-))$, observing that it increases with energies in the range 1.5-100 GeV, [40]. Antiparticles are a small fraction of cosmic rays and they are expected to be produced in interaction between cosmic rays nuclei and atoms in interstellar

medium. Antiparticles can be produced also in pulsars, microquasars or by annihilation of dark matter particles. The interaction of cosmic rays nuclei with interstellar gas produce charged pions that decay in positrons and neutrinos, but the production of positrons from pion decays is in tension with PAMELA results. Understanding the excess of positrons is not simple because it requires a reliable model of positron production by pulsars or other astronomical objects. A recent measure of the positron flux on Earth confirm pulsars as a source of positrons but may exclude pulsars as the origin of the excess of positrons in cosmic rays [41]. FERMI experiment measured the excess of positrons in cosmic rays with energies in the range 20-200 GeV, confirming PAMELA measurement [42]. At the same way, AMS experiment confirmed what observed by PAMELA and FERMI up to 500 GeV, observing also a tendency to decrease around 350 GeV [43].

Direct production If the interaction of dark matter with Standard Model particles occurs, it may be possible to produce dark matter particles in Standard Model particle interactions involving hidden mediators. Since dark matter particles have negligible interactions with ordinary matter, they may be detected as missing energy. The search for hidden particles mediating the interaction between dark matter and Standard Model has been actively pursued by several kind of experiments, among which fixed-target experiments and colliders. For what concerns the former, electron-beam and proton-beam fixed-target experiments are sensitive to different mass ranges and both have unique discoveries potential of dark matter particles. In these experiments, dark matter is produced, for example, in meson decays, like $\pi^0 \to \gamma A', A' \to \chi\bar{\chi}$ or in the reactions $pZ \to pZ(A' \to \chi\bar{\chi})$, $eZ \to eZ(A' \to \chi\bar{\chi})$. Moreover, it is also possible to search for visible decays of dark sector mediators, for example the process $\pi^0 \to \gamma A', A' \to e^+e^-$ [44]. A couple of fixed-target experiment and their capabilities in dark matter search is briefly described below:

- *NA*64 is an existing experiment at CERN Super Proton Synchrotron (SPS) [45] combining the active beam dump and missing energy techniques to search for rare events in electron-nuclear fixed-target collisions. Dark matter is produced in beam-target collisions and registered as missing energy, which is measured from the electromagnetic shower of the recoil electron in a downstream electromagnetic calorimeter. The primary goal of the experiment is to search for light dark bosons from dark sector that are coupled to photons, such as dark photons, or sub-GeV Z' coupled only to quarks. The experiment can also search for meson (π^0, K_S, K_L, η) invisible decays. Recent results on upper limits to the kinetic mixing parameters are reported in Reference [46];

- *LDMX* [47] is a proposed experiment designed to search both for dark matter and mediator particles produced in the sub-GeV mass region in electron-nuclear fixed-target collisions. It is similar to *NA*64 and will use reaction $eZ \to eZ(A' \to \chi\bar{\chi})$ for the dark photon search. *LDMX* sensitivity to the kinetic mixing parameter ε is expected to be $\sim 10^{-7}$ for $m_{A'} = 1$ MeV/c^2.

- *PADME* at Laboratori Nazionali di Frascati (LNF) [48] is used to search for dark photon through the process $e^+e^- \to \gamma A', A' \to inv.$. The expected sensitivity on kinetic mixing parameter is $\varepsilon^2 \geq 10^{-7}$ for $m_{A'} < 26$ MeV/c^2.

For what concerns the latter, many experimental techniques exist, such as experiments at e^+e^- colliders that search for light dark matter with a mass of $\mathcal{O}(\mathrm{MeV}/c^2) - \mathcal{O}(\mathrm{GeV}/c^2)$, but also for visible and invisible light dark sector mediators introduced in the theory through Standard Model extensions. Light dark matter particles can be produced also at high-energy colliders through direct production in the collisions or in the decays of heavy gauge bosons or in the Higgs decays. These production mechanisms are predicted by many rich dark sector models, for this reason the ATLAS, CMS and LHCb experiments have a wider research program focused on dark sector searches that comprises:

- the search for Higgs decays in different final states as dark sector particles, dilepton resonances, b-quark resonances, low-mass dark matter particles and photons [49, 50];
- the search for new lepton resonances in semileptonic B meson decays [51];
- the search for lepton number violating processes in which the B mesons decay in sterile neutrinos [52] or new low-mass, long-lived, hadronically decaying particles [53]. Sterile neutrinos are hypothetical particles that does not interact with Standard Model particles through any Standard Model interaction, except for the gravitational interaction. They are right-handed neutrinos introduced in the Standard Model in order to give rise to the neutrino mass term naturally [54].

1.4.1 Searches at e^+e^- colliders

Since the thesis is focused on the search for a light dark sector mediator produced at *Belle II*, only constraints on dark sector from e^+e^- colliders will be discussed here, while in the next section we will also present the existing experimental constraints to different dark sector models from different experiments.

The light dark sector mediators can in principle be produced copiously at e^+e^- colliders. Many searches for the direct production of a dark photon have been performed by *BABAR* and *Belle* in the past, limiting the parameter region of different dark sector theoretical models, and even excluding some of them that would result in significant discrepancies with the observations. The advantages of e^+e^- colliders are the high luminosity, the perfectly known initial state and a clean environment with low multiplicity final states. In general, the processes being searched are $e^+e^- \to A'X$, where A' is the dark photon and X is the standard model component in the final state. The differential cross section of these processes are usually proportional to the square of the kinetic mixing coupling constant $\varepsilon^2\alpha^2$ and inversely proportional to the square of the energy in the center-of-mass frame s, $d\sigma \sim \varepsilon^2\alpha^2/s$.
If a light dark matter candidate χ exists and it couples with a massive dark photon with a mass at least $2m_\chi$, then the dark photon decays in an invisible final state like $A' \to \chi\bar{\chi}$. Additionally, the dark photon can be invisible also if it is cosmologically stable: this is possible if there are not other states in the dark sector, and the mass is small enough that the decay into Standard Model particles is heavily suppressed. The good acceptance coverage and the detector hermeticity make this search perfectly suitable to B-factory experiments. The *BABAR* experiment searched for an invisible dark photon through the process

$e^+e^- \to \gamma A'$, detecting events with a single initial-state-radiation photon in the final state [55]. The same search can be better performed by *Belle II*, which is equipped with a first level single photon trigger sensitive to single photon final states that was not available at *Belle* and was available only for $\sim 10\%$ of data at *BABAR* [56].

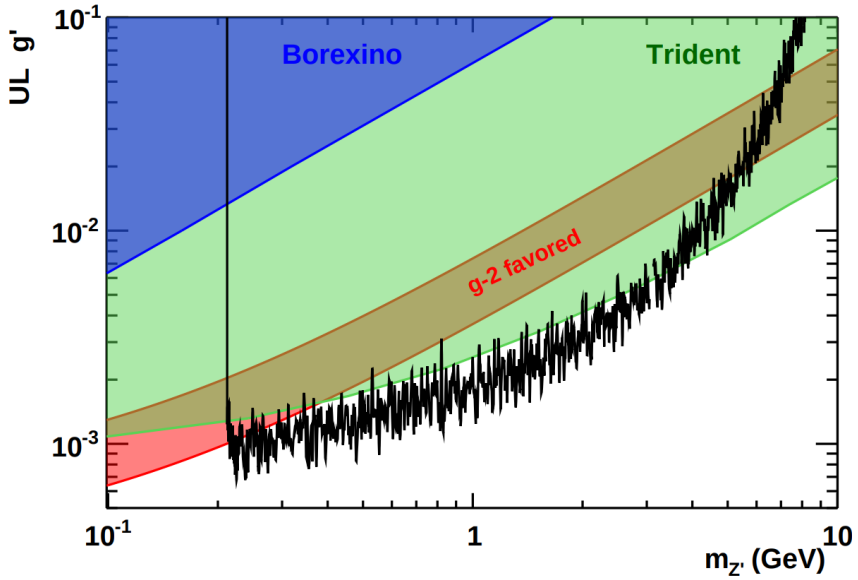

Figure 1.8 90% *CL* upper limit on the gauge coupling of the $L_\mu - L_\tau$ model, g', as a function of the Z' mass set by the *BABAR* experiment through the search for $Z' \to \mu^+\mu^-$.

Belle II already searched for an invisible Z' produced in association with a muon pair with the very first 0.276 fb^{-1} data collected in 2018, searching for the channel $e^+e^- \to \mu^+\mu^- Z', Z' \to inv.$ [57], where the invisible decay of the Z' can be in neutrinos, $Z' \to \nu\bar{\nu}$, or in light dark matter candidate χ if kinematically accessible. The analysis allowed to put 90% confidence level on the coupling constant of Z' to leptons, g', and exclude the region above $g' \sim 5 \times 10^{-2}$. It has been a first time search, and the first *Belle II* physics publication. I worked on this first *Belle II* dark sector search during my master thesis.
Belle II searched also for axion-like particles produced in e^+e^- collisions using the first 0.445 fb^{-1} collected in 2018, searching for $e^+e^- \to \gamma a, a \to \gamma\gamma$, where the axion-like particle ALP is prompt and photons can be well resolved by *Belle II*. The analysis allowed to put 95% confidence level upper limits on the coupling constant of the axion-like particle with photons, $g_{a\gamma\gamma}$, excluding the region above $g_{a\gamma\gamma} \sim 10^{-3}$ [58]. It has been the second *Belle II* physics publication, and the first on axion-like particles at *B*-factories.
The dark mediator can also be the lighter dark matter candidate and decay in visible Standard Model particles. *BABAR* performed the search for a visible Z' produced in the process $e^+e^- \to \mu^+\mu^- Z', Z' \to \mu^+\mu^-$ using a data sample of 514 fb^{-1} [59], and for a leptophilic dark scalar produced in the process $e^+e^- \to \tau^+\tau^-\phi_L, \phi_L \to l^+l^-$, where $(l = e, \mu)$ [33]. Figure 1.8 shows the upper limit on the coupling constant g' set by *BABAR* in the case of $Z' \to \mu\mu$, at 90% *CL*. Also *Belle* recently searched for a visible Z' produced in the process $e^+e^- \to \mu^+\mu^- Z', Z' \to \mu^+\mu^-$ using 643 fb^{-1} of data [60]. The *Belle II* data collected in

2020 will allow to extend these searches to $Z' \to \tau^+\tau^-$.

1.4.2 Experimental constraints to some dark matter and dark mediator models

Many constraints on several models exist from different experiments, such as fixed-target and collider experiments, briefly discussed above, but also from cosmological data and astrophysical data. The cosmological and astrophysical bounds are not discussed in this thesis, however the interested reader can found details in References [61–63]. Below, the state of the art of the existing constraints for some classes of dark sector models are presented. Figure 1.9 shows the existing constraints on the dark photon kinetic mixing parameter ε as a function of the dark photon mass for a invisibly-decaying (top) and a visibly-decaying (bottom) dark photon. In the latter plot, the expected upper limits on ε at *Belle II* are shown, assuming a integrated luminosity of 20 fb^{-1}. Even using a lower data sample, the expected result at *Belle II* is better than the measurement performed by *BABAR* with 53 fb^{-1} (green exclusion region) because of the larger acceptance of the detector, the better hermeticity and performance of the electromagnetic calorimeter and the veto on the photons undetected by the calorimeter, which is applied using the information provided by the K_L and μ detector, described in Chapter 2, allowing to reject a large component of background. For the sake of completeness, the main background component expected for this analysis at *Belle II* is the QED process with two photons in the final state one of which remains undetected. Finally, Figure 1.10 shows the existing limits and projections of future experiments, in particular *LDMX* and *Belle II*, searching for invisibly–decaying dark photons as a function of the hypothetical dark matter mass.

For what concerns the search for ALPs at the accelerators, experimental constraints come from studies of processes involving the coupling between ALPs and photons or ALPs and leptons. Being a the axion-like particle, the main channels include: $e^+e^- \to \gamma a$ at B factories or $pp \to \gamma a$ at LHC, Standard Model Higgs boson and electroweak Z boson decays ($h \to Za$, $h \to aa$ and $Z \to \gamma a$) where a decays in a photon pair or a lepton pair. Figure 1.11 shows the existing constraints on the couplings of ALPs respectively with leptons (right) and photons (left), coming from particle physics experiments, astroparticle physics and cosmological observations. However, the plot does not include the measurement performs by *Belle II* [58] and by some recent studies performed at LHC and discussed in Reference [64]. Recently, *BABAR* measured the coupling of ALPs to W boson [65]. The searches for ALPs at collider are sensitive to the couplings C_i/Λ in the range $\mathcal{O}(1\,\text{TeV})^{-1} \div \mathcal{O}(100\,\text{TeV})^{-1}$, where C_i are some appropriate coefficients in the effective Lagrangian of ALP interactions. The Λ parameter indicates a new-physics energy scale, which is the characteristic scale at which the spontaneous global symmetry breaking occurs. The $|C^{eff}_{\gamma\gamma}|$ and $|c^{eff}_{ll}|$ parameters are effective coefficients appearing in the axion decay width, respectively, in 2γ and in $2l$, which are reported for completeness in the following [37, 38]:

$$\Gamma(a \to \gamma\gamma) \sim \alpha m_a^2 \left(|C^{eff}_{\gamma\gamma}|/\Lambda\right)^2, \Gamma(a \to l^+l^-) \sim m_a m_l^2 \left(|c^{eff}_{ll}|/\Lambda\right)^2 \sqrt{1-4m_l^2/m_a^2}.$$

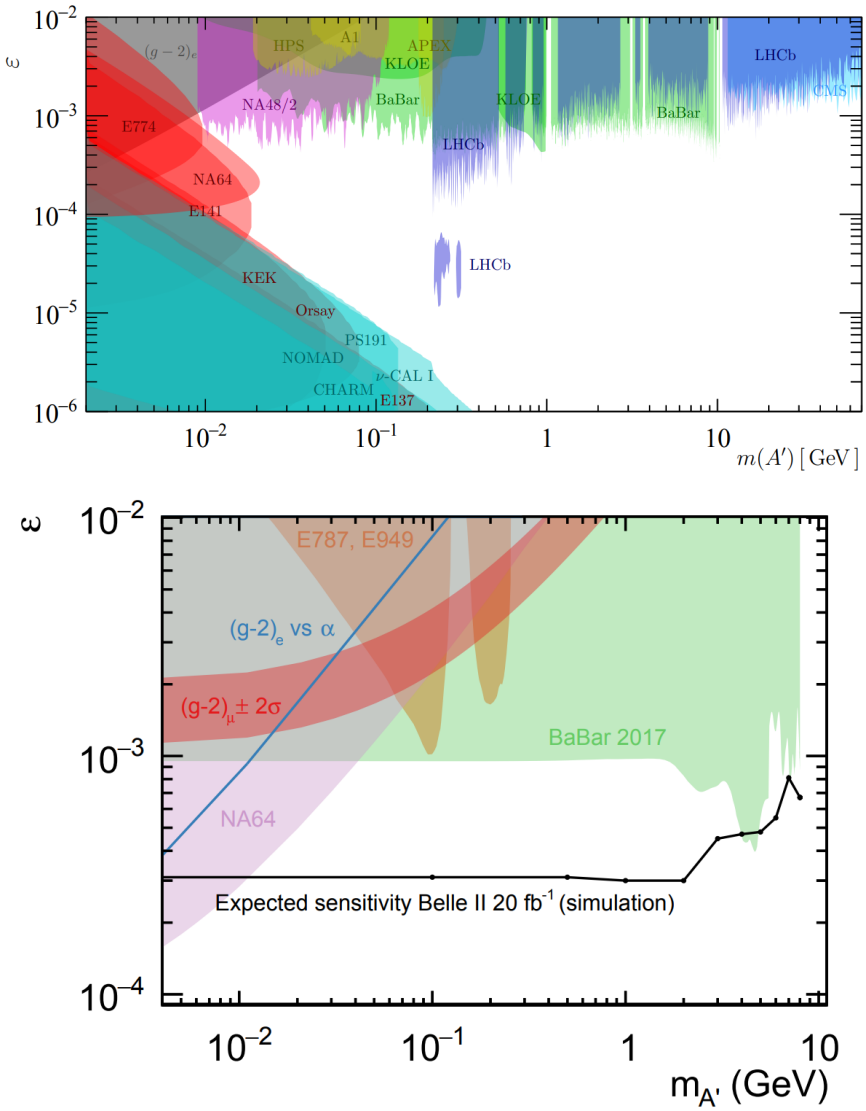

Figure 1.9 Top: Existing exclusion regions at 90% *CL* on the dark photon mixing parameter and mass m'_A for $A' \to ll$ [66]. Bottom: Existing exclusion limits regions at 90% *CL* to the kinetic mixing parameter ε as a function of the dark photon mass $m_{A'}$. In this case, also the upper limits expected at *Belle II* with 20 fb^{-1} are shown [56].

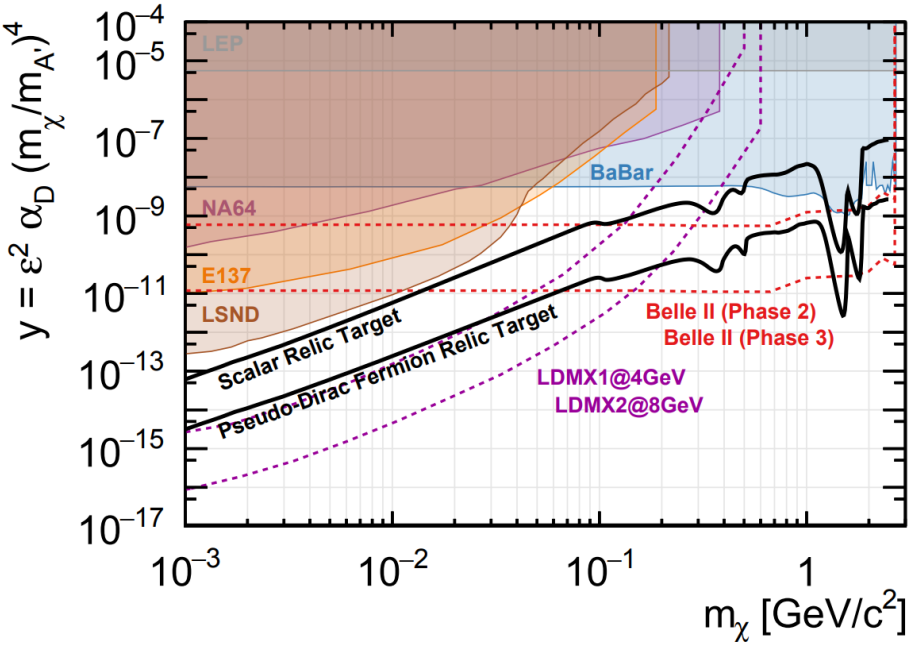

Figure 1.10 Projections (LDMX, Belle II) and constraints on the dark matter yields y from searches for a kinetically mixed dark photon coupled to a (nearly) elastically scattered light dark matter state at beam-dump, missing mass and missing momentum experiments, as a function of the dark matter candidate mass. Common assumptions for the limits are: the mass of the dark photon satisfies $m_{A'} = 3m_\chi$; the dark photon coupling to dark matter is $g_\chi = 0.5$ [56].

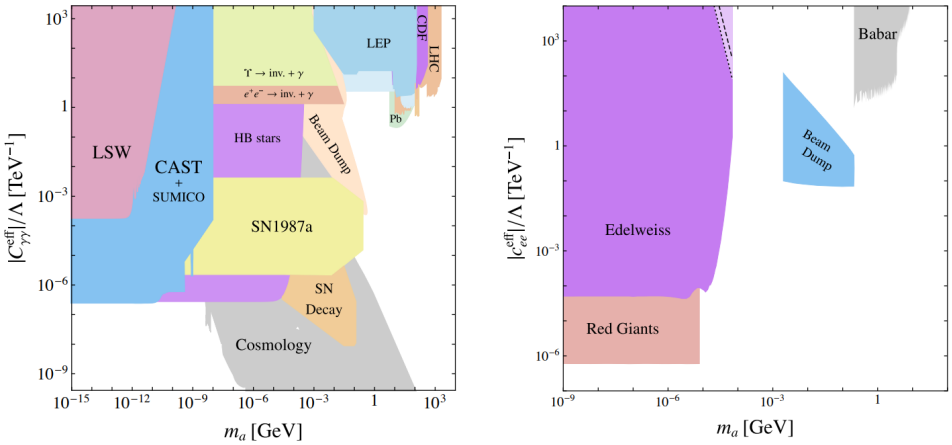

Figure 1.11 Left: Existing constraints on the ALPs-γ coupling. Right: Existing constraints on the ALPs-leptons coupling. The limit established by the *BABAR* experiment is a constraint on $|c_{\mu\mu}^{eff}|$ that can be interpreted as a limit on $|c_{ee}^{eff}|$ assuming $c_{\mu\mu} \approx c_{ee}$. The constraints are provided by particle physics experiment and astrophysical and cosmological observations [67].

2. The Belle *II* experiment

The *Belle II* experiment operates at the asymmetric collider SuperKEKB, located at the KEK laboratory in Tsukuba, Japan. It is a major upgrade of the *Belle* experiment. The SuperKEKB facility is a second generation B-factory designed to collide electron and positron at the energy in the center-of-mass frame corresponding to the Υ resonances. The collider is designed to operate with asymmetric beam energies to provide a boost to the center-of-mass system and thereby allow for time-dependent *CP* violation measurements. Most of data are collected at the $\Upsilon(4S)$ resonance, i.e. $\sqrt{s} = 10.58$ GeV.
SuperKEKB is designed to reach the highest world instantaneous luminosity of 6.5×10^{35} $\mathrm{cm}^{-2}\mathrm{s}^{-1}$, about 30 times higher than the luminosity reached by KEKB, thanks to the nano-beam scheme, originally developed for the SuperB concept [68], that allows to achieve high luminosity with only a moderate increase of beam currents. The basic idea of the nano-beam scheme is to reduce the beam size at the interaction point in order to improve the interaction probability and therefore the luminosity.
The *Belle II* detector is a magnetic spectometer with an angular coverage which exceeds the 90% of 4π and it is composed of several subdetectors installed around the interaction point, which allow to detect and reconstruct all the products of the e^+e^- interaction. Both SuperKEKB collider and *Belle II* detector are described in the following Sections.

2.1 Introduction to the *B*-factories

BABAR and *Belle* experiments are the first generation of *B*-factories. They were located respectively at the PEP-II (SLAC National Accelerator Laboratory) and at the KEKB (KEK) electron-positron colliders and they have been operational from 1999 to 2008. In the period of their activity they obtained important results in the study of beauty physics, charm physics, τ physics and in the search of new physics beyond the Standard Model. In particular their most relevant result was the discovery of *CP* violation in the *B* sector complemented by many precision measurement of CKM matrix elements as well as rare decay processes. *Belle II* is the upgrade of the *Belle* experiment and it is located at the SuperKEKB collider, which is the upgrade of the previous accelerator KEKB.

As discussed in Chapter 1, Standard Model has a lot of open questions and *Belle II* is designed to answer these questions through searches of new physics, thanks to the very high performance detector and the very high luminosity by the SuperKEKB collider that provides luminosity to the *Belle II* experiment. *Belle II* is planning on a thirty times higher statistics and improved performances with respect to the first generation of experiments at *B*-factories, so it can be very competitive in new physics searches. Some examples of the *Belle II* experiment searches are detailed below [56].

- The possibility that in the quark sector more than one *CP* violating phases able to explain the baryon/anti-baryon asymmetry are present. This possibility can be investigated examining the difference between B and $\bar{B}$ meson decay rates through time dependent *CP* violation measurements in transitions $b \to s$ and $b \to d$ or in the

charm mixing mechanism that, being suppressed in the SM, could be sensitive to new phenomena involving u-type quarks.

- Investigate models that foresee multiple Higgs bosons, also electromagnetically charged, in addition to the neutral Standard Model Higgs boson. The signature of these additional Higgs bosons can be searched in B meson leptonic and semileptonic decays involving τ leptons, for example $B \to \tau\nu_\tau$ and $B \to D^*\tau\nu_\tau$.

- The presence of flavour-changing neutral currents beyond Standard Model, improving measurements of $b \to s$, $b \to d$ and $c \to u$ transitions, for which the measurement of the $B \to K\nu\bar{\nu}$ decay is of great interest.

- Search of *Lepton Flavour Violating* processes, such as $\tau \to \mu\gamma$, which is forbidden in Standard Model.

- Search of hidden particles, coupling with Standard Model particles through new gauge symmetries, at the mass scale in the range MeV/c^2-GeV/c^2 predicted by *dark sector* models. These models predict a wide variety of dark matter candidates and new gauge bosons. An example is the *dark photon* search through the process $e^+e^- \to \gamma A'$, where A' is the dark photon that can decay visibly or invisibly.

- Detailed analysis of bound states of quark or multiquark states, as quarkonium, to better understand the nature of the strong force in hadrons.

In this section the physics of the B-factories is introduced.

2.2 Overview of experimental methods of B-Factories

B-factories are e^+e^- colliders designed to study the physics of B mesons providing a clean environment and a perfectly known initial state. The idea of B-Factories was born from the necessity to have big samples of B mesons in order to measure the CP violation in the B sector. The advantages of these experiments are the asymmetric beam energies, necessary for time-dependent measurement, and the possibility to reach a very high peak luminosity ($\mathcal{O}(10^{34})$). For the sake of completeness, it is worth saying that the CP violation in K meson system was observed for the first time in 1964 in the experiment performed by physicist J. Cronin and V. Fitch realized at the Alternating Gradient Synchrotron installed at the BNL, Brookhaven, New York [69].
At B-factories, $B^0\bar{B}^0$ meson pairs and B^+B^- meson pairs are produced through electron-positron collisions at the $\Upsilon(4S)$ resonance energy peak in the center-of-mass reference system: $\sqrt{s} = M_{\Upsilon(4S)} = 10.58$ GeV. The $\Upsilon(4S)$ resonance is a bound state of one b quark and one $\bar{b}$ anti-quark and it is the first bottomonium state whose mass allows the decay in a B meson pair. The properties of the $\Upsilon(4S)$ resonance, of B mesons produced by the decay of the $\Upsilon(4S)$, and the production cross sections for different processes at the $\Upsilon(4S)$ energy in the center of mass are listed in Table 2.1. The branching ratio of the $\Upsilon(4S)$ decay in B mesons is higher than 96% [2, 56, 70], however many other particles are produced in

	M (MeV/c^2)	J^{PC}	Γ (MeV)	Composition in quarks
$\Upsilon(4S)$	10579 ± 1.2	1^{--}	20.5 ± 2.5	$b\bar{b}$

	M (MeV/c^2)	J^P	τ_B ($\cdot 10^{-12} s$)	Composition in quarks
B^0	5279.58 ± 0.17	0^-	1.519 ± 0.007	$d\bar{b}$
B^+	5279.25 ± 0.17	0^-	1.641 ± 0.008	$u\bar{b}$

$e^+e^- \rightarrow$	$b\bar{b}$	$c\bar{c}$	$s\bar{s}$	$u\bar{u}$	$d\bar{d}$	$\tau^+\tau^-$	$\mu^+\mu^-$	e^+e^-
Cross section (nb)	1.05	1.30	0.35	0.39	0.35	0.94	1.16	$\sim$40

Table 2.1 The table reports the properties of the $\Upsilon(4S)$ and of B mesons B^0B^+. The values have been taken from the PDG [2]. B mesons are not eigenstates of charge conjugation, indeed they are composed by two quarks, one of which is heavier than the other, hence J^P, and not J^{PC}, is listed for B mesons. In the last two lines: the production cross sections in e^+e^- annihilation for different processes evaluated at the $\Upsilon(4S)$ energy in the center of mass, $\sqrt{s} = 10.58$ GeV/c^2 [71].

e^+e^- collisions at B-factories, like D mesons and τ leptons, allowing to explore different sectors of physics.

The relevant features of B-factories are reported in the following [70], with the indication they are modified in SuperKEKB:

- an asymmetric e^+e^- collider is needed because the Q-value of the process $\Upsilon(4S) \rightarrow BB$ is $Q = M_{\Upsilon(4S)} - 2M_B \simeq 20\text{MeV}/c^2$, hence the momentum of the B meson in the CM frame is very small, about $p^*_B \approx 300$ MeV/c, so B mesons are produced almost at rest in the CM reference system. In the case of symmetric colliders, like the CLEO experiment at CESR [72], the short lifetime of B mesons leads a displacement between the primary interaction vertex and the decay vertex of B mesons of about 30 μm that is hardly measurable, considering the state-of-the-art of vertex detectors. An asymmetric collider provides a Lorentz boost of the CM frame in order to improve the decay length $l = c\tau\beta\gamma$ of B mesons in the laboratory frame. The boost allows to reconstruct the decay vertices and to extract temporal information;

- high luminosity was required for CP violation studies in the B sector, since B mesons have many decay channels with a small branching ratio. For example, the process $B^0 \rightarrow J/\psi K_S$, $J/\psi \rightarrow l^+l^-$ is very interesting for CP violation studies since it is directly related to the measurement of the β parameter of the unitarity triangle shown in Figure 1.1, however its B meson decay branching ratio is around

10^{-4}. In the new generation of B-factories an even higher luminosity is required for studies of processes that are suppressed in the Standard Model and are sensitive to new physics. The first generation of B-factories reached a peak luminosity of about $2 \cdot 10^{34}\,\mathrm{cm}^{-2}\mathrm{s}^{-1}$, while SuperKEKB aims to reach a peak luminosity of $6.5 \cdot 10^{35}\mathrm{cm}^{-2}\mathrm{s}^{-1}$;

- a clean environment with a high signal-to-noise-ratio for $b\bar{b}$ events. These events are characterized by a higher mean charged multiplicity, around 11 tracks for event, with respect to background events, as shown in Figure 2.1. Furthermore, the clean environment allows to apply simple trigger strategies;

- a hermetic detector designed to observe all decay products of the interaction between e^+ and e^- in the collider: the detector covers the greatest possible geometric acceptance around the interaction region and it incorporates multiple sub-detectors. The performance of the detector in the reconstruction of neutral particles as π^0 and γ is also relevant, such as the performance in reconstruction of missing energy;

- the initial state and the energy of B mesons in the center of mass reference system are completely known and it is possible exploit these information to apply kinematical constraints on reconstructed candidates. This is relevant for the rejection of the background.

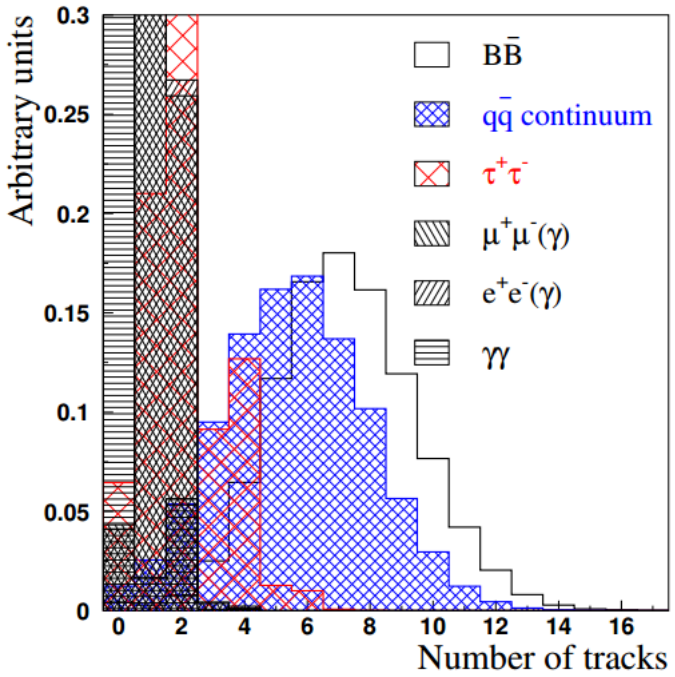

Figure 2.1 The figure shows the number of charged tracks per event for different processes. The graph was taken from section 9.4.1 of *The Physics of the B factories* [70].

B-factories detectors

The main requirements of the *B*-factories detectors and some solutions adopted by *Belle II* are in the following.

- Low material budget for inner detectors in order to reduce multiple scattering effects: for example, beryllium was chosen for the central part of the beam pipe, since it has a low atomic number, so multiple scattering and the loss of energy of particles crossing the beam pipes are minimized.

- Vertex detection capability in order to determine the B meson decay vertex with high precision: it is fundamental for time dependent CP violation measurements. Strip-vertex detectors are used for this purpose. The *Belle II* vertex detector is composed by a Pixel Vertex Detector and a Silicon Vertex Detector based on double-sided strip detectors.

- Particle identification (PID) capability to classify particles in the final state. A Central Drift Chamber able to provide measures of dE/dx to perform PID of low momentum tracks is installed into the detectors. In addition to the Central Drift Chamber, a Time-of-Propagation detector and an Aerogel Ring-Imaging Cherenkov detector for PID of high momentum tracks are installed on the *Belle II* detector.

- An electromagnetic calorimeter, to accurately measure photon and electron energies and providing good electron ID. In *Belle II* is composed of CsI(Tl) crystals, in order to measure the energy of both electron and neutral particle final states.

- K_L mesons and μ detectors because, the K_L mesons have a long mean lifetime, $\tau_{K_L} \approx 5 \cdot 10^{-8}$ s, hence they cross the whole detector and can only be detected through their hadronic interactions in the outer detector. Muons also cross the whole detector because they interact little compared to electrons. It is very important detect efficiently K_L and μ because some processes, as for example $B^0 \to J/\psi K_S$ and $B^0 \to J/\psi K_L$ where $J/\psi \to l^+ l^-$, are fundamental to verify CP violation in B meson decays. *Belle II* is equipped with a K_L and μ detector.

- A fast and reliable trigger system with high efficiency for hadronic events from $\Upsilon(4S) \to B\bar{B}$ and continuum production of quark pairs and a configuration that is flexible and robust.

- Significant computing power is needed to manage the big data flow from the detectors electronic to the storage system. This is achieved by a combination of local computing farms for prompt event reconstruction and high level trigger, and a distributed (Grid) computing environment

A detailed description of the *Belle II* apparatus is provided in Section 2.5.

2.3 *B*-factories colliders

To reach a peak luminosity higher than $10^{33}\text{cm}^{-2}\text{s}^{-1}$ and a Lorentz boost factor $\beta\gamma$ that allows to observe the time evolution of B meson decays, the accelerators of B-factories are constituted of two different storage rings, one for electrons and one for positrons, allowing asymmetric beam energies. Only one interaction region for the detectors is present, to optimize the luminosity. The general expression for peak luminosity of e^+e^- colliders is:

$$\mathscr{L} = \frac{N_b n_{e^+} n_{e^-} f}{\mathscr{A}_{eff}} \tag{2.1}$$

The number of bunches is N_b, the number of electrons and positrons for each bunch are respectively n_{e^+} and n_{e^-}, the circulation frequency is f and $\mathscr{A}_{eff}$ is the effective overlapping area of the two beams at the interaction point. When high currents circulate in the rings the $\mathscr{A}_{eff}$ parameter becomes strongly beam-current dependent and increases together with $N_b n_{e^+} n_{e^-}$.
Increasing the beam current to enhance the peak luminosity can lead to bunch instabilities along the entire ring that can be caused by coupling between bunches. For example, if the number of bunches N_b increases, the separation between bunches decreases and they can feel effects of near bunches. Another cause for bunch instabilities are the interactions between electrons in the bunches and the residual gas ions in the beam pipes, or between positrons and photoelectrons emitted by the interactions between synchrotron X-rays and beam pipe walls. High currents can also be harmful for hardware components of the accelerator and of the detectors: a very good vacuum level throughout the beam pipes is necessary in order to limit the damage due to high currents in an environment in which hardware components already suffer a large bombardment of synchrotron radiation. In order to achieve a high luminosity is necessary to optimize the fundamental parameters in the definition of the luminosity.

PEP-II and KEKB are the first generation of B-factories providing luminosity respectively to *BABAR* and *Belle* experiments. In Figure 2.2, a schematic representation of PEP-II and KEKB colliders is shown. In Table 2.2 the data set size achieved by *BABAR* and *Belle* experiments are reported [70, 73].

		On-Resonance		Off-Resonance
		$\int \mathscr{L}$ [fb^{-1}]	$\Upsilon(4S)$	$\int \mathscr{L}_{int}$ [fb^{-1}]
BABAR and *Belle*		424.2	$(471.0 \pm 2.8) \cdot 10^6$	43.9
Belle	SVD-1	140	$(152 \pm 1) \cdot 10^6$	15.6
	SVD-2	571	$(620 \pm 9) \cdot 10^6$	73.8

Table 2.2 Summary of the time integrated luminosity on- and off-peak at the energy of the $\Upsilon(4S)$ achieved by *BABAR* and *Belle* experiments, and of the number of $\Upsilon(4S)$ particles collected by the two experiments.

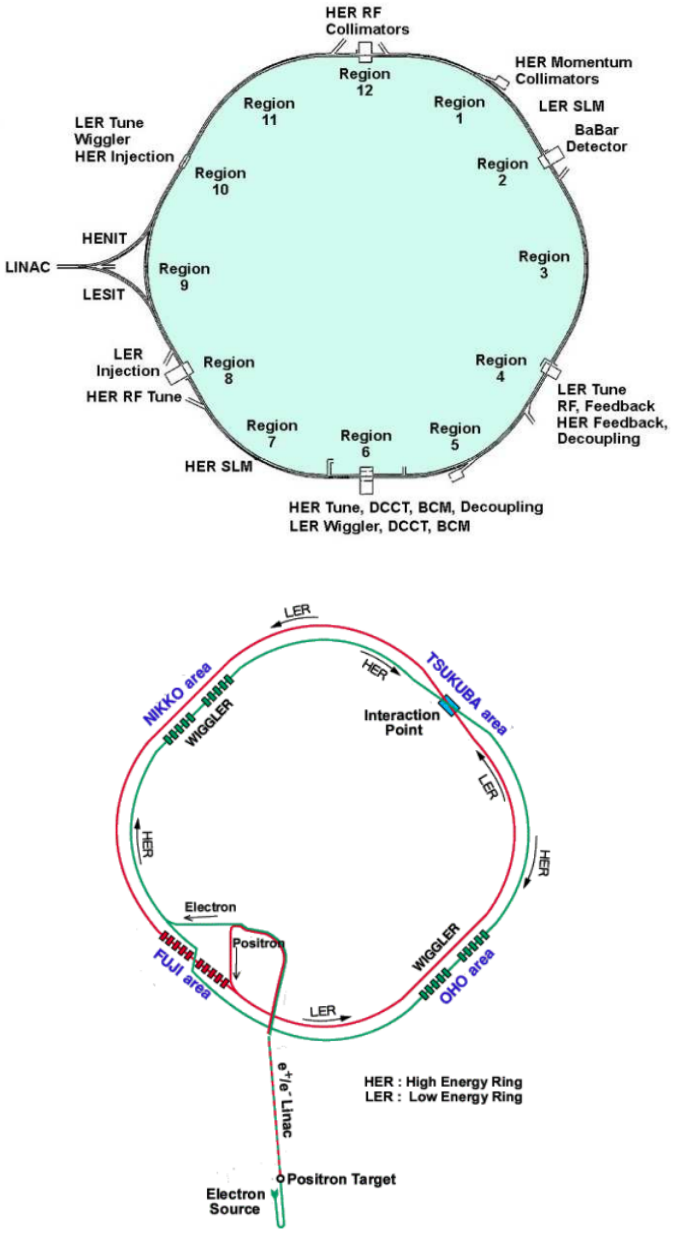

Figure 2.2 Schematic view of PEP-II and KEKB accelerators (top and bottom respectively). In KEKB the two beams circulate inside the rings one next to the other, while in PEP-II the two rings are one on the top of the other. The images are taken from Section 1.2.4 of *The Physics of the B factories* [70].

The second generation of *B*-factories starts from the KEKB to SuperKEKB upgrade, which is the accelerator designed to provide the luminosity to the *Belle II* experiment.

2.4 The SuperKEKB collider

SuperKEKB is an asymmetric electron-positron collider operating at the $\Upsilon(4S)$ energy peak in the center of mass (CM). The electron beam is generated in the pre-injector, located at the beginning of the linear accelerator (LINAC), through a short-pulse photons laser irradiating a cold cathode. The positron beam is generated irradiating a fix target of tungsten with electrons produced in a different higher intensity pre-injector. Positrons are produced as secondary particles of interactions between electrons and tungsten nuclei.
The electron beam is characterized by low emittance, which is a property of charged particle beams that measures the average spread of the beam in momentum and position phase-space. Low emittance beams are composed of particles with nearly the same momentum and confined in a small space, an essential requirement to obtain high luminosity. The emittance of the positron beam at its production is much higher because of the mechanism used to produce positrons. In order to reduce the emittance of the positron beam before storage in the main ring, a damping ring reducing the emittance by a factor of 130 has been built as part of the SuperKEKB upgrade. After the beam production, the electron beam is accelerated in the LINAC up to the energy of $E_{e^-} = 7$ GeV and then it is stored in the High Energy Ring (HER); the positron beam is accelerated in the LINAC up to an energy of $E_{e^+} = 4$ GeV and then stored in the Low Energy Ring (LER). The e^- and e^+ beams collide at the interaction point inside of the *Belle II* detector. The energy in the CM is [73]:

$$\sqrt{s} = \sqrt{(p_{e^+} + p_{e^-})^2} \simeq 2\sqrt{E_{e^+}E_{e^-}} \simeq 10.58 \text{ GeV} \tag{2.2}$$

The asymmetric energy of electron and positron beams produces a Lorentz boost $\beta\gamma$ of the CM in the laboratory reference system:

$$\beta\gamma = \frac{E_{e^-} - E_{e^+}}{\sqrt{s}} \simeq 0.28 \tag{2.3}$$

The boost allows to separate the decay vertices of B mesons. A schematic view of the SuperKEKB collider realized in the same tunnel as KEKB is shown in Figure 2.3.

The nano-beam scheme is schematically shown in Figure 2.4, is necessary to achieve higher luminosity with only a moderate increase of beam currents. The basic idea of the nano-beam scheme is to reduce the vertical betatron function β_y^* at the IP in order to improve the instantaneous luminosity $\mathscr{L}$ of the accelerator that depends on β_y^* as $\mathscr{L} \sim (\beta_y^*)^{-1}$. The betatron function is associated to the transverse size of beams at position x along the trajectory and is related to the width $\sigma(x)$ and the emittance ε of the beam in the position x: $\sigma(x) = \sqrt{\varepsilon\beta(x)}$. The reduction of β_y^* is possible minimizing the size of the overlapped region d of the HER and LER beams that limits the minimum value of β_y^*. The overlap region d depends on the angle ϕ and on the horizontal size of the beam σ_x^* as shown in Equation 2.4 [73].

$$d \cdot sin(2\phi) = 2\sigma_x^* \rightarrow d \simeq \frac{\sigma_x^*}{\phi} \tag{2.4}$$

SuperKEKB is equipped with a final focus system, called QCS [74], composed of four quadrupole magnets installed very close to the IP to achieve the goal of reducing β_y^* up to

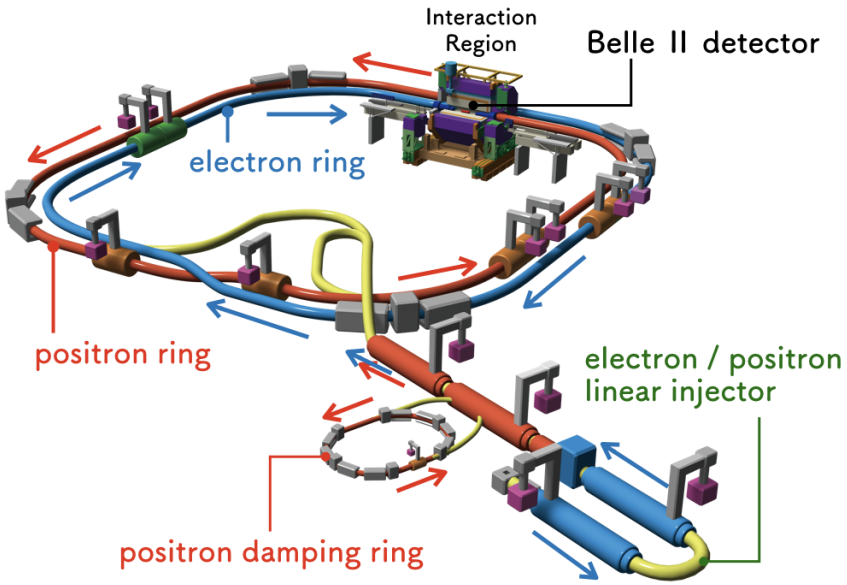

Figure 2.3 Schematic view of the SuperKEKB collider.

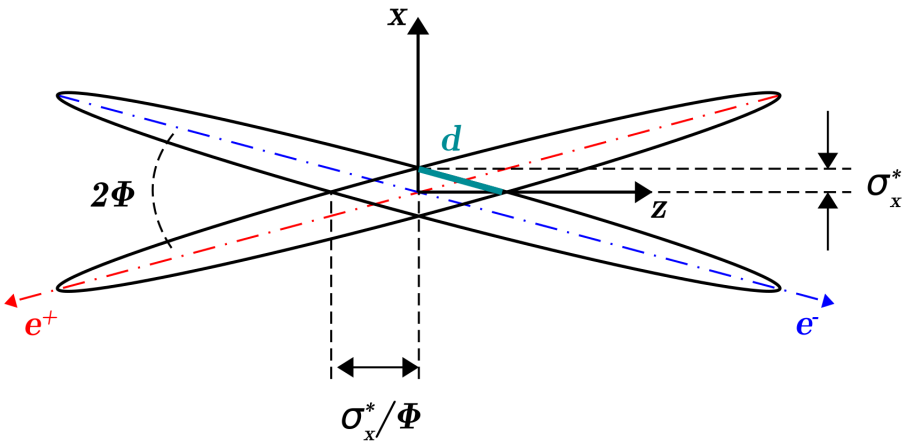

Figure 2.4 Representation of the nano-beam scheme: σ_x^* is the horizontal beam size, d is the size of the overlap region and ϕ is half of the horizontal crossing angle.

0.3 mm.
Assuming flat beams, the expression of the instantaneous luminosity is [73]:

$$\mathscr{L} = \frac{\gamma_\pm}{2er_e}\left(1+\frac{\sigma_y^*}{\sigma_x^*}\right)\frac{I_\pm \xi_{y\pm}}{\beta_{y\pm}^*}\frac{R_L}{R_{\xi_y}} \tag{2.5}$$

where $+$ and $-$ subscripts are respectively for the LER and for the HER, γ is the Lorentz factor, e is the electron charge, r_e is the electron classical radius, I is the total beam current, $\xi_{y\pm}$ is the vertical-beam parameter and β_y^* is the vertical betatron function. The R_L and R_{ξ_y} parameters are reduction factors for the luminosity and the vertical beam-beam parameter.

The ratio R_L/R_{ξ_y} is approximately 1, so the most relevant parameters in the luminosity definition are the total current of the beams $I_\pm$, the vertical beam-beam parameter $\xi_{y\pm}$ and the betatron function $\beta^*_{y\pm}$. The beam-beam parameter quantifies the strength of the interaction between the beams and a higher value of this parameter is related to a higher value of the luminosity. The tuning of these parameters allows to achieve the luminosity goal of SuperKEKB that is 30 times higher than the luminosity peak achieved by KEKB: $\mathscr{L} = 6.5 \cdot 10^{35}$ cm^{-2}s^{-1}. The main machine parameters of the three B-factories colliders are reported in Table 2.3 [70, 73].

Parameters		Units	PEP-II achieved (LER/HER)	KEKB achieved (LER/HER)	SuperKEKB (LER/HER)
Beam Energy	E	GeV	3.1/9	3.5/8	4/7
Beam Current	I	A	2.7/1.8	1.6/1.2	3.6/2.62
Beam sizes at the IP	σ^*_x	μm	140	80	10.2/11.2
	σ^*_y	μm	3	1	0.048/0.062
	σ_z	mm	8.5	5	6/5
Betatron function	β^*_y	mm			0.3/0.3
Lorentz boost factor	$\beta\gamma$		0.56	0.43	0.28
Number of bunches	N_b		1732	1584	2503
Beam crossing angle	2ϕ	mrad	0	22	83
Beam-beam parameter	ξ^*_y			0.129/0.090	0.090/0.088
Horizontal emittance	ε_x	nm			3.2/5.1
Emittance ratio	$\varepsilon_y/\varepsilon_x$	%			0.27/0.25
Luminosity	$\mathscr{L}(\cdot 10^{34})$	cm^{-2}s^{-1}	1.2	2.11	65

Table 2.3 The main machine parameters achieved by PEP-II and KEKB at the end of their activity compared to those chosen for SuperKEKB in order to achieve the luminosity goal.

In SuperKEKB the boost is reduced with respect to KEKB to improve the luminosity of the accelerator and the decay length of B mesons varies from ∼200 μm to ∼130 μm. The reduction the decay length is compensated by reducing the distance of the vertex detector from the interaction point and by introducing a pixel detector that improves the vertex resolution.

The *Belle II* experiment has two data taking period called Phase-2 and Phase-3. Phase-2, started in February 2018 and ended in July 2018, has been a test bench in preparation for Phase-3. It has been dedicated to the study of the response of the *Belle II* detector and of the accelerator. This phase was relevant also for tuning the machine parameters and measure the background. In this phase the vertex detector was not installed inside *Belle II*, to avoid possible damage in early machine operations. Instead, the BEAST II detector was installed. It was composed of several different radiation monitor systems and of a sector of the vertex detector. A sample of 505 pb^{-1} of data at the $\Upsilon(4S)$ peak has been collected and it has been used to measure the luminosity reached, to validate the simulations through the comparison between data and Monte Carlo samples, to calibrate the individual sub-detectors, and to perform material mapping. In particular the Phase-2 has been very

important to learn how to operate the whole machine, to better understand the problems to be faced in future, and for the commissioning of the sub-detectors for Phase-3. The data sample collected during the Phase-2 has been also used to do initial physics analysis, in particular to establish reconstruction of well known particles. Moreover, data collected has been used for dark sector analyses, which do not require the vertexing system and can be done also with low statistics: the search for and invisible Z' [57] and the search for axion-like particles [58] are the first physics results of the *Belle II* experiment. Phase-3 started on March 2019 and it is ongoing. In this phase the whole detector is installed and thanks to the complete vertex detector is be possible to do flavour physics analysis. The target integrated luminosity is of $\mathscr{L}_{int} = 50$ ab^{-1}: thirty times the total integrated luminosity collected by *BABAR* and *Belle*. At least 70% of the total data set is estimated that will be on-peak at the energy of the $\Upsilon(4S)$ [73].
Up to now *Belle II* collected more than 260 fb^{-1}, and Figure 2.5 shows the profile of integrated luminosity collected from the beginning of Phase-3. Table 2.4 shows the integrated luminosity collected in the different data taking periods. During Phase-3:

Data taking period	$\int \mathscr{L}$ on-$\Upsilon(4S)$ [fb]$^{-1}$	$\int \mathscr{L}$ off-$\Upsilon(4S)$ [fb]$^{-1}$
2019	8.6	0.8
2020a-b	54.7	8.7
2020c	16.4	-
2021a-b	110.2	8.4
2021c	55.4	-
Total	245.3	18

Table 2.4 Integrated luminosity collected during the different run periods. Run period a-b is from February to the beginning of July, while run period c is from October to the end of December.

- SuperKEKB set a new luminosity record on June 22nd 2021, reaching the peak luminosity of 3.12×10^{34} cm^{-2}s^{-1};
- *Belle II* has come to integrate 2 fb^{-1} a day and 12 fb^{-1} a week;

Table 2.5 shows some of the main machine parameters achieved by SuperKEKB in 2021 run. Figure 2.6 shows the mid-term schedule for the integrated luminosity delivered by SuperKEKB to Belle II, assuming two different scenarios:

- target scenario: extrapolation from early 2021 run including expected improvements. SuperKEKB will deliver 1.3 ab^{-1} by Summer 2024;
- base scenario: conservative extrapolation of SuperKEKB parameters from early 2021 runs. SuperKEKB will deliver 0.9 ab^{-1} by Summer 2024.

Both scenarios consider a long shutdown that it is scheduled at the beginning of 2023, necessary mainly to install a completely new Pixel Detector and to replace the photo-multipliers of the Time-of-propagation detector, whose performances are reduced by high background levels.

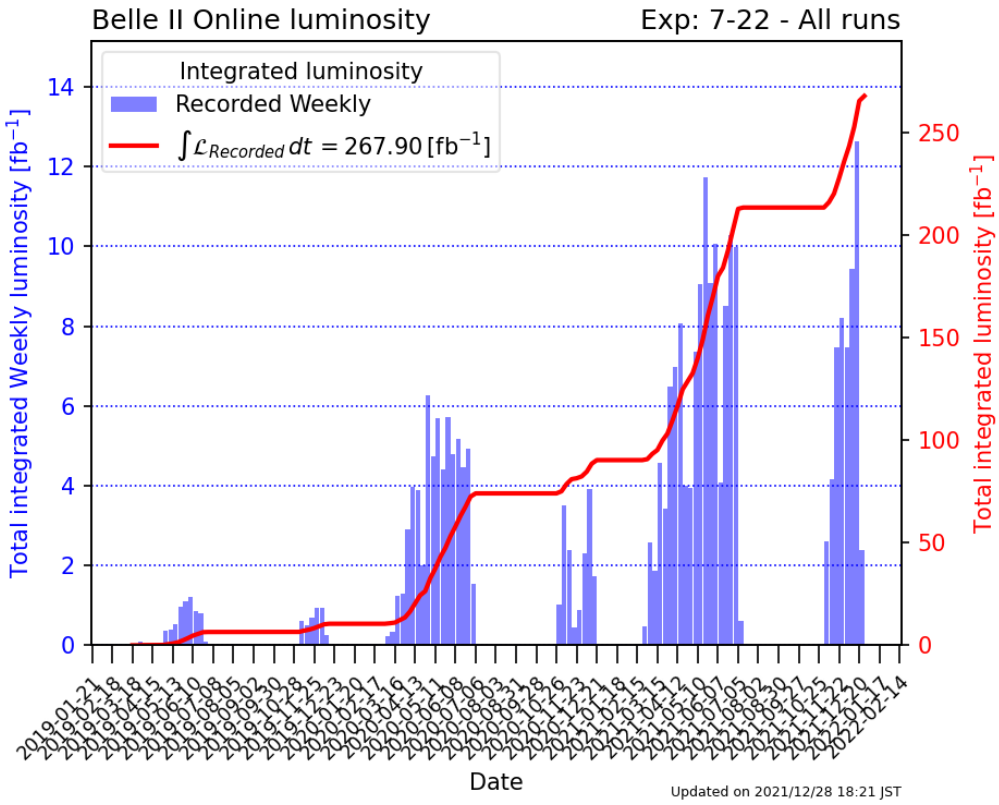

Figure 2.5 Total recorded integrated luminosity during Phase-3.

Parameters		Units	SuperKEKB achieved (LER/HER)
Beam Energy	E	GeV	4/7
Beam Current	I	A	1.015/0.797
Beam sizes at the IP	σ_x^*	µm	17.9/16.6
	σ_y^*	µm	0.24/0.24
Lorentz boost factor	$\beta\gamma$		0.28
Number of bunches	N_b		1370
Beam-beam parameter	ξ_y^*		0.0433/0.0315
Betatron function	β_y^*	mm	1.0/1.0
Luminosity	$\mathscr{L}(\cdot 10^{34})$	cm^{-2}s^{-1}	3.81

Table 2.5 Some of the main machine parameters achieved by SuperKEKB in 2021 run.

At the time of writing this thesis, the analysis is meant to be performed on 54.7 fb^{-1} collected at $\Upsilon(4S)$ resonance at *Belle II* in 2020a-b, while the original plan was to use data collected at $\Upsilon(4S)$ in 2019 and 2020a-b-c corresponding to 80 fb^{-1}. The reason is mainly due to the different software release used to produce the official MC that we use (the only available during most of the period of the analysis) and to reprocess data collected

in 2020c and in 2021. Furthermore, we does not include data collected in 2019, to avoid possible additional discrepancies mainly due to trigger lines used in the analysis that were not fully available in the 2019 dataset. Data collected off-resonance were not considered because we can not validate the analysis on them since the official MC does not exist for off-resonance.

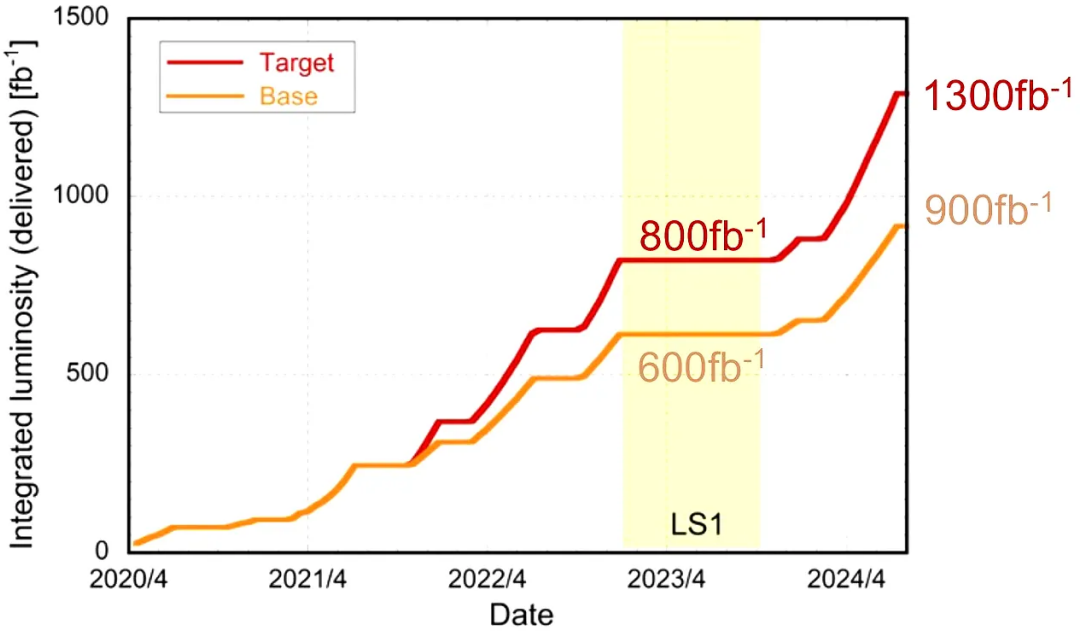

Figure 2.6 Schedule for the integrated luminosity delivered by SuperKEKB to *Belle II* by Summer 2024, assuming two different scenarios.

2.5 The Belle *II* detector

The *Belle II* detector is designed to maintain high performances in an environment characterized by high background levels, with an improvement in luminosity and precision with respect to the *Belle* detector. Because of higher currents, smaller beam size and modified IR, the background hit rate is estimated to be twenty times higher and the event hit rate is estimated to be fifty times higher with respect to those of *Belle*. The main components of the *Belle*II detector are listed here and described in more detail in the following sections:

- two layers of silicon Pixel Detector, just outside the beam pipe. The PXD is based on DEPFET technology and it has an excellent spatial resolution that improves the vertex resolution;

- a Silicon Vertex Detector based on double-sided silicon strip sensors used for the reconstruction of charged particles, which occupies a larger volume and is positioned closer to the interaction point compared to the *Belle* Silicon Vertex Detector: this improves the efficiency of event reconstruction for events as $K_S \to \pi^+\pi^-$. Silicon

Vertex Detector signals are read by APV25 chips that are faster than chips used in the *Belle* detector in order to face the high hit rate;

- an axial-stereo Central Drift Chamber that occupies a larger volume and has a higher granularity than the *Belle* CDC;
- a particle identification system based on Cherenkov effect, with the Time-of-propagation detector located in the barrel region and the Aerogel Ring Imaging Cherenkov detector located in the forward endcap region, are completely new and have a fast readout system. They especially improve the separation efficiency between pions and kaons;
- an electromagnetic calorimeter that reuses the CsI(Tl) crystals from *Belle*, but it has a faster readout electronics that reduces the occupancy and pileup. This is very important for missing energy studies;
- a K_L and μ detector composed of resistive plate chambers in the outermost layers of the barrel region and of scintillators, which are read by silicon photo-multipliers, in the innermost layers of the barrel region and in the endcaps;
- a fast readout electronics of the sub-detectors and a fast trigger system able to face the high hit rate.

Finally some details of the software framework will also be given. The full detector is described in detail in Reference [73]. The schematic view of the detector is shown in Figure 2.8, while Figure 2.7 shows the coordinate system of *Belle II*. In Table 2.6, the design performances of the detector discussed in the following sections are summarized.

	Belle II detector design performances
B vertex reconstruction	σ_z = 26 μm
Tracking	$\sigma_{pt}/pt = 0.0011\,pt[\mathrm{GeV}/c] \oplus 0.0025/\beta$
K/π ID	$\varepsilon_K \simeq 0.90$ with pion fake rate $\varepsilon_\pi \simeq 0.04$ for $p = 2$ GeV/c tracks
Calorimeter resolution	$\sigma_E/E = 7.7\%$ at 0.1 GeV and 2.25% at 1 GeV
Muon ID	$\varepsilon_\mu = 0.92 - 0.98$, fake rate $\varepsilon = 0.02 - 0.06$ for $p > 1$ GeV/c
L1 Trigger	30 kHz max average rate, with efficiency for hadronic events $\varepsilon_{hadron} \simeq 1$
Data Acquisition System (DAQ)	<3% dead time at 30 kHz L1 rate

Table 2.6 Summary table of the detector design performances. The table has been taken from Reference [76].

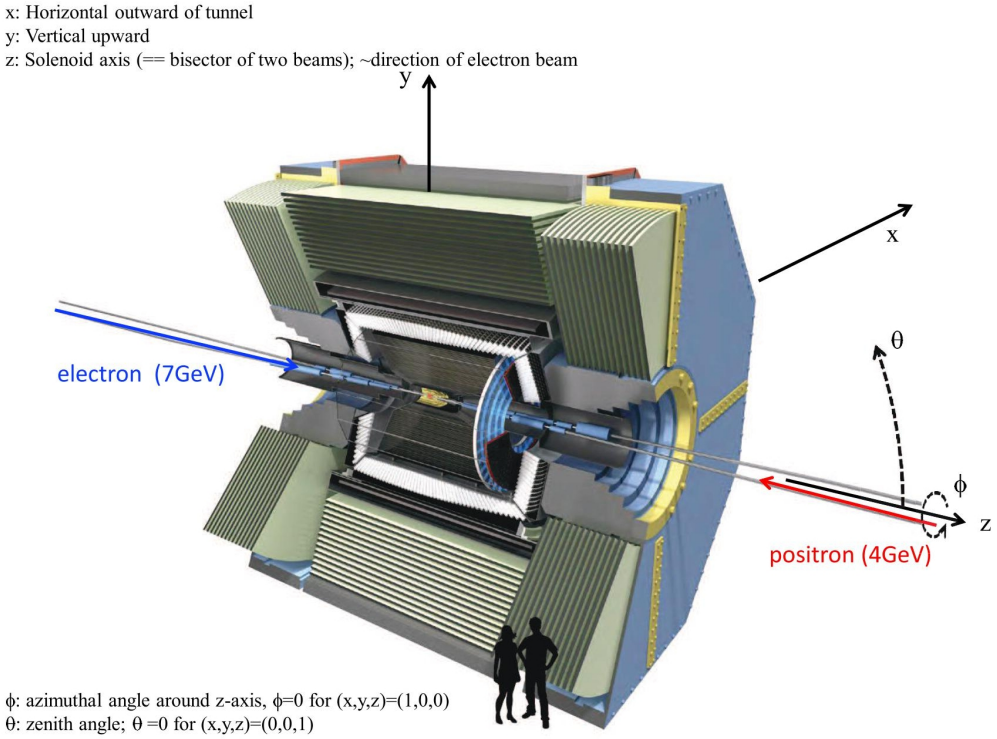

Figure 2.7 3D representation of the *Belle II* detector. The coordinate system is shown: the x coordinate is directed opposite compared to the center of the accelerator, the y coordinate is directed upward and the z coordinate is the bisector of the two beams and is directed towards the forward region, which is defined by the Lorentz boost of the center of mass (the interaction point is in $x = y = z = 0$, $+z$ is the forward region of the detector, while $-z$ is the backward region of the detector). The θ angle is the polar angle and $\theta = 0$ for $(x, y, z) = (0, 0, 1)$, while ϕ is the azimuthal angle and $\phi = 0$ for $(x, y, z) = (1, 0, 0)$. The image is taken from [75].

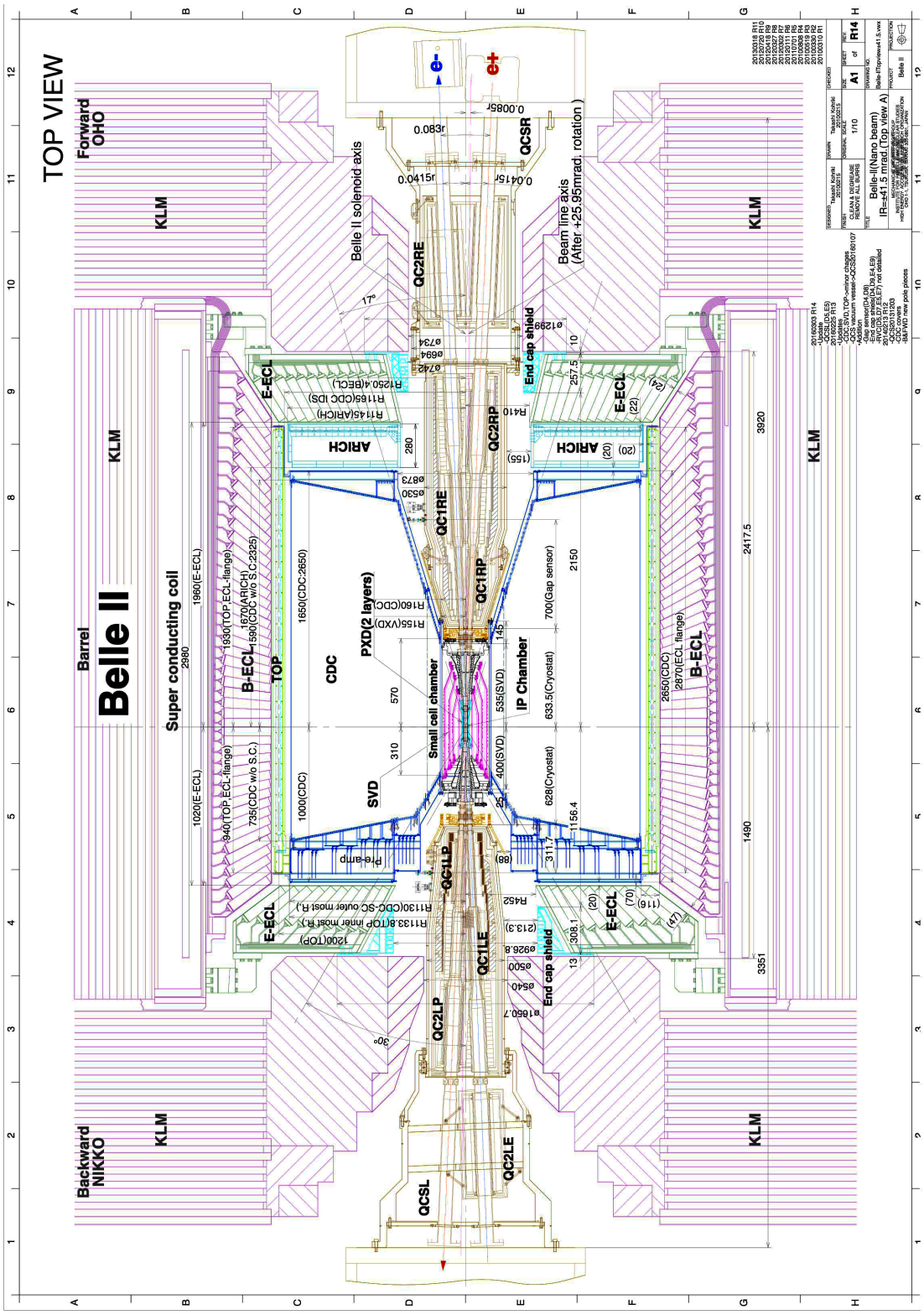

Figure 2.8 Side section of the *Belle II* detector. The image is taken from Reference [76].

2.5.1 The Vertex Detector (VXD)

Figure 2.9 shows the cross-section view of the *Belle II* Vertex Detector. It consists of the 2-layer Pixel Detector made of DEPFET sensors, and the 4-layer Silicon Vertex Detector made of ladders with double-sided silicon strip detectors.

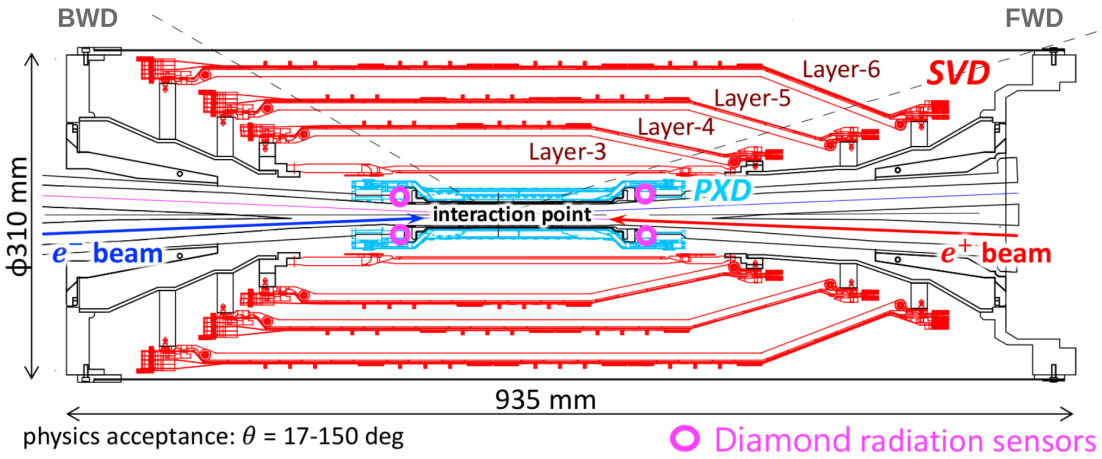

Figure 2.9 The cross-section view of the VXD: Silicon Vertex Detector and Pixel Detector are represented with red and light blue color, respectively. The pink circles indicate the positions of the diamond sensors [77], used both in the beam abort system and to measure the radiation dose on SVD, are installed on the beam pipe.

Pixel Detector (PXD) Because of the higher beam background levels of SuperKEKB expected at the nominal luminosity, the detectors close to the beam pipe suffer very high hit rates. In *Belle II*, the innermost layers of the tracking system are closer to the interaction point than the *Belle* innermost vertex detector, in order to compensate a smaller Lorentz boost factor ($\beta\gamma = 0.28$) and maintain a good vertex resolution. The background levels significantly increase at small radius, and the silicon strip-based vertex detectors are not usable because of the large occupancy. The PXD can cope with higher background rate keeping a lower occupancy, because of the higher granularity.

The *Belle II* PXD is a barrel system consisting of two cylindrical layers of active pixel sensors. The two layers are coaxial with the beam pipe and located at 14 mm and 22 mm from the IP, respectively. The innermost layer is composed of 8 planar modules, called ladders, and the outermost layer is composed of 12 ladders. The ladders overlap in the ϕ direction, where ϕ is the azimuthal angle, in such a way that the active pixel area of one of the two layers covers the insensitive area of the other layer. The geometric acceptance covered by the sensitive sensors is in the range $17^{\circ} \lesssim \theta \lesssim 155^{\circ}$, where θ is the polar angle. The PXD is composed of around 8 million pixels in total, organized into arrays. In order to improve the resolution on the position of individual hits, which is limited by multiple scattering, a very thin technology is required: the sensitive area of each PXD sensor is 75 µm thick, while the mechanical supports are 525 µm thick, in order to satisfy the thickness required to reduce the material budget. The size of the pixel surface is 50×50 μm^2 and

50×75 μm^2, respectively in the innermost and outermost layers, and it is determined by the requirements on the vertex resolution, which should be larger than 20 µm. The readout system of the PXD is located at both ends of the cylindrical structure of the PXD, and it exploits high level of parallelization in order to guarantee a readout time of 20 μs for the entire matrix of pixels. The sensors are mounted on a supporting structure that can slide on the beam pipe in order to compensate the thermal expansion of the beam pipe and of its support. A schematic view of the PXD is shown in Figure 2.10.

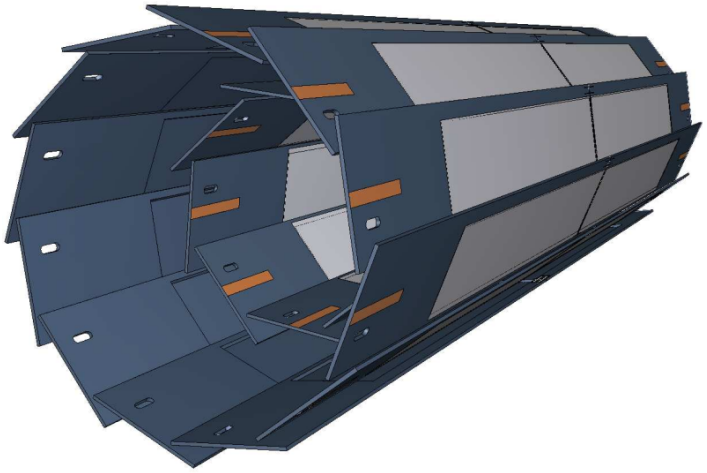

Figure 2.10 3D representation of the PXD that shows the geometric arrangement of the sensors. The light gray areas are the DEPFET sensitive ones, 50 µm thick, that cover the whole geometric acceptance. The dark blue area are the insensitive areas of the modules. The total length of the outermost modules is 174 mm.

PXD sensors are based on the DEPleted Field Effect Transistor (DEPFET) technology. A DEPFET device is a semiconductor-based device that detects and amplifies signals. Because it works also as amplifier, it is a thin device that does not need other devices for signal amplification. A DEPFET is also a low power device and the readout electronic, which needs of a cooling system, is located out of the geometric acceptance of the detector. For all this reason, DEPFET technology is excellent to minimize the material budget. A section of a DEPFET device is shown in Figure 2.11. The basic idea of the DEPFET is the full depletion of the n-type substrate applying a high negative voltage to the p^+ contact in the backside of the device. In this way a potential well, in which the potential has its minimum, is created and it becomes an accumulation region for electrons inside the device. A particle crossing the device produces electron-hole (e-h) pairs: electrons are collected very quickly in the potential minimum, called internal gate, while holes move towards the p^+ back contact. When the transistor is on, being the internal gate capacitively coupled with the gate, the charge into the internal gate modulates the drain current that circulates through the pMOSFET towards the source contact. In order to reset the sensor, a n^+ doped contact, called clear, is put to a positive potential: it attracts the accumulated electrons in the internal gate emptying it. A polycrystalline silicon additional structure called clear gate modulates the potential difference between the clear and the internal gate.
The DEPFET readout is relatively slow, using a rolling shutter system that requires 20

μs for a full readout. If the background occupancy goes beyond 3%, the data acquisition bandwidth limit is reached. In order to reduce the amount of data from the PXD, the Regions Of Interest (ROI) are defined onto the PXD sensors. A preliminary reconstruction of tracks is done online using the SVD and the CDC only during the High-Level Trigger process, those tracks are then extrapolated onto the PXD sensors. The extrapolation of the tracks on sensors defines the ROIs, which are rectangular regions whose size is defined by the statistical and systematic uncertainties on the position of the track.

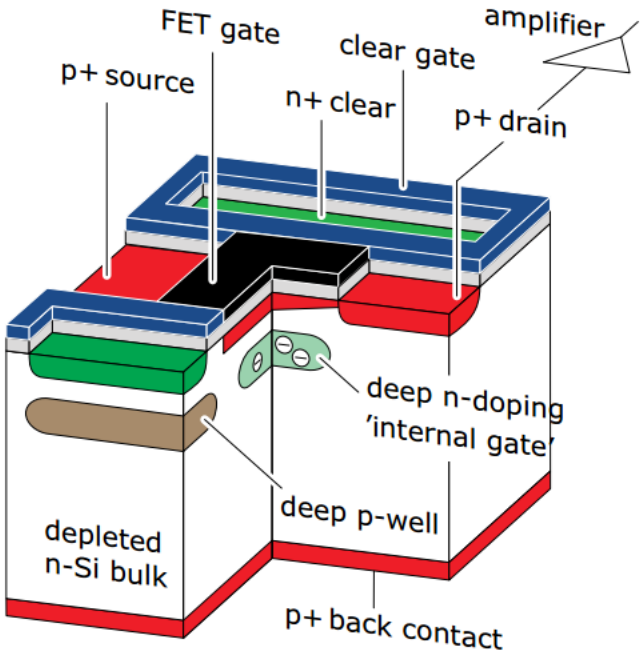

Figure 2.11 Schematic view of a section of a DEPFET device. It is composed of *p*-channel Metal Oxyde Semiconductor Field Effect Transistor (*p*MOSFET) installed onto a *n* doped silicon substrate, called *bulk*. A *p*MOSFET is equipped with four contacts: *source*, *gate*, *drain* and *bulk*. The *bulk* is connected to the *source* contact: they are at the same potential. In the backside of the device there is p^+ contact to which is possible to apply a high voltage in order to fully deplete the *n* substrate. Just below the *gate* there is a *n* doped internal gate. It is a potential well that works as a region of accumulation for the negative charges. The distance between the *gate* and the internal gate is 1 µm. Above the substrate there is a n^+ contact, called clear, that is used to empty the internal gate. The clear gate is a polycrystalline silicon structure. The image has been taken from Reference [73].

Currently, only two of the twelve ladders of the second PXD layer are installed in the *Belle II* detector. In the current detector, the hit efficiency is above 98% in all modules. Preliminary measurements on data show an impact parameter resolution of about 14 µm [78].

Silicon Vertex Detector (SVD) SVD [79], together with the PXD, makes up the Vertex Detector of *Belle II*. SVD is composed of four layers numbered from 3 to 6 and respectively placed at distance of 3.9 cm, 8.0 cm, 10.4 cm and 13.5 cm from the interaction point.

Each layer consists of a different number of modules, called ladders, arranged around the interaction point to form a nearly cylindrical geometry: layers 3-6 are composed respectively by 7, 10, 12 and 16 ladders that are supported by carbon fiber ribs. Each ladder is equipped with Double-Sided Silicon Strip Detectors (DSSD). The geometrical acceptance covered by SVD goes from $\theta = 17^o$, in the forward region, to $\theta = 150^o$, in the backward region. Ladders are equipped with three different kind of sensors: each ladder of layer 3 consists of two equal rectangular sensors of size 123 mm $\times$ 38 mm, while each ladder of layers 4, 5 and 6 has respectively 2, 3, 4 rectangular sensors of size 123 mm $\times$ 58 mm and one trapezoidal sensor in the forward region. Trapezoidal sensors are slanted of an appropriate angle with respect to the other sensors in order to improve the angular acceptance and optimize the incident angle on the sensor of particles coming from the interaction point. Rectangular sensors have a thickness of 320 µm while trapezoidal sensor have a thickness of 300 µm.
In total, SVD has 172 DSSD sensors, covering a sensible area of 1.2 m^2, with a total of 224k readout strips. The sensors, with depletion voltage in the range 20-60 V, are operated by applying a bias voltage of 100 V. Figure 2.12 shows a schematic view of the SVD and the 3-dimensional representation of the VXD. Table 2.7 reports the main features of the

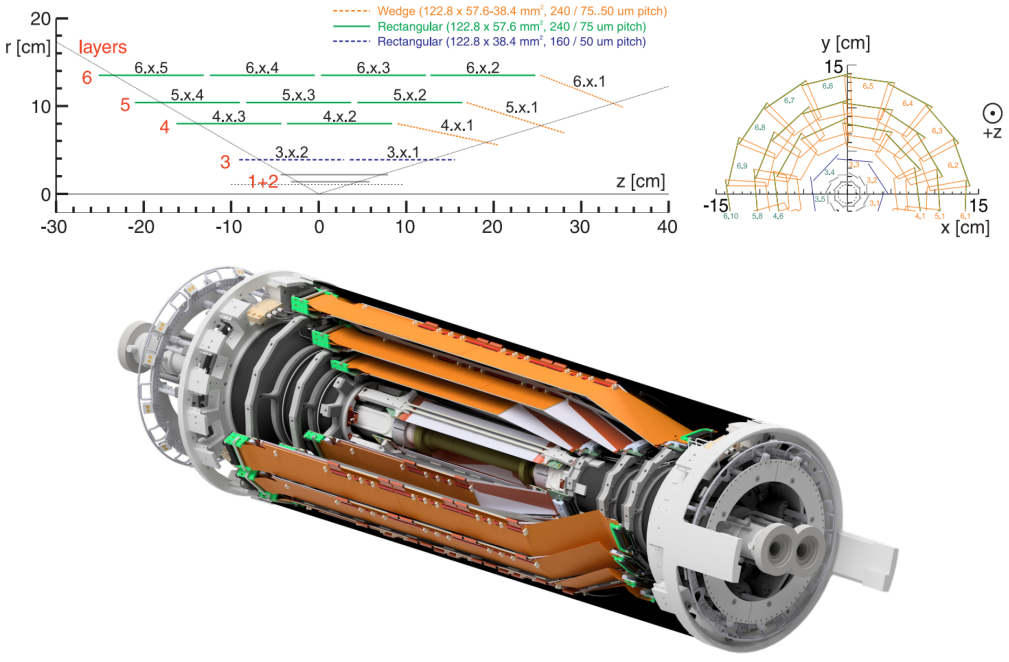

Figure 2.12 Above: Schematic view of SVD in the *r*-*z* plane and *r*-ϕ projection showing the different sensor composition in each layer, with their main properties. Below: 3D representation of VXD , composed of PXD and SVD. The images have been taken from [79].

SVD layout and sensor structure. The main purpose of SVD, together with PXD, is to measure with extreme precision the tracks near the interaction point and to reconstruct the decay vertices of B mesons, D mesons and τ leptons. SVD is also able to reconstruct K_S mesons that decays outside of the PXD volume, and provide particle identification using

Layer	Ladder/Layer	Sensor/Ladder	FWS slant angle
3	7	2	0^o
4	10	3	11.9^o
5	12	4	17.2^o
6	16	5	21.1^o
	Small Sensors	Large Sensors	Trapezoidal Sensors
Readout strips p-side	768	768	768
Readout strips n-side	768	512	512
Readout pitch p-side	50 μm	75 μm	50 - 75 μm
Readout pitch n-side	160 μm	240 μm	240 μm
Sensor thickness	320 μm	320 μm	300 μm
Active area (mm^2)	122.90×38.55	122.90×57.72	122.76×(38.42-57.59)
Manufacturer	Hamamatsu	Hamamatsu	Micron

Table 2.7 Summary of the main features of SVD layout.

the SVD's dE/dx information, and provide a standalone reconstruction of low momentum particles which do not reach the CDC. In order to reconstruct tracks characterized by low transverse momentum, which are affected particularly by multiple scattering, it is required to maintain a low material budget giving a 2-dimensional information. DSSD sensors satisfy both requirements: they provide a very precise measurement of the position of charged particles on sensors and they allow to maintain a low material budget.

The SVD front-end readout ASIC is the APV25 chip [80] with 128 input channels, characterized by a short shaping time of 50 ns. It was originally developed for the CMS silicon tracker, and it can tolerate more than 100 Mrad of radiation dose. APV25 chips are operated in multi-peak mode with a clock frequency of 32 MHz. Since the experiment is running at low luminosity and beam background levels, currently 6 subsequent analog samples are recorded to reconstruct the output waveform of each channel. However, in order to reduce bandwidth and data size with increased beam background, the possibility to readout only 3 samples has been studied and can be used.

For the ladder design, SVD adopts the chip-on-sensor concept. It consists of flex circuits directly installed on the sensors, with a thermal isolation foam in between, to reduce the length of the strips and, consequently, the capacitive noise. Moreover, all APV25 chips are installed on the same side of the sensors, and the signal of the strips of the other side is propagated to the APV25 chips thanks to the flex circuits called pitch adapters wrapped around the edge. This scheme is named origami with reference to the folding action. This design allows to cool all the sensor chips using only one cooling pipe, reducing the material budget. Figure 2.13 (left) shows the APV25 chips installed on the sensor and the pitch adapters to connect strips on the other side of the sensor to the APV25. The sensors in the central part of the ladders are readout using the origami chip-on-sensor, while the sensors at the edge of each ladder, called forward and backward sensors, are read out from the ends using hybrid boards. Figure 2.13 (right) shows the design of a ladder of layer 6. In contrast, layer 3 ladders only consist of two small rectangular sensors and do not have

a slanted section, as said above. More details on the ladder design and construction can be found in Reference [81].

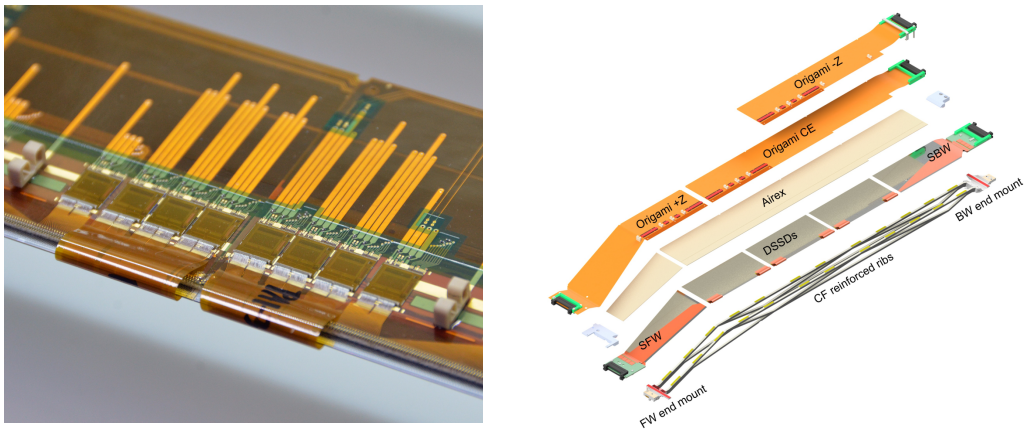

Figure 2.13 Left: APV25 chips installed on the sensor and pitch adapters to readout both strip sides. This scheme is called origami. Right: design of a ladder of layer 6.

Excellent SVD performance have been confirmed on data: the averaged hit efficiency over the four layers is higher than 99.5%, the cluster position resolution is 10-15 µm in the p-side and 15-30 µm in the n-side with some room for improvement in reconstruction and tuning of simulation. Also, the hit-time resolutions are very good, 2.9 ns for the p-side and 2.4 ns for the n-side of layer 3. When running at higher luminosity and increased beam background, the hit-time based selection will be crucial to reject off-time background hits to reduce SVD occupancy, and consequently maintain good tracking performance.

2.5.2 Central Drift Chamber (CDC)

The Central Drift Chamber (CDC) performs three important tasks:

- it reconstructs charged particles tracks with a precise measurement of charged particle momenta;
- it provides PID through the information about the particle energy loss, dE/dx, within its gas volume with a high resolution. The dE/dx resolution depends on the incident angle of particles: it is around 12% for particles crossing perpendicularly the CDC;
- it provides 3D trigger information.

A comparison between the main parameters of the CDC of *Belle* and *Belle II* are listed in Table 2.8. The CDC is composed of 56 layers of wires divided in 9 superlayers with axial-stereo readout, the 9 superlayers and the configuration of the wires is shown in Figure 2.14, where the axial and the stereo wires are represented respectively in blue and red.
The layers are immersed in a gas, composed of 50% helium and 50% ethane, able to provide a high drift speed. The sense wires are interspaced with aluminium field wires.

	Units	*Belle*	*Belle II*
Radius of the innermost cylinder	mm	77	160
Radius of the outermost cylinder	mm	880	1130
Radius of the innermost sensitive wire	mm	88	168
Radius of the outermost sensitive wire	mm	863	1111.4
Number of sensitive wires		8400	14336
Gas		$He\text{-}C_2H_6$	
Diameter of sensitive wire		30	

Table 2.8 Some relevant parameters of the CDC of *Belle* and *Belle II* are listed. The largest number of sensitive wires of *Belle II* CDC allows to have a better granularity and a better spatial resolution on the tracks. Respect to the *Belle* CDC, the *Belle II* CDC must face higher levels of background and a higher trigger rate. The higher inner radius allows to avoid the high radiation levels near the IP and provides more space to place the SVD. The values are taken fom *The Belle II Technical Design Report* [73].

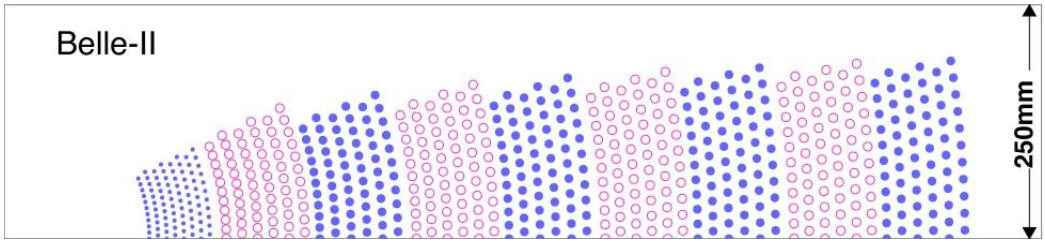

Figure 2.14 The 9 superlayers composing the CDC with the configuration of the wires. The innermost superlayer is composed of two layers while the other eight are composed of 6 layers each. Image taken from Reference [76].

The configuration of wires and the properties of the gas allow to reduce dead time and handle high trigger rates. The CDC is supported by two carbon-fiber cylindrical supports that end with aluminium endplates. The geometrical acceptance on the polar angle covered by the CDC goes from $\theta = 17^o$ to $\theta = 150^o$. The measured spatial resolution on the individual hit is around 100 μm. The readout electronics is composed of 15 thousand channels with a timing resolution of about 1 ns located on the backward side. The forward side used exclusively to connect high-voltage cables. The main structure of the CDC is shown in Figure 2.15. The CDC tracking efficiency measured on data using the SVD as reference is higher than 99% for $p_T > 1$ GeV/c.

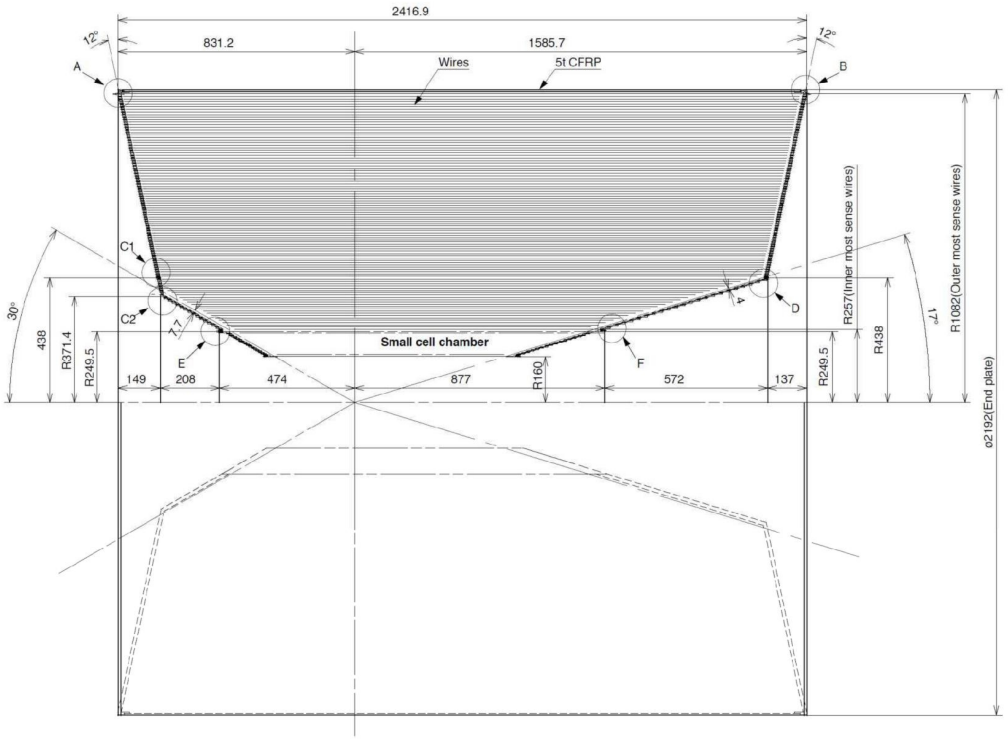

Figure 2.15 Structure of the CDC. The sizes are expressed in mm. The figure is taken from *The Belle II Technical Design Report* [73].

2.5.3 Particle identification system

Particle identification (PID) system is based mainly on two Cherenkov radiation detectors, the Time-of-propagation counter (TOP) and the Aerogel Ring Imaging Cherenkov counter (ARICH), described below.

Time-of-propagation counter (TOP) The TOP detector uses a quartz radiator to measure the time of arrival and impact position of Cherenkov photons at pixelated photodetectors. The radiators are composed of long quartz bars, readout with micro-channel plate photo-multipliers (MCP-PMTs) installed at one of the two final part of the bars. A spherical focusing mirror is installed on the other end of the bars. When particles cross the quartz bar they produce Cherenkov photons that are totally reflected on the walls of the radiator. The direction of Cherenkov photons emitted by particles respect to the direction of the particle momenta is defined by the Cherenkov angle θ_C that characterizes the Cherenkov ring image: the total reflection allows to preserve the Cherenkov ring image. Cherenkov photons are focused and directed towards the MCP-PMTs by the focusing mirror. Before the MCP-PMTs, an expansion prism is installed in order to expand the Cherenkov ring image. Finally the MCP-PMTs measure the time of propagation, t_{TOP}, of the Cherenkov photons and provide information on the arrival (x,y) coordinates of the photons. The Cherenkov ring image is reconstructed from the 3-dimensional information, (x,y,t_{TOP}), provided by the MCP-PMTs. The time resolution can be limited by chromaticity of Cherenkov photons. The focusing mirror minimize the effect of the

chromaticity avoiding the dispersion of photons. The Cherenkov ring image is divided in different MPC-PMTs, according with the wavelength of the photons. Figure 2.16 shows a schematic view of the TOP detector and the chromaticity effect.

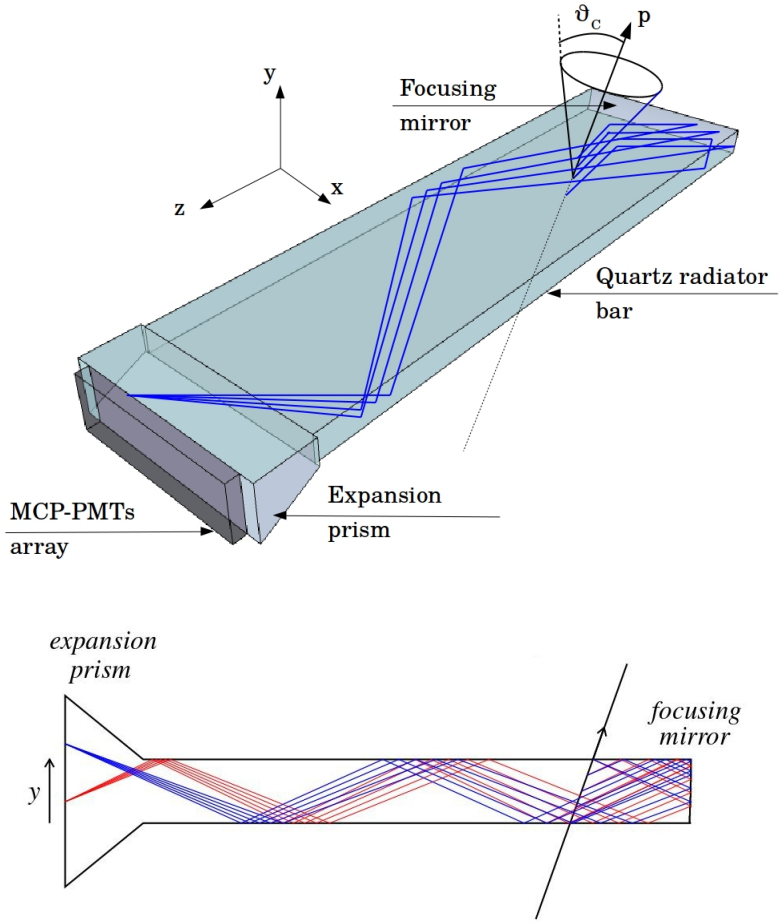

Figure 2.16 Above: Schematic view of the TOP counter. The blue lines represent the direction of Cherenkov photons that are focused by the focusing mirror. The dimension of the quartz radiator are 2.7 m $\times$ 45 cm $\times$ 2 cm. The expansion prism is 10 cm long. Photons are focused and directed towards a 2 $\times$ 16 matrix of MCP-PMTs. Each MCP-PMT has a size of 27.5 $\times$ 27.5 mm^2 with a sensitive area of 22 $\times$ 22 mm^2 divided in 16 anodes. The MCPs have a diameter of 10 µm. Below: chromaticity effect, image taken from [82].

The TOP counter is installed in the barrel region of the *Belle II* detector between the ECL inner support and the CDC outer cover. It is composed of 16 modules surrounding the CDC, the radius of the TOP is around 1.24 m. The MCP-PMTs are characterized by a gain of $\sim 10^6$ and by a very fast response. Furthermore they can work inside the 1.5 T magnetic field of *Belle II*. The spatial resolution of the photon detectors is of few mm and the time resolution is lower than 50 ps.
To evaluate the K/π separation, the probability distribution functions ($p.d.f$s) for K and π particle hypothesis are introduced: respectively they are $\mathscr{P}^K(x,t)$ and $\mathscr{P}^\pi(x,t)$. Photons detected by MCP-PMTs for each track are tested against this two $p.d.f$s hypothesis. From

the *p.d.f*s it is possible to determine the likelihood defined as $\mathscr{L}^{K,\pi} = \prod_{i=1}^{N_\gamma} \mathscr{P}_i^{K,\pi}(x,t)$, where N_γ is the number of photons detected. If $\Delta\mathscr{L} = \log\mathscr{L}^{\pi} - \log\mathscr{L}^{K}$ is positive the particle is classified with a pion otherwise with a kaon. Figure 2.17 shows $\Delta\mathscr{L}$ in the two cases.

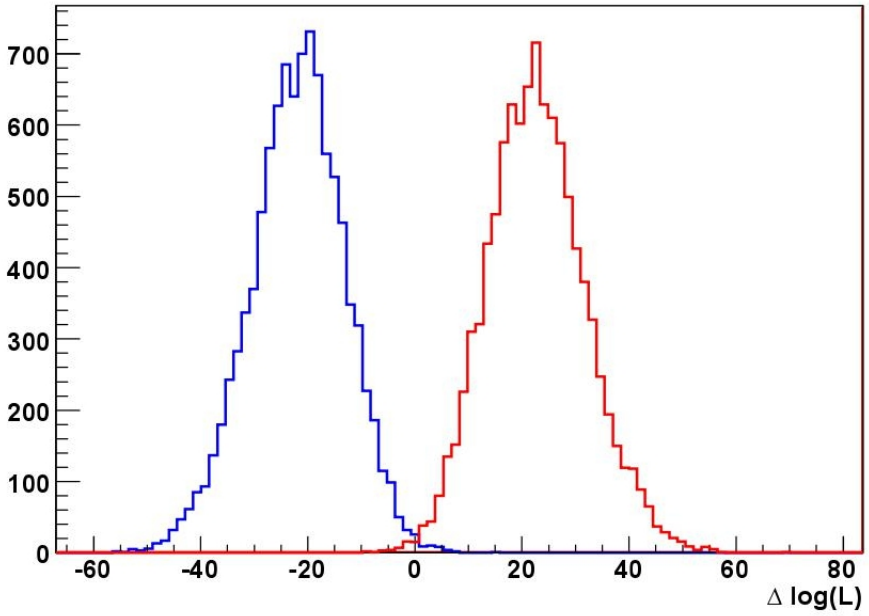

Figure 2.17 $\Delta\mathscr{L}$ distributions for pions, in red, and kaons in blue, corresponding to 500 tracks of 300 GeV/c that cross the quartz bars perpendicularly.

Aerogel Ring Imaging Cherenkov counter (ARICH) ARICH is the other Cherenkov effect-based detector used for PID inside the *Belle II* detector. It is located in the forward endcap and it is designed to improve the separation between pions and kaons up to momenta of 4 GeV/c and between pions, muons and electrons below momenta of 1 GeV/c. ARICH is composed of an aerogel radiator in which charged particles produce Cherenkov photons that are detected by an array of photon detectors. Aerogel can be produced with any desired refractive index n between 1.01 and 1.2. Between the aerogel radiator and the array of photon detectors there is a 20-cm-thick expansion volume necessary to produce large enough Cherenkov rings. For ARICH two radiators with different refractive index are used: $n_1 = 1.046$ and $n_2 = 1.056$. In this configuration the number of photons detected and the Cherenkov angle resolution improves since the slight difference in refractive index make the photon from the two radiators arrive in the same point of the focal plane. Figure 2.18 shows the focusing configuration. Photon detectors are based on Hybrid Avalanche Photo-Detectors (HAPD) technology: they consists of a vacuum tube with containing an avalanche-diode type photo-detector (APD). Cherenkov photons generate photoelectrons from a photocatode through photoelectric effect. Electrons are accelerated by a potential difference of 8 kV towards the APDs that provide a gain of a factor 40. HAPDs are arranged in 9 concentric rings, in total 540 sensors of size 73 mm $\times$ 73 mm are required:

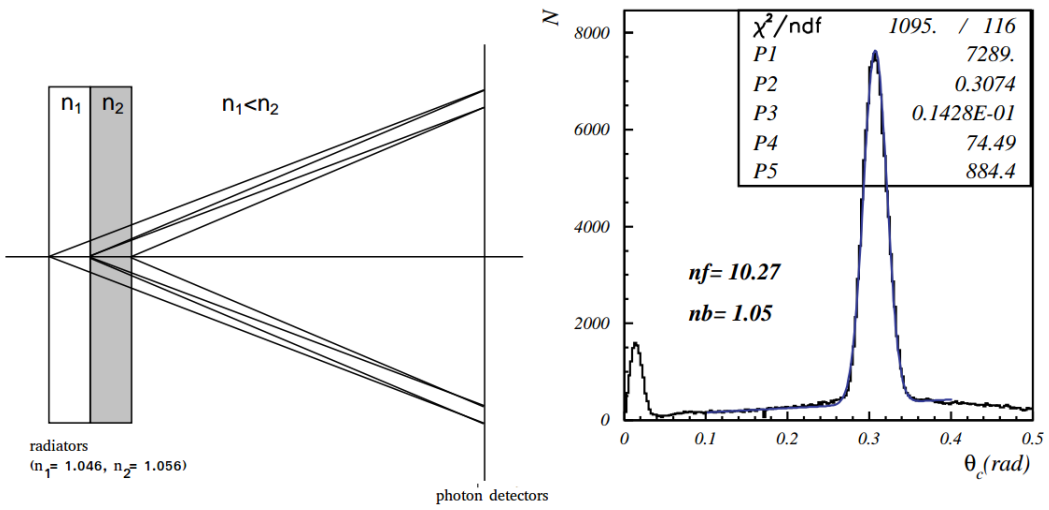

Figure 2.18 Left: Focusing configuration of the ARICH. It is based on the use of an inhomogeneous aerogel radiator. Right: θ_C distribution in the focusing configuration (with refractive index of $n_1 = 1.046$ and $n_2 = 1.056$); the resolution is $\sigma_{\theta_C} \approx 14$ mrad. Events have been simulated with radiator 4 cm thick. The image is taken from *The Belle II Technical Design Report* [73].

they are composed of a matrix of APD pixels 12 x 12, each APD is 4.9 mm $\times$ 4.9 mm. The inner radius of the ARICH is 410 mm, the outer radius is 1140 mm and ARICH covers a geometric acceptance from $\theta \simeq 15^o$ to $\theta \simeq 30^o$.

2.5.4 Electromagnetic Calorimeter (ECL)

About 1/3 of B meson decays provide photons in an energy range from 20 MeV to 4 GeV, for this reason a high resolution ECL is very important. The tasks of ECL are: the detection of photons with high efficiency, the precise determination of the energy of the photons and a precise determination of angular coordinates, the identification of electrons, provide an appropriate trigger signal for the other detectors, provide the online and offline measurement of the luminosity and the detection of K_L together with the KLM.
For ECL it has been chosen to reuse *Belle* CsI(Tl) crystals changing the readout electronics in order to handle the higher background levels. CsI(Tl) crystals are characterized by scintillation light with a decay constant of 1.3 μs and by an average output of about 5000 photoelectrons per MeV with a noise level of 200 keV (the values reported was measured using calibration with cosmic rays muons) [73]. ECL consists of 3 m long barrel section, the inner radius is 1.25 m and the endcaps are located at $z = 1.96$ m and $z = -1.02$ m from the IP. ECL covers an angular acceptance from $\theta = 17^o$ to $\theta = 150^o$ except for two gaps of about 1^o wide between the barrel ECL (BECL) and the endcaps. The total amount of ECL crystals is 8736, divided in 6624 crystals in the BECL and 2212 crystals in the endcaps. The average size of each crystal is 6 $\times$ 6 cm^2 in cross section and 30 cm in length that corresponds to 16.1 X_0. The lateral size of crystals is chosen to be comparable with the Moliere Radius and the thickness is enough to prevent significant energy loss for photons up to several GeV.
In order to face the high background level in SuperKEKB, electronics based on wave-

form sampling with pipelined readout has been designed. The former allows to use time information in order to reject off-time events hits, the latter allows to parallelize readout process in order to reduce dead times (16 crystals are read at a time). The scintillation light detection is done using two sets of silicon photodiodes, with a sensitive area of 10 mm $\times$ 20 mm, glued in the back of crystals. A preamplifier is connected to each set of photodiode in order to have two independent output for each crystal. The two pulses are added and processed by two shaper boards, one characterized by a time constants of 0.2 μs used to generate the trigger signal, the other characterized by a time constant of 0.5 μs. The signal waveform produced by the second shaper board is sampled through 16 samples that are used to extract amplitude and timing. This new electronic allows to reduce the cluster fake rate of a factor of 7 maintaining an efficiency on photon detection of 97%, in accordance with simulations. Figure 2.19 shows a schematic view of the ECL.

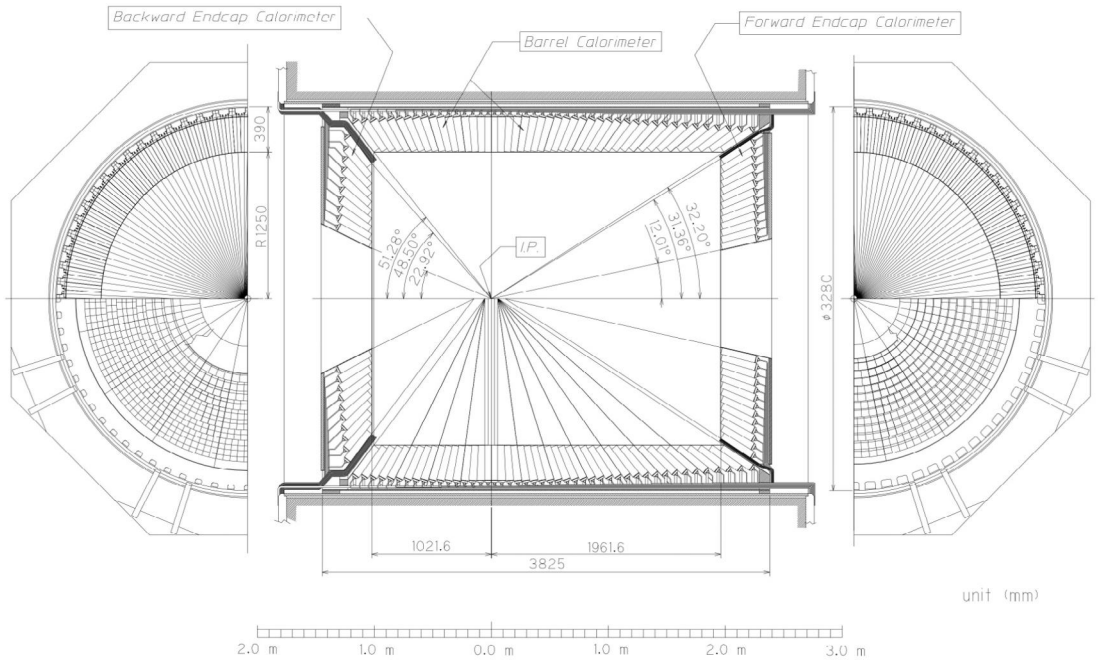

Figure 2.19 Schematic view of the ECL, all three detector regions, barrel as well as the forward and backward end-caps are shown in the image. The total number of crystals amounts to 8736 and the ECL covers about 90% of the solid angle in the center of mass reference system .The image was taken from Reference [76].

2.5.5 The K_L and μ detector (KLM)

KLM is the detector used for K_L and μ reconstruction. It consists of active detector elements instrumenting the iron return yoke of the magnets, which provide 3.9 interaction length of material. Inside the iron plates the K_L can shower hadronically. The KLM is composed of Resistive Plate Chambers (RPCs), located in the outermost layers of the barrel region, and by scintillator strips coupled with silicon photomultiplier (SiPM), arranged in the endcaps and in the two innermost layers of the barrel region. The barrel region

covers a angular acceptance from $\theta \simeq 45^o$ to $\theta \simeq 125^o$ that is extended by endcaps from $\theta = 20^o$ to $\theta = 155^o$.
The RPCs are composed of two electrodes (2 parallel planes 2 mm thick) made by high resistivity glass spaced of 2 mm. The space between electrodes is filled with a gas mixture of 62% HFC-134a freon, 30% argon and 8% butane. The outer surface of each electrode is coated with a carbon-doped paint that allows to distribute high voltages to electrodes, in this way an uniform electric field of 4.3 kV/mm in the gas filled gap is generated.
Deposited charge induces a signal on 5-cm-wide metal strips located on each side of RPCs, used for the readout. The metal strips are separated from an external ground plane by a dielectric foam layer: this structure work as a transmission line with a characteristic impedance of 50 Ω. Two RPCs are coupled to form a single superlayer in order to improve the detection efficiency of particles. The metal strips are arranged orthogonally in the two RPCs in order to measure both z direction and ϕ direction. Figure 2.20 shows a section of a RPC superlayer.

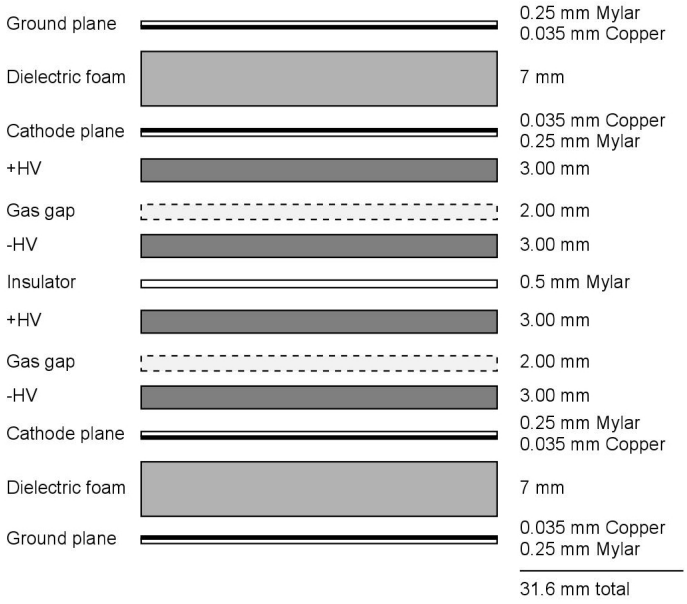

Figure 2.20 Cross section of a RPC superlayer. Superlayers are 2.20 m long and the width of each superlayer varies from 1.67 m to 2.75 m. A module is composed of two superlayers disposed side by side above the iron plate. Each module is 4.40 m long.

Because of the limited rate capability of RPCs, the first two barrel layers and the endcaps of the KLM are equipped with scintillator strips coupled to SiPM for the signal readout: the whole system consists of 16800 scintillator strips up to 2.8 m long and with a cross section between 7 mm and 10 mm $\times$ 40 mm. Strips width has been chosen in order to maximize the spatial resolution for muons and K_L reconstruction and minimize the total number of channels. Each strip has a groove in the center where a wavelenght-shifting optical fiber is inserted. The fiber picks up the scintillation light and carries it to the SiPMs that are composed of 667 photodiodes pixel of 1.3 $\times$ 1.3 mm^2. The system is

characterized by a high time resolution, around $\sigma_t = 0.7$ ns, and by a high output rate capability. Disadvantages of SiPM are the high level of noise, pixel cross-talk and a high ambient temperature dependence.

Since the muon identification is important in this analysis, it is briefly described below.

Muon identification begins from the reconstruction of a charged track in the CDC. The charge track is extrapolated up to the KLM region under the hypothesis that it was a π: 0.6 GeV/c is the minimum momentum that a track needs in order to cross at least one KLM module and be considered into the KLM acceptance. If a KLM hit is near the crossing of the extrapolated track on the KLM module, than it will be associated to the track. Two ranges are defined: the predicted range by the track and the actual range. The predicted range is defined by the outermost KLM module crossed by the extrapolated track considering the interactions that the particle associated to the track makes inside the KLM. The actual range is defined by the outermost KLM module in which there is a hit associated to the track. If the predicted range and the actual range differ significantly, the track is classified as hadron, otherwise the same procedure is repeated starting from the extrapolation of the track under the hypothesis that the track is generated by a μ. Hits associated to the track with an appropriate fitting technique are used to predict the path of the track into the KLM. The goodness of fit and the difference between the measured range and the predicted range are used in a likelihood ratio test in order to test the hypothesis of μ against the hypothesis of hadron.

The muon detection efficiency in the barrel KLM is about 89% for momenta $p \geq 1$ GeV/c. The contamination from hadrons is around 1.3% rising up to 3.8% at 0.7 GeV/c. Fake muons are pions that do not decay in flight and do not produce inelastic hadronic interactions in the KLM. The contribution from kaons to the hadron fake rate is much smaller because they are identified efficiently from the particle identification systems. The K_L detection efficiency is of the 80% for momenta $p \geq 3$ GeV/c. Muon and K_L detection efficiencies in the endcaps KLM are similar. Figure 2.21 shows the side view of the *Belle II* KLM.

2.5.6 Trigger

In order to apply an efficient event selection at the designed luminosity of $\mathscr{L} = 6.5 \times 10^{35}$ cm^{-2} s^{-1} of SuperKEKB, the trigger system must satisfy the requirements listed in the following:

- around 100% efficiency for hadronic events from $\Upsilon(4S)$ B meson decays and from annihilation events in the continuum;
- maximum average trigger rate of 30 kHz;
- a fixed latency around 5 μs and a timing precision ≤ 10 ns.

The trigger rate and the total cross section of some relevant events at the designed luminosity of SuperKEKB are listed in Table 2.9. Bhabha events and $\gamma\gamma$ events are used to measure the luminosity and to study the response of the detector. $B\bar{B}$ events and hadronic

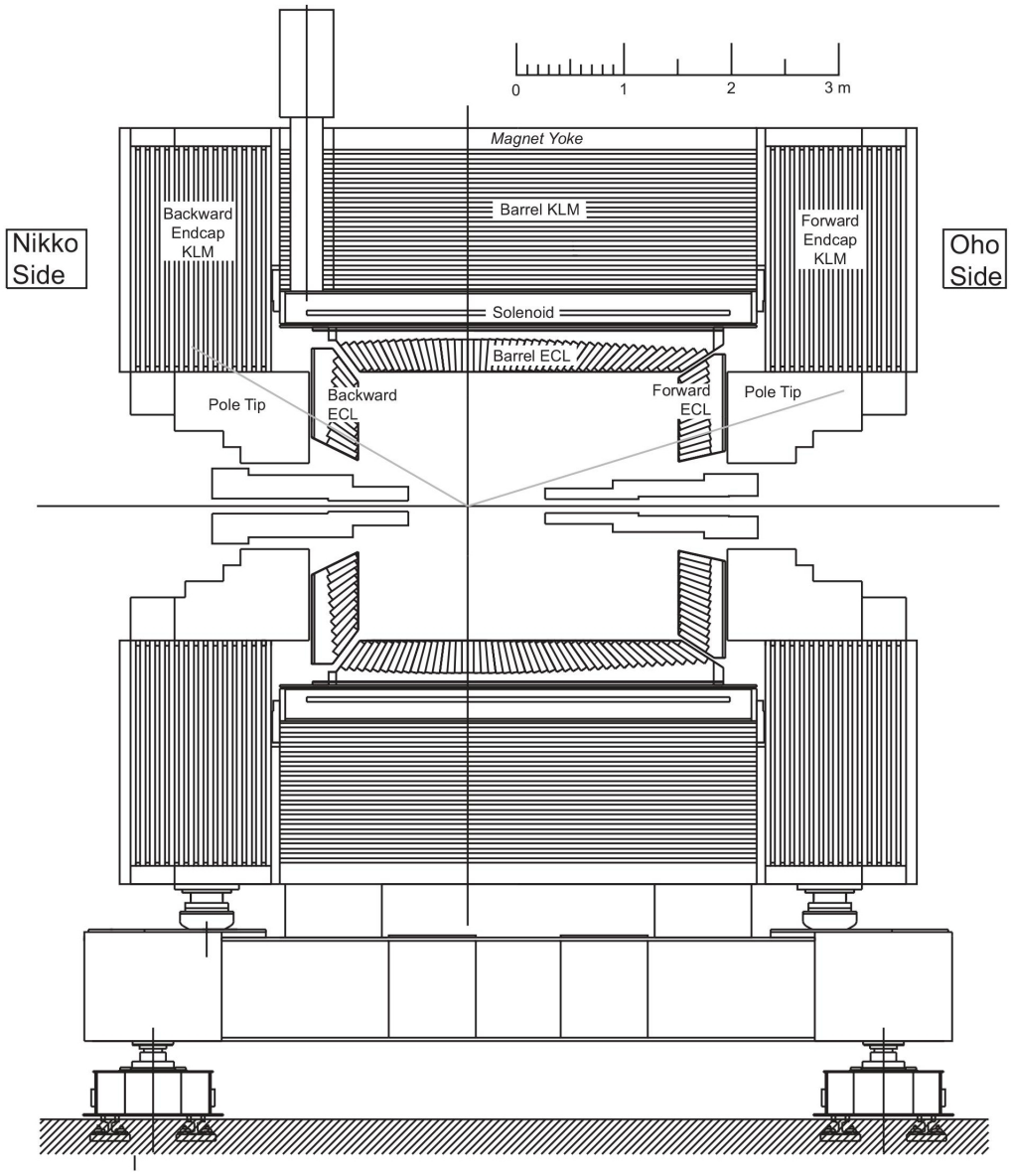

Figure 2.21 Side view of the KLM. The gray lines represent the nominal acceptance. Image taken from *The Belle II Technical Design Report* [73].

events from continuum are characterized by a large multiplicity of tracks in the final states, in order to select efficiently this kind of events it is possible to set the trigger to require a large number of tracks in the final state. It is more complicated design a trigger for low multiplicities events, as for example τ leptonic decays or processes involving dark sector particles, because they are characterized by zero or only two tracks in the final state, for this reason they are hardly distinguishable from background events. Moreover some of low multiplicities process, as for example processes studied in dark sector searches, have a topology quite similar to Bhabha events, $\mu^+\mu^-$ events or $\gamma\gamma$ events that have a very large cross section. It is necessary, therefore, to apply a veto in order to suppress Bhabha, $\mu^+\mu^-$

Process	Cross section σ_X (nb)	Event rate (Hz)
$\Upsilon(4S) \to B\bar{B}$	1.2	960
Hadron production from the continuum	2.8	2200
$\mu^+\mu^-$	0.8	640
$\tau^+\tau^-$	0.8	640
Bhabha events ($\theta_{lab} \geq 17^o$)	44	350 $^{(a)}$
$\gamma\gamma$ ($\theta_{lab} \geq 17^o$)	2.4	19 $^{(a)}$
2γ processes ($\theta_{lab} \geq 17^o$ and $p_T \geq 0.1$ GeV/c)	$\simeq 80$	$\simeq 15000$
Total	$\simeq 130$	$\simeq 20000$

$^{(a)}$ Rate is prescaled by a factor 1/100
since this events have large cross sections

Table 2.9 Total cross sections and trigger event rates of different processes at the $\Upsilon(4S)$ peak at the design luminosity of $\mathscr{L} = 8.0 \times 10^{35}$ cm^{-2} s^{-1} of SuperKEKB. Table taken from *The Belle II Technical Design Report* [73].

and $\gamma\gamma$ events and this cause a loss of trigger efficiency. The trigger system is composed of the Level 1 trigger (L1) and the High Level Trigger (HLT) implemented in the Data Acquisition System (DAQ).

Level-1 trigger (L1) The L1 trigger is a hardware based system that consists of sub-trigger systems that collect the trigger information of the relative sub-detector and send those information to a Global Reconstruction Logic (GRL) where a low level reconstruction is done combining the information of the individual sub-trigger systems. Results obtained by the GRL are sent to the final decision logic, the Global Decision Logic (GDL), that finally generates a trigger signal when its selection criteria are satisfied. In *Belle II*, each trigger primitive is generated using Field Programmable Gate Array (FPGA) technology. The GRL is based mainly on the CDC and ECL trigger information, but also TOP and KLM are included in the system.
The CDC sub-trigger provides information about the tracks detected in the CDC. It consists of a 2D trigger that is based on the track reconstruction in the plane (x,y) and of a 3D trigger that adds information on the z-coordinate near the interaction point. The 3D trigger is very important for the background rejection because tracks from background events are characterized by a z-coordinate not localized near the IP, while tracks produced by e^+e^- collisions come from the IP and their z-coordinate is around zero.
The ECL trigger generates fast signals both for neutral and charged particles. Two different configurations have been designed, one based on the total energy deposit in the ECL and the other on isolated clusters. The former is sensitive to physics events with high electromagnetic energy deposit while the latter is sensitive to multi-hadronic physics events that produce low energy clusters, and to MIPs. Furthermore the ECL trigger can identify Bhabha and $\gamma\gamma$ events that are characterized by a back-to-back topology: this is very use-

ful to measure the luminosity in real time and to ensure a high trigger efficiency for low multiplicity events.
The TOP trigger provides precise timing and hit topology information and the KLM trigger is used for event selection of μ pairs. The KLM trigger is independent from the CDC trigger and it is useful to measure efficiencies of the other sub-triggers and improve the trigger efficiency of low multiplicity events.
The GDL receives all sub-trigger information, and after logic calculations and prescaling it provides the L1 trigger. The total latency of the L1 trigger is around 5 μs. The Trigger is affected by an uncertainty of around 10 ns called trigger jitter.

High-Level trigger (HLT) The HLT is a software based system that consists in a full reconstruction of the event in real time using event data from all detectors apart PXD. The reconstruction is done using the same software used for the offline event reconstruction (*basf*2, see Section 2.6) in order to avoid additional systematic uncertainties different from those of the offline reconstruction.
During the online reconstruction, the HLT decision allows to: further reduce the event rate down to 10 kHz; to define PXD ROIs from the reconstructed tracks using CDC+SVD that are extrapolated back onto PXD (see Section 2.5.1). ROIs are used to select the PXD hits to be combined later; flag the events compatible with interesting physics processes; provide information about data quality through the plots of the data quality monitor.
The HLT has two stages: during the first, events are filtered by applying a selection, for example, on the track multiplicity, on the vertex position of the event and on the total energy deposit in the ECL to define which events are discarded. The final software trigger result coincides with the filter decision; On accepted events, the second stage is calculated and the online tagging of the events is performed. The information from the second stage can be accessed later during reprocessing or for a faster skimming of events, as for example the hadronic selection or the low-multiplicity selection. The HLT filtering has been applied only from the end of 2020.

Dedicated dark sector triggers Dedicated low multiplicity triggers and "dark sector" triggers are implemented in *Belle II* making the dataset collected up to now world-unique. Some dedicated low multiplicity and dark sector triggers are:

- single photon trigger operational for entire dataset. It was not present in *Belle*, while only 53 fb^{-1} of data were recorded with single photon trigger in *BABAR*;
- single muon trigger exploiting the KLM detector has been recently introduced and shows an efficiency of 90%;

Figure 2.22 shows the nearly 100% single photon trigger efficiency for the threshold on single photon energy set to 1 GeV. A, newly designed trigger allows reducing the threshold down to 0.5 GeV for single photons.

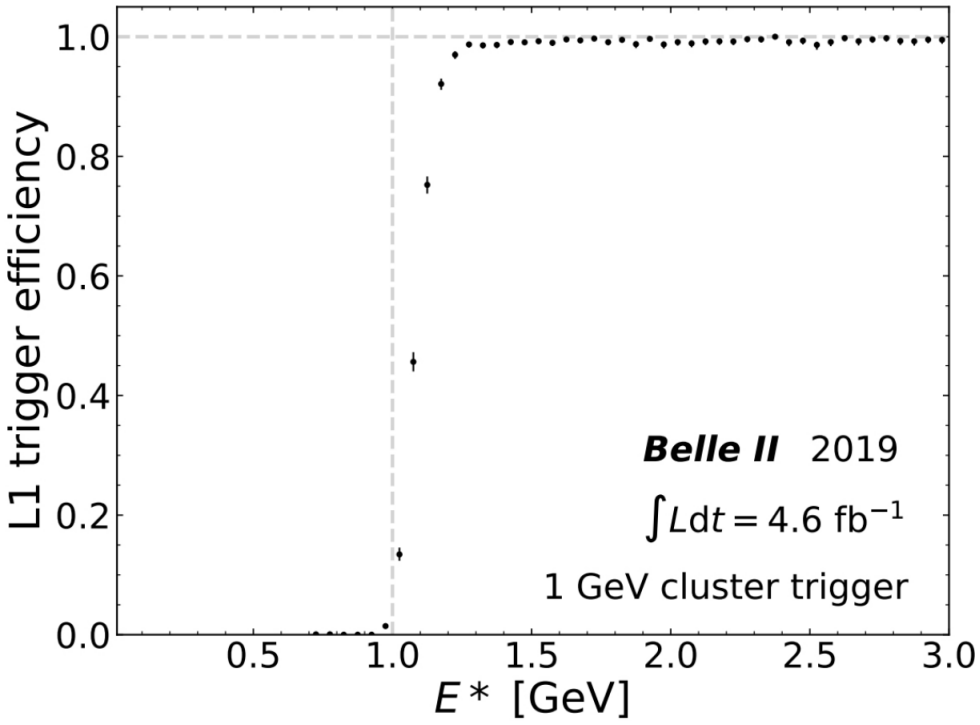

Figure 2.22 L1 single photon trigger efficiency for a 1 GeV cluster in the ECL.

2.6 The *Belle II* software and computing

The *Belle II* software can be divided in three parts: the *Belle Analysis Framework* 2 (*basf*2) [83], that is used both online, as for example for the HLT, and offline, as for example for physics analysis or detector studies; the externals containing third-part code, like EvtGen [84] and PYTHIA [85], used for event generation, Geant4 [86], used for the simulation of the detector and ROOT [87], used for analysis; the tools that are a collection scripts used for the installation and setup of *basf*2 and externals. In particular, *basf*2 is organized into about 40 packages, such as the base-level framework, one package for each sub-detectors, the packages dedicated to reconstruction and simulation, and the analysis package containing the tools used in the analysis.
*Basf*2 is based on modules, mostly written in C++, that allows to implement in the software framework all operations needed for the analysis or the optimization of detectors: from generation of MC samples to simulation of all detector and to reconstruction of tracks, from unpacking of raw data to physics analysis, extracting all parameters required by the user and saving them in appropriate files. The modules are handled using appropriate python scripts, called steering files, that allow to call the necessary modules, set the parameters and insert modules in paths. When the data are processed, *basf*2 executes the modules in the order as they are recalled in the steering file. Each module can access the Data Store, which is a common repository to which all modules have access to writing and reading. Each module can read or write the Data Objects, which are the elementary classes of *basf*2 written in C++ and which contain the information provided by the detector or by other modules. The information written in Data Objects are stored in the Data Store.

Additionally, the Conditions Data contains a number of settings or calibrations that can evolve over time, like the information about the geometry of the detector, the information about the material budget of every single piece of the detector, the calibration constants, the accelerator parameters and all those information needed by the user in order to perform simulation, reconstruction of data and so on. The user can access to Conditions Data in order to update the information of the detector, for example update the calibration constants after a sub-detector calibration run, or in order to recall and use in modules and scripts the information contained in it.

The computing system of *Belle II* uses a grid-based approach: an infrastructure of many facilities distributed to all members of the *Belle II* organization connected to a common software, in order to process the huge amount of data produced during the activity of *Belle II*. It performs several tasks, such as raw data processing, Monte Carlo event production, physics analysis and archiving the data resulting from each of the previous steps.

Raw data coming out of the detector are stored and processed at KEK. The resulting output, called mini data summary table (mDST), will be distributed to the various grid sites. The mDST files contain only the necessary classes to run physics analysis and have a size which is roughly one tenth of the size of the raw data. In addition to data, also MC samples are in mDST format and distributed to the grid. The users will perform analysis processes on the mDST files on the grid and will transfer the resulting lighter output (n-tuples with high-level information and analysis information that the user decides to save) to the local resources.

3. Analysis strategy and event selection

We search for the process $e^+e^- \to \mu^+\mu^- Z'$, $Z' \to \tau^+\tau^-$. We reconstruct only 1-prong τ decays, whose corresponding branching ratios are $BR(\tau \to e\nu_\tau\bar{\nu}_e) \sim 18\%$, $BR(\tau \to \pi\nu_\tau) \sim 50\%$ and $BR(\tau \to \mu\nu_\mu\bar{\nu}_\mu) \sim 17\%$.
The signature of the signal is the appearance of a sharp peak in the mass of the system recoiling against two well identified opposite charge muons ("recoil mass", from now on) in events with four reconstructed tracks. Neutrals can also be present as decay products of the τ's. From now on in this thesis, we name "tagging muons" the two opposite charge well identified muons, and "τ-daughters" the remaining two opposite charged tracks. These last are the decay products of the τ from the Z' in the case of the signal, but do not necessarily come from τ's in background events. Events with more than two identified muons will have multiple candidates: two candidates for 3 muon events and 4 candidates for 4 muon events. We consider all of them, making no attempt to select one specific candidate within the event. We select events with 4 tracks coming from the interaction point: two of them are required to be identified as muons with a $\mu ID > 0.5$ (tagging muons), while the remaining two (τ-daughters) are required to have at least one of the particle identification variables, electron, muon or hadron ($1 - eID - \mu ID$), larger than 0.5. The finite τ lifetime does not produce significantly displaced tracks and they can be selected as if they originated from the interaction point. We use two trigger lines in logical OR: the CDC *fff* and the OR of the CDCKLM lines, that are described in Chapter 5. We select data events with the corresponding bits set and we use measured efficiencies as MC event weights while comparing data with MC. We do not use the trigger simulation at all, since unfortunately it seems to be unreliable for these lines, at least in the present MC release.
Due to the presence of undetected neutrinos in the final state (from two to four, depending on the τ decays) some missing energy is expected. A selection on the reconstructed four-track invariant mass M is then performed: this allows to reject a good fraction of the background components with M peaking on the collision energy. The main

Process	Cross section (nb)	Process	Cross section (nb)
$e^+e^- \to B^0\bar{B}^0$	0.510	$e^+e^- \to \mu^+\mu(\gamma)$	1.148
$e^+e^- \to B^+B^-$	0.540	$e^+e^- \to \tau^+\tau^-(\gamma)$	0.919
$e^+e^- \to u\bar{u}$	1.61	$e^+e^- \to e^+e^-\mu^+\mu^-$	18.9
$e^+e^- \to d\bar{d}$	0.40	$e^+e^- \to e^+e^-\tau^+\tau^-$	0.182
$e^+e^- \to s\bar{s}$	0.38	$e^+e^- \to \mu^+\mu^-\tau^+\tau^-$	0.143×10^{-3}
$e^+e^- \to c\bar{c}$	1.30	$e^+e^- \to \mu^+\mu^-\mu^+\mu^-$	0.342×10^{-3}

Table 3.1 Cross section of the expected main background processes and other secondary processes that could contribute.

expected background components are the Standard Model processes $e^+e^- \to q\bar{q}$ ($q\bar{q} = u\bar{u}, d\bar{d}, c\bar{c}, s\bar{s}, B^0\bar{B}^0, B^+B^-$), $e^+e^- \to \tau^+\tau^-(\gamma)$, $e^+e^- \to \mu^+\mu^-(\gamma)$, $e^+e^- \to e^+e^-\mu^+\mu^-$

and $e^+e^- \to \mu^+\mu^-\tau^+\tau^-$. The Table 3.1 (above) reports the cross sections for the expected main background components and other secondary processes that can contribute. One of the main parts of the analysis is devoted to the background suppression. Distributions of kinematic variables for both background and signal events are studied, and their differences exploited. They are mainly based on two signal features: the presence of a resonance in the recoil mass and the compatibility of the recoil system with a $\tau\tau$ system. A Multivariate Analysis (MVA) technique is implemented to maximize background rejection, while keeping an acceptable signal efficiency.
The signal yield extraction is performed through a fit of the distribution of the recoil mass, which is the main kinematic variable, in which we expect to observe a peak corresponding to the Z' mass for signal events. The same fit procedure allows an estimate of the background directly from data. The presence of the signal is checked with a scanning technique, moving the fit ranges with steps corresponding to half the recoil mass resolution. Control samples are used to check the analysis procedures at each step and to evaluate a significant part of the systematics.
We compute 90% confidence level (CL) upper limits to the process cross section and to the coupling g' by applying a Negative Logarithmic Likelihood (NLL) approach, using the CL_s frequentist technique to the background+signal fits.
The MC samples used for the analysis are shown in Table 3.2: the first column reports the samples used for the background rejection studies, for the training of the MVA and for the sensitivity extraction; the second column reports the samples used for the data validation performed with the control sample $e^+e^- \to \pi^+\pi^-\tau^+\tau^-$ to which mainly $e^+e^- \to \tau^+\tau^-(\gamma)$ and $e^+e^- \to q\bar{q}$ events contribute (see Chapter 5). For what concerns

Process	MC sample $e^+e^- \to \mu^+\mu^-\tau^+\tau^-$	Control sample $e^+e^- \to \pi^+\pi^-\tau^+\tau^-$
$e^+e^- \to u\bar{u}, d\bar{d}, c\bar{c}, s\bar{s}$	1.5 ab^{-1}	100 fb^{-1}
$e^+e^- \to B^0\bar{B}^0$	1.5 ab^{-1}	100 fb^{-1}
$e^+e^- \to B^+B^-$	1.5 ab^{-1}	100 fb^{-1}
$e^+e^- \to \tau^+\tau^-(\gamma)$	1.5 ab^{-1}	100 fb^{-1}
$e^+e^- \to \mu^+\mu^-(\gamma)$	0.5 ab^{-1}	100 fb^{-1}
$e^+e^- \to e^+e^-\mu^+\mu^-$	0.5 fb^{-1}	100 fb^{-1}
$e^+e^- \to e^+e^-\pi^+\pi^-$	0.5 ab^{-1}	1 ab^{-1}
$e^+e^- \to e^+e^-\tau^+\tau^-$	5 ab^{-1}	5 ab^{-1}
$e^+e^- \to \mu^+\mu^-\tau^+\tau^-$	5 ab^{-1}	5 ab^{-1}
$e^+e^- \to \mu^+\mu^-\mu^+\mu^-$	5 ab^{-1}	5 ab^{-1}

Table 3.2 MC samples used in the analysis. The four lepton final state processes have been generated using the AAFH generator [88], while $e^+e^- \to e^+e^-\pi^+\pi^-$ has been geenrated using TREPS [89]; $e^+e^- \to \tau^+\tau^-(\gamma)$ has been generated using KKMC [90] interfaced with TAUOLA [91]; $e^+e^- \to \mu^+\mu^-(\gamma)$ has been generated using the KKMC [90]; $e^+e^- \to u\bar{u}, d\bar{d}, c\bar{c}, s\bar{s}$ have been generated using KKMC [90] interfaced with Pythia [92] and EvtGen [93]; finally , $e^+e^- \to B^0\bar{B}^0$ and $e^+e^- \to B^+B^-$ have been generated using EvtGen [93].

signal events, for studies on discriminant variables, signal modeling and fit procedure we produced 20 thousand events for $3.6 < M_{Z'} < 10$ GeV/c^2 at steps of 25 MeV/c^2 using MadGraph5@NLO. For the training of the MVA method we produced 20 thousand events from 3.6 to 5.0 GeV/c^2 at steps of 50 MeV/c^2, from 5.0 to 8.0 GeV/c^2 at steps of 20 MeV/c^2, from 8.0 to 9.0 GeV/c^2 at steps of 10 MeV/c^2, and finally from 9.0 to 10.36 GeV/c^2 at steps of 5 MeV/c^2.

3.1 Event selection

We remind that, having in mind the signal topology, we name "tagging muons" the two opposite charge well identified muons, and "τ-daughters" the remaining two opposite charge tracks. The latter are the decay products of the τ from the Z' in the case of the signal, but do not necessarily come from τ's in background events. Events with more than two identified muons will have multiple candidates: two candidates for 3 muon events and 4 candidates for 4 muon events.

3.1.1 Characterization of background events

The main expected background components for this analysis are $e^+e^- \to q\bar{q}$, $e^+e^- \to \tau^+\tau^-(\gamma)$, $e^+e^- \to \mu^+\mu^-(\gamma)$ and $e^+e^- \to e^+e^-\mu^+\mu^-$ events. The two additional tracks in $e^+e^- \to \mu^+\mu^-(\gamma)$ events are mostly electrons from ISR photon conversions. Figure 3.1 shows the distribution of the 4-track invariant mass for the different background components. Tagging muons are identified by requiring $\mu ID > 0.5$, while electrons, muons and hadrons in τ-daughters are required to have $eID > 0.5$, $\mu ID > 0.5$ and $(1 - \mu ID - eID) > 0.5$, respectively. Events are classified depending on the particle identification of tracks of the two τ-daughters: $h-h$, $h-l$ or $l-l$, where $l = e, \mu$. The $e^+e^- \to \mu^+\mu^-(\gamma)$ and $e^+e^- \to e^+e^-\mu^+\mu^-$ background components have a large peak at the $\Upsilon(4S)$ mass because the four tracks saturate the energy in the center of mass. The $e^+e^- \to e^+e^-\mu^+\mu^-$ process shows a large tail for small invariant masses, due to events in which the primary electrons are outside acceptance and the τ-daughters coincide with tracks from photon conversions. In order to reject a large fraction of $e^+e^- \to \mu^+\mu^-(\gamma)$ and $e^+e^- \to e^+e^-\mu^+\mu^-$ events we apply a pre-selection requiring the invariant mass of the four tracks in the events to be $M < 9.5$ GeV/c^2. This requirement implies a signal inefficiency of the order of 1%. We also expect to have background contributions from the Standard Model $e^+e^- \to \mu^+\mu^-\tau^+\tau^-$, $e^+e^- \to \mu^+\mu^-\mu^+\mu^-$ and $e^+e^- \to e^+e^-\tau^+\tau^-$ processes. The recoil mass distribution for each background contribution normalized to 500 fb^{-1} is shown in Figure 3.2. The dominant background in the interesting recoil mass region, [3.6, 10.0] GeV/c^2, is made of $e^+e^- \to \tau^+\tau^-(\gamma)$. Other relevant contributions come from $e^+e^- \to q\bar{q}$ and $e^+e^- \to e^+e^-\mu^+\mu^-$ events, especially at very high recoil mass. The component due to the Standard Model $e^+e^- \to \mu^+\mu^-\tau^+\tau^-$, $e^+e^- \to \mu^+\mu^-\mu^+\mu^-$ and $e^+e^- \to e^+e^-\tau^+\tau^-$ events is negligible at this level of the analysis. We focus mostly on $e^+e^- \to \tau^+\tau^-(\gamma)$ and $e^+e^- \to q\bar{q}$ background components, because they are dominant. Figure 3.3 shows, for both background components, the recoil mass distribution of events in which the two candidate tagging muons are selected with $\mu ID > 0.5$ or $\mu ID > 0.9$. For

$e^+e^- \to \tau^+\tau^-(\gamma)$ events (left plots) there is a peak at high recoil masses: this is mostly due to the case in which both candidate tagging muons are fake-μ, and can be reduced requiring $\mu ID > 0.9$ (bottom-left plot). The contribution is mostly due to $\tau \to 3\pi$, where two pions are wrongly identified as muons. The case with two fake muons is also dominant for $e^+e^- \to q\bar{q}$ background (right plots), and again can be reduced with a stronger cut on μID on the tagging muons (bottom-right plot). Fake-muons are observed to contribute mostly at low momenta, where the μID is less effective.

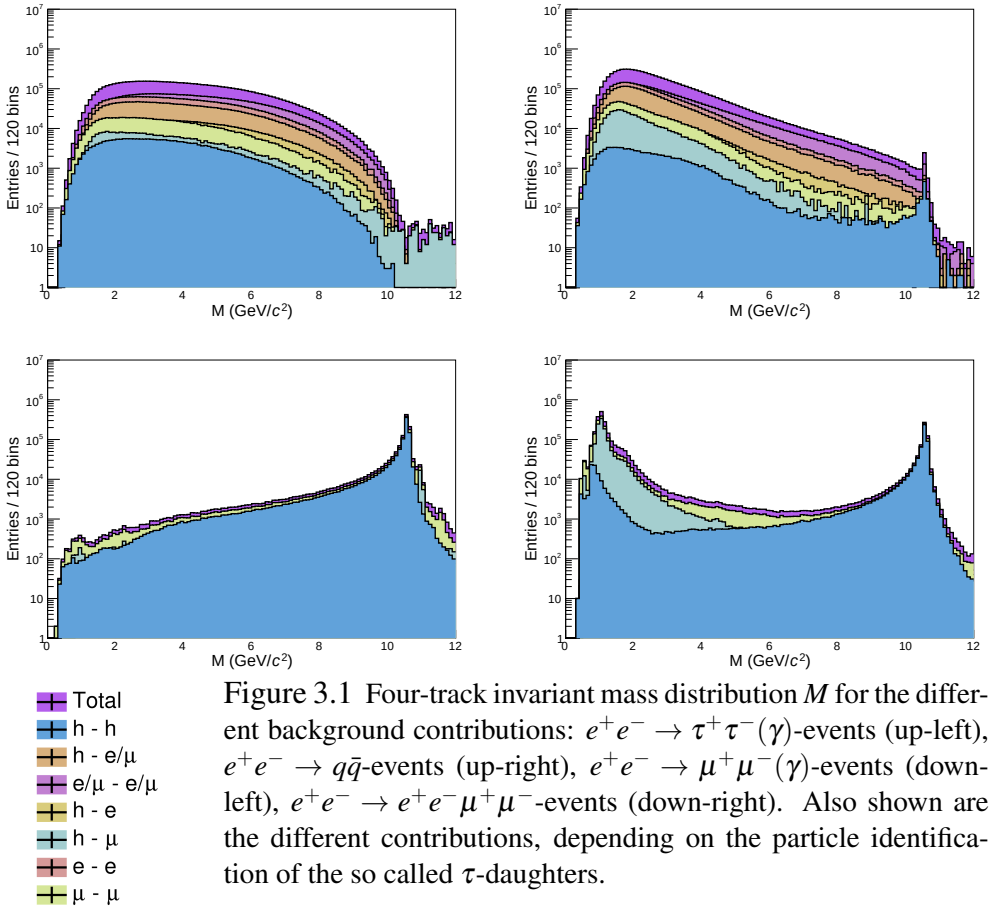

Figure 3.1 Four-track invariant mass distribution M for the different background contributions: $e^+e^- \to \tau^+\tau^-(\gamma)$-events (up-left), $e^+e^- \to q\bar{q}$-events (up-right), $e^+e^- \to \mu^+\mu^-(\gamma)$-events (down-left), $e^+e^- \to e^+e^-\mu^+\mu^-$-events (down-right). Also shown are the different contributions, depending on the particle identification of the so called τ-daughters.

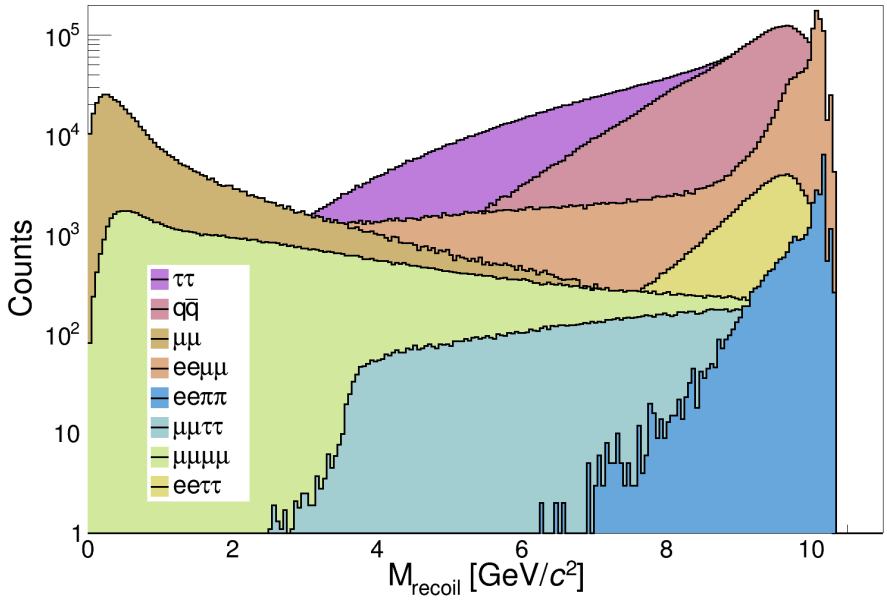

Figure 3.2 Recoil mass (against the tagging muon pair) distribution for each background component after the pre-selection that requires $M < 9.5$ GeV/c^2.

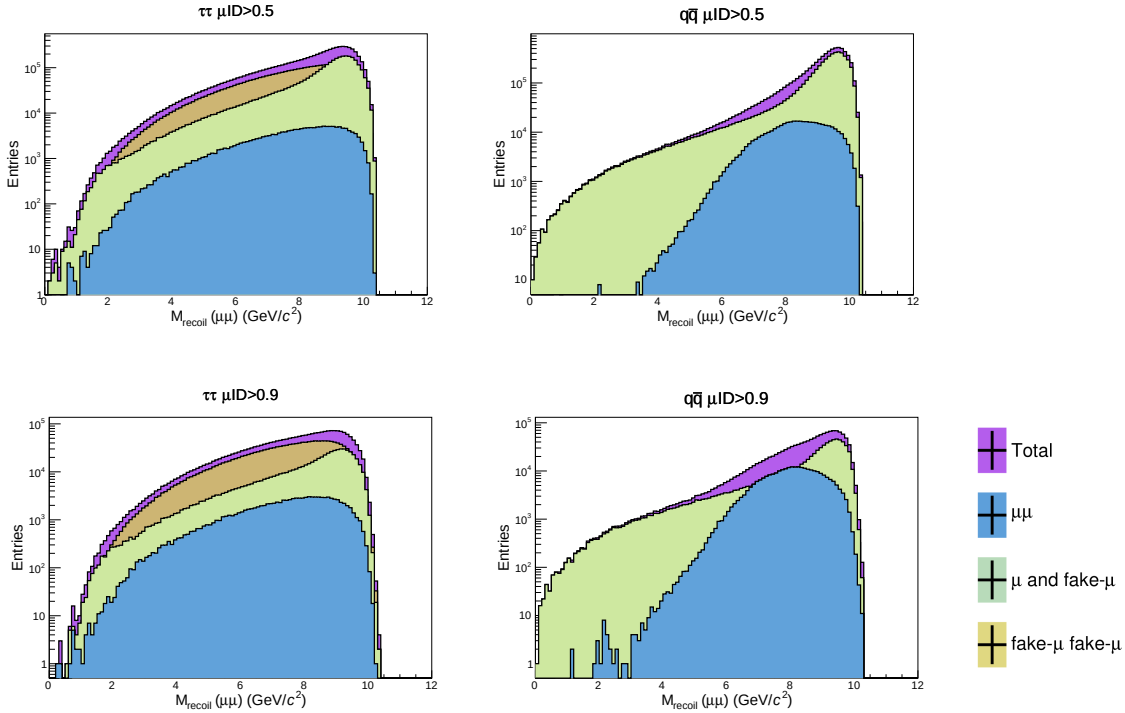

Figure 3.3 Recoil mass distributions. Left plots are for $e^+e^- \to \tau^+\tau^-(\gamma)$ events: tagging muons are required to have $\mu ID > 0.5$ (above) or $\mu ID > 0.9$ (below). Right plots are for $e^+e^- \to q\bar{q}$ events: tagging muons are required to have $\mu ID > 0.5$ (above) or $\mu ID > 0.9$ (below). Also shown are the different contributions corresponding to cases in which, looking at MC truth, both muons are real muons, one is real and the other is fake, both are fake.

3.1.2 Background rejection

Our $e^+e^- \to \mu^+\mu^- Z'$, $Z' \to \tau^+\tau^-$ signal is expected to show up as a peak in the invariant mass of the system recoiling against two tagging muons (recoil mass, from now on), obtained from

$$p_{\mu_0} + p_{\mu_1} + p_{recoil} = p_{e^+} + p_{e^-} \tag{3.1}$$

where p_{μ_0} and p_{μ_1} are the 4-momenta of the two tagging muons, p_{recoil} is the 4-momentum of the recoil system, p_{e^+} and p_{e^-} are the 4-momenta of the positron and electron of the initial state. From the previous equation we obtain the squared recoil mass

$$M^2_{recoil} = s + M^2_{\mu\mu} - 2\sqrt{s}(E^{CMS}_{\mu^+} + E^{CMS}_{\mu^-}), \tag{3.2}$$

where $\sqrt{s}$ is the energy in the center-of-mass frame, $M^2_{\mu\mu}$ is the squared invariant mass of the tagging muon pair and $E^{CMS}_{\mu^\pm}$ is the energy of the tagging muon in the center-of-mass frame. This recoil system is made of the visible remnants of two τ one-prong independent decays. The main features of the signal are:

- two well identified muons (tagging muons);
- a peak in the invariant mass of the system recoiling against these two tagging muons (recoil mass, from now on), the Z', that is made of the charged and neutral remnants of two τ one-prong independent decays;
- the rest frame of the recoil system, which is the rest frame of the Z', is equivalent to the final state of a $e^+e^- \to \tau^+\tau^-$ reaction, with collisions at $\sqrt{s} = M_{Z'}$.

In this subsection we are going to describe the variables that exploit the difference between the above listed signal features and those of the background.

Discriminant variables sensitive to the presence of a resonance in the recoil system We focus mostly on $e^+e^- \to \tau^+\tau^-(\gamma)$ and $e^+e^- \to q\bar{q}$ dominant backgrounds. Studies in this subsection are based on charged tracks only. The most promising discriminant variables or variable combinations that we find are:

- $p(\mu_1)$ vs $p(\mu_0)$, the momenta of the two tagging muons;
- p_T^{max} vs p_T^{min}, where p_T^{max} and p_T^{min} are the transverse components of the projection of the recoil momentum along the momentum of the muon with maximum and minimum momentum, respectively. These variables proved to be very effective in the invisible Z' case. We expect discrimination because the Z' is radiated as final-state-radiation (FSR) from one of the muons, which because of the radiation will be most likely the lowest momentum muon. The direction of the Z' is the direction of the recoil, and we can describe the process with the angle between the direction of the recoil and the direction of the muons (we prefer the transverse momentum rather than the angle, because the former carries more information). For background events the recoil is different, because it is not necessarily related to an FSR process;

- $p(\tau_{D,0}+\tau_{D,1})$ vs $M(\tau_{D,0},\tau_{D,1})$, where $p(\tau_{D,0}+\tau_{D,1})$ and $M(\tau_{D,0},\tau_{D,1})$ are respectively the modulus of the sum of the momenta and the invariant mass of the τ-daughters τ_D: in particular, $p(\tau_{D,0}+\tau_{D,1}) = |\bar{p}(\tau_{D,0})+\bar{p}(\tau_{D,1})|$, where $\bar{p}(\tau_{D,0})$ and $\bar{p}(\tau_{D,1})$ are the three-momenta of the daughter track of each τ-lepton, and $M^2(\tau_{D,0},\tau_{D,1}) = (p(\tau_{D,0})+p(\tau_{D,1}))^2$ where $p(\tau_{D,0})$ and $p(\tau_{D,1})$ are the four-momenta of the daughter track of each τ-lepton. Electron, muon or hadron (pion or kaon) mass is assumed depending on the result of the particle identification.

All momenta are expressed in the center-of-mass frame. Examples of these distributions for $M_{Z'} = 3.6$ GeV/c^2 are shown in Figure 3.4, while for $M_{Z'} = 6.6$ GeV/c^2 and $M_{Z'} = 9.6$ GeV/c^2 are shown in Figures 3.5 and 3.6. Background ($e^+e^- \to \tau^+\tau^-(\gamma)$ + $e^+e^- \to q\bar{q}$) and signal are evaluated at the same recoil mass, within $\pm 5\sigma_{peak}$, where σ_{peak} is the resolution. We observe that the $p(\mu_1)$ vs $p(\mu_0)$ and p_T^{max} vs p_T^{min} work better at small Z' mass, while $p(\tau_{D,0}+\tau_{D,1})$ vs $M(\tau_{D,0},\tau_{D,1})$ works a bit better for high Z' mass. We express these variables in better, less mass dependent, more physics (kinematics)-wise, way for later use: this is important because we will use the variables to train a MVA in which we put together different masses.
The two-dimensional $p(\mu_1)$ vs $p(\mu_0)$ distribution is confined between two lines, which can be expressed by two analytical functions directly related to physics features: the hyperbola and the straight line shown in red and green, respectively, in the top-left plot of Figure 3.4. Both functions can be expressed using half of the energy in the center-of-mass frame ($\sqrt{s}/2$), and the maximum momentum (P) of the system recoiling against the two muons (the Z' in case of signal). The latter corresponds to the case in which a system of mass $M_{Z'}$ recoils against a dimuon system of the minimum possible squared invariant mass $(2m_\mu)^2$.

$$P = \frac{\sqrt{(s+M_{Z'}^2-(2m_\mu))^2-4sM_{Z'}^2}}{2\sqrt{s}} \tag{3.3}$$

With $y = p(\mu_1)$ and $x = p(\mu_0)$, the two functions are

$$\begin{aligned} y &= P - x \\ y &= \frac{k}{x-\sqrt{s}/2} + \sqrt{s}/2, \text{with } k = \sqrt{s}/2(\sqrt{s}/2 - P) \end{aligned} \tag{3.4}$$

We define $d1$ and $d2$ as the distances of a generic point of the distribution from the straight line and from the hyperbola, respectively, and then $A = (d1-d2)/(d1+d2)$. Because background events (grey in Figure 3.4) populate preferentially the edge of the distribution, we expect A peaking at 1 or -1, differently from signal events (black distribution in Figure 3.4). A is the asymmetry between the distances of a generic point with respect to the straight and hyperbolic line which encapsulate the two-dimensional distribution. In order to exploit the orthogonal coordinate, we also use the $|p(\mu_0)_{R=45^o}/(\sqrt{2}/2\cdot P)|$ variable, i.e. the absolute value of the momentum of μ_0 obtained after the rotation by 45^o of the distribution $p(\mu_1)$ vs $p(\mu_0)$ ($p(\mu_0)_{R=45^o} = p(\mu_0)/\sqrt{2} - p(\mu_1)/\sqrt{2}$) and rescaled by $\sqrt{2}/2\cdot P$ in order to be defined between 0 and 1. Figures 3.7, 3.8 and 3.9 show the distribution of A and the distribution of $|p(\mu_0)_{R=45^o}/(\sqrt{2}/2\cdot P)|$ for signal and background events,

respectively for $M_{Z'} = 3.6$ GeV/c^2, $M_{Z'} = 6.6$ GeV/c^2 and $M_{Z'} = 9.6$ GeV/c^2. The background and signal distributions are normalized to the same number of entries to provide a qualitative visualization of the discriminating power of the variables.

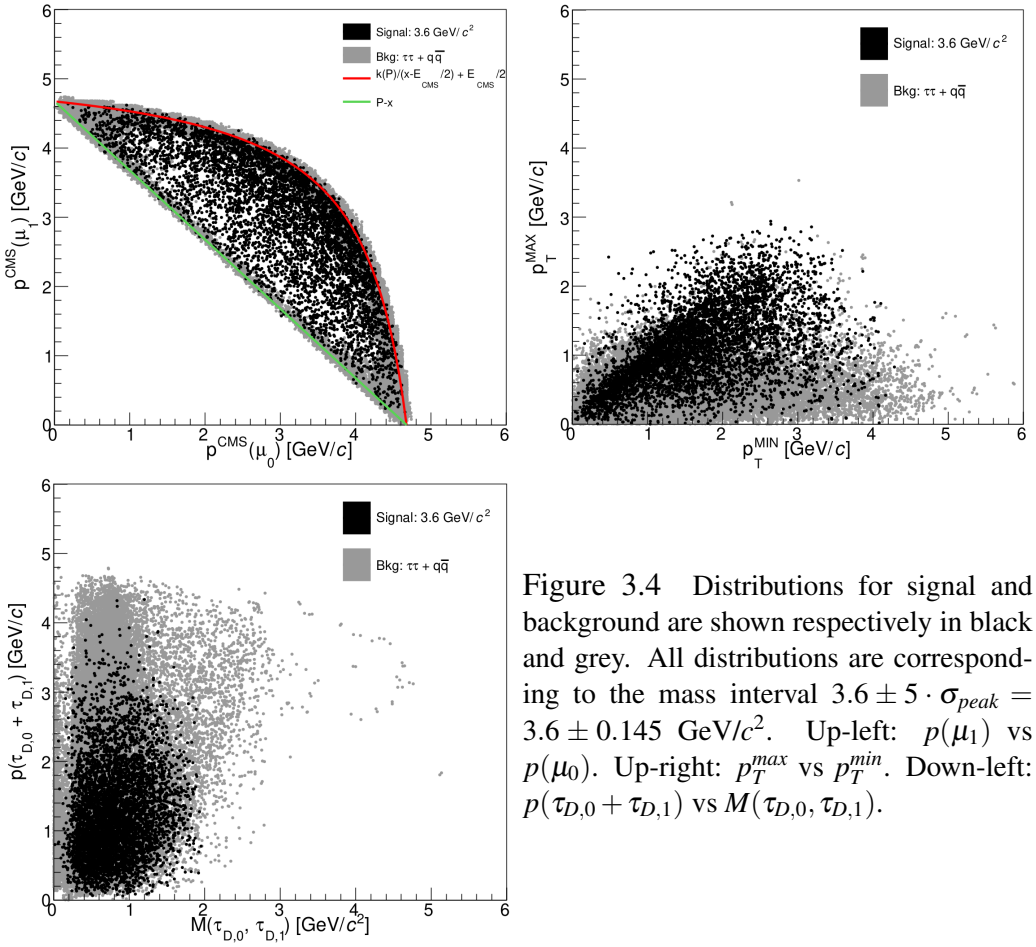

Figure 3.4 Distributions for signal and background are shown respectively in black and grey. All distributions are corresponding to the mass interval $3.6 \pm 5 \cdot \sigma_{peak} = 3.6 \pm 0.145$ GeV/c^2. Up-left: $p(\mu_1)$ vs $p(\mu_0)$. Up-right: p_T^{max} vs p_T^{min}. Down-left: $p(\tau_{D,0} + \tau_{D,1})$ vs $M(\tau_{D,0}, \tau_{D,1})$.

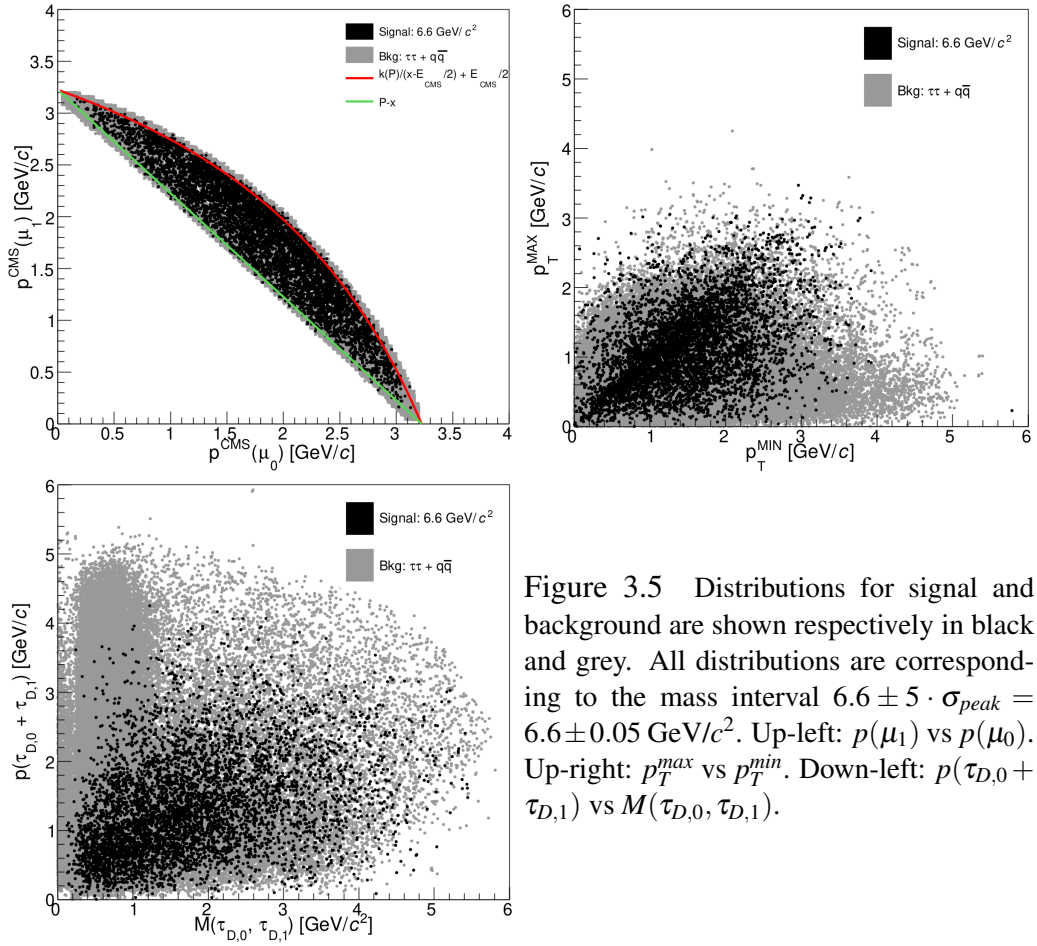

Figure 3.5 Distributions for signal and background are shown respectively in black and grey. All distributions are corresponding to the mass interval $6.6 \pm 5 \cdot \sigma_{peak} = 6.6 \pm 0.05$ GeV/c^2. Up-left: $p(\mu_1)$ vs $p(\mu_0)$. Up-right: p_T^{max} vs p_T^{min}. Down-left: $p(\tau_{D,0} + \tau_{D,1})$ vs $M(\tau_{D,0}, \tau_{D,1})$.

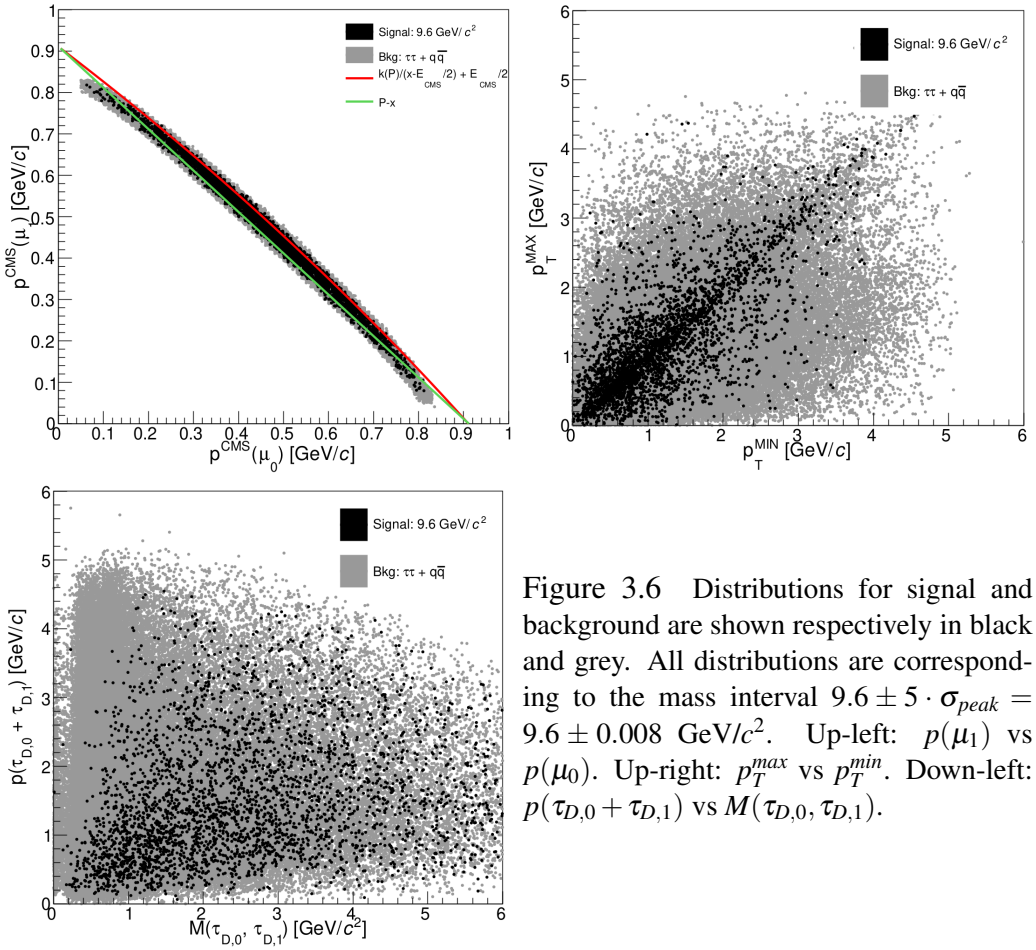

Figure 3.6 Distributions for signal and background are shown respectively in black and grey. All distributions are corresponding to the mass interval $9.6 \pm 5 \cdot \sigma_{peak} = 9.6 \pm 0.008$ GeV/c^2. Up-left: $p(\mu_1)$ vs $p(\mu_0)$. Up-right: p_T^{max} vs p_T^{min}. Down-left: $p(\tau_{D,0} + \tau_{D,1})$ vs $M(\tau_{D,0}, \tau_{D,1})$.

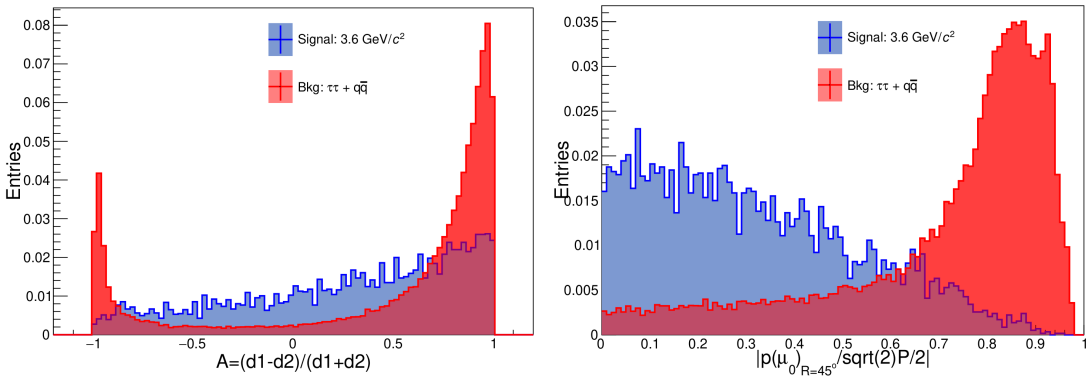

Figure 3.7 Left: distribution of the variable $A = (d1 - d2)/(d1 + d2)$. Right: distribution of $|p(\mu_0)_{R=45^o}/(\sqrt{2}/2 \cdot P)|$. Both are for signal (blue) and background (red), rescaled to the same number of entries, assuming $M_{Z'} = 3.6$ GeV/c^2. All distributions are corresponding to the mass interval $M_{Z'} \pm 5 \cdot \sigma_{peak}$ GeV/c^2.

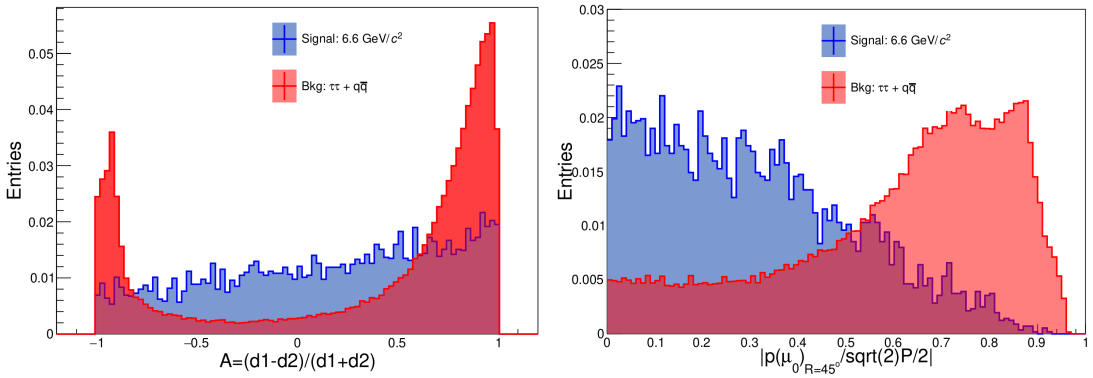

Figure 3.8 Left: distribution of the variable $A = (d1 - d2)/(d1 + d2)$. Right: distribution of $|p(\mu_0)_{R=45^o}/(\sqrt{2}/2 \cdot P)|$. Both are for signal (blue) and background (red), rescaled to the same number of entries, assuming $M_{Z'} = 6.6$ GeV/c^2. All distributions are corresponding to the mass interval $M_{Z'} \pm 5 \cdot \sigma_{peak}$ GeV/c^2.

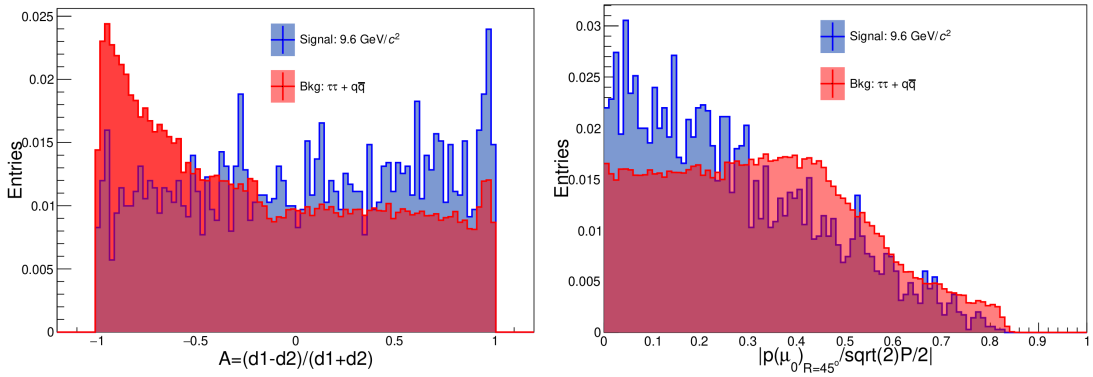

Figure 3.9 Left: distribution of the variable $A = (d1 - d2)/(d1 + d2)$. Right: distribution of $|p(\mu_0)_{R=45^o}/(\sqrt{2}/2 \cdot P)|$. Both are for signal (blue) and background (red), rescaled to the same number of entries, assuming $M_{Z'} = 9.6$ GeV/c^2. All distributions are corresponding to the mass interval $M_{Z'} \pm 5 \cdot \sigma_{peak}$ GeV/c^2.

The p_T^{max} vs p_T^{min} distribution was treated in a different way. We use polar coordinates defined as

$$\begin{aligned} R &= \sqrt{(p_T^{max})^2 + (p_T^{min})^2} \\ \theta &= Atan2\left(p_T^{max}, p_T^{min}\right) \end{aligned} \tag{3.5}$$

and then R was rescaled by P. The discriminant variables R/P and θ work quite well for small Z' masses, with their discriminant power decreasing with mass. Figures 3.10, 3.11 and 3.12 show the two variables for $M_{Z'} = 3.6$ GeV/c^2, $M_{Z'} = 6.6$ GeV/c^2 and $M_{Z'} = 9.6$ GeV/c^2.

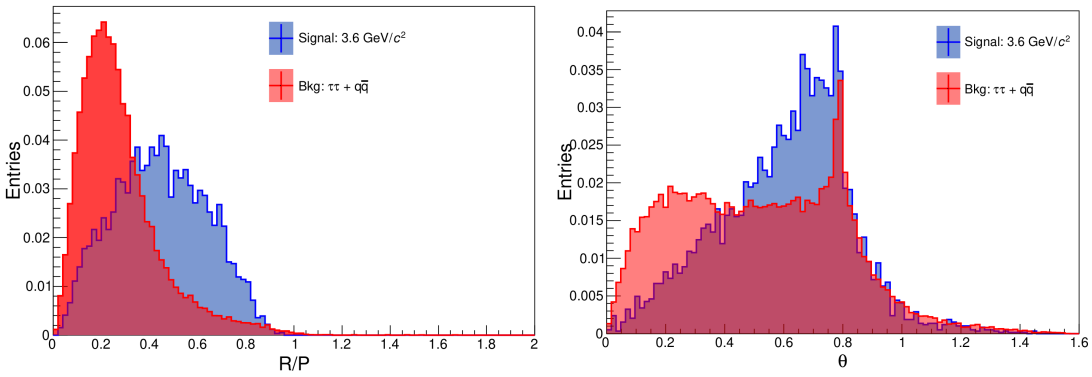

Figure 3.10 Left: distribution of R/P for signal (blue) and background (red) rescaled for the number of entries, assuming $M_{Z'} = 3.6$ GeV/c^2. Right: distribution of θ for signal (blue) and background (red) rescaled to the same number of entries, assuming $M_{Z'} = 3.6$ GeV/c^2. All distributions are corresponding to the mass interval $M_{Z'} \pm 5 \cdot \sigma_{peak}$ GeV/c^2.

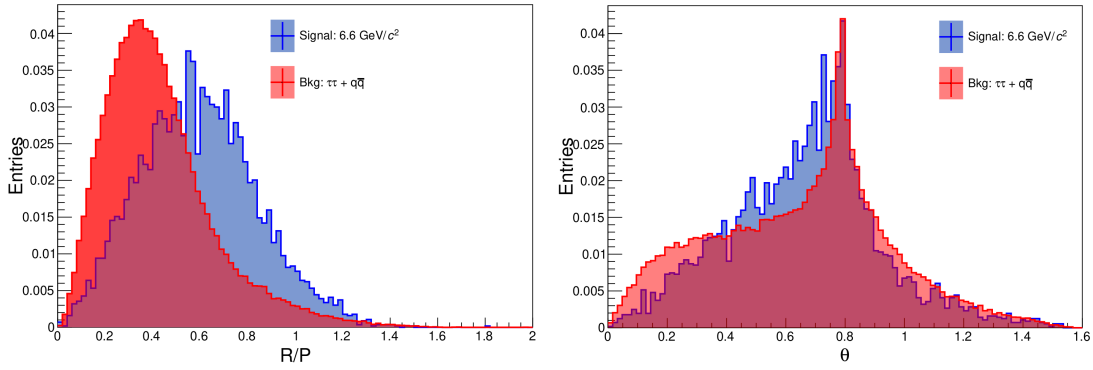

Figure 3.11 Left: distribution of R/P for signal (blue) and background (red) rescaled for the number of entries, assuming $M_{Z'} = 6.6$ GeV/c^2. Right: distribution of θ for signal (blue) and background (red) rescaled to the same number of entries, assuming $M_{Z'} = 6.6$ GeV/c^2. All distributions are corresponding to the mass interval $M_{Z'} \pm 5 \cdot \sigma_{peak}$ GeV/c^2.

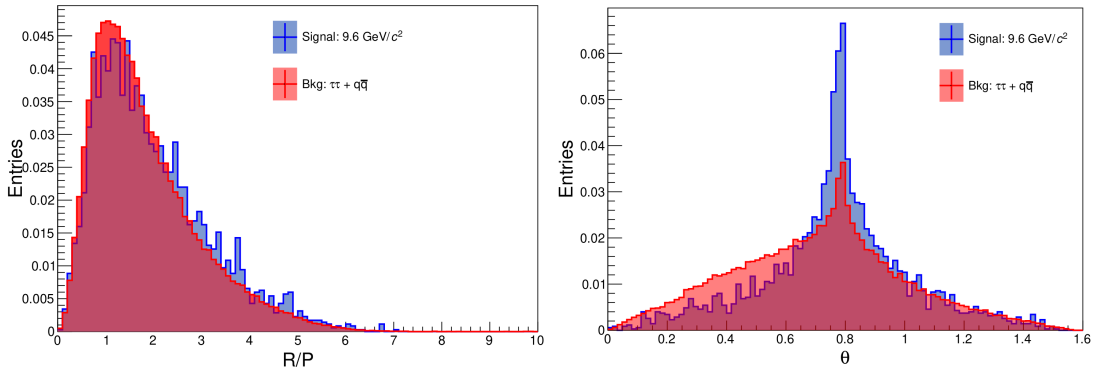

Figure 3.12 Left: distribution of R/P for signal (blue) and background (red) rescaled for the number of entries, assuming $M_{Z'} = 9.6$ GeV/c^2. Right: distribution of θ for signal (blue) and background (red) rescaled to the same number of entries, assuming $M_{Z'} = 9.6$ GeV/c^2. All distributions are corresponding to the mass interval $M_{Z'} \pm 5 \cdot \sigma_{peak}$ GeV/c^2.

The $p(\tau_{D,0} + \tau_{D,1})$ vs $M(\tau_{D,0}, \tau_{D,1})$ distribution was transformed in polar coordinate too, defined as

$$\begin{aligned} R_{1,2} &= \sqrt{(p(\tau_{D,0} + \tau_{D,1}))^2 + (M(\tau_{D,0}, \tau_{D,1}))^2} \\ \theta_{1,2} &= Atan2\left(p(\tau_{D,0} + \tau_{D,1}), M(\tau_{D,0}, \tau_{D,1})\right) \end{aligned} \tag{3.6}$$

Figure 3.13 (above, first two plots from the left) shows the correlation $R_{1,2}$ vs $\theta_{1,2}$ for signal (first plot) and background (second plot). Background events approximately follow the hyperbola of equation $y = \sqrt{2}/2/(\pi/2 - x)$, where $y = R_{1,2}$ and $x = \theta_{1,2}$. A new variable is defined as $y' = R_{1,2} \cdot (\pi/2 - x)$, which satisfies the relation $y' = \sqrt{2}/2$ for background events. Figure 3.13 (above, third and fourth plots) shows the scatter plot y' vs $\theta_{1,2}$ with the straight line with equation $y' = \sqrt{2}/2$ for signal (third plot) and background (fourth plot). Most of background events are accumulated close to the straight line, while most of signal events are not. This heuristic method allows to define the distance $d_{1,2}$ of a generic point from $y' = \sqrt{2}/2$. The two discriminant variables $d_{1,2}$ and $\theta 12$, are shown in Figures 3.13, 3.14 and 3.15 for $M_{Z'} = 3.6$ GeV/c^2, $M_{Z'} = 6.6$ GeV/c^2 and $M_{Z'} = 9.6$ GeV/c^2.

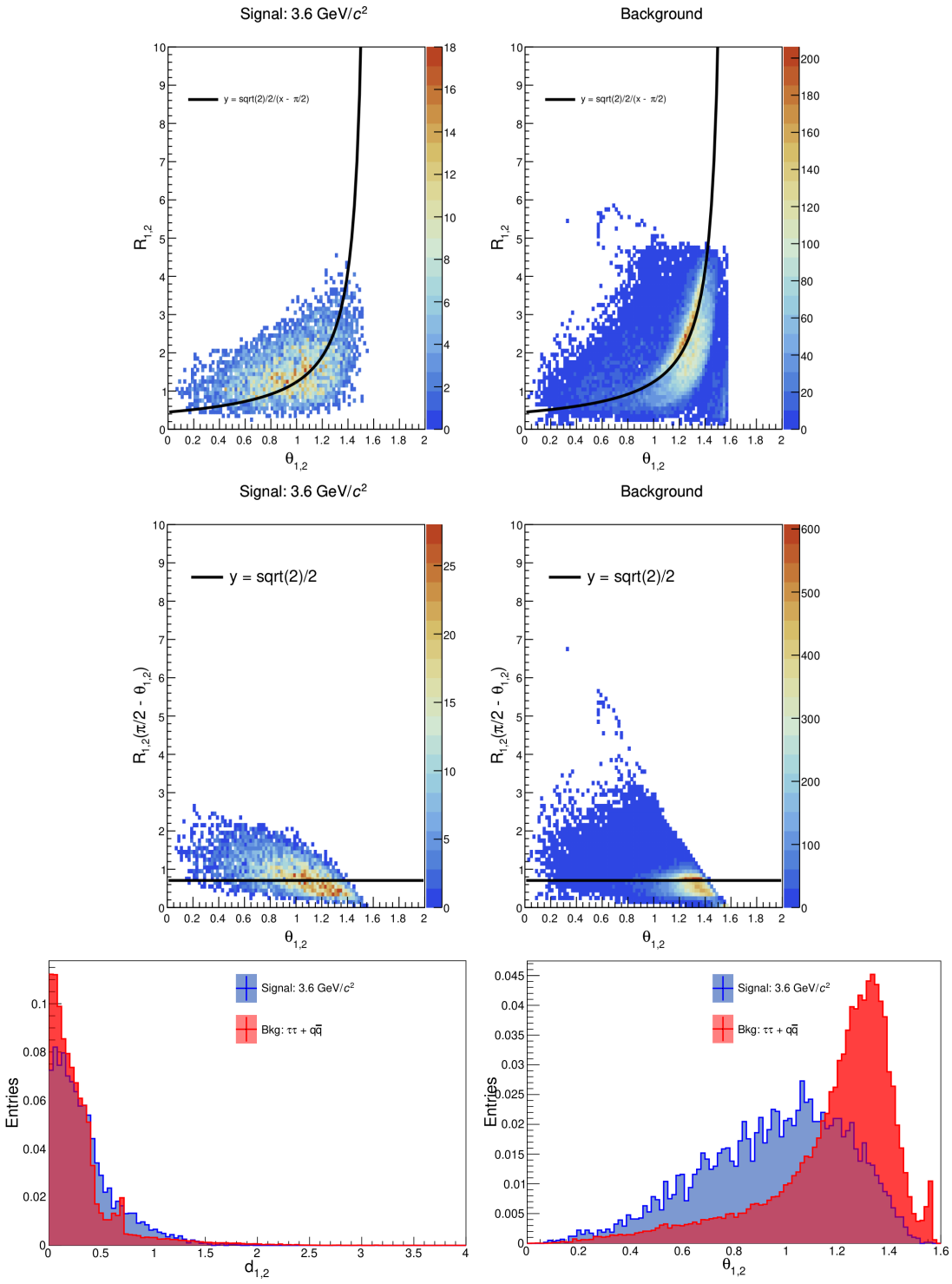

Figure 3.13 Above: correlation $R_{1,2}$ vs $\theta_{1,2}$ for signal (first) and background (second), correlation $y' = R_{1,2} \cdot (\pi/2 - \theta)$ vs $\theta_{1,2}$ for signal (third) and background (fourth). Below: $d_{1,2}$ (left) and $\theta_{1,2}$ (right) distributions rescaled to the same number of entries. All plots are for $M_{Z'} = 3.6$ GeV/c^2. All distributions are corresponding to the mass interval $M_{Z'} \pm 5 \cdot \sigma_{peak}$ GeV/c^2.

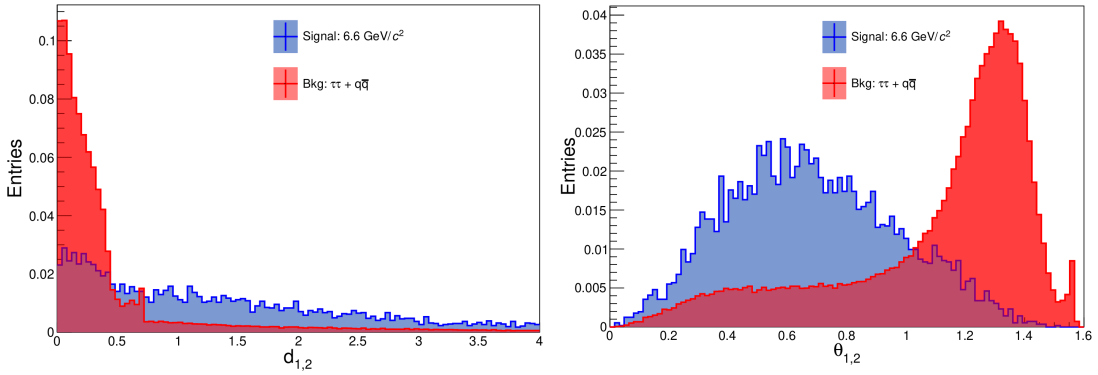

Figure 3.14 $d_{1,2}$ (left) and $\theta_{1,2}$ (right) distributions rescaled to the same number of entries. All plots are for $M_{Z'} = 6.6$ GeV/c^2. All distributions are corresponding to the mass interval $M_{Z'} \pm 5 \cdot \sigma_{peak}$ GeV/c^2.

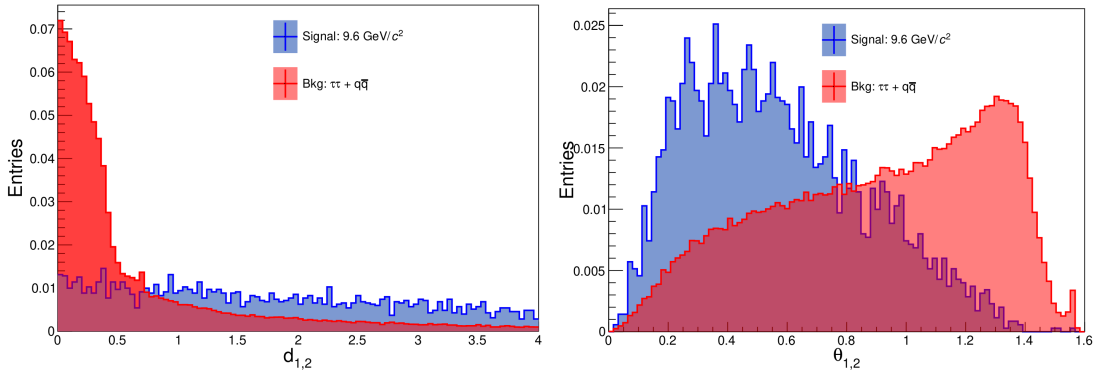

Figure 3.15 $d_{1,2}$ (left) and $\theta_{1,2}$ (right) distributions rescaled to the same number of entries. All plots are for $M_{Z'} = 9.6$ GeV/c^2. All distributions are corresponding to the mass interval $M_{Z'} \pm 5 \cdot \sigma_{peak}$ GeV/c^2.

Discriminant variables sensitive to the presence of a $\tau\tau$ pair in the recoil system Additional discriminant variables can be studied in the recoil system. In particular:

A) we recostruct neutral particles, requiring $E_\gamma > 100$ MeV to reduce the contamination from beam background photons;

B) We define a system containing all the measured particles, charged and neutral, except the tagging muons. This coincides with the Z' frame in case of signal. Using the momentum opposite to the dimuon pair (recoil momentum), we boost the system in the reference frame in which the Z' is at rest (in case of signal). In that frame, for the signal, the process is similar to $e^+e^- \to \tau^+\tau^-$ with $\sqrt{s} = M_{Z'}$. This is not true in general for background events, hence the possibility to built discriminant variables;

C) some combinations with Rest-Of-Event (ROE) variables;

A) Neutral Particles We reconstruct the 10 most energetic photons in the event, and combine them in pairs to search for neutral pions ($\pi^0 \to \gamma\gamma$), selecting only those combinations with an invariant mass compatible with the π^0 mass. Figure 3.16 shows the invariant mass of photon pairs compatible with the π^0 mass, with our selection (grey peak) superimposed, for a Z' mass of 3.6 GeV/c^2 and the $\tau\tau$ and $q\bar{q}$ background components.

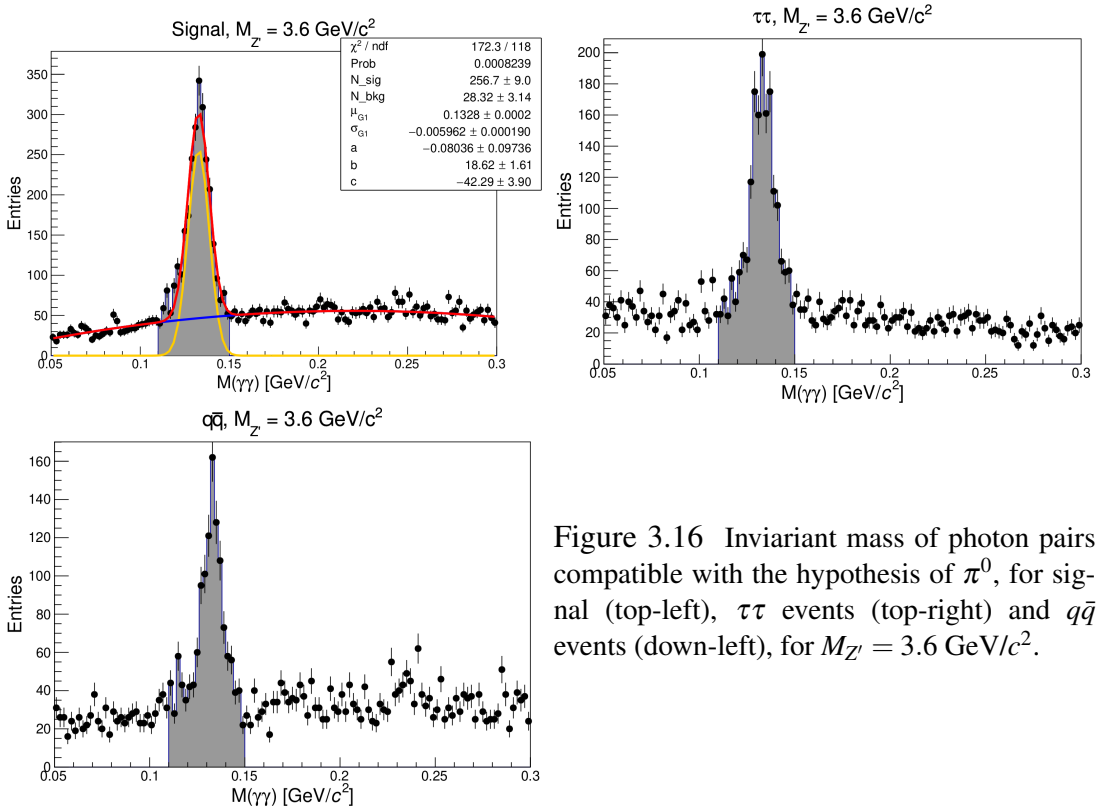

Figure 3.16 Inviariant mass of photon pairs compatible with the hypothesis of π^0, for signal (top-left), $\tau\tau$ events (top-right) and $q\bar{q}$ events (down-left), for $M_{Z'} = 3.6$ GeV/c^2.

We then study the distributions of the angle between the neutral pion momentum and the tagging muon momentum directions in the center-of-mass frame. In particular, we consider two cases:

- the angle between the 3-momentum of the π^0 and the 3-momentum of the tagging muon of minimum momentum, $\alpha(\pi^0, p(\mu)_{min})$;
- the angle between the 3-momentum of the π^0 and the 3-momentum of the tagging muon of maximum momentum, $\alpha(\pi^0, p(\mu)_{max})$;

Figure 3.17 shows these angles for $M_{Z'} = 3.6$ GeV/c^2, and their correlations for signal and main background components. The main background is the $\tau\tau$ process, where one of the two τ decays in one μ that passes the μID selection, and the other τ decays in three charged pions, with one of them mis-identified as a muon, plus a π^0. In this case, the first (real) muon is preferentially the most energetic, and the π^0 goes in the opposite direction. There are also cases in which a τ decays in a charged pion mis-identified as a muon. In this case the π^0 goes in the same direction. Since the angles are not always defined

because in some events there can be zero neutral pions, we use the two-angle correlation to build two new variables, which are also sensitive to the number of neutral pions in the event. Backgrounds concentrate mostly in the up-left (mainly) and up-right corners of the correlation plot (see Figure 3.17, bottom), while signal is more uniformly distributed. We sum the energy of neutral pions that fall inside and outside the corner regions of the plot according to the following condition:

(1) $(\alpha(\pi^0, p(\mu)_{max}) \leq 0.5$ or $\alpha(\pi^0, p(\mu)_{max}) \geq 2.5)$ and
$(\alpha(\pi^0, p(\mu)_{min}) \leq 0.8$ or $\alpha(\pi^0, p(\mu)_{min}) \geq 2.4)$

The two new variables are:

$$\begin{matrix} \Sigma_{i=0}^{n_{\pi^0}} E_i(\pi^0)_{IN}^{CMS} \\ \Sigma_{i=0}^{n_{\pi^0}} E_i(\pi^0)_{OUT}^{CMS} \end{matrix} \tag{3.7}$$

where IN means the above condition (1) is satisfied, while OUT means it is not.

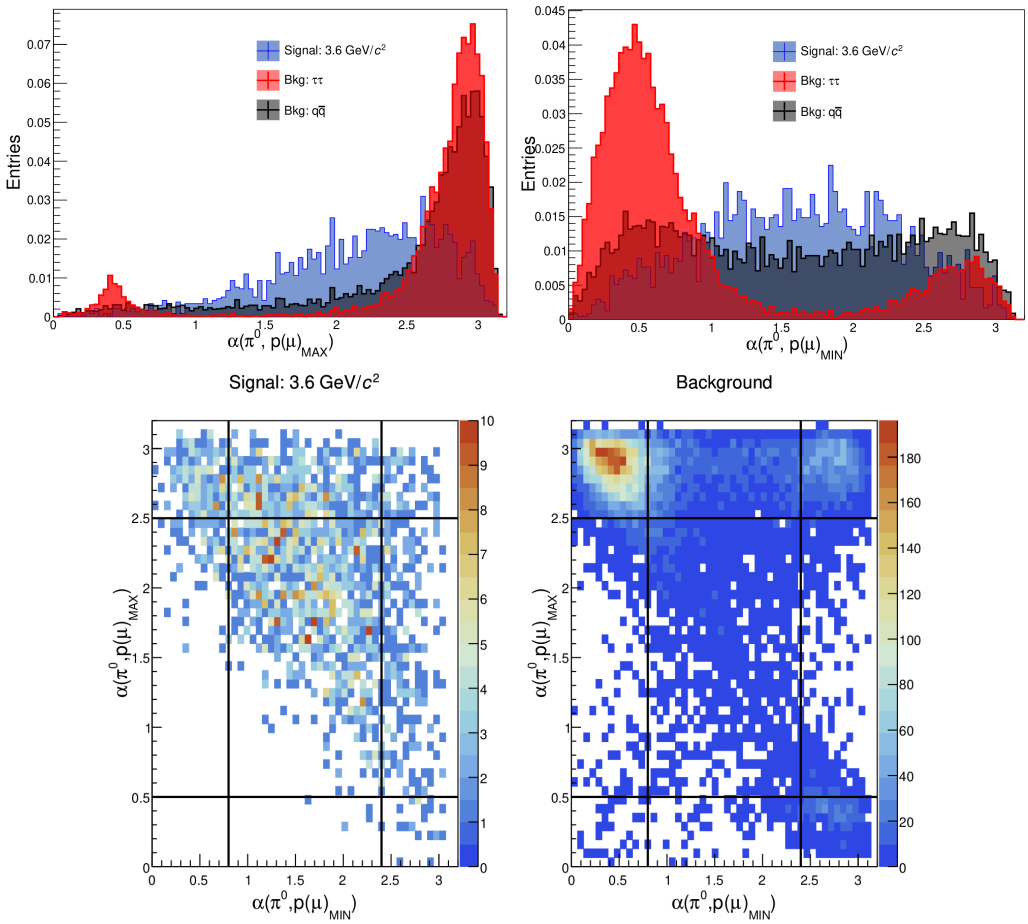

Figure 3.17 $\alpha(\pi^0, p(\mu)_{max})$ (top-right), $\alpha(\pi^0, p(\mu)_{min})$ (top-left), rescaled to the same number of entries, $\alpha(\pi^0, p(\mu)_{max})$ vs $\alpha(\pi^0, p(\mu)_{min}$ (below) for $M_{Z'} = 3.6$ GeV/c^2 and main background components. All distributions are corresponding to the mass interval $M_{Z'} \pm 5 \cdot \sigma_{peak}$ GeV/c^2.

The two variables are shown in Figure 3.18, they look very similar for different Z' masses. The peak at zero is quite different for signal and background and it is related to the number of neutral pions in the events: most of background events with π^0s fall in the corners of the correlation plot in Figure 3.17, while the opposite holds for the signal. For example, for $\Sigma_{i=0}^{n_{\pi^0}} E_i(\pi^0)_{OUT}^{CMS}$ we expect that the number of events where the sum of the energies of the π^0s is equal to zero is higher for background than for signal (because most of background events with π^0s fall IN the corners of the correlation plot), while the number of events where the sum of the energies of the π^0s differs from zero is larger for signal than for background (because most of signal events with π^0s fall OUT of the corners of the correlation plot). We expect the opposite for $\Sigma_{i=0}^{n_{\pi^0}} E_i(\pi^0)_{IN}^{CMS}$.

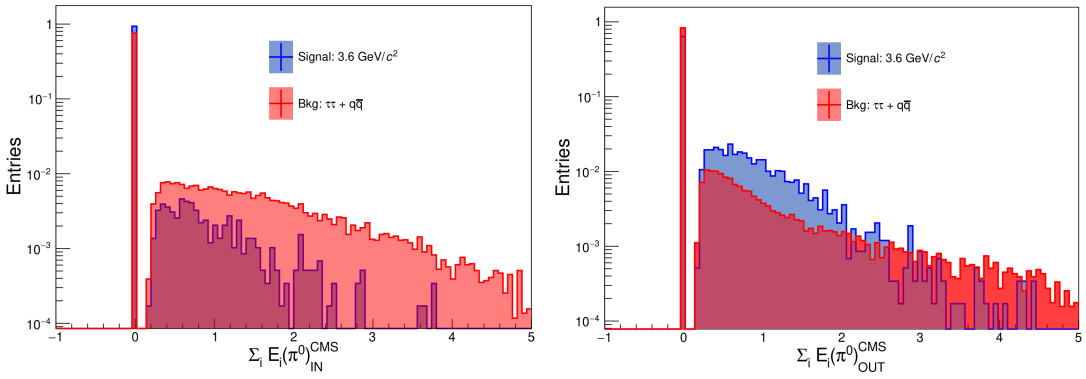

Figure 3.18 $\Sigma_{i=0}^{n_{\pi^0}} E_i(\pi^0)_{IN}^{CMS}$ (left), $\Sigma_{i=0}^{n_{\pi^0}} E_i(\pi^0)_{OUT}^{CMS}$ (right) for $M_{Z'} = 3.6$ GeV/c^2. All distributions are corresponding to the mass interval $M_{Z'} \pm 5 \cdot \sigma_{peak}$ GeV/c^2 and rescaled to the same number of entries.

B) Boosted reference frame We transform to the system where the signal Z' would be at rest and use mostly shape variables [94]:

- thrust T. For a collection of N particles with momenta $\overrightarrow{p}_i$, the thrust axis is the axis $\overrightarrow{n}_T$ that maximizes the projection of the 3-momenta of the particles; the projection, normalized to the sum of the 3-momenta modules is called thrust T. Formally it is defined as

$$T = \max_{\overrightarrow{n}} \frac{\Sigma_i^N |\overrightarrow{p}_i \cdot \overrightarrow{n}|}{\Sigma_i^N |\overrightarrow{p}_i|} \tag{3.8}$$

  where $|\overrightarrow{n}| = 1$ and the sum Σ_i runs over the three-momenta, $\overrightarrow{p}_i$, of all final states. The thrust axis is defined by the vector $\overrightarrow{n}_T$ for which the maximum is obtained. This definition means that for $T = 1$ the event is perfectly back-to-back while for $T = 1/2$ the event is spherically symmetric;

- first Fox-Wolfram moment fox-R1. For a collection of N particles with momenta $\overrightarrow{p}_i$, Fox-Wolfram moments are defined as

$$H_l = \Sigma_{i,j}^N \frac{|\overrightarrow{p}_i||\overrightarrow{p}_j|}{s} P_l(cos\theta_{ij}) \tag{3.9}$$

where P_l is the l^{th} order Legendre polynomial and θ_{ij} is the angle between $\overrightarrow{p}_i$ and $\overrightarrow{p}_j$, $\sqrt{s}$ is the center-of-mass energy. They are an effective way of describing the angular correlations between particles. The first Fox-Wolfram moment will be

$$H_1 = \Sigma_{i,j}^{N} \frac{|\overrightarrow{p}_i||\overrightarrow{p}_j|}{s}(cos\theta_{ij}) = \Sigma_{i,j}^{N} \frac{\overrightarrow{p}_i \cdot \overrightarrow{p}_j}{s} \tag{3.10}$$

We use the ratio

$$\text{fox} - \text{R}_1 = \frac{H_1}{H_0} \tag{3.11}$$

that in case of events with two strongly collimated jet-like structures takes a value close to zero.

- angle between the thrust and the momentum directions of the tagging muons, distinguishing as before the cases of maximum and minimum momentum: muon $\alpha(p(\mu)_{max}, \overrightarrow{n}_T)$ and $\alpha(p(\mu)_{min}, \overrightarrow{n}_T)$.

Figures 3.19, 3.20, 3.21 and 3.22 show the distributions of thrust, first Fox-Wolfram moment and angle between thrust and muons with maximum and minimum momentum for signal and background, for three different masses.

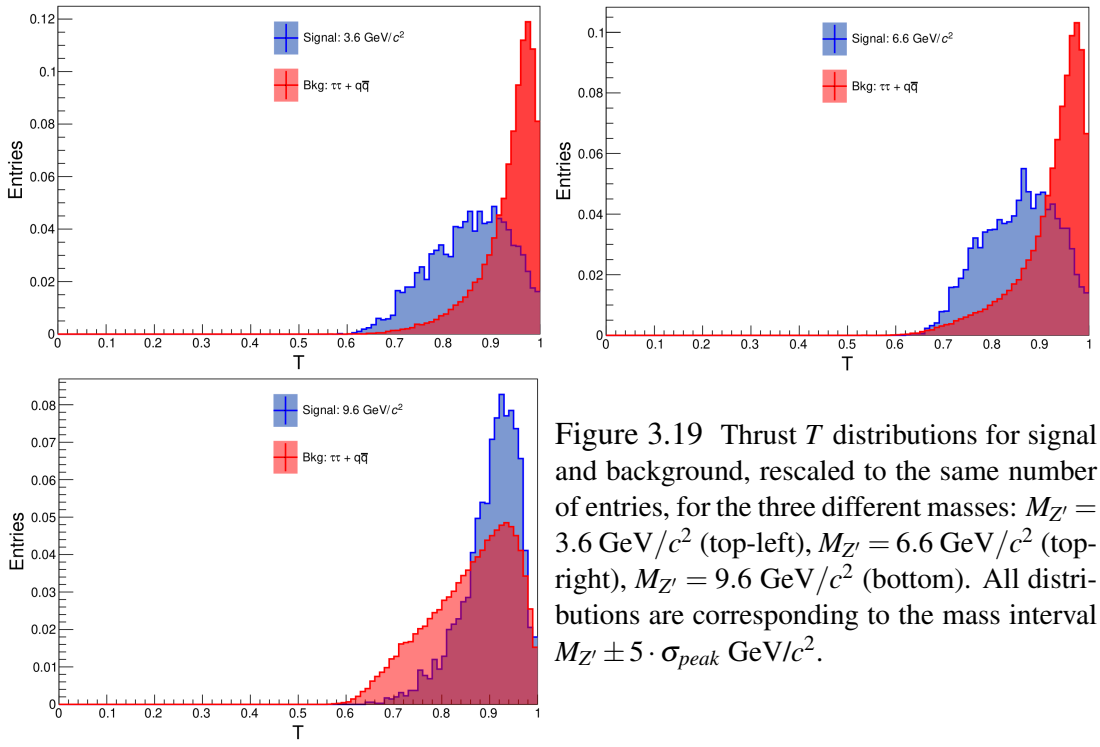

Figure 3.19 Thrust T distributions for signal and background, rescaled to the same number of entries, for the three different masses: $M_{Z'} = 3.6\ \text{GeV}/c^2$ (top-left), $M_{Z'} = 6.6\ \text{GeV}/c^2$ (top-right), $M_{Z'} = 9.6\ \text{GeV}/c^2$ (bottom). All distributions are corresponding to the mass interval $M_{Z'} \pm 5 \cdot \sigma_{peak}\ \text{GeV}/c^2$.

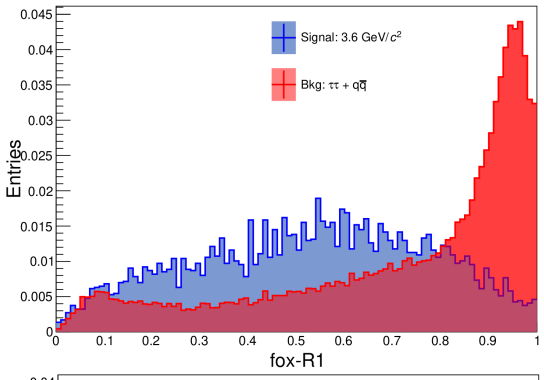

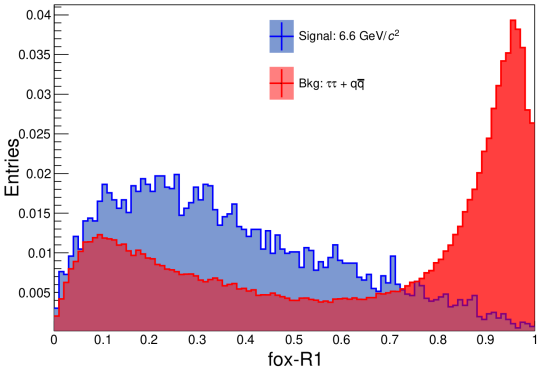

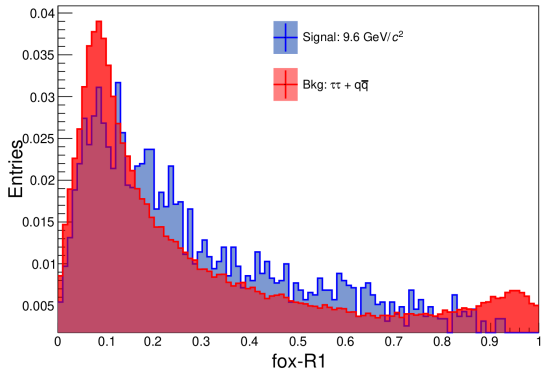

Figure 3.20 First Fox-Wolfram, $foxR1$, momentum distributions for signal and background, rescaled to the same number of entries, for the three different masses: $M_{Z'} = 3.6$ GeV$/c^2$ (top-left), $M_{Z'} = 6.6$ GeV$/c^2$ (top-right), $M_{Z'} = 9.6$ GeV$/c^2$ (bottom). All distributions are corresponding to the mass interval $M_{Z'} \pm 5 \cdot \sigma_{peak}$ GeV$/c^2$.

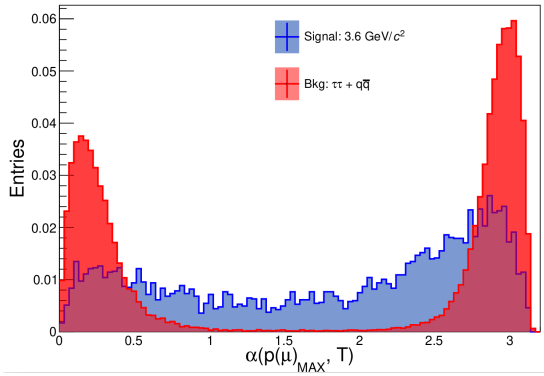

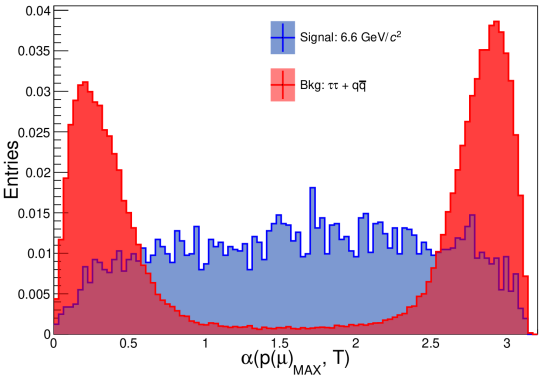

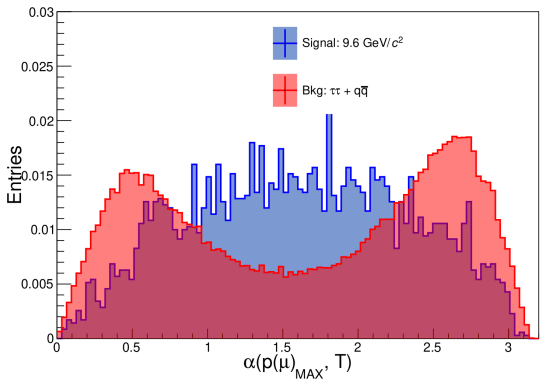

Figure 3.21 Distributions of angles between the momentum of the muons with maximum momentum and the thrust direction, for signal and background, rescaled to the same number of entries, for three different masses: $M_{Z'} = 3.6$ GeV$/c^2$ (top-left), $M_{Z'} = 6.6$ GeV$/c^2$ (top-right), $M_{Z'} = 9.6$ GeV$/c^2$ (bottom). All distributions are corresponding to the mass interval $M_{Z'} \pm 5 \cdot \sigma_{peak}$ GeV$/c^2$.

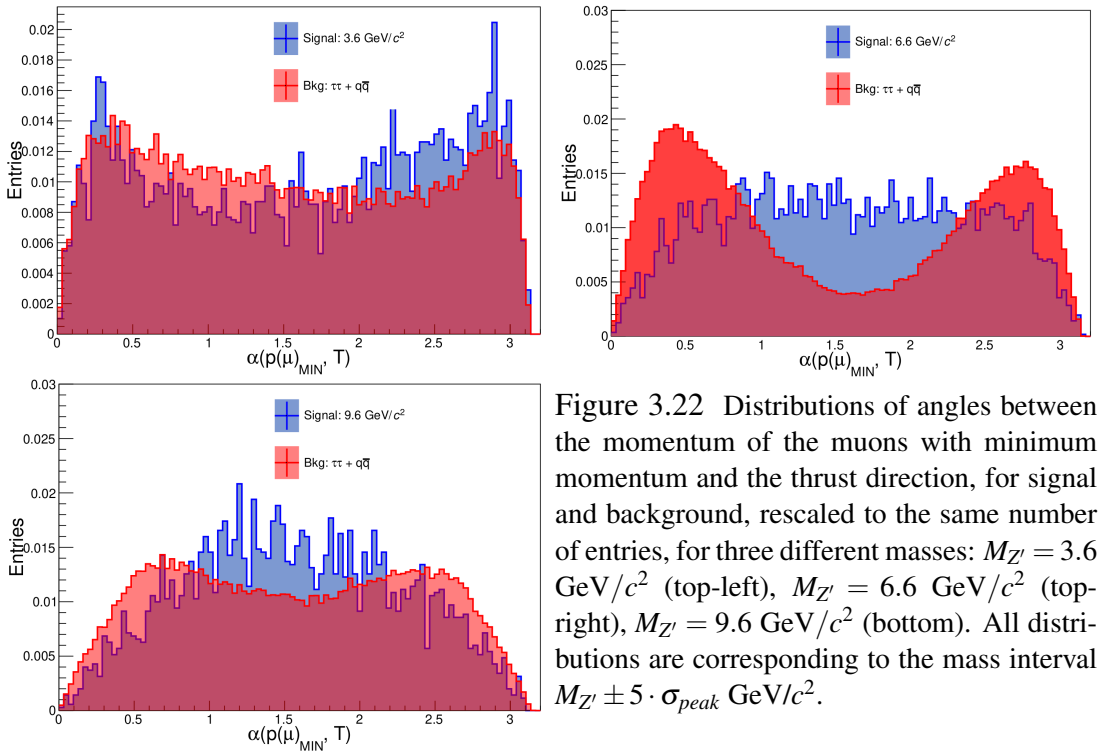

Figure 3.22 Distributions of angles between the momentum of the muons with minimum momentum and the thrust direction, for signal and background, rescaled to the same number of entries, for three different masses: $M_{Z'} = 3.6$ GeV$/c^2$ (top-left), $M_{Z'} = 6.6$ GeV$/c^2$ (top-right), $M_{Z'} = 9.6$ GeV$/c^2$ (bottom). All distributions are corresponding to the mass interval $M_{Z'} \pm 5 \cdot \sigma_{peak}$ GeV$/c^2$.

C) Variables built using Rest-Of-Event We reconstruct the Rest-Of-Event (ROE) with respect to the tagging muon pair, containing all the information of particles not reconstructed as muon pair, and build new discriminating variables:

- $\Delta ROE_M = M - M[\text{ROE}(\mu\mu)] - M(\mu\mu)$
- $\Delta ROE_E = E - E[\text{ROE}(\mu\mu)] - E(\mu_0) - E(\mu_1)$, where energies are calculated in the boosted reference frame (where Z' is at rest)

M and E are the invariant mass and the total energy of the four tracks in the event, $M[\text{ROE}(\mu\mu)]$ and $E[\text{ROE}(\mu\mu)]$ are the invariant mass and the total energy of the ROE system, $M(\mu\mu)$ is the invariant mass of the muon pair and $E(\mu_i), i = 0, 1$ are the energies of the two tagging muons. These are heuristic combinations of kinematic variables, with some discriminant power. They are shown respectively in Figures 3.24 and 3.23, for three different masses.

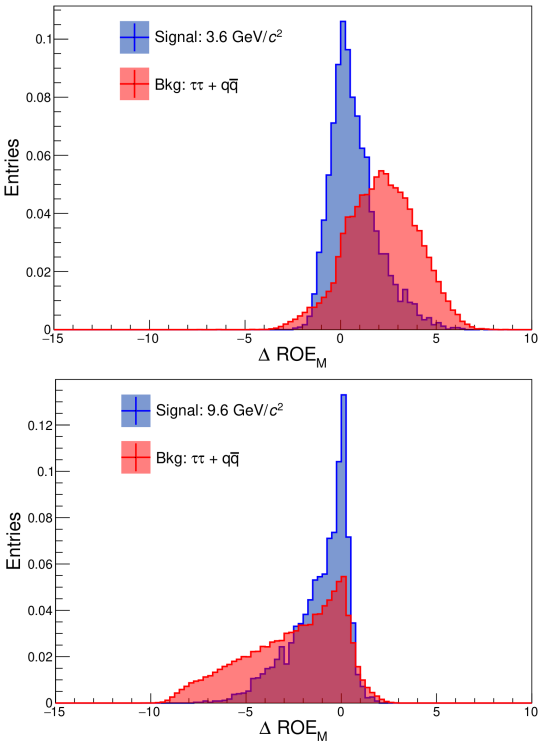

Figure 3.23 Distributions of ΔROE_M for three different masses (signal and background are rescaled to the same number of entries): $M_{Z'} = 3.6\ \mathrm{GeV}/c^2$ (top-left), $M_{Z'} = 6.6\ \mathrm{GeV}/c^2$ (top-right), $M_{Z'} = 9.6\ \mathrm{GeV}/c^2$ (bottom). All distributions are corresponding to the mass interval $M_{Z'} \pm 5 \cdot \sigma_{peak}\ \mathrm{GeV}/c^2$.

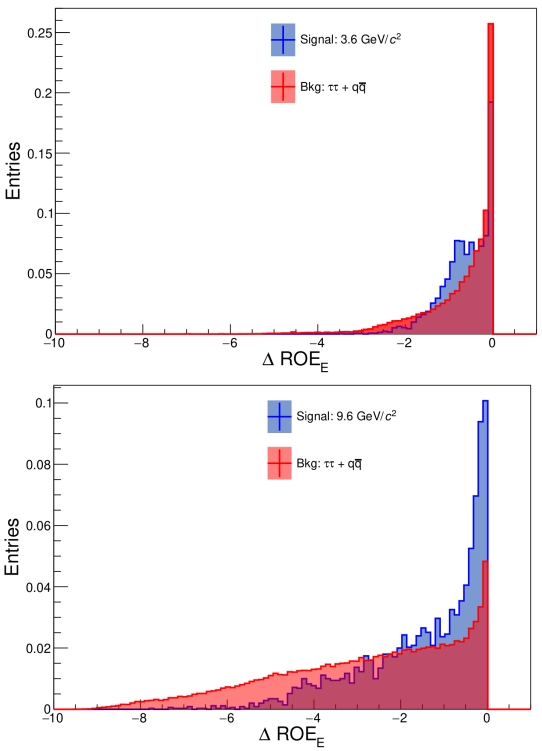

Figure 3.24 Distributions of ΔROE_E for three different masses (signal and background are rescaled to the same number of entries): $M_{Z'} = 3.6\ \mathrm{GeV}/c^2$ (top-left), $M_{Z'} = 6.6\ \mathrm{GeV}/c^2$ (top-right), $M_{Z'} = 9.6\ \mathrm{GeV}/c^2$ (bottom). All distributions are corresponding to the mass interval $M_{Z'} \pm 5 \cdot \sigma_{peak}\ \mathrm{GeV}/c^2$.

3.2 Multivariate Analysis (MVA)

The Multivariate Analysis is the statistical analysis of a problem characterized by many variables that can be correlated in various ways, or also not correlated, that are simultaneously analyzed. The methodology used in MVA is to provide a training sample with already known classification used by MVA to learn how to separate classes of events such as signal and background, which is the main interest for this analysis. In few words, MVA is given a sample of only signal events, a sample of only background events and some input variables with some discriminant power between signal and background. MVA provides a single output variable ranging from 0 to 1 for the two categories, that optimizes the information in the input variables.
There are two main steps in the learning procedure of an MVA: training and testing. During the training phase, MVA learns how to distinguish background from signal events, in a way that depends on the method implemented. During the testing phase, statistical independent background and signal samples are used to check if overtraining has occurred. Overtraining happens if the MVA has learnt "too well" to recognize the specific features of the training sample, like statistical fluctuations. In case of overtraining, the discriminant power of MVA is very high for the training sample, but it does not work well on the other samples. The main reasons for overtraining are: low statistics for the training sample or excessive depth of the training. In the first case, the training sample is dominated by fluctuations that MVA learns to recognize, while in the second case the training is so deep that MVA is able to learn the little fluctuations, becoming too specialized to recognize them. The overtraining can be spotted by checking whether the MVA results on testing and training samples are statistically compatible or not: if they are not, than ovetraining has occurred.
There exist many MVA methods, and two of them will be explored below: Multi-Layer Perceptron and the Boosted Decision Tree, both studied during the analysis. More details can be found in Reference [95].

Multi-Layer Perceptron (MLP) Artificial Neural Networks (ANNs) are inspired by biological neural networks and consist of simulated collection of interconnected artificial neurons producing certain output response to a given set of input signals. The basic operation of a neuron is the following: given a set of input variables $x_i = x_1, x_2, ..., x_n$ and a set of weights $w_i = w_1, w_2, ..., w_n$, the neuron performs a weighted sum of the inputs, in our case

$$x = c + \Sigma_i w_i x_i \tag{3.12}$$

where c is an offset. The weighted mean x is then tested against a smoothed step-like function like the sigmoid $\sigma(x)$ or the hyperbolic tangent $tanh(x)$:

$$\begin{aligned} \sigma(x) &= \frac{1}{1+e^{-x}} \\ tanh(x) &= \frac{e^{x}-e^{-x}}{e^{x}+e^{-x}} \end{aligned} \tag{3.13}$$

The behaviour of an ANN is determined by the layout of the neurons, the weights of the inter-neuron connections and the response of the neurons to the input. In principle,

an ANN can have n neurons with n^2 connections, however the complexity is reduced by organizing the neurons in layers and allowing connections directly from a layer to the following one. This particular ANN is called Multi-Layer Perceptron. The first layer is called input layer, the last layer is the output layer and all the other layers in between are called hidden layers. Considering a classification problem with $x_i = x_1, ..., x_{n_{var}}$ input variables, they are handled by n_{var} neurons, while there is one neuron in the output layer that holds the output variable, the estimator y_{ANN}. Figure 3.25 shows the structure of a Multi-Layer Perceptron with one hidden layer. The main parameters used to define the architecture of the MLP are: the number and the structure of hidden layers, the activation function and the number of training cycles the MLP runs over to optimize the search of the weights. For our MLP, we choose to use:

- one hidden layer, which is sufficient to approximate a given continuous correlation function to any precision, provided that a sufficiently large number of neurons is used in the hidden layer, according to the Weierstrass theorem [95];
- $n_{var} + 1$ neurons;
- *tanh* as activation function;
- 500 training cycles.

We tried different, more complex, architectures, for example by increasing the neurons of the hidden layer, but we got very similar final results. Actually, for large numbers of hidden neurons, it turned out that MVA did not use some of them.

Boosted Decision Trees (BDT) The working principle of a decision tree is that starting from a root node, a sequence of splits in different nodes is applied to data, using a single discriminant input variables x_i. At each node, the variables that gives the best separation between background and signal are used. The same variables can be used in different nodes, and some variables might not be used at all. In general, the procedure goes on until each terminal node is labelled as background or signal depending on the majority of events that end up in the respective nodes. Subsequently every processed events undergoes the selection criteria, following a different path down the tree from the root to the leaves depending on the values of its variables, until it arrives to the last node, and there it is classified as background or signal. Figure 3.26 shows the schematic view of a decision tree. The boosting extend the concept from a single decision tree to several decision trees, a forest, and classifying an event on a majority vote of the classifications done by each tree in the forest. In spite of the straightforward interpretation of the single tree, boosting increases the statistical stability of the classifier and is able to drastically improve the separation performance compared to a single decision tree. For more details on BDT see [95]. The main parameters of the BDT are number of trees the forest is composed of and the max allowed depth of the single decision tree.

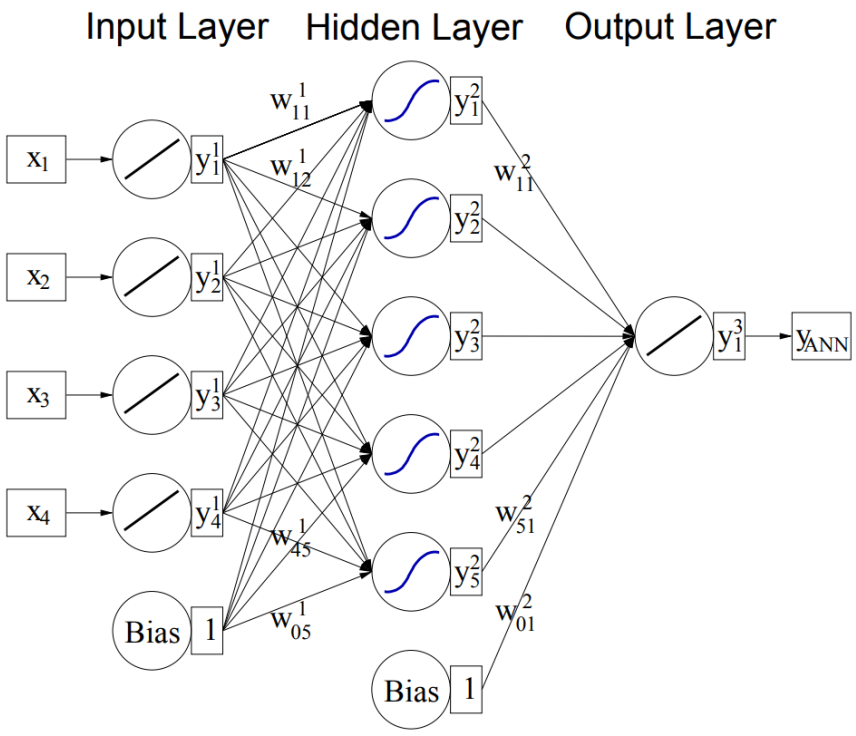

Figure 3.25 Multi-Layer Perceptron with one hidden layer [95].

In our case we use the following settings:

- 200 trees in the forest;
- max depth for the single decision tree of 3;
- boost algorithm is the adaptive boost

The adaptive boost starts with a single decision tree.When the training of the first tree has completed, all misclassified events are re-weighted with a weight, α, derived from the misclassification rate, *err*, of the previous tree

$$\begin{aligned} \alpha &= \frac{1-err}{err} \\ err &= \frac{n_{mis}}{n_{total}} \end{aligned} \tag{3.14}$$

Then a new tree is trained, using the entire sample, and the procedure is repeated re-weighting the misclassified events for an arbitrary number of trees. The final output is a number which is the weighted sum of the binary output of the single trees, -1 for background and +1 for signal, where the weight of each tree is the logarithm of the α value associated to it.

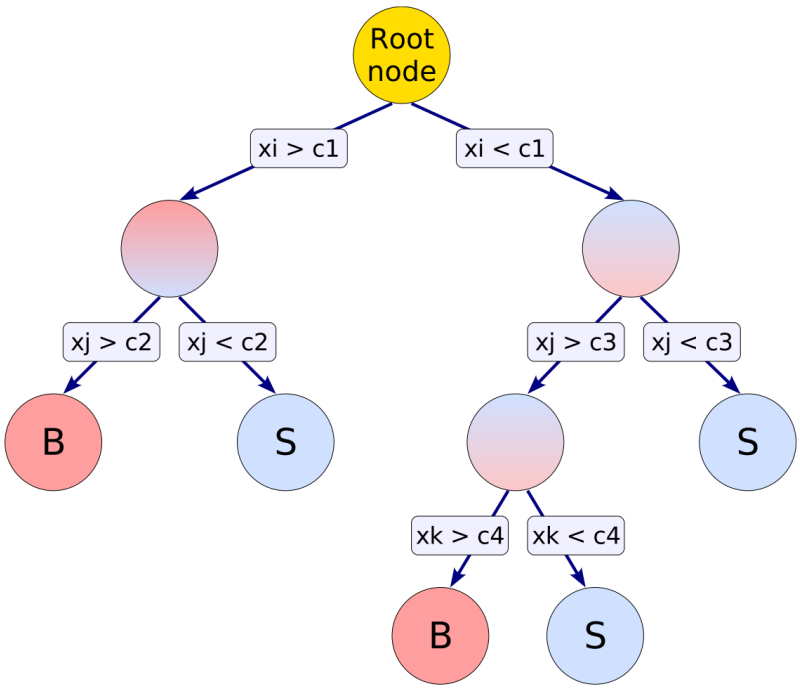

Figure 3.26 Schematic view of a decision tree [95].

3.2.1 MVA strategy

For this analysis, we use the TMVA package (v4.3.0) [95] implemented in ROOT [87] (version v6-20-04). The list of variables used in the training of the MVA strategies are (see Section 3.1.2):

- Sensible to the presence of a resonance in the recoil system:
  R/P, θ, A, $|\frac{p(\mu_0)_{R=45^o}}{\sqrt{2}/2 \cdot P}|$, $d_{1,2}$, $\theta_{1,2}$;

- Sensible to the presence of a $\tau - \tau$ resonance in the recoil system:
  $\Sigma_{i=0}^{n_{\pi^0}} E(\pi^0)_{IN}^{CMS}$, $\Sigma_{i=0}^{n_{\pi^0}} E(\pi^0)_{OUT}^{CMS}$, T, fox-R1, $\alpha(p(\mu)_{max}, \overrightarrow{n}_T)$, $\alpha(p(\mu)_{min}, \overrightarrow{n}_T)$, ΔROE_E, ΔROE_M.

As a guideline, the ranking of all the variables studied in the previous section in order of decreasing discriminant power, is shown in Table 3.3 for a specific training of MLP. The ranking of discriminant variables can change depending on the specific recoil mass range used to train the MVA and on the MVA method used for the training. To minimize as much as possible the dependence upon $M_{Z'}$ we use, in the case of signal, a flat distribution in recoil mass for the training: this prevents the MVA from learning the position of the signal peak and using the information to reject the background. We produced 20 thousands events from 3.6 to 5.0 GeV/c^2 at steps of 50 MeV/c^2, from 5.0 to 8.0 GeV/c^2 at steps of 20 MeV/c^2, from 8.0 to 9.0 GeV/c^2 at steps of 10 MeV/c^2, and finally from 9.0 to 10.36 GeV/c^2 at steps of 5 MeV/c^2. The recoil mass distribution of the merged samples is shown in Figure 3.27 (left). We apply a procedure that reject events to create

Ranking	Variables
1.	R/P
2.	$d_{1,2}$
3.	ΔROE_E
4.	fox-R1
5.	$\Sigma_{i=0}^{n_{\pi^0}} E(\pi^0)_{OUT}^{CMS}$
6.	$\Sigma_{i=0}^{n_{\pi^0}} E(\pi^0)_{IN}^{CMS}$
7.	T
8.	ΔROE_M
9.	A
10.	$\alpha(p(\mu)_{max}, \overrightarrow{n}_T)$
11.	$\alpha(p(\mu)_{min}, \overrightarrow{n}_T)$
12.	$\theta_{1,2}$
13.	$\lvert\frac{p(\mu_0)_{R=45^o}}{\sqrt{2}/2 \cdot P}\rvert$
14.	θ

Table 3.3 Ranking of discriminant variables described in Section 3.1.2 for a specific MLP training of example.

a flat distribution in recoil mass, as shown in Figure 3.27 (right). For what concerns the background, we reconstructed the MC official campaign samples reported in Table 3.4. For the different background components considered, reported in the first column of the table, we reconstructed a sample correspondent to the integrated luminosity reported in the second column. For the training of the MVA, we use $\tau\tau$ and $\bar{q}q$ events, for which we study the discriminant variables (as explained in previous Section 3.1.2). However, also the inclusion of the $ee\mu\mu$ background process in the learning sample proved to be necessary: without that, a large fraction of events surviving the MLP selection was due to this source. The samples used for the training are reported in the third column of the table, while all the further studies, described in the following chapter, have been performed on independent MC samples corresponding to the integrated luminosity reported in the fourth column. Events have been weighted according to the different luminosities of the generated samples and to the trigger efficiency (see Section 5.2). In order to find the optimal cut to be applied on the MLP neuron output, we use the Punzi Figure-of-Merit (Punzi-FOM) [96], which is defined as

$$\frac{\varepsilon_S(t)}{\frac{a}{2} + \sqrt{B(t)}} \tag{3.15}$$

where t is the selection, $\varepsilon_S(t)$ is the signal efficiency of the selection, a is the number of sigmas corresponding to a Gaussian test with significance α and $B(t)$ is the number of background events for a selection t. For this analysis, a confidence level (CL) of 90% ($\alpha = 0.1$) was chosen, which corresponds to $a = 1.28$.

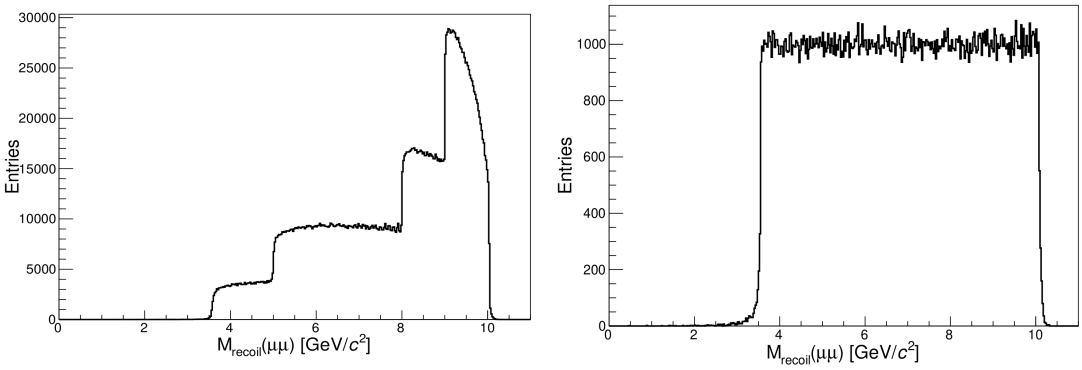

Figure 3.27 Left: Recoil mass distribution of the merged signal samples produced. Right: flattened recoil mass distribution for signal.

Process	Total	MVA training/test	MVA application
$q\bar{q}$	1.5 ab^{-1}	1 ab^{-1}	0.5 ab^{-1}
$\tau\tau$	1.5 ab^{-1}	1 ab^{-1}	0.5 ab^{-1}
$\mu\mu$	0.5 ab^{-1}	-	0.5 ab^{-1}
$ee\mu\mu$	1.0 ab^{-1}	0.5 ab^{-1}	0.5 ab^{-1}
$ee\pi\pi$	0.5 ab^{-1}	-	0.5 ab^{-1}
$ee\tau\tau$	5 ab^{-1}	-	0.5 ab^{-1}
$\mu\mu\tau\tau$	5 ab^{-1}	-	0.5 ab^{-1}
$\mu\mu\mu\mu$	5 ab^{-1}	-	0.5 ab^{-1}

Table 3.4 MC samples used to train and test the MVA.

3.2.2 Refinement of the MVA strategy

We studied in great detail several different strategies of practical implementations of the MVA technique, with the aim of getting the best possible results in terms of sensitivity. Ideally, we get the best performances when the training intervals are centered around single recoil mass points, with an infinite number of ranges. Obviously this is not realistic, and some compromises must be reached.
After much experimentation, two solutions proved to give the best results, i.e. the highest values of the Punzi-FOM as shown below: usage of overlapping training intervals (mass ranges where the MLP is trained) and decoupling of training intervals from application interval (mass ranges where that same MLP is applied in the analysis flow). We finally focus on three options:

- one single range trained from 3.6 GeV/c^2 to 10 GeV/c^2;
- ranges 3 GeV/c^2 wide, with 1.5 GeV/c^2 overlap;
- ranges 1 GeV/c^2 wide, with 0.5 GeV/c^2 overlap;

The training of the MLPs used 1/ab (2/3 training, 1/3 test) of simulated data for the main sources of background (see previous section), while the optimization was run on additional independent samples of 420 fb^{-1}. The value of the Punzi-FOM has been evaluated counting the number of signal and background events in a range of [-5,5]σ_{peak} (recoil mass resolution) around the nominal mass values. Actually, background events were counted in a [-20,20]σ_{peak} range and then normalized to [-5,5]σ_{peak}. Moreover, they were scaled to 80 fb^{-1}. The plot on the left in Figure 3.28 shows the Punzi-FOM value corresponding to the optimal cut found as function of the Z' mass for the different cases taken into account: the single range, the first four 1 GeV-wide ranges and the four 3 Gev-wide ranges. We obtain, as expected, the best performances with narrower training ranges. In particular, 1 GeV-wide ranges seem to guarantee the overall best results. As said, the plot shows only the first four 1 GeV-wide ranges (to make it more readable) applied to a wider range with respect to the 1 GeV-wide range used for the training, however we train 12 MLPs in 1 GeV-wide ranges in total to cover all the recoil mass range $[3.6, 10]$ GeV/c^2. The plot on the right shows the Punzi-FOM value corresponding to the optimal cut found as function of the Z' mass for all MLP 1 Gev-wide ranges. In the following, we show some plots of

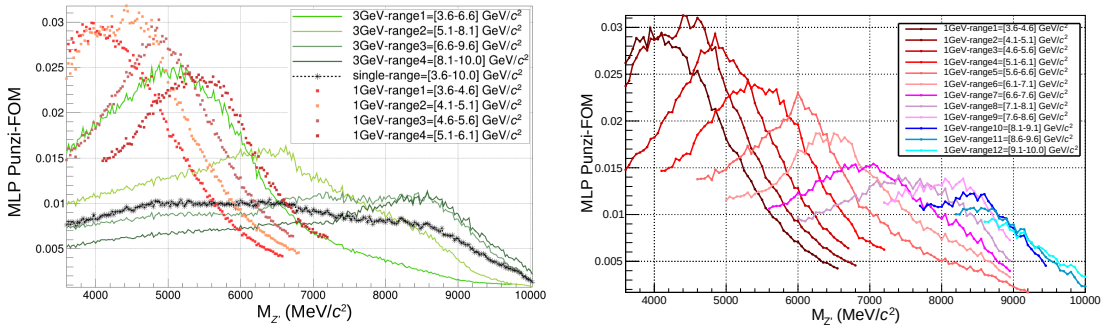

Figure 3.28 Left: Punzi-FOM values obtained for different training ranges. Only the first four 1 GeV-wide training ranges are shown in the plot as example. Right: Punzi-FOM values obtained for all MLP 1 GeV-wide ranges.

example produced in the training of the MVA. Additional plots are shown in Appendix B. Figure 3.29 shows the linear correlation matrix of the discriminant variables for the first 1 GeV-wide training. We observe that correlations between most of variables are different for signal and background. However, as the recoil mass increases, the correlations become more and more similar reducing the performance of MVA.
Figure 3.30 shows the receiver operating characteristic (ROC) curves for the 1 GeV-wide ranges, where also the two different MVA methods (MLP and BDT) are compared: MLP method turns out to be a bit better than BDT, providing a better background rejection and higher values of the Punzi-FOM. Finally, Figure 3.31 shows the MLP neuron output for the MLP 1 GeV-wide ranges. Looking at the values obtained from the Kolmogorov-Smirnov test, we conclude that the training and testing samples are statistically compatible, so no sensible over-training seems to be in force.

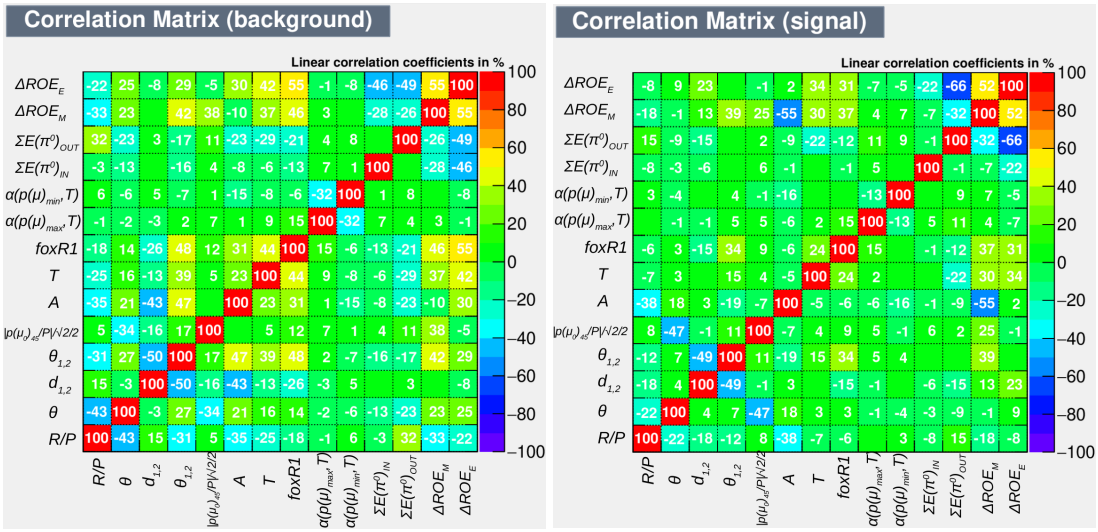

Figure 3.29 Linear correlation coefficients for signal (right) and background (left) of the discriminant variables used in the MLP training for the first training range.

To further improve the performances of the system, we study, again through a Punzi-FOM, the optimal cut to be applied on a MLP output neuron at the level of the single mass distributions. Optimal values are shown (grey points) in Figure 3.32 for the first four 1 GeV-wide MLPs. We then model the optimal MLP cut as a function of the mass using a Savitzky–Golay [97] filter to smooth the points, and we linearly interpolate them. We have then analytical expressions which allow to set a cut on a given MLP output of a given MLP for any value of the recoil mass. Figure 3.32 shows the modeling of the optimal cut using a Savitzky–Golay filter (29,2) with a smoothing of 14.5. From now on in this thesis, we always perform the MLP selections by using this cut. We use the same method to model the signal efficiencyto obtain a value of the signal efficiency for a generic Z' mass. It will be used in the sensitivity computation. Figure 3.33 shows the modeling of the signal efficiency using a Savitzky–Golay filter (19,2) with a smoothing of 9.5.

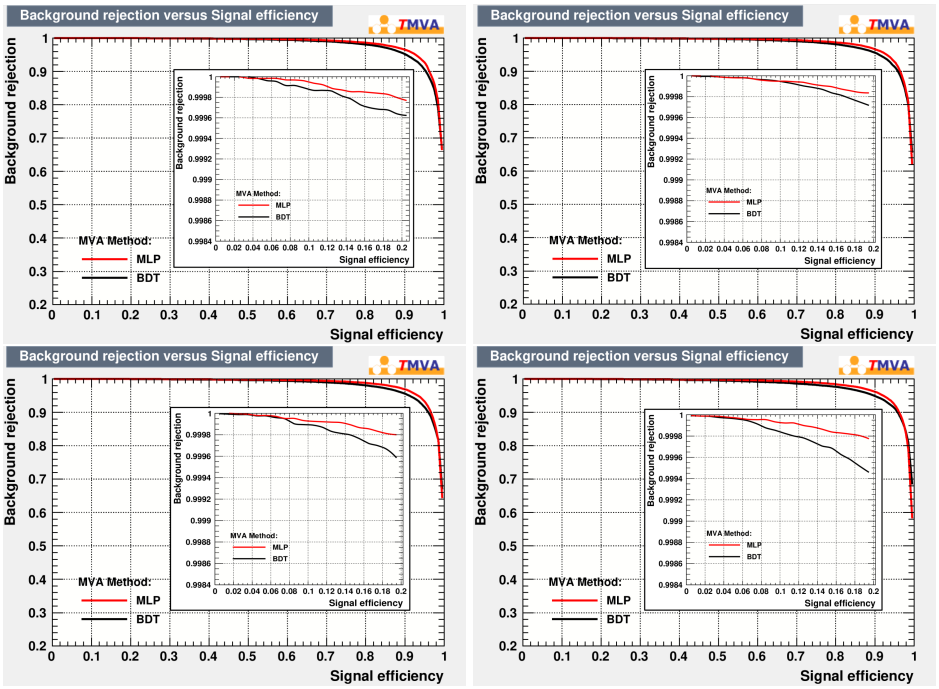

Figure 3.30 ROC curves for the first four 1 GeV-ranges which are the one with better performance, according with the PunziF FOM values shown in Figure 3.28. MLP is a bit better than BDT. From top-right to bottom-left: MLP training range1, 2, 3 and 4.

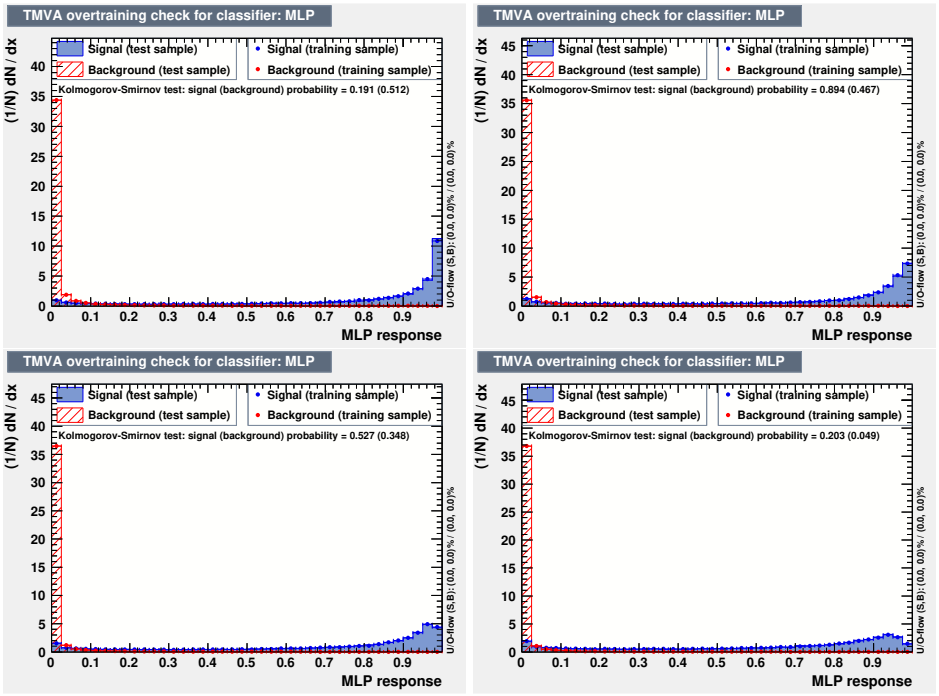

Figure 3.31 MLP output neuron for the first four 1 GeV-ranges. Top-left: MLP training range1. From top-right to bottom-left: MLP training range1, 2, 3 and 4.

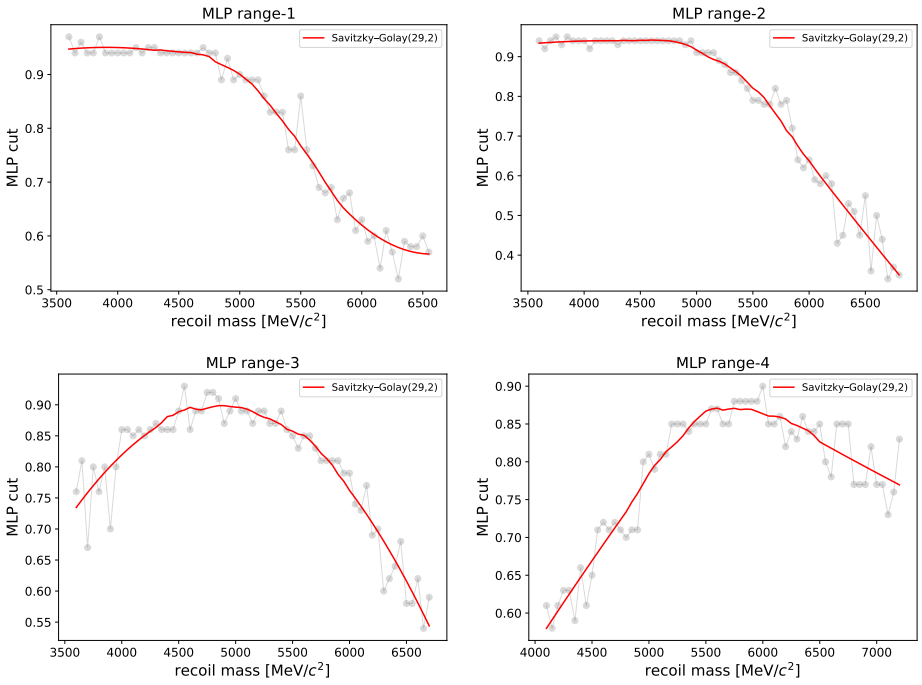

Figure 3.32 Modeling (red line) of the optimal MLP cut (grey points) with a Savitzky-Golay(29,2) filter, for the first four MLPs trained in 1 GeV-ranges.

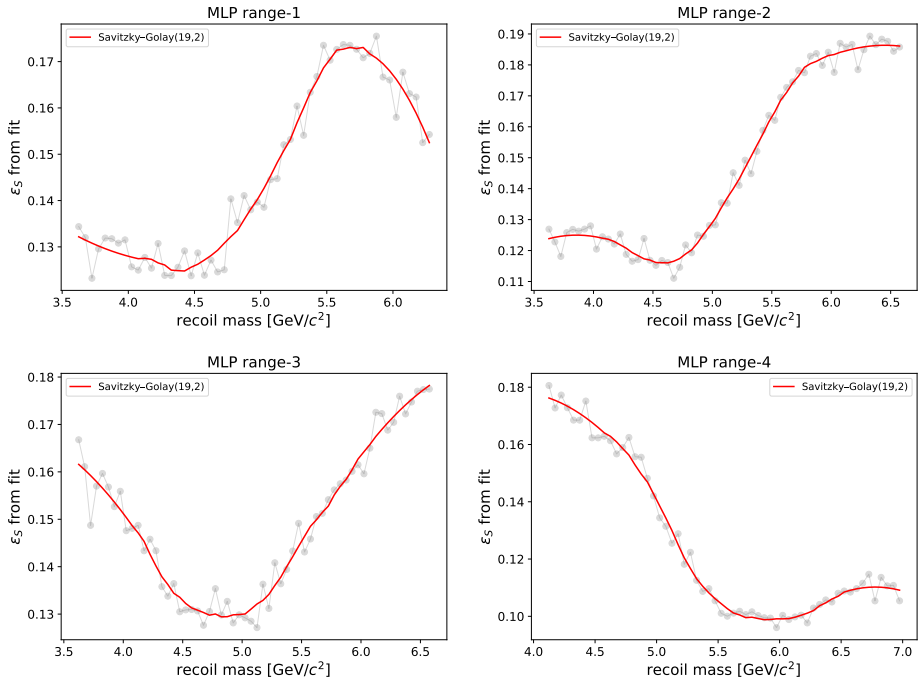

Figure 3.33 Modeling (red line) of the signal efficiency (grey points) with a Savgol(19,2) filter, for the first four MLPs trained in 1 GeV-ranges.

Figure 3.34 shows the signal efficiency as a function of the Z' mass before the MLP selection (left), i.e. with only the selection on PID and the invariant mass of the four tracks, and after the MLP selection, for the MLP 1 GeV-ranges (right). In the latter case, the signal efficiencies are shown for the MLP 1 GeV-ranged that are applied to a wider recoil mass range. For what concerns the application of the different MLPs, we build a set of contiguous, not overlapping recoil mass intervals (called application ranges) looking at the sensitivity plot, shown in Figure 6.3, as discussed in Chapter 6.
To check the effect of the MLP on background, Figure 3.35 shows the recoil mass distribution for 80 fb^{-1} of background with the different contributions stacked (left) and the background distribution after the application of the MLP 1 GeV-ranges (right). The included backgrounds are $e^+e^- \to q\bar{q}$, $e^+e^- \to \tau^+\tau^-$, $e^+e^- \to ee\mu^+\mu^-$, $e^+e^- \to \mu^+\mu^-$, $e^+e^- \to e^+e^-\pi^+\pi^-$, $e^+e^- \to e^+e^-\tau^+\tau^-$, $e^+e^- \to \mu^+\mu^-\mu^+\mu^-$ and $e^+e^- \to \mu^+\mu^-\tau^+\tau^-$ events. In spite of the $e^+e^- \to \mu^+\mu^-\tau^+\tau^-$ and $e^+e^- \to e^+e^-\tau^+\tau^-$ components seemed to be negligible before the application of the MLP because of the low cross section, as shown in Figure 3.2, a considerable part of them survive the MLP selection.

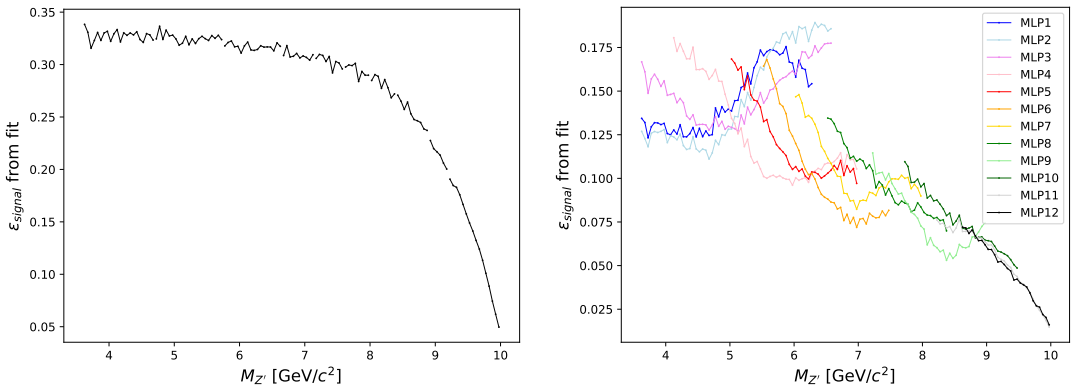

Figure 3.34 Left: Signal efficiencies before MLP selection (only selection on PID and the invariant mass of the four tracks). $\varepsilon_S \sim 33\%$ at low masses and decreases up to 5%. Right: Signal efficiencies for the MLP 1 GeV-ranged applied to a wider range with respect to the 1 GeV-wide training range. $\varepsilon_S \sim 13\%$ at low masses and decreases up to 2.5%.

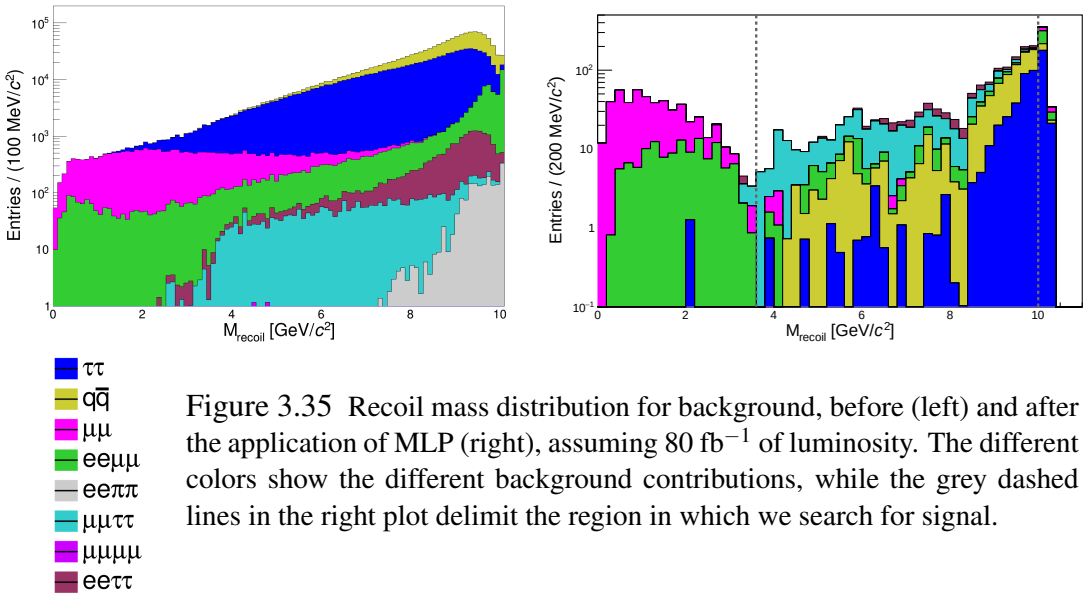

Figure 3.35 Recoil mass distribution for background, before (left) and after the application of MLP (right), assuming 80 fb^{-1} of luminosity. The different colors show the different background contributions, while the grey dashed lines in the right plot delimit the region in which we search for signal.

3.3 Checks of Model Independence

One of the main motivations of this work is to develop an analysis aimed at the $L_\mu - L_\tau$ and use it as a benchmark model. We perform some checks of model independence to verify that there is the possibility a) to reinterpret the results in other (even not existing yet) models, and b) to search for the unexpected presence of a $\tau\tau$ resonance in a $\mu\mu\tau\tau$ final state. The obvious requirement for both cases a) and b) is that the analysis selection, here developed for the search of a $Z' \to \tau^+\tau^-$, keeps a good efficiency in these new scenarios. This can be checked with existing theoretical models. Our conclusion is that, should an unexpected resonance decaying in $\tau\tau$ show up in $\mu\mu\tau\tau$ final states with a sufficient cross-section, we would catch it in most of the cases.

Leptophilic dark scalar A good example is the case of a leptophilic dark scalar [33–36] with a mass larger than twice the τ mass, radiated off a muon: it leads again to a $\mu^+\mu^-\tau^+\tau^-$ final state, with a scalar resonance decaying to a τ pair. Our aim is solely a check of the model independence of our selection, not a reintepretation of the $L_\mu - L_\tau$ results in terms of the coupling of the leptophilic scalar model.
We produced 20k events for a dark scalar of mass 3.6, 4.6, 5.6, 6.6, 7.6 and 8.6 GeV/c^2 using MadGraph5NLO, and we applied the same selections described in this thesis for the Z'. Figures 3.36 and 3.37 show the comparison of the signal efficiency for the Z' boson and the leptophilic dark scalar: they are remarkably similar, with differences typically of a few percent and less than 10% in the worst case.

Axion-like particles Another example is the case of an axion-like particle a (ALP) with non-zero coupling to fermions [37, 38], with a mass larger than twice the τ mass. Generally speaking, this pseudo-scalar particle couples to the photon and to the Z^0 bosons.

The final state $\mu^+\mu^-\tau^+\tau^-$ with $a \to \tau^+\tau^-$ will receive contributions in $e^+e^- \to \mu^+\mu^-$ reactions (mediated by a photon or, to a lesser extent, by a Z^0) from the case in which a is radiated off a muon or from the case in which a is radiated off the boson propagator. The event topology will depend upon the relative weight of the ALP couplings to bosons compared to that to leptons. We study here in detail the case $C_{\gamma\gamma} = 0$ and $C_{Z\gamma} = 0$, restricting therefore to topologies with an ALP particle a radiated off a final state muon leg. We expect that in such a case the correlation between the tagging muon momenta is similar to the one we have for the Z' boson.
We produced 20k events for a ALP of mass 3.6, 4.6, 5.6, 6.6, 7.6 and 8.6 GeV/c^2 using MadGraph5NLO, and we applied the same selections described in this thesis for the Z'. Figures 3.38 and 3.39 show the comparison of the signal efficiency for the Z' boson and the ALP, with the couplings $C_{\gamma\gamma}$ and $C_{Z\gamma}$ negligible w.r.t to the couplings to leptons: they are also very similar. We checked that these results do not generally hold for non-vanishing couplings $C_{\gamma\gamma}$ and $C_{Z\gamma}$ of a to bosons making the reinterpretation more problematic in these cases.

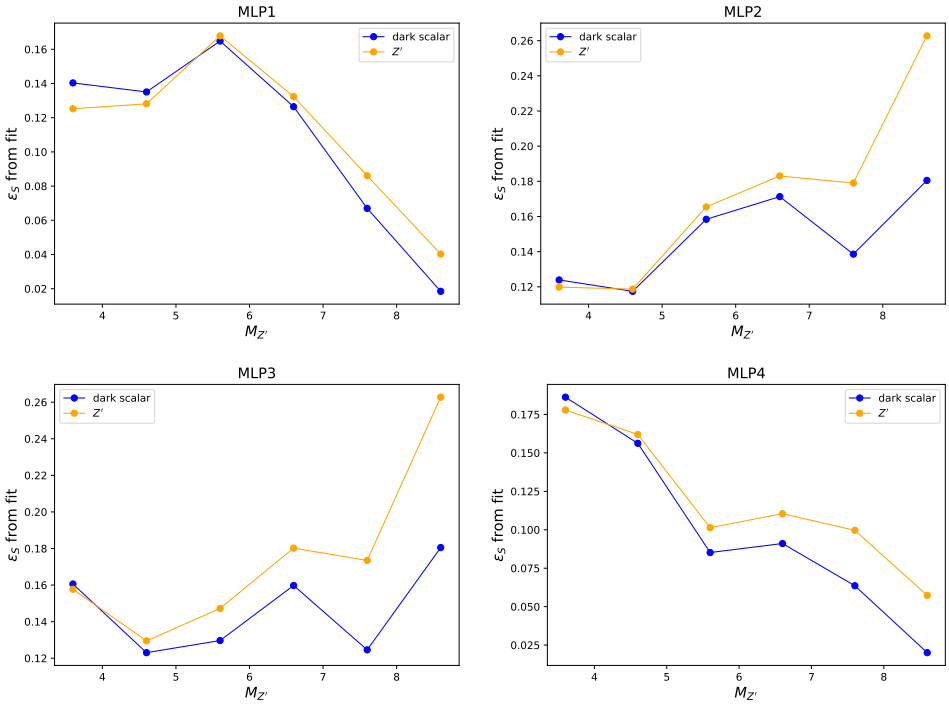

Figure 3.36 Comparison of the signal efficiencies for a Z' boson and a leptophilic dark scalar for MLP1, 2, 3 and 4.

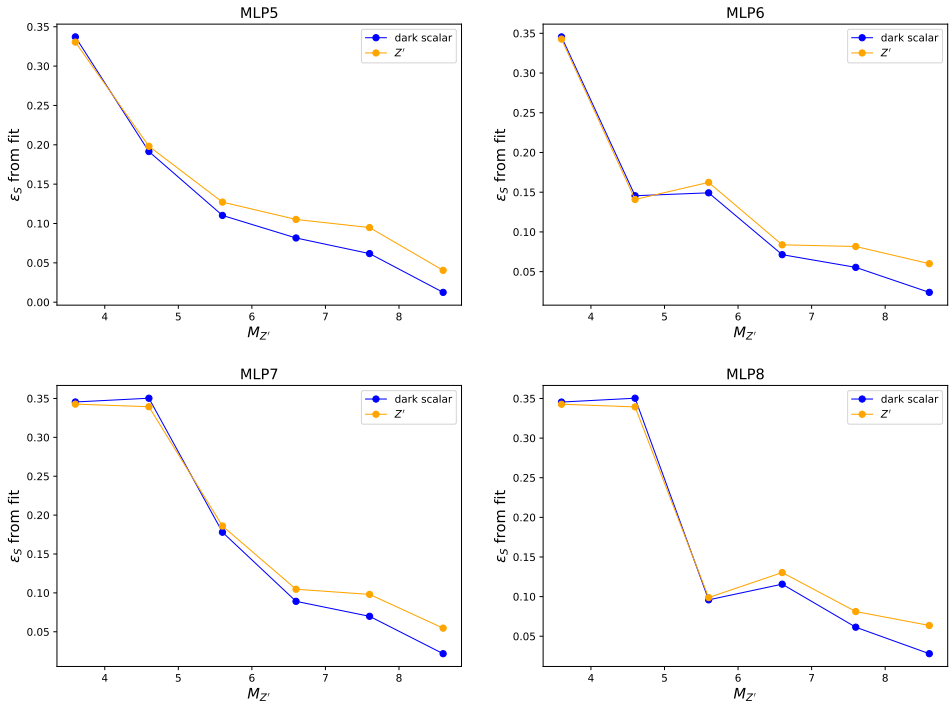

Figure 3.37 Comparison of the signal efficiencies for a Z' boson and a leptophilic dark scalar for MLP5, 6, 7 and 8.

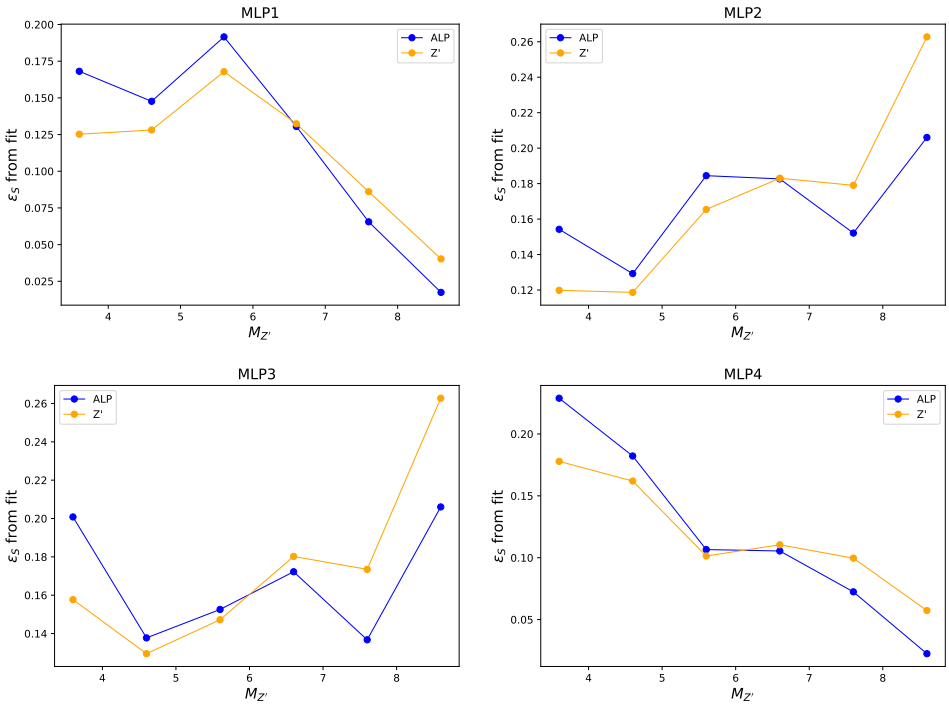

Figure 3.38 Comparison of the signal efficiencies for a Z' boson and an ALP for MLP1, 2, 3 and 4.

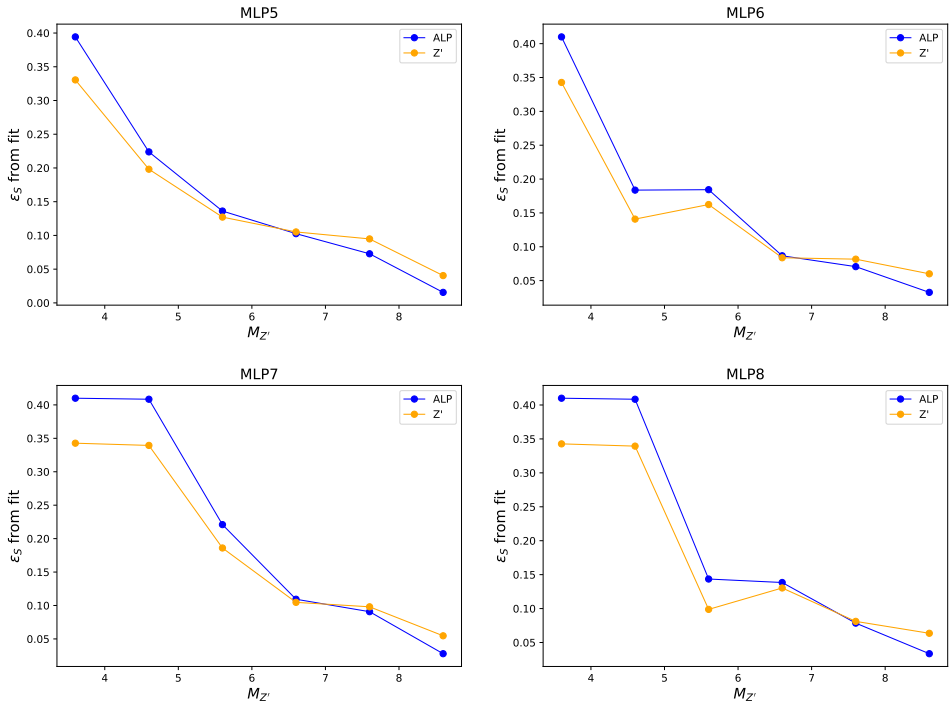

Figure 3.39 Comparison of the signal efficiencies for a Z' boson and an ALP for MLP5, 6, 7 and 8.

4. Signal modeling and signal yield extraction

This Chapter describes the signal modeling methodology and the fit procedure implemented to extract the signal yield.

4.1 Modeling of the signal *p.d.f*

As already introduced in the previous Chapter, let has remember that the squared recoil mass (against the tagging muon pair) can be expressed as

$$M^2_{recoil} = s + M^2_{\mu\mu} - 2\sqrt{s}(E^{CMS}_{\mu^+} + E^{CMS}_{\mu^-}), \tag{4.1}$$

where $\sqrt{s}$ is the energy in the center-of-mass frame, $M^2_{\mu\mu}$ is the squared invariant mass of the muon pair and $E^{CMS}_{\mu^\pm}$ is the energy of the tagging muon in the center-of-mass frame. The recoil mass distribution is expected to show a peak corresponding to the Z' mass in case of signal events. Some examples of signal peaks for different Z' mass values, obtained requiring the MC truth, are shown in Figure 4.1. Requiring the MC truth does not introduce any bias, it just ensures that we are really selecting signal events for the modeling. The fit of the signal peaks was performed using the sum of two Crystal Ball (*CB*) distributions, which were chosen because of the presence of two asymmetric tails in the recoil mass distribution. The right tail of the distribution is mostly due to initial-state-radiation (ISR), while the left tail is mostly due to high-p_T tracks with intrinsically lower momentum resolution. The fit was performed fixing the mean of the distributions at the nominal value of the Z' mass.
The *CB* function is (see Appendix-F of Reference [98])

$$\begin{aligned} CB(x;\mu,\sigma,\alpha,n) &= N \cdot \begin{cases} \exp\left(\frac{(x-\mu)^2}{2\sigma^2}\right), & \text{for } \frac{x-\mu}{\sigma} > -\alpha \\ A \cdot \left(B - \frac{x-\mu}{\sigma}\right)^{-n}, & \text{for } \frac{x-\mu}{\sigma} \leq -\alpha \end{cases} \\ A &= \left(\frac{n}{|\alpha|}\right)^n \cdot \exp\left(-\frac{|\alpha|^2}{2}\right) \\ B &= \frac{n}{|\alpha|} - |\alpha| \end{aligned} \tag{4.2}$$

where N is a normalization factor, μ is the mean value and α, n and σ are parameters which are fitted. The signal pdf is

$$f_{signal}(M_{Z'}) = N_{sig} \cdot (CB_1 + CB_2) \tag{4.3}$$

We decided to model the signal shapes before the application of the MVA selection (MLP), because the statistics we have is higher, and to use the model to extract the signal yield after the MLP selection (after testing that the modeling works well also for signal peaks obtained after the MLP selection, without introducing any bias).
The Z' mass resolution is extracted from the fit as $\sigma_{peak} = \sqrt{f_{CB1} \cdot \sigma^2_{CB1} + (1 - f_{CB1}) \cdot \sigma^2_{CB2}}$,

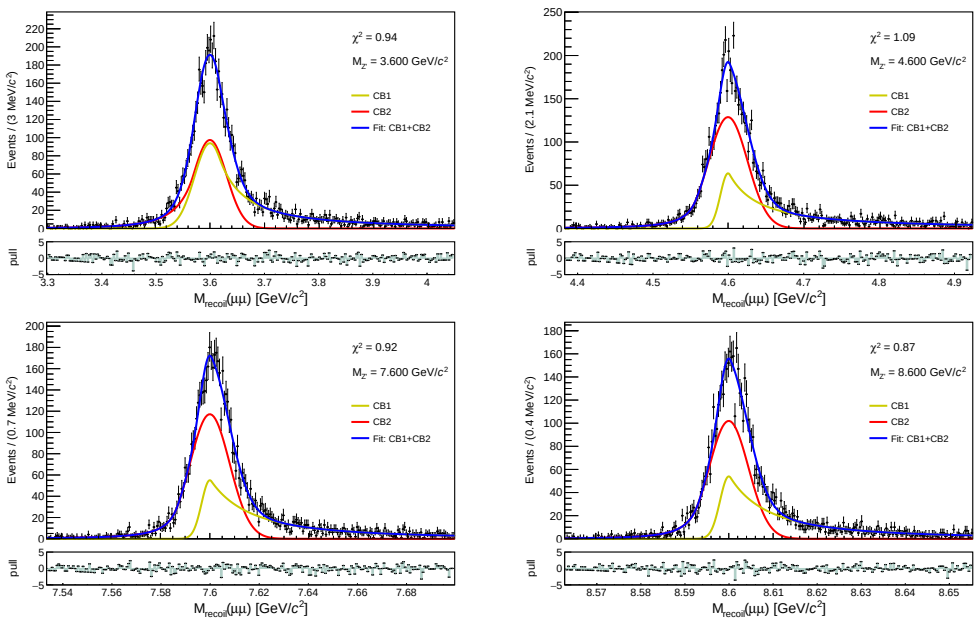

Figure 4.1 The fit to the recoil mass distribution for the MC signal samples respectively for a generated Z' mass of 3.6 GeV/c^2 (up-left), 4.6 GeV/c^2 (up-right), 7.6 GeV/c^2 (down-left) and 8.6 GeV/c^2 (down-right). The MC truth was required to produce the plots. The red and yellow curves are the two Crystal Ball functions used for the fit. The blu line is the fit performed in the range $[-10,15]\sigma_{peak}$.

where σ_{CB1} and σ_{CB2} are the widths of the two Crystal Ball *p.d.f*, and f_{CB1} is the fraction of $CB1$ with respect to the normalized signal distribution. The resolution as a function of the Z' mass is shown in Figure 4.2: it varies from ~ 35 MeV/c^2 at $M_{Z'} = 3.6$ GeV/c^2 down to ~ 2 MeV/c^2 at $M_{Z'} = 10.0$ GeV/c^2.

4.1.1 Modeling the signal model parameters

Seven parameters are needed to express the shape of the signal: the fraction f_{CB1} and 3 more parameters for each of the two CBs. Namely: f_{CB1}, σ_{CB1}, α_{CB1}, n_{CB1}, σ_{CB2}, α_{CB2}, n_{CB2}. Our aim is to express each of these 7 parameters analytically as a function of the Z' mass. In principle we could generate >3000 mass samples and fit them one by one, but it is less practical than modeling the CB fit parameters. The procedure we apply to obtain analytical functions for the parameters (with the exception of f_{CB1}) is the following:

- perform different fits of the signal shapes in different recoil fit ranges [-5,5]σ_{peak}, [-5,10]σ_{peak}, [-10,10]σ_{peak}, and so on up to [-30,30]σ_{peak} around the nominal Z' mass values. The CB parameters depend on the fitting range and, in particular, some CB parameters (α_{CB1} , n_{CB1} , α_{CB2} , n_{CB2}) are fitted better with wide ranges (smaller fluctuations and smaller errors), others with small ranges;

- fit one the CB parameters as a function of the Z' mass for all ranges with polynomials;

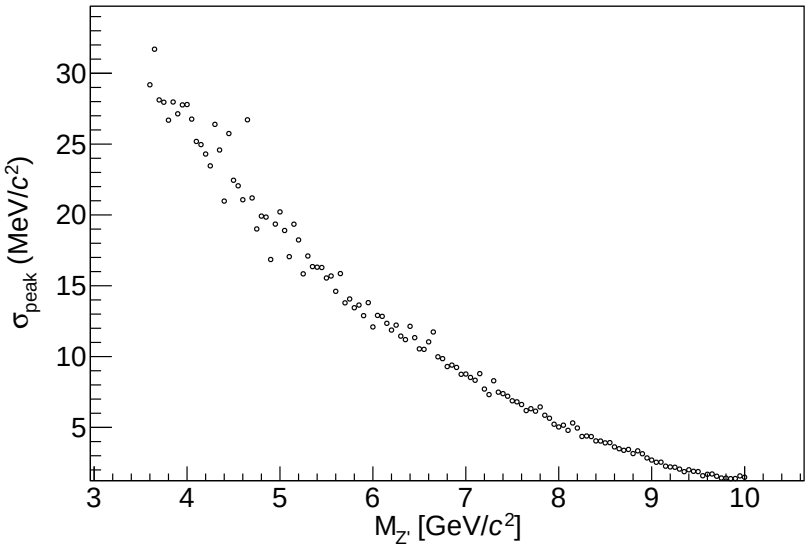

Figure 4.2 Resolution evaluated from the fit of the recoil mass distribution for the different Z' masses. Resolution was calculated as $\sigma_{peak} = \sqrt{f_{CB1} \cdot \sigma^2_{CB1} + (1 - f_{CB1}) \cdot \sigma^2_{CB2}}$, where σ_{CB1} and σ_{CB2} are the widths of the two Crystal Ball *p.d.f* used for the fit, and f_{CB1} is the fraction of $CB1$ with respect to the normalized signal distribution.

- calculate the average polynomial, in order to reduce fluctuations: this is done by computing the mean values of the polynomial coefficients obtained from the fits;
- keep the *CB* parameter polynomial fixed to this analytical function
- repeat the same operation on another *CB* parameter
- proceed until all *CB* parameter analytical functions are fixed.

The modeling of f_{CB1} proceeded in a different way. We observed that fitting f_{CB1} as a function of the Z' mass did not help so much to model the other *CB* parameters. The easiest way we found is to fix it to the same value for all Z' masses. Fixing f_{CB1} in the fit allows to stabilize a little the trend of all the other *CB* parameters. To find an optimal value, we looked at the distribution of f_{CB1} for all the values in the plot shown in Figure 4.3 (left) and performed a Gaussian fit (right). We fixed f_{CB1} at the mean value extracted from the Gaussian fit. For what concerns the order considered to model the *CB* parameters, after fixing one *CB* parameter, the next *CB* parameter that we model is the one for which the polynomial fits converge with a better reduced χ^2. Following this criteria, we model the *CB* parameters in this order: f_{CB1}, σ_{CB2}, σ_{CB1}, α_{CB1}, n_{CB1}, α_{CB2} and n_{CB2}.

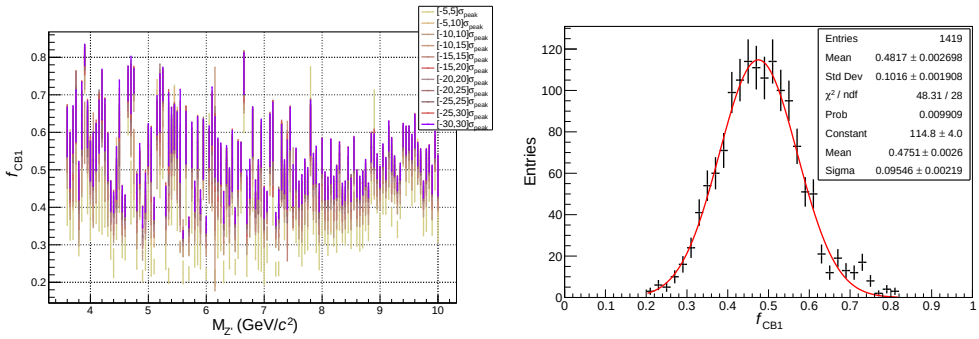

Figure 4.3 Left: f_{CB1} vs Z' mass for different fit ranges (between [-5,5]σ_{peak} to [-30,30]σ_{peak}). It seems there is a trend for signal peak fit performed in the range [-5,5]σ, but it is not good to model the parameters that describe the tails of the signal distribution, which are not well fitted in that range. Right: Distribution of all values shown in Figure 4.3, fitted with a Gauss distribution.

σ_{CB2} modeling We perform polynomial fits to σ_{CB2} vs Z' mass in three different Z' mass ranges: [3.6, 5.6], [5.6, 9.0], [9.0,10.05], GeV/c^2 for the different signal peak fit ranges. Then we average over polynomials. The distribution we fit are shown in Figure 4.4 obtained for f_{CB1} fixed in the signal peak fits.

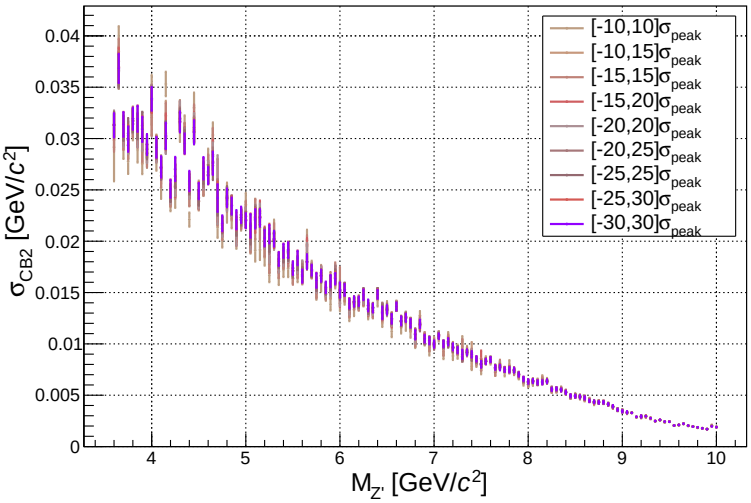

Figure 4.4 σ_{CB2} vs Z' mass for all the fit ranges shown in the legend.

Functions obtained for the first Z' mass range [3.6, 5.6] GeV/c^2 from the fit with a 2nd order polynomial for each signal peak fit range are shown in Figure 4.5. The dashed blue line is the average function, and to calculate it we do not use the fit ranges [-5,5]σ_{peak} and [-5,10]σ_{peak} because the fits were not converging properly. We apply the same procedure for the the second and the third Z' mass ranges: [5.6, 9.0] GeV/c^2, [9.0, 10.05] GeV/c^2. In particular in the third Z' mass range all functions overlap. Second and third Z' mass ranges are shown respectively in Figure 4.6 and 4.7. The final result of the modeling of

σ_{CB2} is shown in Figure 4.8. We use the same procedure for the other 5 parameters. We do not use the results obtained fitting the signal peak in fit ranges [-5,5]σ_{peak}, [-5,10]σ_{peak}, [-10,10]σ_{peak}, where the fit does not converge properly and correspondingly the parameter values are unreliable. Therefore we use the values from [-10,15]σ_{peak}. Few details for the modeling of each parameter are given in the following paragraphs, while the final results for σ_{CB1} and the other parameters are respectively in Figures 4.9 (right) and 4.10.

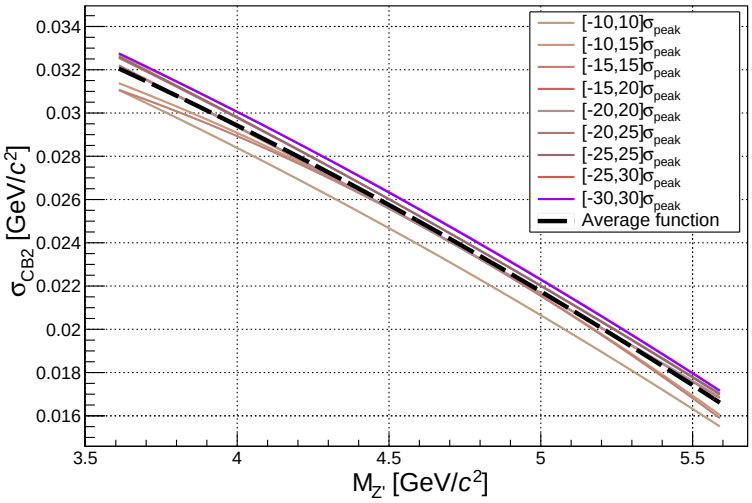

Figure 4.5 Functions obtained fitting σ_{CB2} vs Z' mass for all the fit ranges shown in the legend, in the Z' mass range [3.6, 5.6] GeV/c^2. The dashed line is the average function.

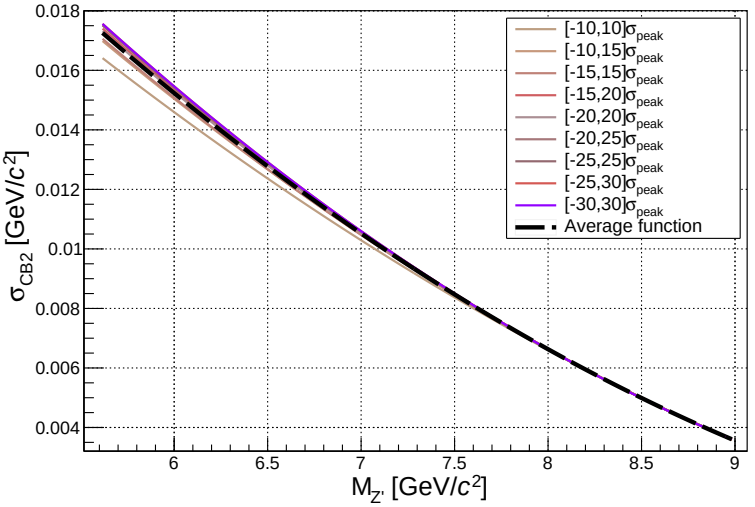

Figure 4.6 Functions obtained fitting σ_{CB2} vs Z' mass for all the fit ranges shown in the legend, in the Z' mass range [5.6, 9.0] GeV/c^2. The dashed line is the average function.

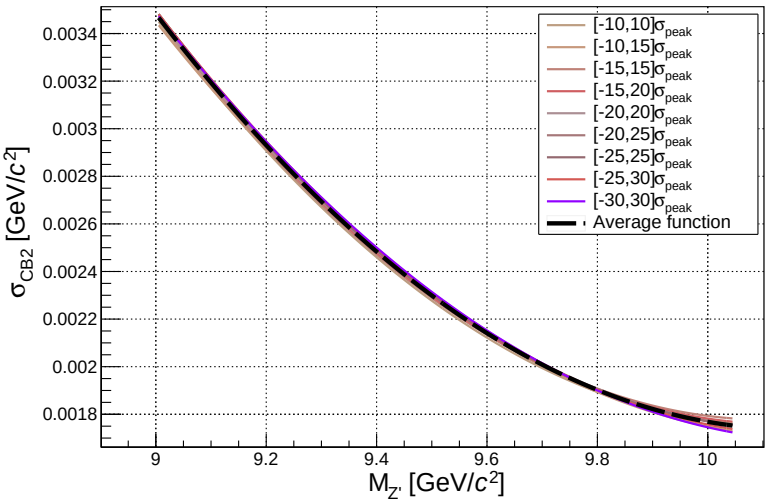

Figure 4.7 Functions obtained fitting σ_{CB2} vs Z' mass for all the fit ranges shown in the legend, in the Z' mass range [9.0, 10.05] GeV/c^2. The dashed line is the average function.

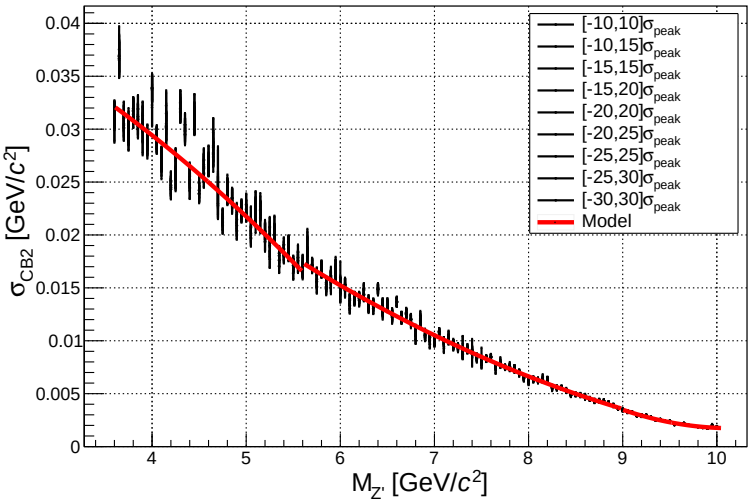

Figure 4.8 Final modeling of σ_{CB2} vs Z' mass. The red line is the piecewise modeling, obtained from the average over functions obtained for the different fit ranges.

σ_{CB1} modeling Following the same procedure applied for σ_{CB2} in the same Z' mass ranges. Points shown in Figure 4.9 (left) are obtained keeping f_{CB1} and σ_{CB2} fixed in the signal peak fits. The final result of the modeling of σ_{CB1} is shown in Figure 4.9 (right).

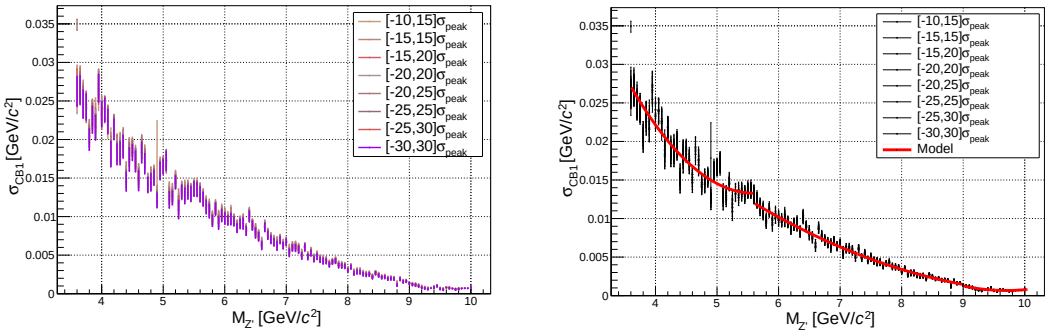

Figure 4.9 Left: σ_{CB1} vs Z' mass for all the fit ranges shown in the legend. Right: Final modeling of σ_{CB1} as a function of Z' mass. The red line is the modeling, obtained from the average over functions obtained for the different fit ranges.

α_{CB1} modeling In this case f_{CB1} , σ_{CB2} and σ_{CB1} have been kept fixed in the signal peak fits. Following the same procedure described above in the same Z' mass ranges.

n_{CB1} modeling In this case f_{CB1} , σ_{CB2}, σ_{CB1} and α_{CB1} have been kept fixed in the signal peak fits. The same procedure described above have been followed in the same Z' mass ranges.

α_{CB2} modeling In this case f_{CB1} , σ_{CB2}, σ_{CB1}, α_{CB1} and n_{CB1} have been kept fixed in the signal peak fits. The same procedure described above has been followed also in this case, but in the following Z' mass ranges: [3.6, 5.6], [5.6,7.0], [7.0,10.05] GeV/c^2.

n_{CB2} modeling Finally, f_{CB1} , σ_{CB2}, σ_{CB1}, α_{CB1}, n_{CB1} and α_{CB2} have been kept fixed in the signal peak fits. Again, the procedure followed is the same in the following Z' mass ranges: [3.6, 5.6], [5.6,9.0], [9.0,10.05] GeV/c^2. In this case, fit ranges [-5,5]σ_{peak}, [-5,10]σ_{peak}, [-10,10]σ_{peak} and [-10,15]σ_{peak} have not been used.

To model the signal *p.d.f* we took some arbitrary decisions. We checked the systematics associated to the modeling of the signal *p.d.f* observing any significant difference with respect to the case in which we perform the fits leaving all the *CB* parameters floating, as discussed in Section 5.4.

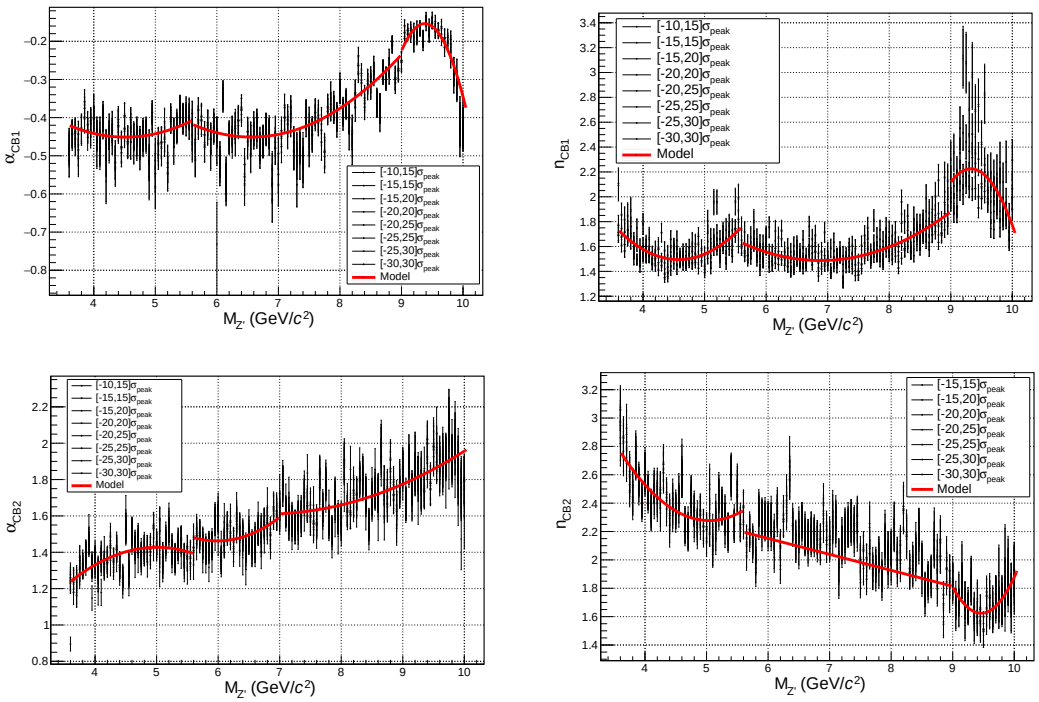

Figure 4.10 Final modeling of α_{CB1}, n_{CB1}, α_{CB2} and n_{CB2} as a function of Z' mass. The red line is the modeling, obtained from the average over functions obtained for the different fit ranges.

4.1.2 Results of the signal modeling before the MVA selection

To test the signal modeling construction, we perform a series of fits to signal shapes using only the parameter N_{sig} floating. We expect that the fit returns the right counting of the number of events in the fit range. Figure 4.11 shows the results of the fit for few masses (the same shown in Figure 4.1, for comparison) taken as examples. Figure 4.12 shows the comparison of the reduced χ^2 (left) and mass resolution as a function of the Z' (right) obtained from the fit with all the *C*B parameters free with the one obtained keeping all *CB* parameters fixed. The reduced χ^2 is a bit larger on average, but still between 0.7 and 1.3 depending on the mass, also for mass points not used for the modeling of the signal peak, while the resolution curve follows very well the points obtained without fixing the parameters in the fit.

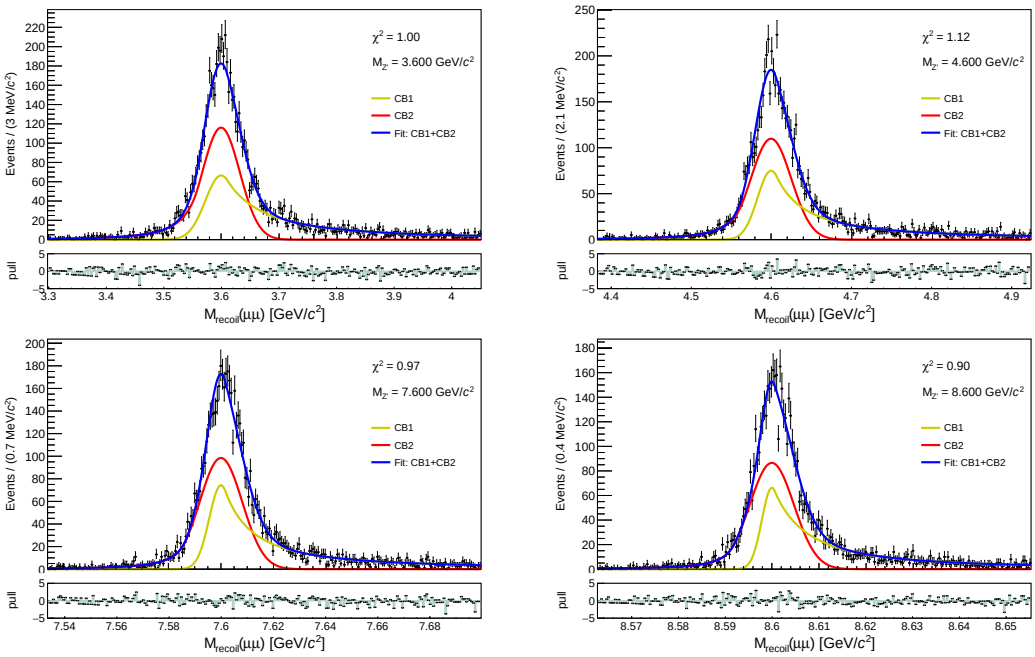

Figure 4.11 The fit to the recoil mass distribution for the MC signal samples respectively for a generated Z' mass of 3.6 GeV/c^2 (up-left), 4.6 GeV/c^2 (up-right), 7.6 GeV/c^2 (down-left) and 8.6 GeV/c^2 (down-right). The MC truth was required to produce the plots. The fit is performed in the range $[-10, 15]\sigma_{peak}$ keeping fixed all the *CB* parameters except N_{sig} in the signal *p.d.f.*

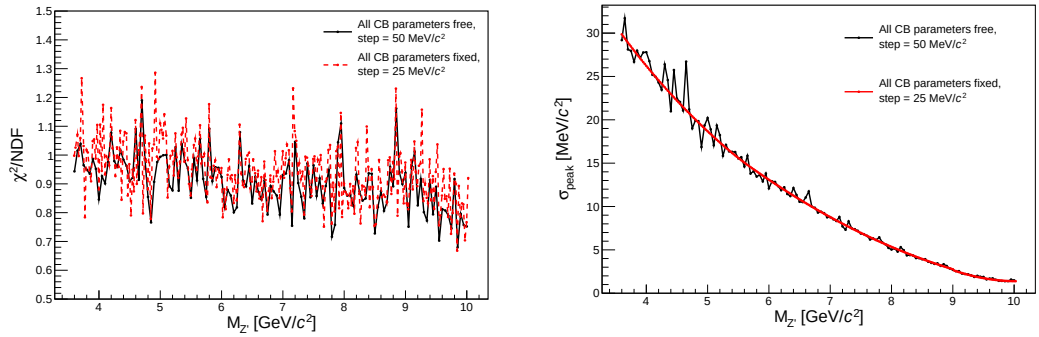

Figure 4.12 Left: Comparison of reduced χ^2 vs Z' mass obtained from the fit with all *CB* parameters free (black) and the reduced χ^2 vs Z' mass obtained from the fit with all *CB* parameters fixed (red). Right: Comparison of σ_{peak} vs Z' mass obtained from the fit with all CB parameters free (black) and σ_{peak} vs Z' mass obtained from the fit with all CB parameters fixed (red).

4.1.3 Results of the signal modeling after the MVA selection

Figure 4.13 shows the results of the fit for few masses of example obtained keeping fixed all parameters.In this case the peaks are obtained after the application of the MVA selection with three separate ranges. In general, the shapes are well fitted. Figure 4.14 shows the number of fitted signal events as a function of the number of generated signal events for $M_{Z'} = 3.6$ GeV/c^2: the fit returns exactly the number of generated events. The result is the same also for the other Z' masses.

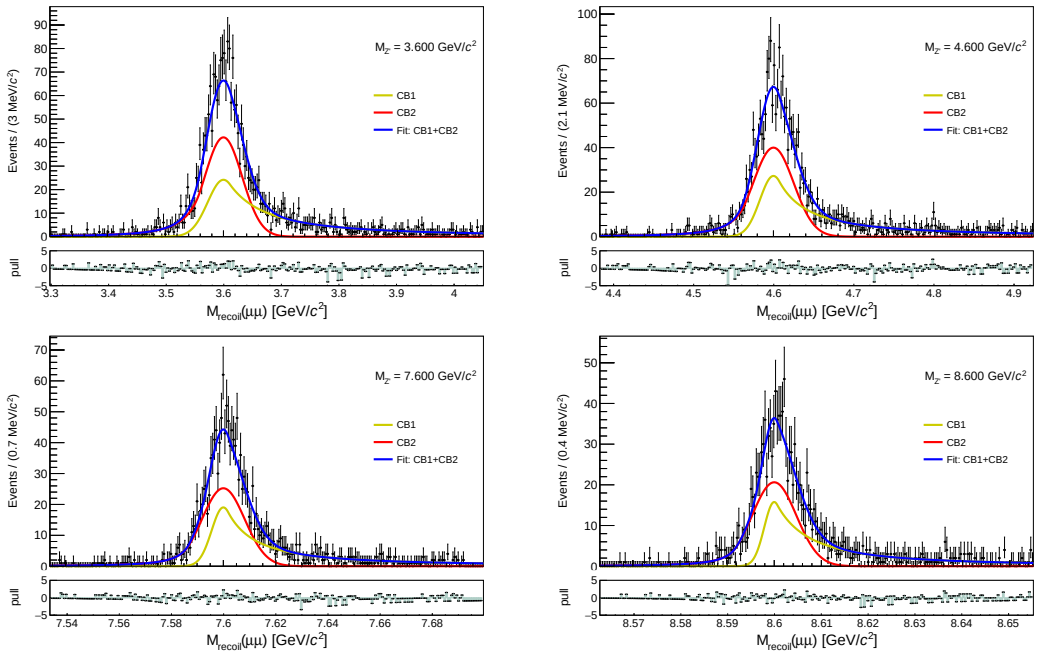

Figure 4.13 The fit to the recoil mass distribution for the MC signal samples respectively for a generated Z' mass of 3.6 GeV/c^2 (up-left), 4.6 GeV/c^2 (up-right), 7.6 GeV/c^2 (down-left) and 8.6 GeV/c^2 (down-right). The MC truth was required to produce the plots. The fit is performed in the range $[-10, 15]\sigma_{peak}$ keeping fixed all the CB parameters except N_{sig} in the signal *p.d.f.* In this case the peaks are obtained after the application of the MVA.

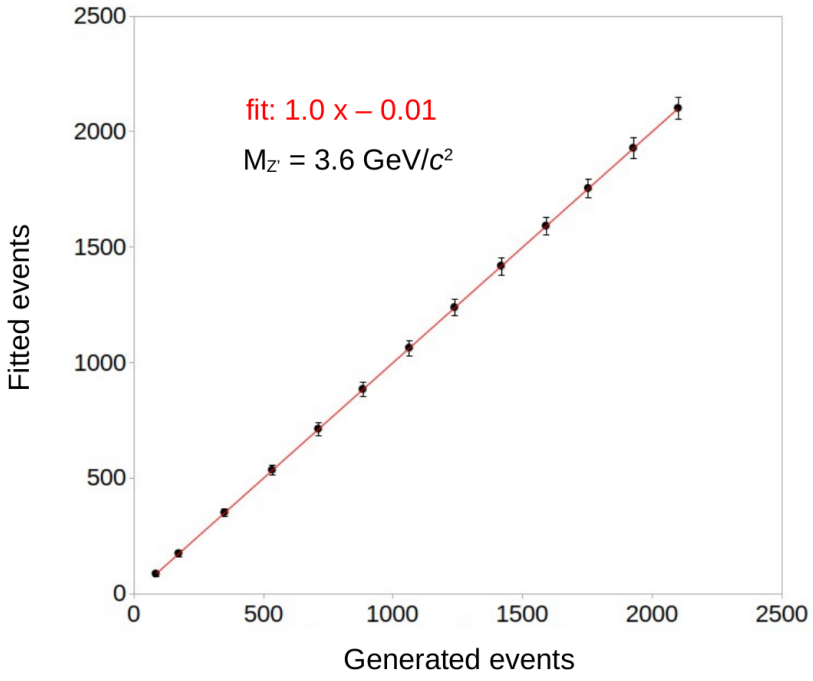

Figure 4.14 Number of fitted signal events as a function of the number of generated signal events for $M_{Z'} = 3.6$ GeV/c^2.

4.2 Fit procedure

For the signal extraction we use a fitting procedure to the recoil mass distributions. This is technically based on the RooFit package [99], version v3.60, included in ROOT [87] v6-20-04. For a given Z' mass, we perform unbinned signal+background fits to the recoil mass distribution centered around the nominal mass value, according to the following steps:

- we first fit with a background only constant *p.d.f* the sideband region, ie the full chosen recoil mass range without the interval in the range [-5,5]σ_{peak} (which accounts typically for 80% of the total signal amount) around the nominal peak position.

- from the fit to the sidebands we estimate the number of background events expected in the signal region, and consequently the total number of background events

- we use the total number of signal events estimated from the sidebands as initial parameter for the full signal+background fit

- we perform the full signal+background fit. We also allow negative values for N_{sig} to avoid bias in combining the results, while N_{bkg} is constrained to be positive. To avoid the *p.d.f* to be negative in regions with few events we put a reasonable inferior limit to N_sig depending on the number of background events in the signal region, N^{SR}_{bkg}, expected from the fit to the sidebands: N_sig can not be lower than $-N^{SR}_{bkg}$.

Since the recoil mass resolutions at peaks are small, as shown in Figure 4.12 (right), the fit ranges, especially for high Z' masses, are narrow too: this implies that the background distributions can be considered constant inside the fit range. We also considered to use a first-order Chebyshev polynomial function obtaining very similar results. Figure 4.15 shows the four signal peaks for a signal+background fit with a *p.d.f*

$$f_{total}(M_{Z'}) = N_{sig} \cdot (CB_1 + CB_2) + N_{bkg} \cdot Chebyshev0 \tag{4.4}$$

obtained fitting the distribution in the fit range $\pm 20\sigma_{peak}$. We use this modeling of background and signal to verify that the fit is not biased. Even if all the described fits are unbinned, we have to choose a binning to show plots and compute χ^2. This binning is chosen depending on the signal peak resolution: we find that a good compromise is obtained setting the bin width at $\sigma_{peak}/2.5$. The reduced χ^2 (in the Baker-Cousins' χ^2 formulation [100]) as a function of the Z' mass is shown in Figure 4.16 for different fit ranges: toyMC samples, corresponding to the chosen signal and background modeling, are here employed. The usage of toyMC samples has also the benefit of removing the correlations between fit ranges, although the number of events for each fit range is taken from the original distribution and so this source of correlation remains and causes the fluctuations in the reduced χ^2.

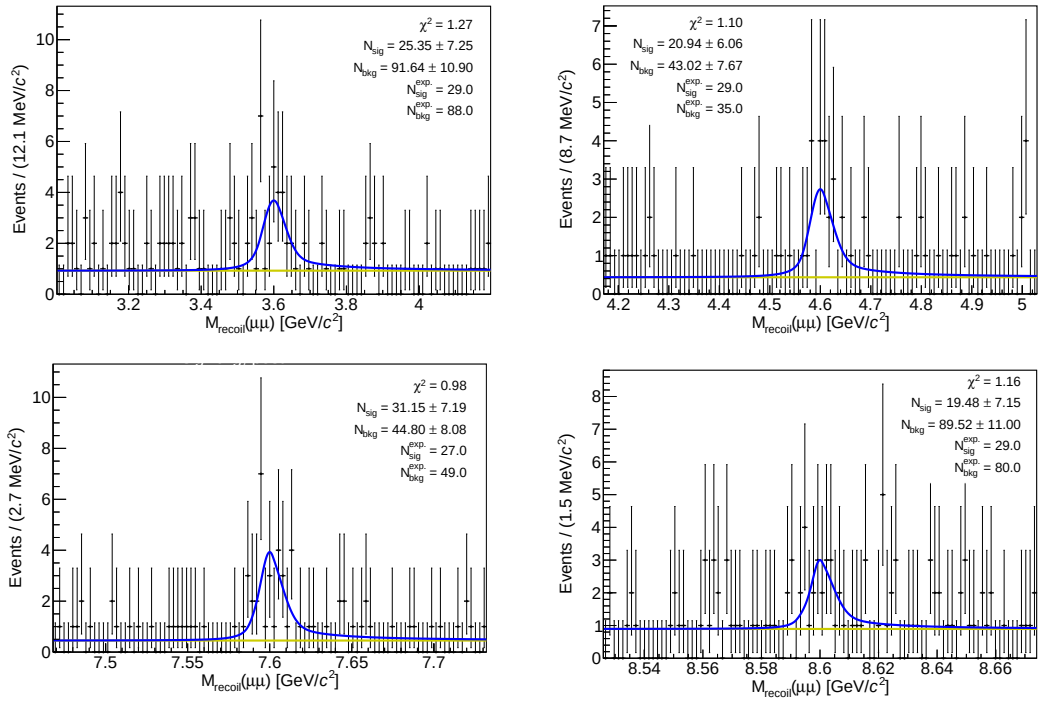

Figure 4.15 The fit signal+background to the recoil mass distribution for the MC signal samples respectively for a generated Z' mass of 3.6 GeV/c^2 (up-left), 4.6 GeV/c^2 (up-right), 7.6 GeV/c^2 (down-left) and 8.6 GeV/c^2 (down-right).

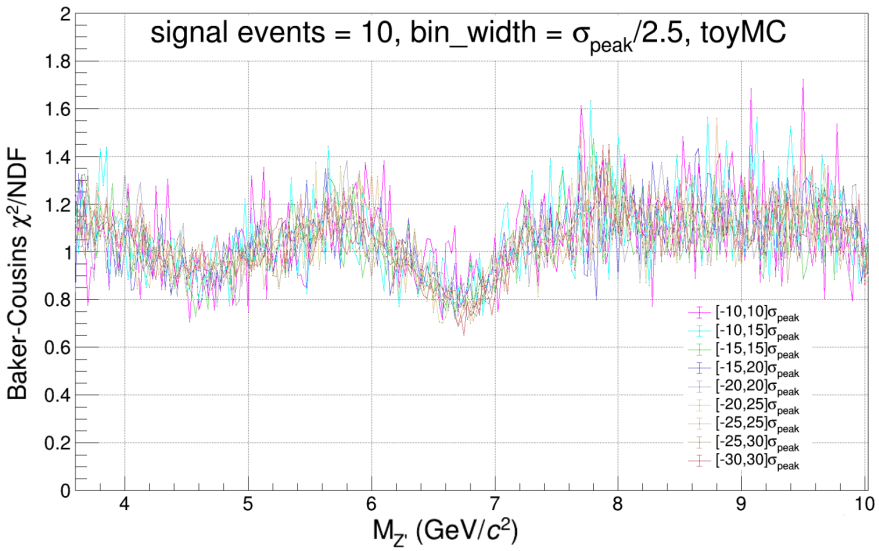

Figure 4.16 Reduced χ^2 vs Z' mass for different fit ranges, for a toy-MC

We run 300 toys, and for each of them:

- we consider a specific number of signal events n_S, corresponding to a specific cross section;
- we inject a number n_{inj} of signal events extracted from a Poissonian of expected value n_S;
- we sample n_{inj} events from the fitted signal *p.d.f*;
- for the background we generate a number of events that corresponds to those we expect from MC after the application of the MVA selection, scaled to 80 fb^{-1}, according to the assumed (constant) *p.d.f.*

Each toy returns a value of the fitted number of events. We then compute the pulls P, i.e:

$$P = \frac{n_{fit} - n_S}{\sigma(n_{fit})} \tag{4.5}$$

The chosen mass values are:

- 3.625, 4.45, 5.6, 6.375, 7.4, 8.2, 8.825, 9.25, 9.8 GeV/c^2

and the number n_S of signal events:

- 0, 10, 30, 50.

We perform a Gaussian fit of the signal and background pull distributions for the different combinations of Z' masses and number n_S of signal events. We show the resulting RMS and mean for the signal in Figure 4.17, and for the background in Figure 4.18. Almost all of the fits agree with a normal distribution within 1-2 sigmas. We observe a slight negative bias that will also be described in the systematics.

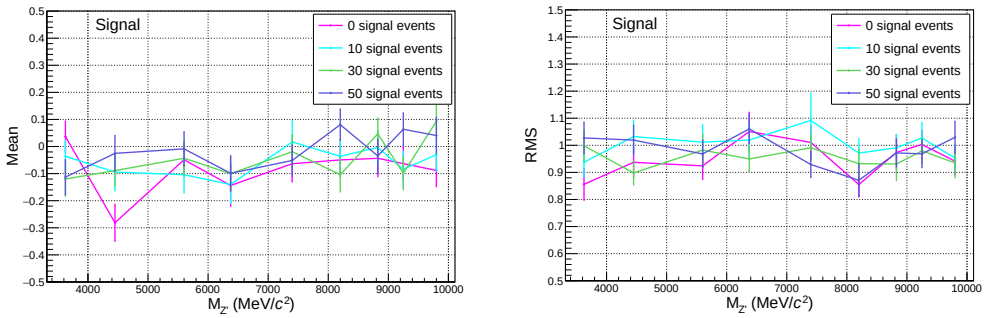

Figure 4.17 Mean (left) and RMS (right) from Gauss fit of pull distribution obtained from signal fit from toy-MC

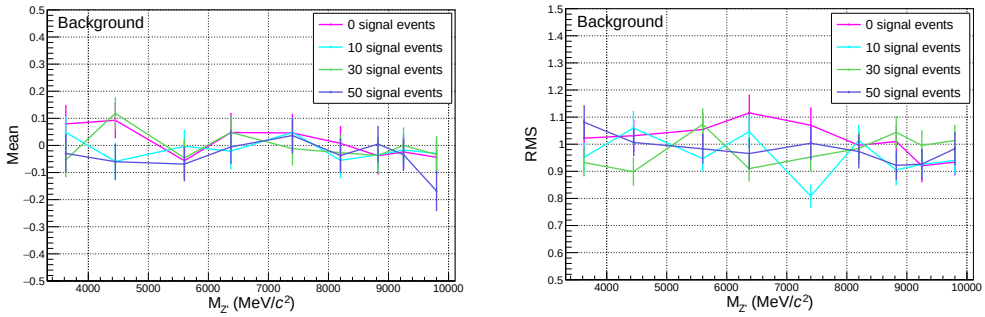

Figure 4.18 Mean (left) and RMS (right) from Gauss fit of pull distribution obtained from background fit from toy-MC

As an example, Figure 4.19 shows the pull distributions for signal and background for the different number of signal events injected for $M_{Z'} = 6.375$ GeV/c^2. The plot for other Z' masses can be found in Appendix C. We perform further studies aimed at the determination of an optimal fit range, using toy-MC samples. We assume that the best range is the one that gives the smallest χ^2 for each Z' mass hypothesis. We inject different numbers of signal events and looked also at the expected sensitivity. It turned out that a good compromise between having wide enough ranges to get good background estimates from the sidebands still keeping the constant *p.d.f*, is to perform the fits is the range [-20,20]σ_{peak}. Figure 4.20 shows the average reduced χ^2 from the signal+background fits for all Z' masses for specific fit ranges and for different numbers of signal events injected.

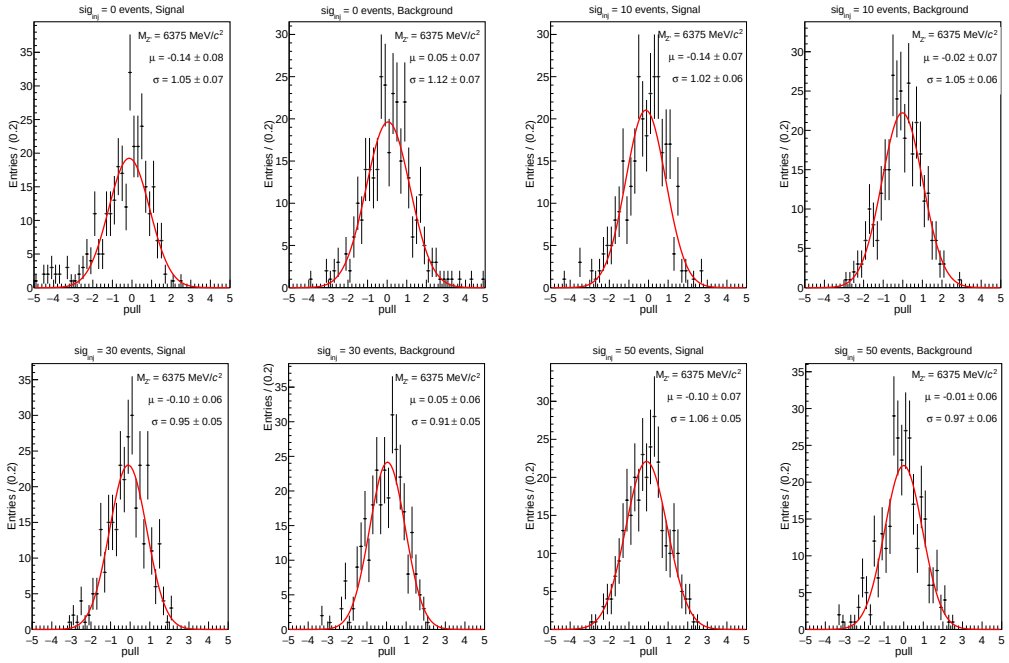

Figure 4.19 Pull distributions for signal and background for the different number of signal events injected, for $Z' = 6.375$ GeV/c^2.

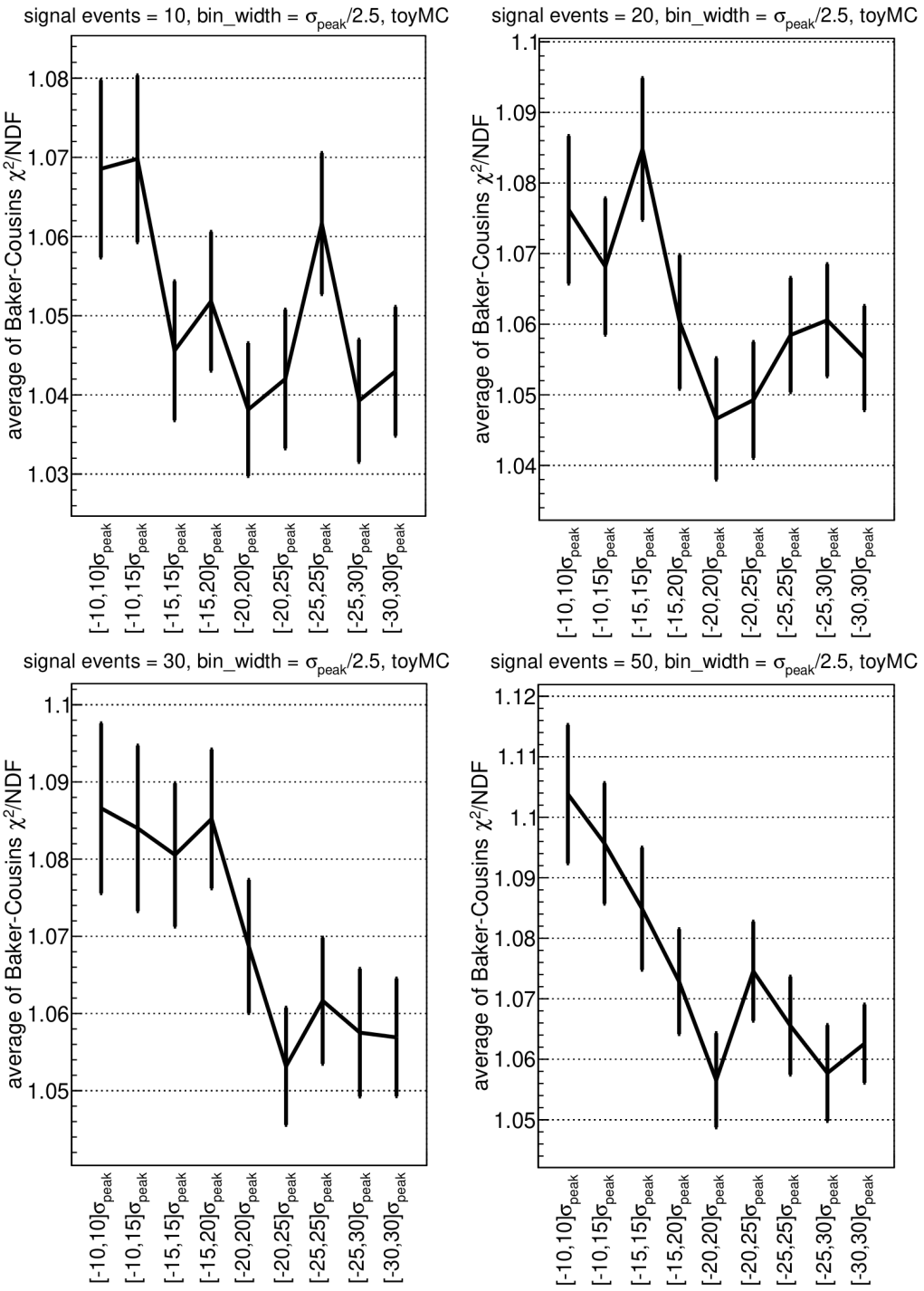

Figure 4.20 Average reduce χ^2 for different fit ranges and different number of signal events injected. The error bar is the RMS of the χ^2/NDF distribution over the fits performed in a given fit range.

5. Control samples, data validation and systematic uncertainties

This Chapter will describe the control samples used in the data validation of the analysis. Moreover, Section 5.2 will show the work done to measure the *fff* trigger efficiency on data. The *fff* trigger requires at least three tracks reconstructed inside the *Belle II* detector. Finally, the preliminary systematic uncertainties on signal, estimated on simulation, will be shown in Section 5.4.

5.1 Control samples

To perform data validation, we compare the distributions of discriminating variables, described in Section 3.1.2, and of interesting variables, like the recoil mass and the invariant mass of the four tracks distributions, obtained for MC and data. We perform most of the data validation with two control samples:

1) Control sample 1 (CS1) is obtained selecting events with two pions rather than with two muons, with $\pi ID > 0.5$. We name it "$\pi^+\pi^-\tau^+\tau^-$" control sample or CS1;

2) Control sample 2 (CS2) is obtained selecting events of the same kind of the signal, but with a recoil mass lower than 3.4 GeV/c^2 (5σ from $2m_\tau$). We name it "$\mu^+\mu^-\tau^+\tau^-$" control sample or CS2.

The CS2 control sample has limitations, since data/MC comparison is here limited to a small region of the recoil mass distribution. Moreover, with this control sample we are outside the signal region and consequently outside the region of application of the MLPs. It will be discussed in more depth in Appendix A, where plots of data/MC comparison for all discriminating variables are shown.
The $\pi^+\pi^-\tau^+\tau^-$-CS1 control sample is useful for many checks, validations and measurements and, specifically:

- it produces a recoil mass distribution for signal events that does not peak at the nominal Z' mass, as shown in Figure 5.1;

- it has a signal efficiency of 0.01% - 0.1% across the full recoil mass range in the mass bin defined as $M_{Z'} \pm 2\sigma_{peak}$. On the other hand, we can consider one large bin defined as [7.5,10.5] GeV/c^2 where most of the signal falls for every Z' mass hypothesis (see Figure 5.1). In this case, the signal efficiency is $\sim$6%, however the number of background events in the large bin is very high resulting in a negligible sensitivity to signal;

- it allows data/MC comparison for a wide region of the recoil mass distribution, keeping the signal hidden.

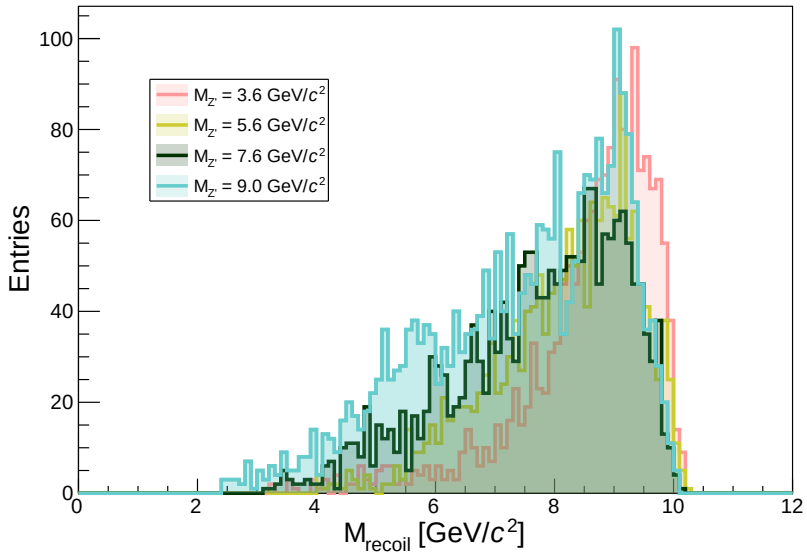

Figure 5.1 Signal events for CS1 for different Z' mass do not peak at the nominal values of the Z' mass.

Figure 5.2 shows the comparison between the 90% confidence level upper limit on the cross section and on the g' coupling constant obtained with the CS1 control sample with 100 fb^{-1} for different choices of the mass intervals in which signal events are counted (blue and red) compared with the sensitivity obtained from a cut and count method on the MC sample. The sensitivity for this control sample is orders of magnitude lower, so that we do not risk any accidental unhiding.

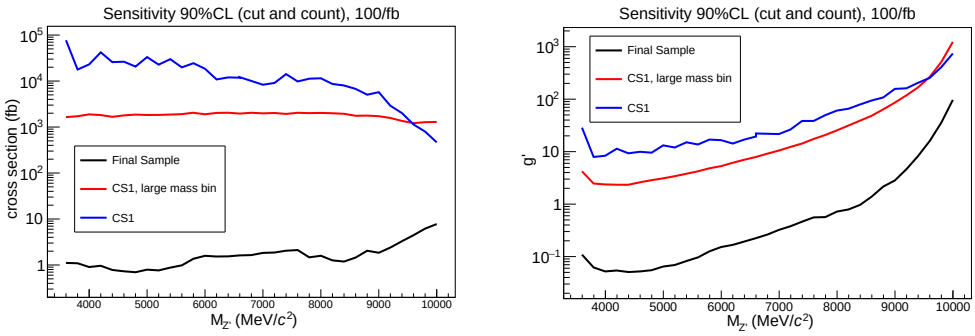

Figure 5.2 90% confidence level upper limit on the cross section and g' coupling constant for the control sample $\pi^+\pi^-\tau^+\tau^-$ (CS1) in the case of usual mass bins (blue), and in the case of one large bin [7.5,10.5] GeV/c^2 where most of the signal accumulates (red), compared with the sensitivity obtained for the final sample. All sensitivities are estimated applying a cut and count method.

5.2 Trigger efficiency study

The simulation of the trigger is missing in the official MC production so, to perform data-MC comparison it is necessary to estimate the trigger efficiency directly from data and use it to re-weight MC events. For this measurement we use two trigger lines in logical OR: the CDC *fff* and the CDCKLM. This last, in turn, is the logical OR of the four CDCKLM*n* exclusive trigger lines, that require the number of matched CDC tracks and KLM hits to be exactly n, where $n = 1,2,3,4$. On data we use the logical OR of the 4 lines. For the CDCKLM single muon (CDCKLM1) trigger efficiency we rely on the results contained in an existing study within the *Belle II* collaboration [101].
We then compute a KLM event trigger probability, based on the logical OR of the single muon efficiencies, which will depend on the number of identified muons in the event (from two to four). The CDC *fff* trigger requires the presence of at least 3 tracks reconstructed using all CDC superlayers (see Chapter 2 for the description of the CDC). The available measured efficiencies in *Belle II*, which are expressed as a function of the lowest transverse momentum in the event mostly in $\tau^+\tau^-$ final states, do not fit our needs, as they turn out to heavily depend on the process used for the measurement. We then setup a procedure to measure such efficiencies in conditions much closer to those of our analysis. Being N the number of events, the *fff* trigger efficiency is defined as:

$$\varepsilon(fff) = \frac{N_{fff\&cal}}{N_{cal}} \tag{5.1}$$

where *cal* are trigger lines orthogonal to *fff* (not based on CDC); $cal = hie \;\; OR \;\; lmlX, \;\; (X = 1,..,10)$. In particular: *hie* requires the total energy deposit in ECL higher than 1 GeV and the bhabha veto, while *lmlX* are the low multiplicity dedicated triggers. The latter apply a selection on the number of cluster in the ECL, on the energy of the cluster in the ECL, on the polar angle and on the difference of ϕ angle of the clusters and the bhabha veto: as example, *lml6* requires only one cluster with an energy higher than 1 GeV in the barrel region of the ECL and no other ECL cluster with energy higher than 300 MeV anywhere, *lml8* requires two ECL cluster with energy higher than 250 MeV and with a difference of ϕ angle in the center of mass frame of $170^o \leq \Delta\phi_{CM} \leq 190^o$ and without any cluster of 2 GeV in the event.

To perform the measurement, we use subsamples of events from the $\pi^+\pi^-\tau^+\tau^-$ control sample and from the full $\mu^+\mu^-\tau^+\tau^-$ sample (for which we do not look at any distribution, in order to keep the sample hidden). We require the presence of at least one electron with a momentum of $p > 1$ GeV/c: in this condition the ECL trigger is fired in more than 97% of events. The requirement on the electron momentum, rather than on the cluster energy (which was not available in our NTuples) induces a small correlation with the CDC info, which we verify to be negligible. The signal efficiency obtained requiring the electron momentum to be higher that 1 GeV/c is compatible with the one obtained without apply this selection, as it possible to see in Figure 5.12 (respectively purple and green points). We use 54.7 fb^{-1} collected on the $\Upsilon(4S)$ resonance. In order to minimize the dependence on the process, the *fff* trigger efficiency is studied as a function of the two lowest transverse momenta of the 4 tracks (third and fourth in decreasing order of p_T). We

soon realized, by repeating the studies on differently selected samples, that the process dependence was not fully removed. We went therefore one step forward, and computed *fff* trigger efficiencies still as a function of the two lowest transverse momenta, separating for topologies which depend on the number of track in the barrel CDC:

- number of tracks in the barrel $= 4$
- number of tracks in the barrel $= 3$
- number of tracks in the barrel $= 2$
- number of tracks in the barrel < 2 (the case with a number of tracks in the barrel = 0 is negligible)

A track is considered in the barrel if its polar angle θ is $51^o < \theta < 117^o$. For each of these cases we provide 2D efficiency tables (and corresponding errors): they are shown in Figures 5.3, 5.4, 5.5 and 5.6. We use a finer binning for low transverse momenta, due to quick variations of the efficiency in those regions.
We finally combine, on event by event basis, the *fff* trigger efficiency with the CDCKLM one with a logical OR, neglecting possible correlation effects, which we estimate to be negligible. This number is used as an event weight for MC, while in data we simply require the OR of the CDC *fff* trigger bit with the CDCKLM lines. The single *fff* and CDCKLM trigger efficiencies and their combined *fff*-OR-CDCKLM effect are shown in Figure 5.7. For masses below 7 GeV/c^2 it reaches a plateau of $\sim$95%. The drop of the CDCKLM trigger efficiency for high Z' masses is caused by the fact that the higher the Z' mass is, the softer the tagging muons are, with a consequent decrease of the KLM capabilities. The systematic uncertainties associated to both CDCKLM*n* and *fff* trigger lines are discussed in Section 5.4.

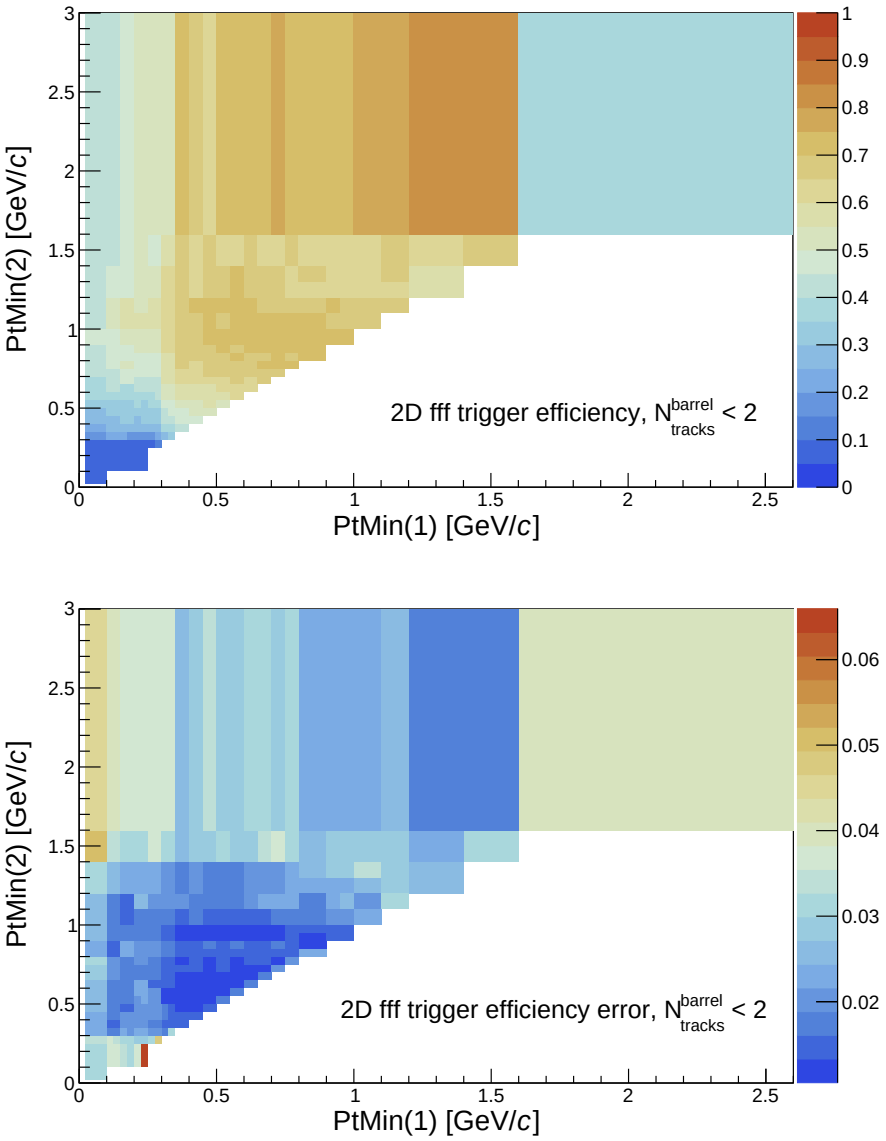

Figure 5.3 Above: *fff* trigger efficiency as a function of the two minimum transverse momenta for events with less than 2 tracks in the barrel. Under: *fff* trigger efficiency statistical errors.

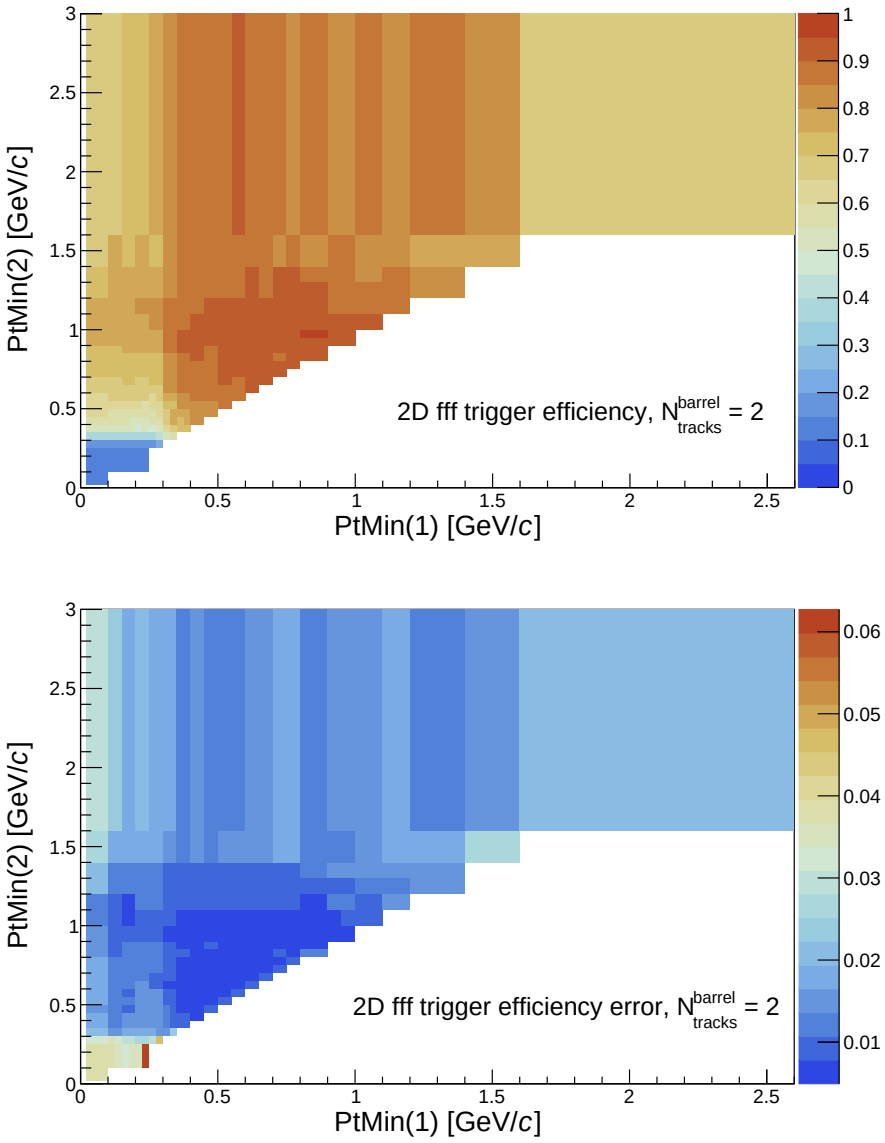

Figure 5.4 Above: *fff* trigger efficiency as a function of the two minimum transverse momenta for events with 2 tracks in the barrel. Under: *fff* trigger efficiency statistical errors.

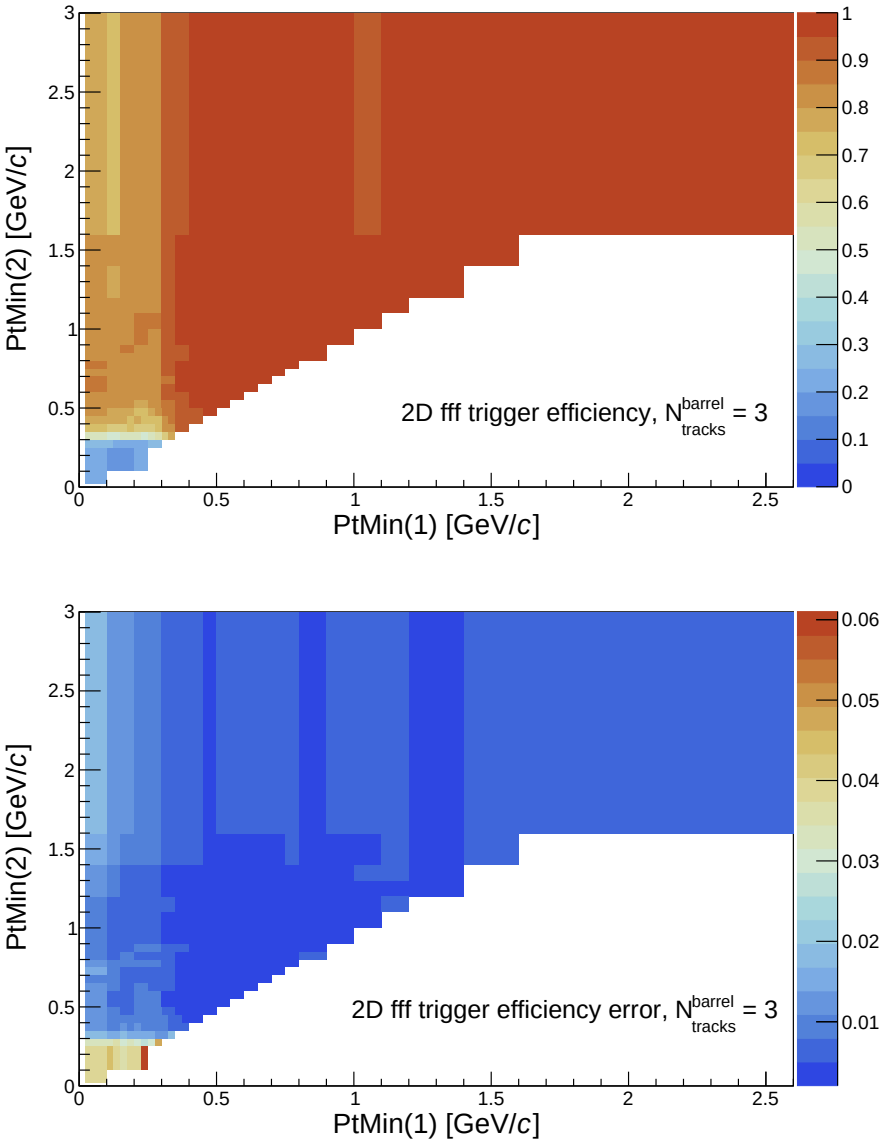

Figure 5.5 Above: *fff* trigger efficiency as a function of the two minimum transverse momenta for events with 3 tracks in the barrel. Under: *fff* trigger efficiency statistical errors.

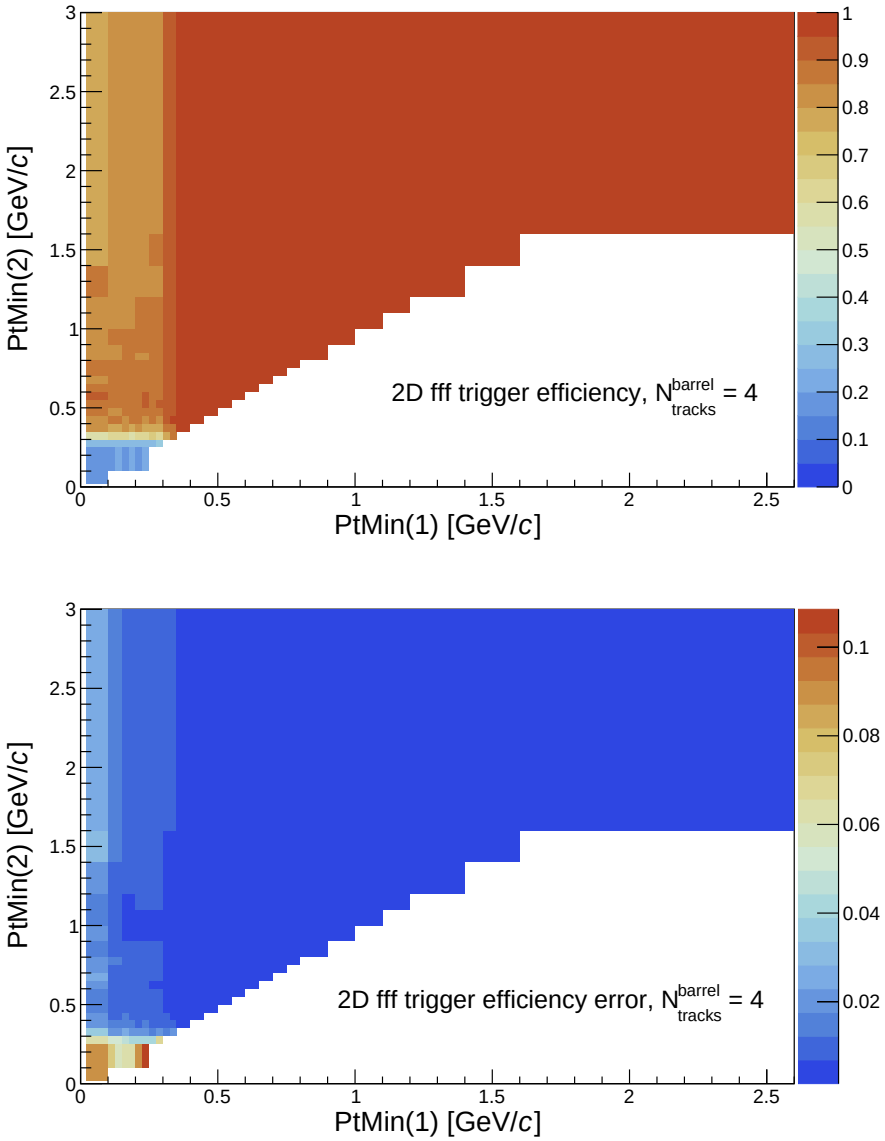

Figure 5.6 Above: *fff* trigger efficiency as a function of the two minimum transverse momenta for events with 4 tracks in the barrel. Under: *fff* trigger efficiency statistical errors.

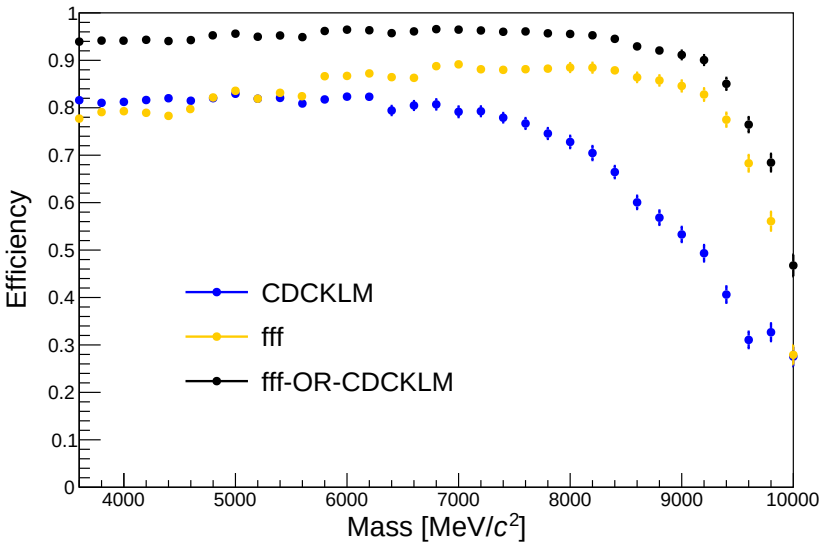

Figure 5.7 Signal efficiency requiring *fff*-OR-CDCKLM trigger (black), only *fff* trigger (yellow) and only CDCKLM trigger (blue).

5.3 Data Validation

In this section we perform data-MC comparisons before the usage of the MVA selection. As the signal region is currently still hidden, we use mostly the control samples introduced above.

5.3.1 Control sample $\pi^+\pi^-\tau^+\tau^-$

In this control sample we have two identified pion tracks, which we call "tagging pions" (in analogy with the tagging muons of the signal case) and two additional tracks that can be eletrons, pions or muons. We use here only the *fff* trigger, with efficiencies evaluated in the previous Section. The KLM trigger is not suitable in this case because of the presence of the tagging pions rather than the muons. Moreover we apply the PID corrections from internal *Belle II* studies, necessary for the data-MC comparison. We apply the following selection:

- $\pi ID > 0.5$ for the two tagging pions;
- $\mu ID > 0.5$ OR $eID > 0.5$ OR $(1 - \mu ID - eID) > 0.5$ for the other two tracks in the event (also named τ-daughters);
- $M < 9.5$ GeV/c^2, the standard pre-selection;
- $M_{\pi\pi} > 2$ GeV/c^2. This selection was necessary to remove a large part of hadronic structures, which are not well reproduced in MC.

For this study we use 54.7 fb^{-1} of data collected at the $\Upsilon(4S)$ resonance, and 100 fb^2 of MC. Figure, 5.8 shows the data/MC comparison for the recoil mass calculated with respect to the dipion. The main contributions to the $\pi^+\pi^-\tau^+\tau^-$ control sample are $q\bar{q}$ and $\tau\tau$ processes, while other contributions coming from $\mu\mu$, $ee\mu\mu$ and $\mu\mu\tau\tau$, $\mu\mu\mu\mu$, $ee\tau\tau$ and $ee\pi\pi$ processes are negligible. The agreement is generally good, with mass dependent discrepancies at most of 20%, but on average better than this. The highest discrepancy in the recoil mass distribution is lower than 20% and happens at masses $M_{recoil} > 8$ GeV/c^2, due most probably to surviving hadron components not included in MC, and not fully removed by the cut $M_{\pi\pi} > 2$ GeV/c^2.

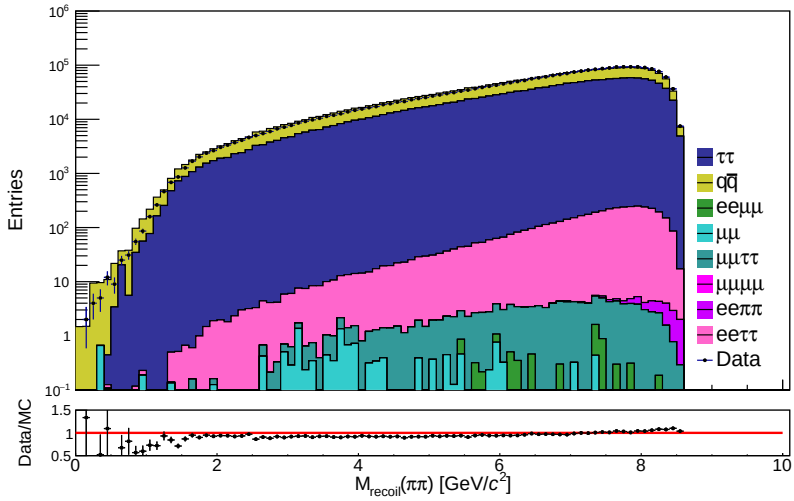

Figure 5.8 Data/MC comparison for the recoil mass calculated with respect to the dipion.

In order to better characterize the pattern of the data-MC comparison, we study the distribution of the event thrust, shown in Figure 5.9, which is expected to separate to some extent the $\tau\tau$- and $q\bar{q}$ contributions. The event thrust is evaluated in the recoil reference frame, which, for signal events, corresponds to the Z' rest frame. As expected, the distribution peaks close to 1 for $\tau\tau$ events, and to lower values for $q\bar{q}$, and can be used to enrich one of the two components. Figure 5.10 shows the data/MC comparison for the recoil mass distribution in events with a thrust larger than 0.92, enriched in $\tau\tau$-like events (up), and lower than 0.87, enriched in $q\bar{q}$-like events (down). Discrepancies are generally lower for the $\tau\tau$-like enriched case, which is believed to be properly reproduced by the available generators, compared to the $q\bar{q}$-like one, more complicated due to the presence of hadronic processes in low multiplicity events.
Figure 5.11 shows again the recoil mass distribution to the dipion system. In this case, also shown is the $\pm 1\sigma$ band corresponding to the uncertainties on the MC correction factors (trigger efficiency and PID corrections). There is a good data/MC agreement at 1σ level. It is important to remember here that the background will be measured directly from data with the recoil mass fitting procedure. Therefore data/MC comparison, while useful to better understand data and to check systematic uncertainties, do not directly affect the measurement error. More plots showing data/MC for all discriminant variables are shown

in Appendix A. More studies performed with this control sample, namely data/MC comparisons after the MVA selections, will be shown in the following section. In particular, we will show the ratio data/MC of background efficiency due to MLP selection, $\varepsilon_{Data}/\varepsilon_{MC}$, that we use to estimate the systematic uncertainty due to MLP.

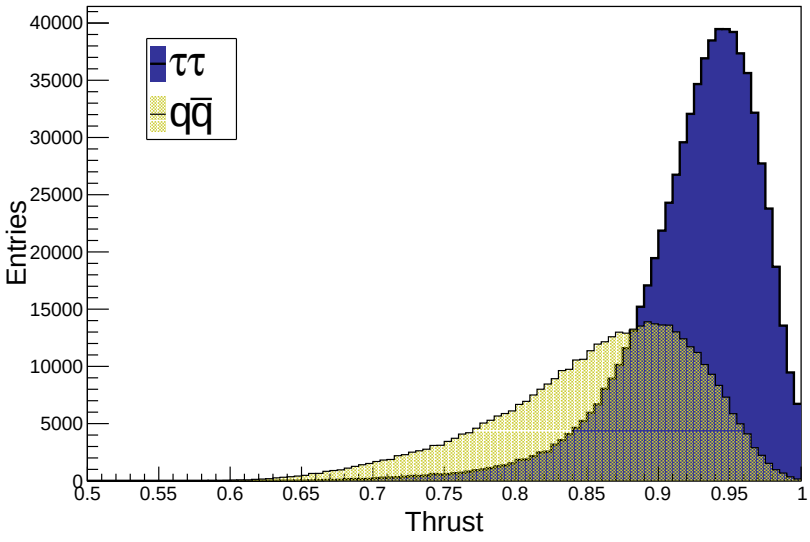

Figure 5.9 Thrust distribution for $\tau\tau$ (blue) and $q\bar{q}$ (yellow) events. The thrust of the event is evaluated in the recoil reference frame, which in signal events corresponds to the reference system where the Z' is at rest.

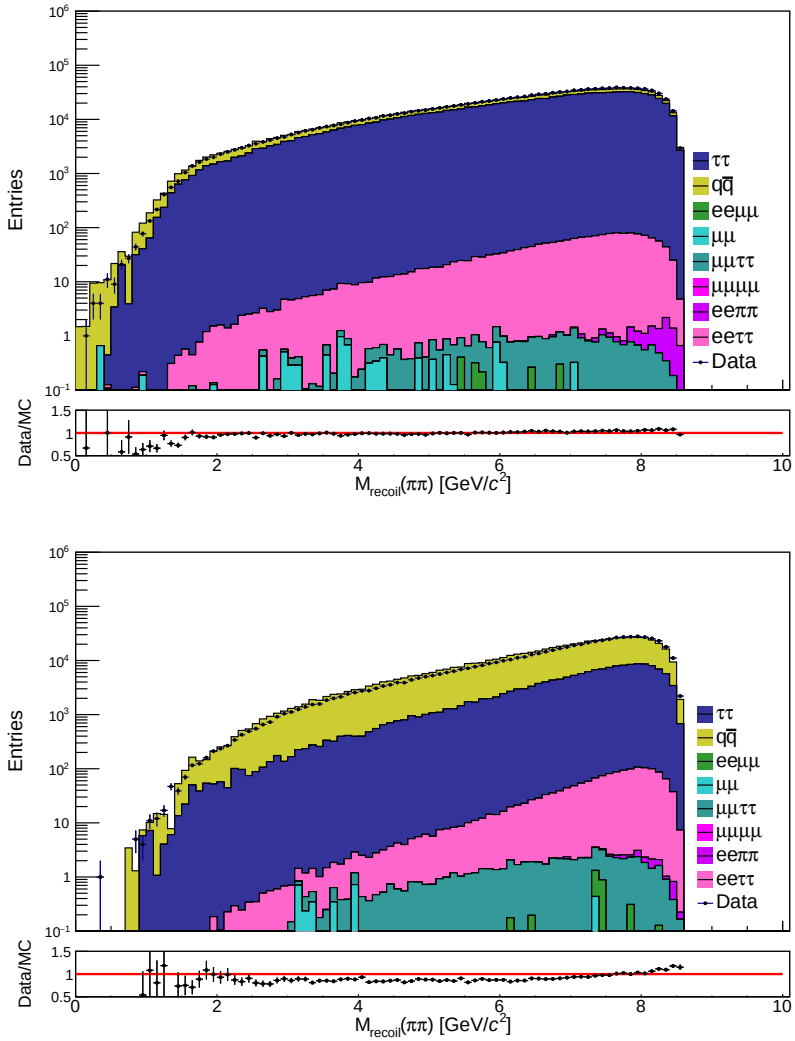

Figure 5.10 Data/MC comparison for the recoil mass calculated with respect to the dipion, for events with a thrust higher than 0.92, enriched in $\tau\tau$-like events (up), and lower than 0.87, enriched in $q\bar{q}$-like events (down).

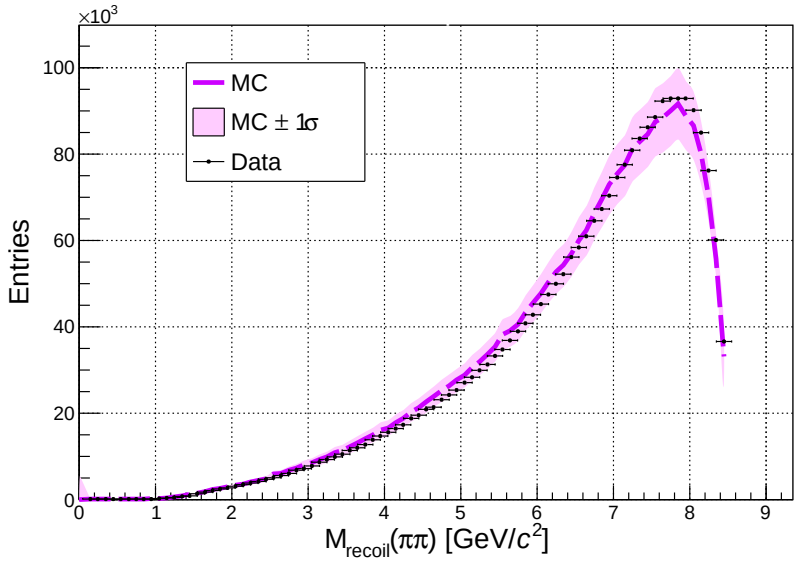

Figure 5.11 Data/MC comparison for the recoil mass calculated with respect to the dipion. Black points are data, while the violet dashed line is MC. The pink band is the MC 1σ band evaluated combining the uncertainties of the correction applied to MC: *fff* trigger efficiency and PID corrections.

5.4 Systematic uncertainties

Systematic uncertainties are evaluated on the signal efficiency, since the background is estimated directly in data from the fit. The main systematic contributions affecting this measurement come from the signal+background fit procedure (signal extraction), the MLP selection, the trigger efficiency, the particle identification selections and the tracking efficiency. A preliminary estimate of the systematic uncertainties on the signal efficiency is evaluated here, and the strategy used for all of them is described below.

5.4.1 Tracking

The tracking efficiency is taken from an existing study within the *Belle II* collaboration where a data-MC per track discrepancy of efficiency is found to be $[0.13 \pm 0.16(stat) \pm 0.89(syst)]\%$ [102]. Since exactly 4 tracks are required in this analysis, losing even one track would cause the event to be discarded. For this reason, the data-MC efficiency correction has to be multiplied by 4 while the associated systematic uncertainty is propagated in quadrature 4 times, taking into account both statistic and systematic errors:

$$syst = \sqrt{4 \cdot (0.16^2 + 0.89^2)} \tag{5.2}$$

The final systematic uncertainties due to this source is thus evaluated to be 1.80%.

5.4.2 Trigger

We evaluate the *fff* trigger systematic uncertainty by computing the spread of the trigger signal efficiencies, as a function of the Z' mass, corresponding to different combinations of CDCKLM and *fff* lines. The CDCKLM efficiency, taken from the internal *Belle II* study in Reference [101], is expressed as a function of the momentum p and the polar angle θ of the track. We evaluate the CDCKLM systematic uncertainty considering 100% correlated $p-\theta$ bins, i.e we vary the CDCKLM efficiencies of all $p-\theta$ bins proportionally to the systematic uncertainty associated to each of them, where the constant of proportionality is equal for all the different $p-\theta$ bins. The procedure to determine the systematic uncertainty associated to the CDCKLM trigger is described in detail in Paragraph 5.4.2.

***fff* trigger systematic uncertainties** The *fff* trigger efficiency has been measured on different samples, with different PID selections, requiring or not the presence of muons, pions, electrons (they are indicated in the legenda of Figure 5.12). Figure 5.12 shows the *fff*-OR-CDCKLM combined efficiency as a function of the Z' mass for different *fff* configurations. The measurement of the trigger efficiency used in the analysis is represented with the purple points (last line of the legend). Figure 5.13 shows the distribution of the highest difference for each tested mass point. We take half of the band shown in Figure 5.12 as a systematic contribution, i.e. half of the mean of the 1D histogram of Figure 5.13: it corresponds $\sim$2.5%.

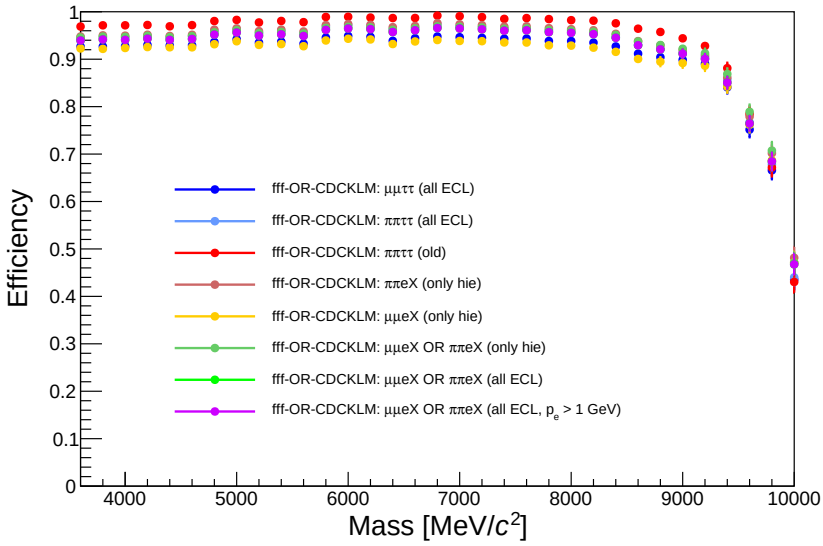

Figure 5.12 Signal efficiency as a function of the Z' mass for different configuration of the *fff*-OR-CDCKLM triggers. In particular, the process used to evaluate the *fff* trigger efficiency is what changes in the different curves.

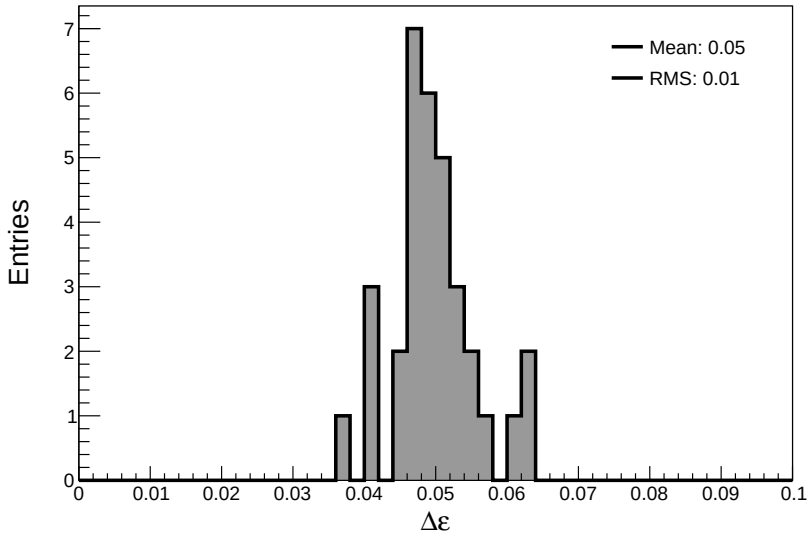

Figure 5.13 Distribution of the highest difference between all the configuration of *fff*-OR-CDCKLM tested for each Z' mass point.

CDCKLM trigger systematic uncertainties The procedure applied is the following:

- we extract a random number r from a Gaussian distribution centered in 0 with standard deviation 1;
- we vary the measured CDCKLM efficiencies expressed in terms of $p-\theta$ bins (see Reference [101]) by adding $r \times sys$, where sys is the systematic uncertainty associated to the measured CDCKLM efficiency for those particular values of $p-\theta$;
- we compute the signal efficiency by applying *fff*-OR-CDCKLM trigger efficiencies, where the *fff* trigger efficiency is taken from Section 5.2, while the CDCKLM efficiency is the one obtained in the previous step;
- we repeat the procedure 1000 times to get a distribution of signal efficiencies from which we take the mean μ and the standard deviation σ;
- the CDCKLM systematic uncertainty considered is σ/μ.

Signal efficiencies are evaluated after the MLP selection on simulated signal samples, just as the number of events before the application of trigger corrections by the number of events after the application of trigger corrections. Figure 5.14 shows the systematic uncertainty associated to the CDCKLM trigger as a function of the Z' mass. Except for the point at 10 GeV/c^2, the systematic uncertainties are $\mathcal{O}(1\%)$ in the whole mass range, so we take 1% as systematic uncertainty .

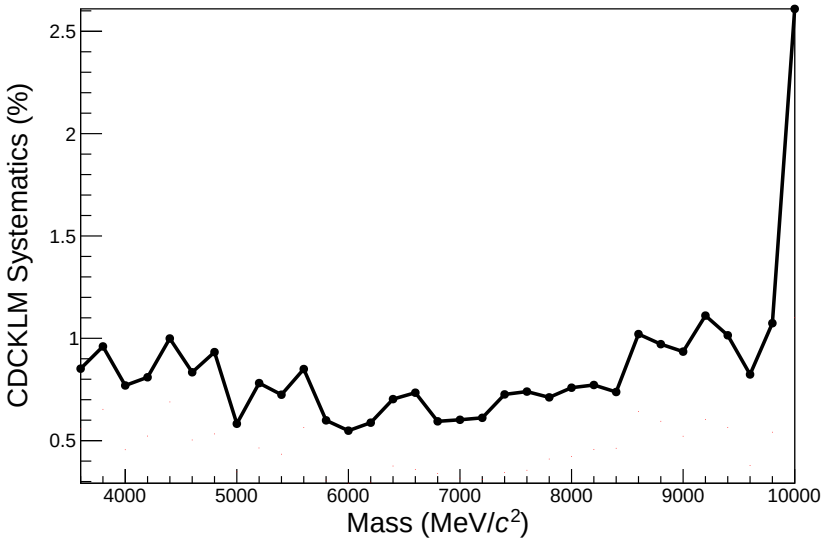

Figure 5.14 Systematic uncertainties associated to the CDCKLM trigger as a function of the Z' mass.

5.4.3 Particle identification

As for the CDCKLM trigger efficiencies, the PID corrections are expressed in terms of the momentum p and the polar angle θ of the track, and they are used as weights to the simulated events. All PID corrections have been produced in internal *Belle II* studies for the MC campaign we are using to simulate signal events [103]. The corrections depend on the PID selection cut applied, so in our case $\mu ID > 0.5$ for the tagging muons and $\mu ID > 0.5$ OR $eID > 0.5$ OR $(1 - \mu ID - eID) > 0.5$ for the two additional tracks. Since the correction for the PID variable $(1 - \mu ID - eID)$ does not exist yet, we apply the corrections available for the πID, assuming they are valid for all hadrons. Morever, we also apply the fake-rate corrections. For example: considering a track identified as a muon by requiring $\mu ID > 0.5$ with a given (p,θ), we obtain the correction from the correspondent table. If the MC truth tells us that it is a pion mis-identified as a muon, we take the correction from the correspondent fake-rate table. The weight that we apply to the event is the product of the corrections obtained for the four tracks.

To estimate the systematics associated to the PID selections, we apply the same procedure used to estimate the systematic uncertainty associated to the CDCKLM trigger. In this case we have a table expressed in terms of $p - \theta$ bins for each PID selection that we require on the four tracks and for the fake-rate corrections. We vary the values of the tables by a random number r extracted from a Gaussian centered in 0 and with standard deviation 1, which is considered equal for all the $p - \theta$ bins in the tables, multiplied by the systematic uncertainty of each $p - \theta$ bin. We repeat this procedure 1000 times, and each time we calculate the signal efficiency for each Z' mass. Finally we have a distribution of signal efficiencies with mean μ and the standard deviation σ for each Z' mass, and we consider σ/μ as systematic uncertainty.

Also in this case, signal efficiencies are evaluated after the MLP selection on simulated signal samples as the number of events before the application of the PID corrections divided by the number of events after the application of the PID corrections. Figure 5.15 shows the PID systematics evaluated for different Z' masses. The systematic uncertainty varies from a minimum of 3.9% to a maximum of 6.2% as a function of the Z' mass.

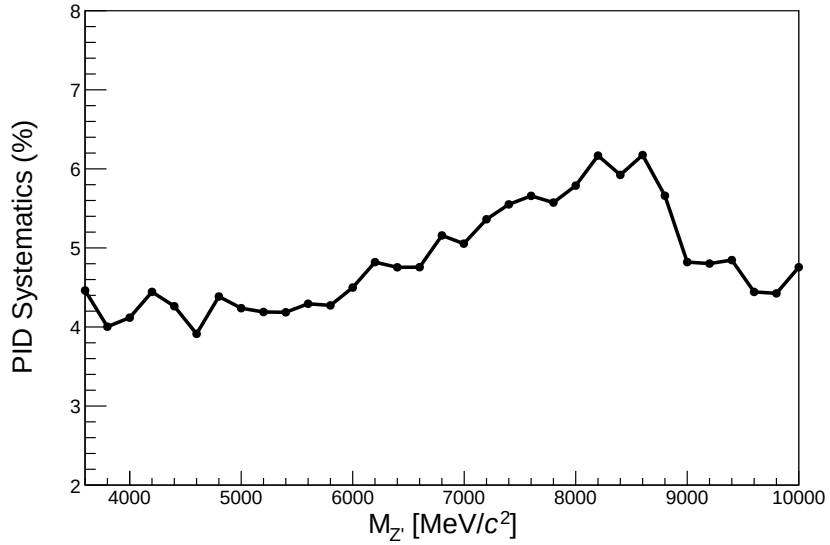

Figure 5.15 PID systematics as a function of the Z' mass.

5.4.4 MLP selection

Systematic uncertainties due to the usage of the background suppressing MVA techniques are estimated by comparing the relative efficiency ε, ie the fraction of surviving events, in data and MC after applying the MLP selection. We use the control sample $\pi^+\pi^-\tau^+\tau^-$, whose recoil mass distribution, after the selections, goes up to 8 GeV/c^2. For this reason we apply 7 MLPs, covering the recoil mass range from 3.6 GeV/c^2 to 7.6 GeV/c^2. Figures 5.16-5.17 show the data/MC comparison of the fraction of events surviving the MLP selection, for the different MLPs. A constant fit was used to quote a data/MC ratio for each MLP. We use 54.7 fb^{-1} collected on the $\Upsilon(4S)$ resonance. An overall discrepancy is evaluated with a constant fit to the $\varepsilon_{Data}/\varepsilon_{MC}$ ratios of the different MLPs: it's shown in Figure 5.18. We consider the largest between the distance of the fit result from 1 and the fit error as an estimate of the systematic contribution due to this source: it turned out to be 2.8%.

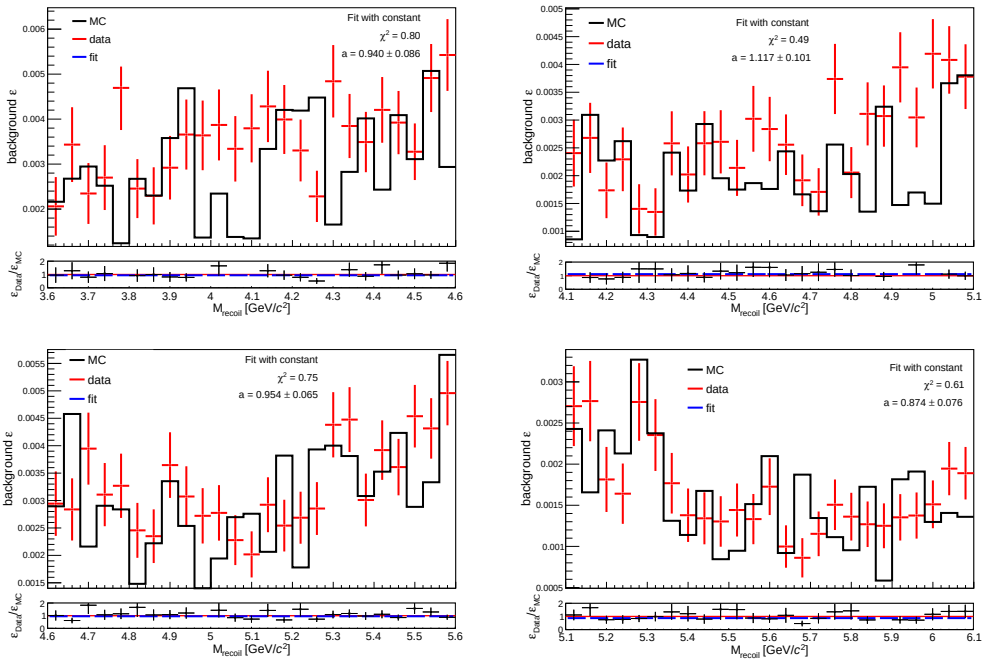

Figure 5.16 Data/MC comparison of the MLP efficiency on background, evaluated using control sample $\pi^+\pi^-\tau^+\tau^-$, for four different MLPs (MLPs from 1 to 4).

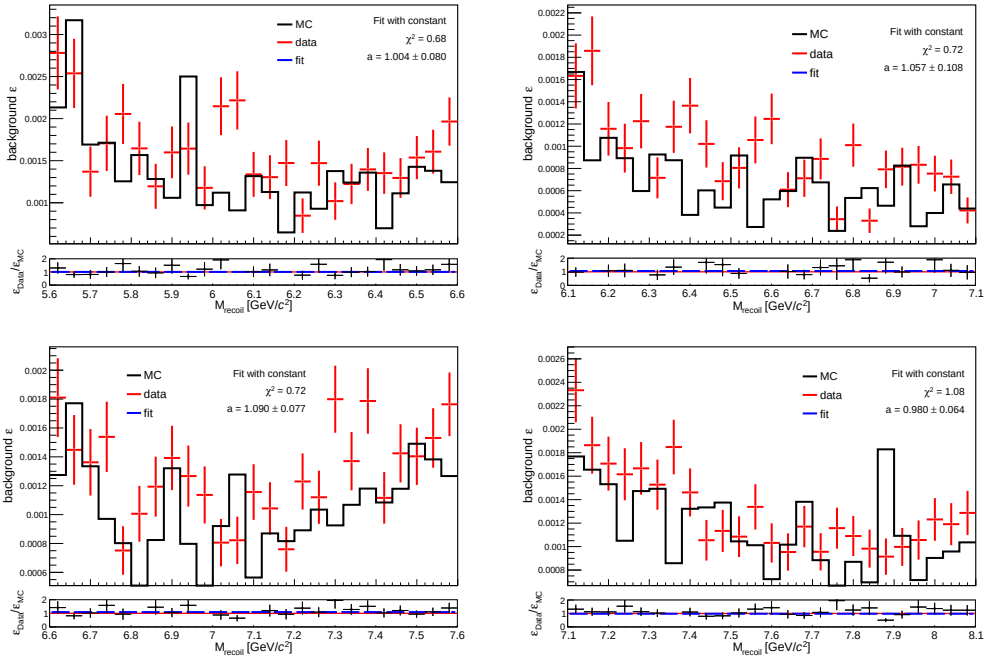

Figure 5.17 Data/MC comparison of the MLP efficiency on background, evaluated using control sample $\pi^+\pi^-\tau^+\tau^-$, for three different MLPs (MLPs from 5 to 8).

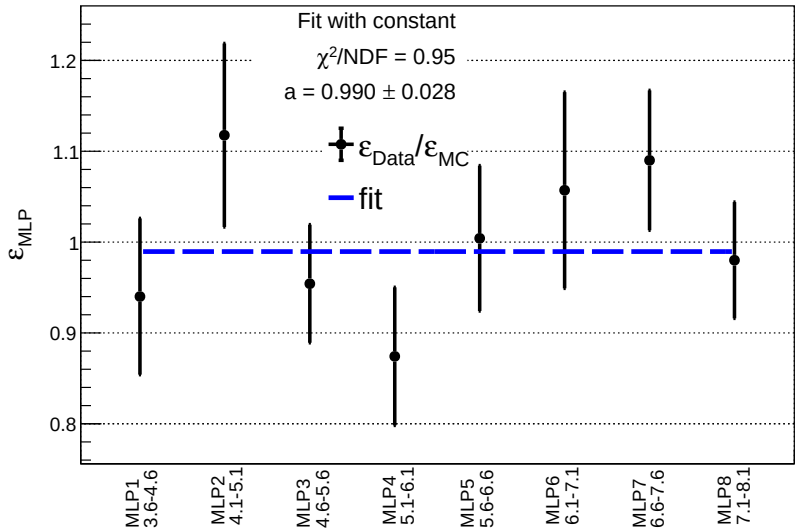

Figure 5.18 Constant fit to the ratio $\varepsilon_{Data}/\varepsilon_{MC}$ in the full range covered by the $\pi^+\pi^-\tau^+\tau^-$ control sample. The uncertainty of the fit is considered as systematic.

5.4.5 Fit

To evaluate the systematic uncertainties due to the fit procedure, we apply a toyMC study to check whether allowing first-order floating polynomial components to the background (for which we normally use a constant, see Chapter 4), induces a bias on the extracted signal yield. The study is repeated for different Z' mass hypotheses, with different MLP selections applied, depending on the mass. The background is Poisson generated and signal is injected on it with a yield corresponding to $1.64 \cdot \sqrt{N_{bkg}}$, corresponding to the 90% CL upper limit on the number of observed events in a counting experiment, and with a mass distribution following its *p.d.f* (see Chapter 4). The result is then fitted with a fixed *p.d.f* for the signal shape parameters and with a floating first-order polynomial for the background, with a floating signal yield. Basically, we check the stability of the fit when we add one floating parameter to the background *p.d.f*, while keeping fixed the signal *p.d.f*. The newly extracted yield, N_{sig}, is then compared to the true number of events injected, N_{sig}^{true}, divided by the uncertainty on N_{sig}, $\sigma(N_{sig})$, with pull defined as

$$\frac{N_{sig} - N_{sig}^{true}}{\sigma(N_{sig})} \tag{5.3}$$

This procedure is repeated 500 times for each Z' mass hypothesis for the different MLPs, and the distribution of the pulls is then fitted with a Gaussian distribution, from which the mean μ and the variance σ^2 are extracted.
Figure 5.19 shows the distribution of the means returned by the Gaussian fit of the pulls for each mass point. We find that the extracted yield is underestimated by 6.7% on average

and we assume this value as the systematic contribution due to this source.

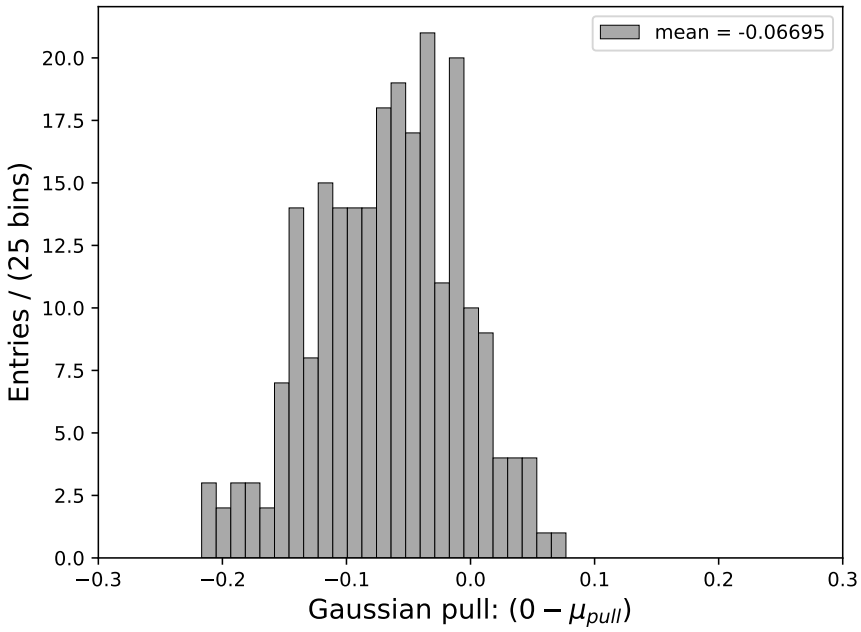

Figure 5.19 Distribution of the difference of the means μ returned by the Gaussian fit of the pulls from 0 for each mass point, evaluated as $(0-\mu)$. The signal yield is underestimated of 6.7% on average.

To check the contribution due to the modeling of the signal *p.d.f*, the sum of two Crystal Ball distributions where all Crystal Ball parameters have been modeled as a function of the Z' mass (see Chapter 4), named "default" signal *p.d.f*, we apply the following procedure based on toyMCs:

- perform a fit for different Z' mass hypothesis with all floating Crystal Ball parameters, to obtain different Crystal Ball parameters;
- define an "alternative" signal *p.d.f* obtained fixing the Crystal Ball parameters to the new values obtained from the previous step;
- run 500 toyMCs to get the pull distributions (see Equation 5.3) from the fits performed with both the "default" signal *p.d.f* and the "alternative" signal *p.d.f*;
- fit the pull distributions with a Gaussian distribution to get the means and standard deviations: $(\mu_{\text{default}}, \sigma_{\text{default}})$ and $(\mu_{\text{alternative}}, \sigma_{\text{alternative}})$;
- compare the results of the pulls.

We do not observe any significant difference using the "default" with respect to the "alternative" signal *p.d.f*.

5.4.6 Pre-selection: $M < 9.5$ GeV/c^2

To evaluate the systematic due to the preselection requiring the four-track mass $M < 9.5$ GeV/c^2, we change the cut by ± 100 MeV/c^2, corresponding to the full width half maximum of the mass measured at the $\Upsilon(4S)$ resonance peak: we assume, in practice, that the four-track mass resolution does not change from 10.58 to 9.5 GeV. The higest variation we find in the signal efficiency for different Z' mass hypotheses for the different MLPs is 0.04%, which we assume as an estimate of the systematic contribution due to this source.

5.4.7 Beam energy shift

For the beam energy shift an uncertainty of 1.5 MeV was considered, as it was the case for the *Belle* experiment. This is a conservative assumption, as the preliminary corresponding values from the *Belle II* experiment are better, of the order of 0.5 MeV. The 1.5 MeV contribution is separately summed and subtracted to the center-of-mass energy $\sqrt{s}$ in signal events and the recoil mass recomputed. The largest difference in the signal efficiency is estimated to be 0.068%, assumed as the systematic contribution associated to this source.

5.4.8 Momentum resolution

Momentum resolution has been estimated in two different momentum intervals in a internal study at *Belle II* [104]. The two relevant plots are shown in Figure 5.20. For the momentum intervals covered by the two plots, we compute an additive term σ_p which, added in quadrature to the Monte Carlo, gives approximately the measured resolution in data: they are 0.31% and 0.2% for $p_t < 2$ GeV/c and $4.4 < p_t < 5.3$ GeV/c, respectively. For intermediate values in the range $2 < pt < 4.4$ GeV/c a linear interpolation between 0.31% and 0.2% was used. A Monte Carlo procedure was then put in place by adding to each track a value extracted from a Gaussian of expected mean 0 and width set to σ_p and then recomputing the recoil masses for different signal samples. The analysis selections were then applied and the variation of efficiencies estimated. We take as systematic the average of the differences in the efficiency for every mass points, and it results in a systematic of about 0.01%.

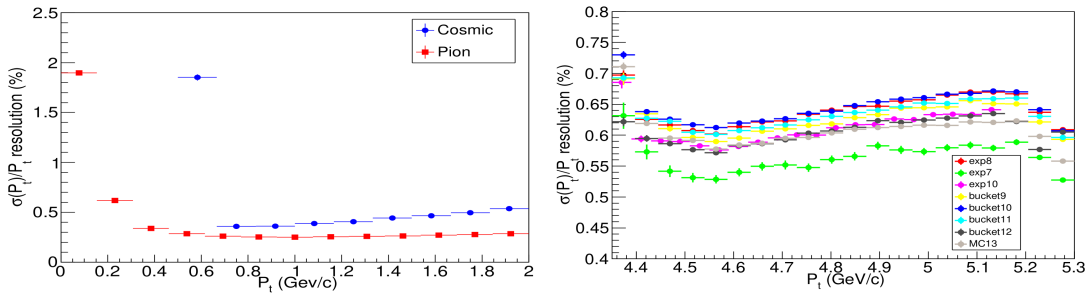

Figure 5.20 Left: $\sigma(p_t)/p_t$ resolution in bins of p_t for slow pions (MC) and cosmics. Right: $\sigma(p_t^*)/p_t^*$ resolution in bins of p_t^* for a dimuon sample, for MC13 and data. From the internal note [104].

5.4.9 Summary of systematic uncertainties

Table 5.1 shows all the systematic uncertainties evaluated on the signal efficiency. The total value depends on the Z' mass, due to the dependence from the Z' mass of the PID systematics, and it varies from a minimum of 8.9% to a maximum of 10.2%. The systematic uncertainties associated to the beam energy shift, the pre-selection $M < 9.5$ GeV/c^2 the momentum resolution are negligible. For this analysis we are mainly limited by the statistics rather than systematic uncertainties that, as shown in Figure 6.6, worsen the sensitivity to the cross section of the process of 1%.
To model the systematic uncertainties as a function of the Z' mass, it is possible to model them using a Savitzky–Golay filter to smooth the points, and then linearly interpolate them. Figure 5.21 shows the modeling of the systematic uncertainties using a Savitzky–Golay(9,2).

Source	Systematic Uncertainty
fff trigger efficiency	2.5%
CDCKLM trigger efficiency	1%
PID selection	(3.9 - 6.2)%
MLP selection	2.8%
Tracking efficiency	1.8%
Fit (sig+bkg)	6.7%
Luminosity	1%
Others (preselection, beam energy shift, momentum resolution)	0.08%
Total	(8.9% - 10.2%)

Table 5.1 Summary of systematic uncertainties.

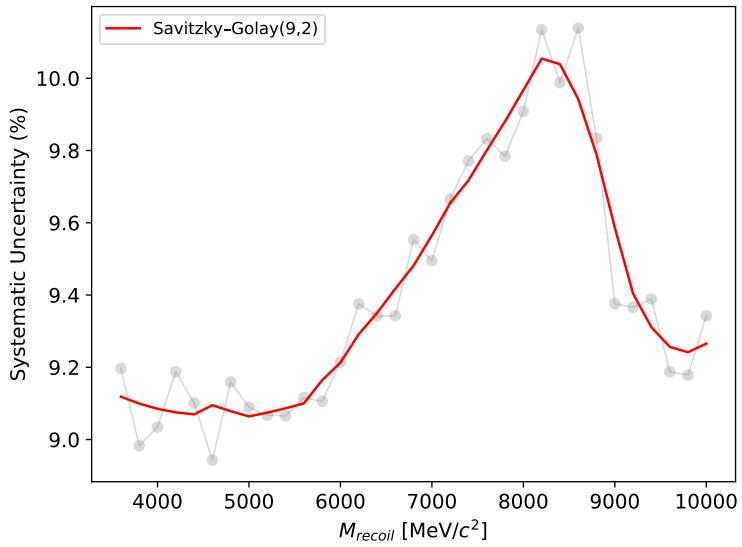

Figure 5.21 Modeling of systematic uncertainties as a function of the Z' mass.

6. Sensitivity Estimate and first look at data

This Chapter will describe the method used to estimate the sensitivity on the cross section of the process and on the coupling constant g' at 90% of confidence level, discussing also the effect of systematic uncertainties on the sensitivity. The method used to estimate the significance from fit and the procedure applied to determine the look-elsewhere effect are described too.

Finally, the results obtained from the unhiding of 10% of the dataset expected for this analysis, corresponding to 5.47 fb^{-1}, are discussed.

6.1 Sensitivity evaluation from simulation

From the relation

$$N_{sig} = \sigma_{Z'} \cdot \mathscr{L} \cdot \varepsilon_S \tag{6.1}$$

where $\mathscr{L}$ is the integrated luminosity and ε_S is the signal efficiency, the sensitivity on the cross section of the process is:

$$UL(\sigma_{Z'})_{90\%CL} = \frac{UL(N_{sig})_{90\%CL}}{\mathscr{L} \cdot \varepsilon_S} \tag{6.2}$$

where $UL(N_{sig})_{90\%CL}$ is the 90% CL upper limit on the number of signal events. In $UL(N_{sig})_{90\%CL}$, the theoretical model assumed enters mainly with the signal efficiency ε_S, that depends on the kinematics of the process.
We use the CL_s frequentist method [105, 106] to derive $UL(N_{sig})_{90\%CL}$ by fitting the MC background only distributions with the signal+background $p.d.f$ (see Chapter 4). This is technically done in the RooStats framework [107] included in ROOT v6-20-04 [87]: specifically, we use the asymptotic calculator strategy [108], which provides directly upper limits on the cross section computed with a Negative Logarithmic Likelihood (NLL) [109] approach, using the CL_s method.
These limits can be easily converted into upper limits on the coupling constant g', since $\sigma_{theory} \sim g'^2$, provided the model cross section is known for some value of g' (which is the case, using MadGraph5@NLO generator). To estimate the cross section for every possible Z' mass we use a linear interpolation, as shown in Figure 6.1. The upper limit on g' are obtained with:

$$UL(g'_{Z'})_{90\%CL} = \sqrt{\frac{g'^2_{gen} \cdot UL(\sigma_{Z'})_{90\%CL}}{\sigma_{theory}}} \tag{6.3}$$

In our case $g'_{gen} = 0.01$ and σ_{theory} is the cross section provided by MadGraph5@NLO assuming $g'_{gen} = 0.01$ for the $L_\mu - L_\tau$ model.

We implement a scanning technique, by performing a series of fits to the recoil mass distribution in sliding intervals, with a step $1\sigma_{peak}$, the mass resolution of the signal peak. Figure 6.2 shows the estimate at 90% CL of the sensitivity to the cross section of the process $e^+e^- \to \mu^+\mu^- Z', Z' \to \tau^+\tau^-$ (left)and to the coupling constant g' (right) as a function of the Z' mass, with trigger efficiency and systematic uncertainties included. The

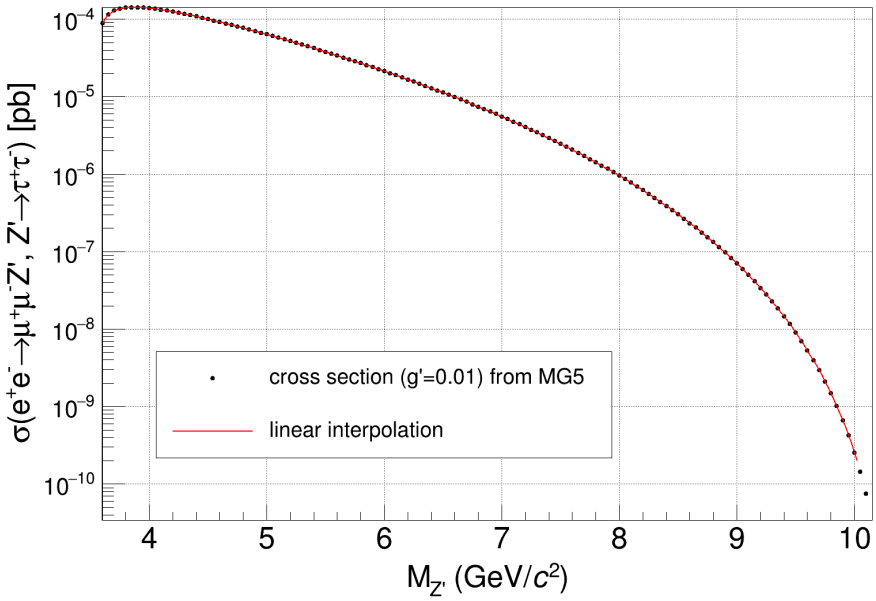

Figure 6.1 Cross section of the process estimated from the MadGraph5@NLO generator assuming $g' = 0.01$, and linearly interpolated. The cross section is expressed in pb.

systematic uncertainties are reported in Section 5.4, resulting to be $\mathcal{O}(10\%)$, as a function of the Z' mass. They are included in the signal+background fit as a Gaussian constraint of width equal to the systematic uncertainties to the fitted signal yield.

The full set of overlapping MLPs is used to produce the sensitivity curves in Figure 6.2.

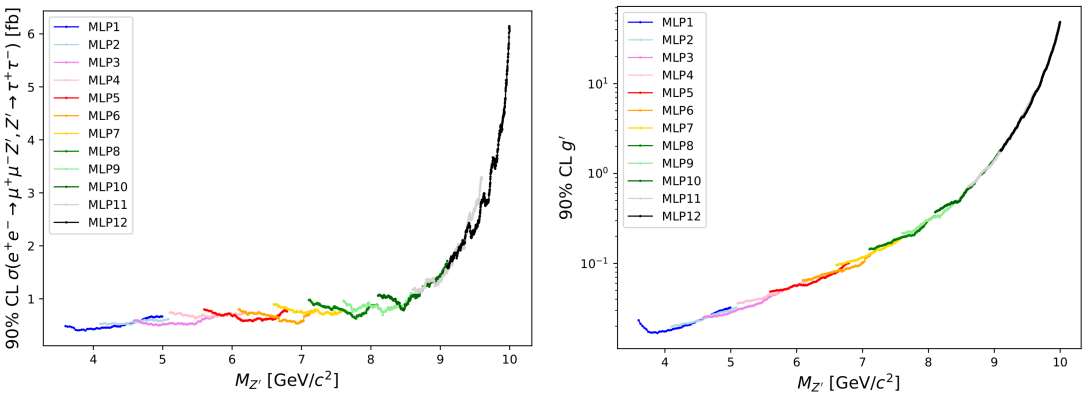

Figure 6.2 Preliminary estimate at 90% *CL* expected sensitivity to the cross section of the process $e^+e^- \to \mu^+\mu^- Z', Z' \to \tau^+\tau^-$ (left) and to the coupling constant of the $L_\mu - L_\tau$ model (right), with trigger efficiency and preliminary systematic uncertainties included.

Using this plot, we build a set of contiguous, not overlapping recoil mass intervals, which we call application ranges, in each of which the MLP giving the best sensitivity is finally used. They are shown in Figure 6.3. The application ranges are the following:

- MLP1 applied in range [3.60 - 4.70[GeV/c^2

- MLP3 applied in range [4.70 - 5.75[GeV/c^2
- MLP5 applied in range [5.75 - 6.65[GeV/c^2
- MLP6 applied in range [6.65 - 7.15[GeV/c^2
- MLP7 applied in range [7.15 - 7.60[GeV/c^2
- MLP8 applied in range [7.60 - 8.00[GeV/c^2
- MLP9 applied in range [8.00 - 8.40[GeV/c^2
- MLP10 applied in range [8.40 - 8.90[GeV/c^2
- MLP11 applied in range [8.90 - 9.20] GeV/c^2
- MLP12 applied in range [9.20 - 10.0] GeV/c^2

The usage of this construction is the following: for a point of generic mass M_{rec}, the MLP corresponding to the interval including M_{rec} is used. As far as the signal extraction is concerned, the fit procedure uses the mass interval $\pm 20\sigma_{peak}$ wide containing points which passed the same MLP selection of the central point, even if this last extends beyond the MLP application range. This is done to avoid discontinuities in the mass distributions which could distort the fit.

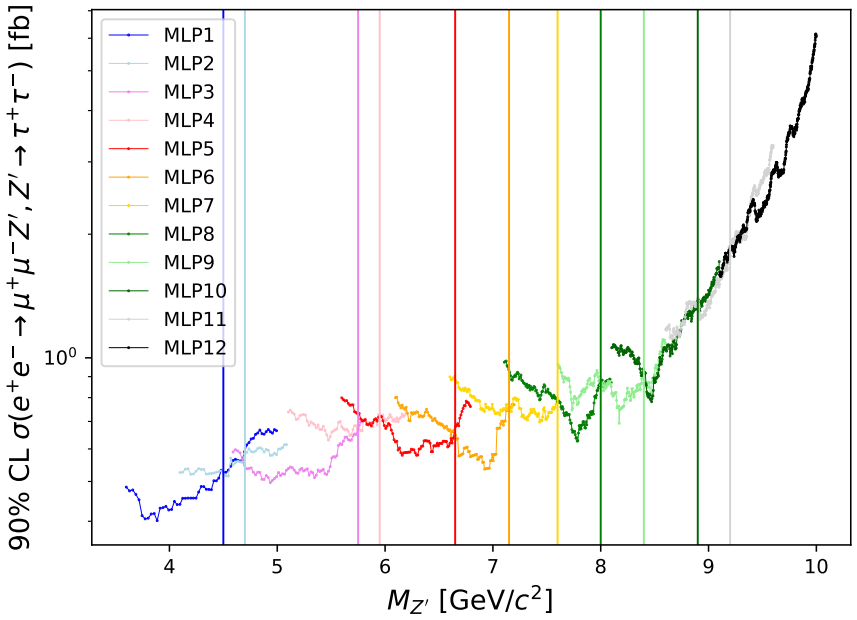

Figure 6.3 Preliminary estimation at 90% *CL* of the sensitivity to the cross section of the process $e^+e^- \to \mu^+\mu^- Z', Z' \to \tau^+\tau^-$, with trigger efficiency and preliminary systematic uncertainties included. Vertical lines show where the different MLP ranges of application end.

Finally, we estimate the expected sensitivity at 90% confidence level assuming 80 fb^{-1} of data and compared it with the existing limit from *BABAR* [59] and *Belle* [60], from the $Z' \to \mu\mu$ analysis, *Belle II* [57], from the $Z' \to$ *inv.* analysis, and the constraints derived from the production of a $\mu^+\mu^-$-pair in ν_μ scattering, the Trident production [110]. Figure 6.4 (right) shows the 90% *CL* expected sensitivity of g' for the $L_\mu - L_\tau$ model and the green/yellow bands corresponding to $\pm 1\sigma$ and $\pm 2\sigma$ for the expected limits under the background-only hypothesis, known as Brazilian band, obtained with the CL_s frequentist method. The red band shows the parameter space that could explain the $(g-2)_\mu$ discrepancy. Figure 6.4 (left) shows the Brazilian band for the 90% *CL* sensitivity to the cross section of the process: dashed line is the median expectation from simulation, while black dots are the upper limits computed with a sample of simulated dataset.
The analysis $Z' \to \tau\tau$ performed at *Belle II* results to not be competitive to exclude the $L_\mu - L_\tau$ model with respect to the existing limits assuming a luminosity of 80 fb^{-1}, and the best sensitivity we get on g' is 1.67×10^{-2}. We are sensitive to cross section below 0.4 fb^{-1}, at 90% *CL*.

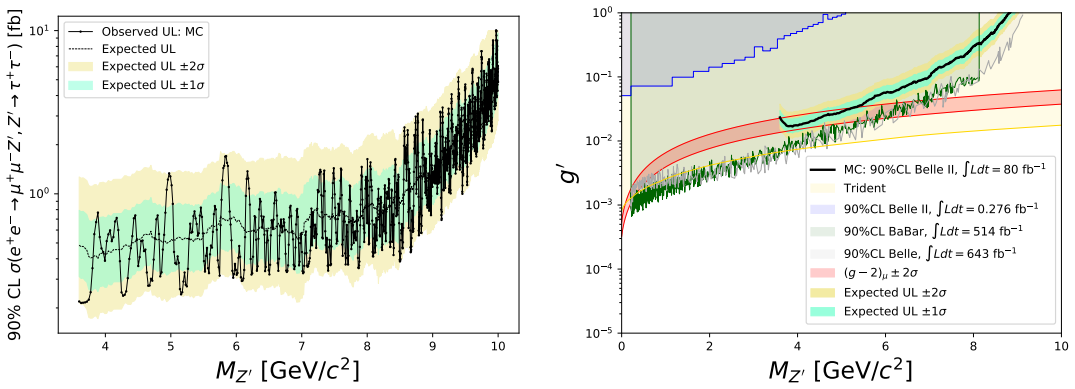

Figure 6.4 Left: 90% *CL* expected sensitivity to the cross section of the process: The green/yellow bands indicate $\pm 1\sigma$ and $\pm 2\sigma$ intervals for the expected limits under the background-only hypothesis. The median expectation is shown with the dashed line, while black dots are the results from a simulated dataset. Right: Preliminary 90% *CL* expected sensitivity of g' for the $L_\mu - L_\tau$ model at *Belle II* assuming 80 fb^{-1}, compared with the existing observed upper limits from *BABAR* [59], *Belle* [60] ($Z' \to \mu\mu$), *Belle II* [57] ($Z' \to$ *inv.*) and the constraints from Trident production [110]. The red band shows the parameter space that can explain the $(g-2)_\mu$.

Effect of systematic uncertainties on sensitivity Figures 6.5 shows the 90% *CL* sensitivity for the cross section of the process (left) and for the coupling constant g' (right) evaluated with and without systematic uncertainties included. Figure 6.6 show the ratio between the two curves of Figure 6.5, in particular the curve obtained without systematic uncertainties included divided by the curve obtained with the systematic uncertainties included. The effect of 10% systematic uncertainties on the sensitivity to the cross section and g' is respectively of the order of 1% and 0.5%, and the difference is due to the square

root in the definition of g':

$$UL(g'_{Z'})_{90\%CL} = \sqrt{\frac{g'^2_{gen} \cdot UL(\sigma_{Z'})_{90\%CL}}{\sigma_{theory}}} \tag{6.4}$$

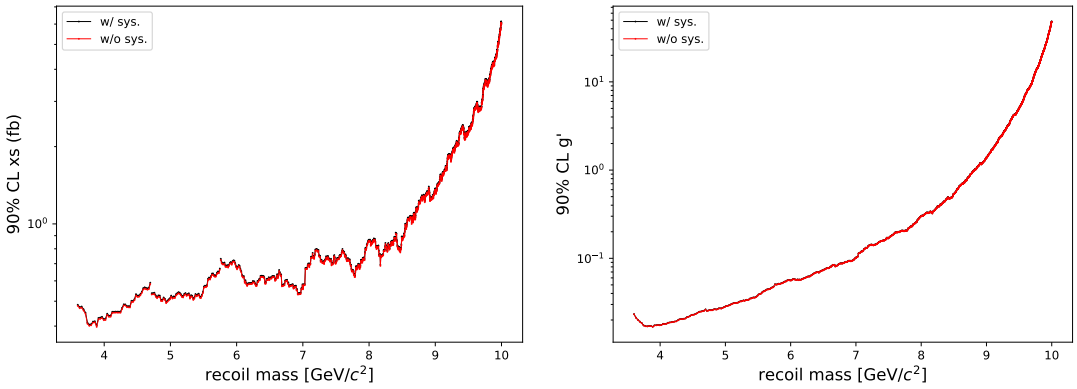

Figure 6.5 Comparison of the expected sensitivity to the cross section (left) and to g' (right) evaluated with (black) and without (red) systematic uncertainties included.

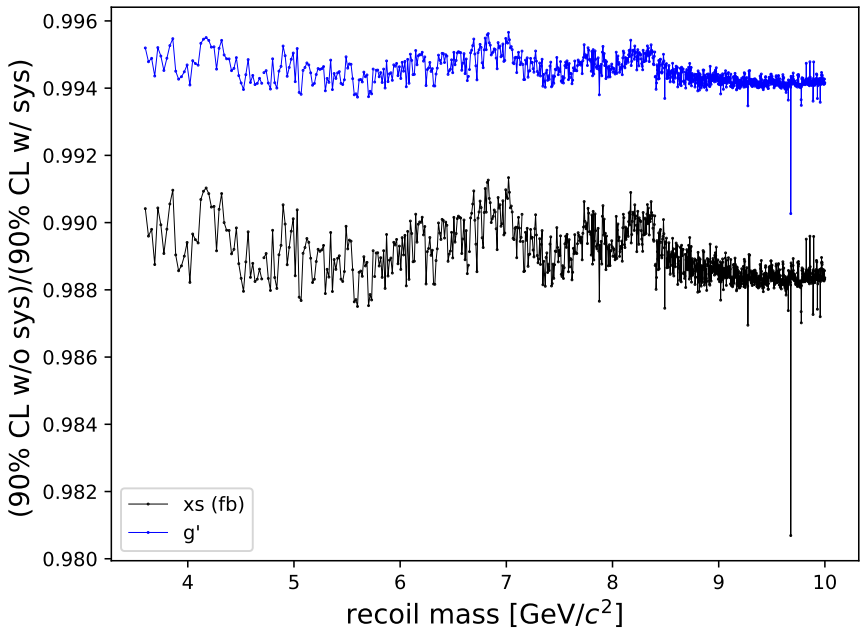

Figure 6.6 Ratio of the sensitivity to the cross section (black) and to g' (blue) evaluated with and without systematic uncertainties included.

6.2 Significance calculation study

We also test the calculation of the significance on simulation. The significance is computed as the square root of twice the difference between the negative logarithm of the likelihoods (NLL) of the fits on background only samples with signal+background and background pdf:

$$S = \sqrt{2 \cdot (NLL_{signal+bkg} - NLL_{bkg})} \tag{6.5}$$

More in detail, the signal+background fit is performed first and $NLL_{signal+bkg}$ is computed. Then, NLL_{bkg} is evaluated setting the signal strength obtained in the previous step to zero and re-computing NLL. Figure 6.7 shows the significance, multiplied by the sign of the signal yield, obtained allowing negative signal yields (left) and the significance obtained allowing only positive signal yields (right), for the different MLPs, as consistency check. The highest signal yield is 3.02 in both cases. Negative signal yields do not make sense physically, but they allow to avoid bias.

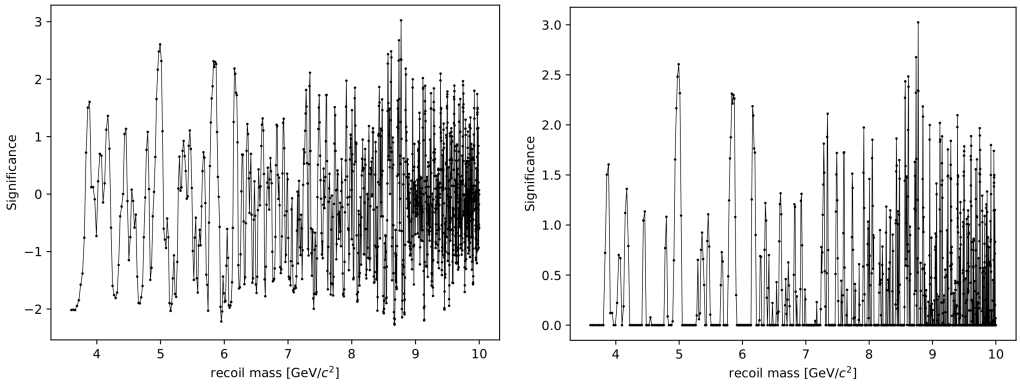

Figure 6.7 Significance obtained allowing negative (left) and only positive (right) signal yields. The significance is considered negative when the signal yield returned for the fit is negative. The two cases are consistent.

6.3 Look-elsewhere effect (LEE) study

Since we search for a signal of a Z' with unknown mass, the significance of observing a local excess from background fluctuations anywhere in the search range must be taken into account to get the global significance. We approximate the global p-value p_{global} in the asymptotic limit by introducing trial factor, which is the ratio between the probability of observing the excess at some fixed Z' mass point, to the probability of observing it anywhere in the range [111]:

$$N_{trial} = 1 + \frac{1}{p_{local}} \left\langle n_{up} \left\langle Z_{test} \right\rangle \right\rangle e^{\frac{Z^2_{test} - Z^2_{local}}{2}} \tag{6.6}$$

where $\langle n_{up}\langle Z_{test}\rangle\rangle$ is the average number of times where the significance Z is larger than a reference significance Z_{test} determined using multiple background-only MC samples. The global significance is given by

$$p_{global} = p_{local} + \langle n_{up}\langle Z_{test}\rangle\rangle e^{\frac{Z_{test}^2 - Z_{local}^2}{2}} \tag{6.7}$$

The number of up-crossings $n_{up}\langle Z_{test}\rangle$ can be determined with good accuracy using a rather small test significance of e.g. 1σ.
We implement the LEE study with a toyMC technique, using the bootstrap method to generate 1000 different toy background distributions starting from the realistic one we get from MC, normalized to a luminosity of 80 fb^{-1}. For each toy distribution, we scan the mass performing 2385 fits with steps of 0.5σ, and compute the number of upcrossings for each toy. We allow negative signal yields and define a negative significance in those cases. From the distribution of the number of upcrossing, using a significance test of 1σ, we obtain $\langle n_{up}\langle Z_{test}\rangle\rangle$. Figure 6.8 shows the distribution of the number of upcrossings. The mean value is $n_{up}\langle Z_{test}\rangle = 69.96$. For a local $p_{local} \sim 3\cdot 10^{-7}$, corresponding to a 5σ significance, we obtain:

- $N_{trial} = 1433$
- $p_{global} = 0.00043$, corresponding to a significance of 3.33σ

To get a 5σ global significance, we need to observe a local significance of 6.3σ.

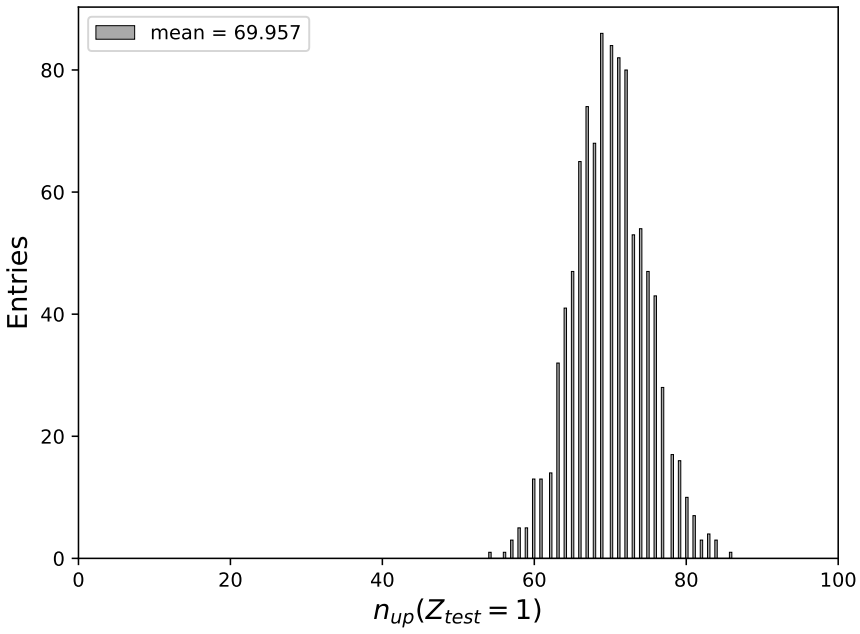

Figure 6.8 Distribution of the upcrossings considering $Z_{test} = 1$.

6.4 Partial data unhiding

The results shown below are still not approved by the *Belle II* collaboration, since the internal review of the analysis is still ongoing. We measure the 90% confidence level upper limits using 5.47 fb^{-1} of data, that allows to test the whole analysis procedure on data and gives us a preliminary result on what it will be possible to obtain from this measurement performing the measurement wth higher luminosity.

Data-MC comparison before the application of the MLP We apply the final event selection and we also require events with $M_{\mu\mu} > 2$ GeV/c^2, which is necessary to remove a large part of hadronic structures, which are not well reproduced in MC.
Figure 6.9 shows that the data-MC agreement in the interesting region, $3.6 < M_{recoil} < 8.5$ GeV/c^2 is reasonable without applying the MLP selection.

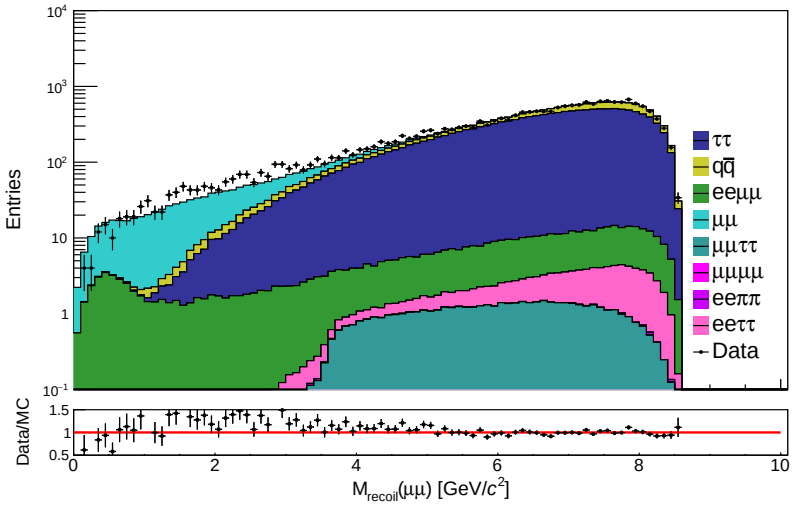

Figure 6.9 Data/MC comparison for the recoil mass calculated with respect to the dimuon.

Data-MC comparison after the MLP selection Figure 6.10 shows the data/MC comparison of the recoil mass distribution for the 10% data unhided, after the MLP selection. The plot shows that data is more or less two times higher than MC, this can be explained by the fact that we have missing components, like $\mu\mu\pi\pi$ that is not available at the moment, and by some differences between simulation and data, like the ISR effect that it is not simulated in many contributing processes: $ee\mu\mu$, $ee\pi\pi$, $\mu\mu\mu\mu$, $\mu\mu\tau\tau$ and $ee\tau\tau$. For example, $ee\mu\mu$ and $\mu\mu\mu\mu$ components close to the $\Upsilon(4S)$ resonance and, being the ISR effect not simulated, we expect an excess of MC events on the $\Upsilon(4S)$ that we remove selecting $M < 9.5$ GeV/c^2, while an excess of data is expected below this cut.
One can also suppose that the contribution is due to hadronic resonances, however, if so, the excess of data would be concentrated only for recoil mass higher than 8.5 GeV/c^2, and it is not case. The excess is not removed applying the cut $M > 2$ GeV/c^2, the same

applied for the data-MC comparison with control samples, and the excess of data for $M_{recoil} > 8.5$ GeV/c^2 seems to be similar to the rest of the distribution. As a consequence, we can deduce that the MLP selection remove entirely, or at least for the most part, the hadronic resonances present before the application of MLP selection for $M < 2$ GeV/c^2 ($M_{recoil} > 8.5$ GeV/c^2). Also, requiring $\mu ID > 0.95$ for the two tagging muons does not remove the excess of data, so we conclude that it is not due to contamination from $\pi\pi$ events. Additional studies are needed to better understand the discrepancy observed, but it is worth to remember here that we will measure the background directly with the fit. Of course, the excess will reduce our sensitivity to the cross section by a factor $\sim 1/\sqrt{2}$ with respect to what estimated from MC studies.

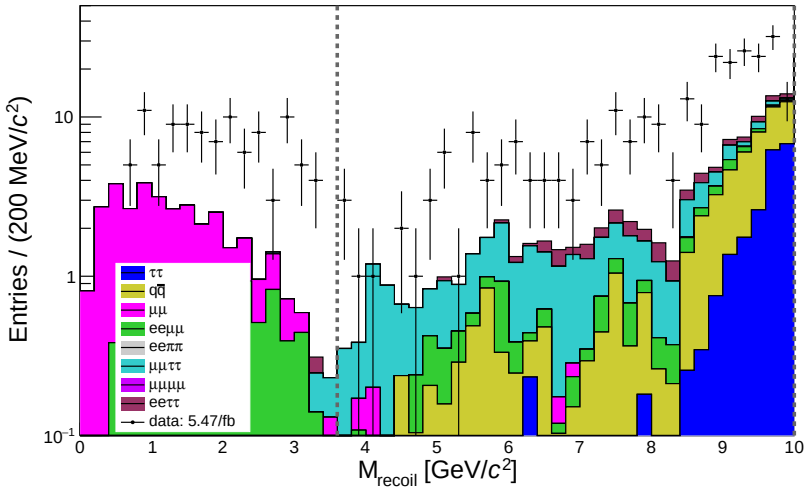

Figure 6.10 Recoil mass distribution for 10% data unhided compared with the different MC components.

Figure 6.11 show the 90% *CL* upper limits respectively on cross section of the process (up) and g' (down) measured on 10% data unhided (5.47 fb^{-1}), extracted as explained in Chapter 6. In particular, plots show the expected upper limits in dashed black line, the observed upper limits in black points, the $\pm 1\sigma$ and $\pm 2\sigma$ bands.
Figure 6.12 shows the significance distribution as a function of the Z' mass, obtained from the fit scan, (left) and the fit of that particular mass point for which we get the highest significance. The highest significance obtained is 3.26, corresponding to a local p-value of $p_{local} \sim 5.4 \times 10^{-4}$, for a mass of 5.5655 GeV/c^2. Assuming that the LEE effect factor obtained from MC studies for 80 fb^{-1} in Section 6.3 is valid also for 5.47 fb^{-1}, the observed local p-value correspond to a $p_{global} \sim 0.57$, that indicates a statistical fluctuation.

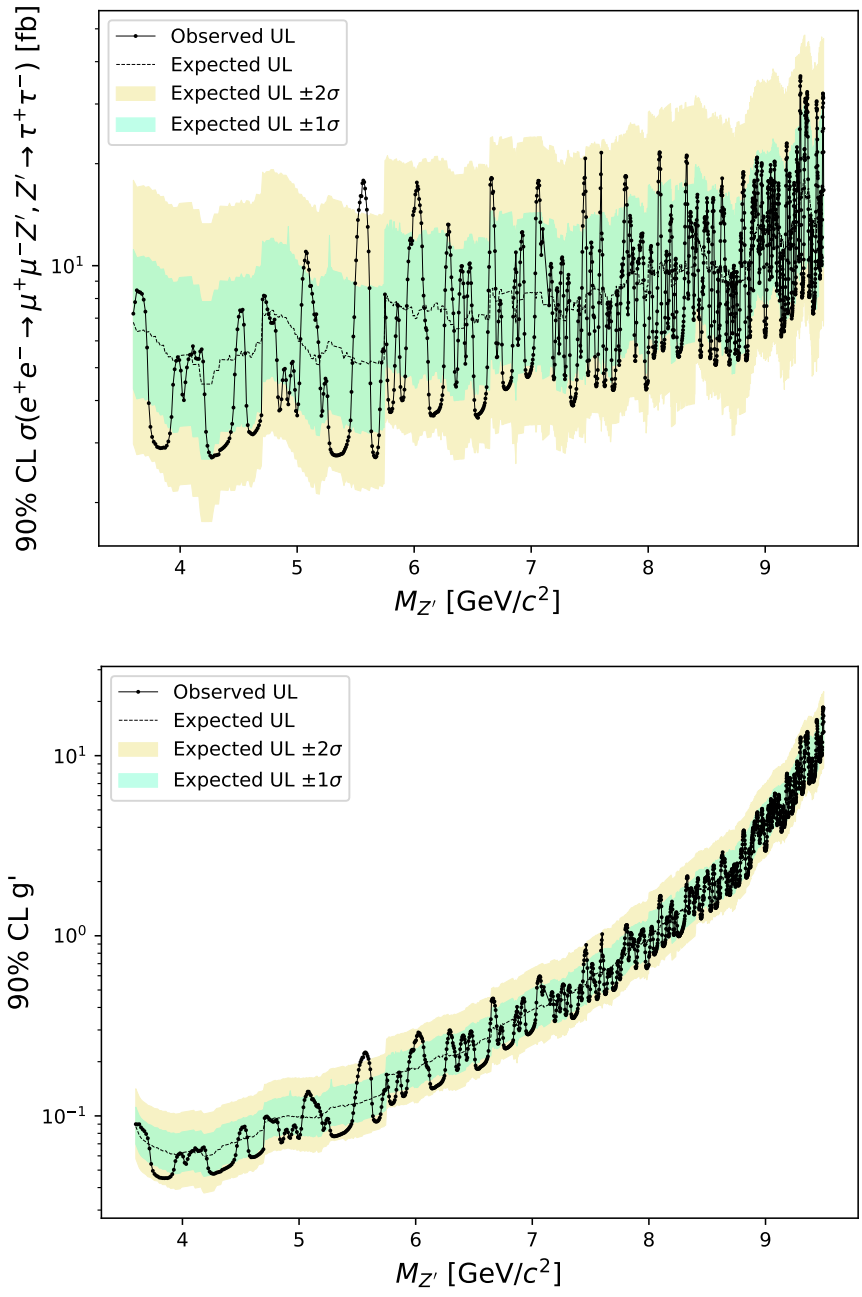

Figure 6.11 90% *CL* observed upper limits on the cross section of the process $e^+e^- \to \mu^+\mu^- Z', Z' \to \tau^+\tau^-$ (up) and on the coupling constant of the $L_\mu - L_\tau$ model, g', (down) measured on 5.47 fb^{-1}. The black dashed line shows the median expected upper limits from data, the green and yellow bands are respectively the $\pm 1\sigma$ and $\pm 2\sigma$ intervals for the expected limits under the background-only hypothesis, while black points are the observed upper limits. The measure has been performed applying the CL_s frequentist technique [105].

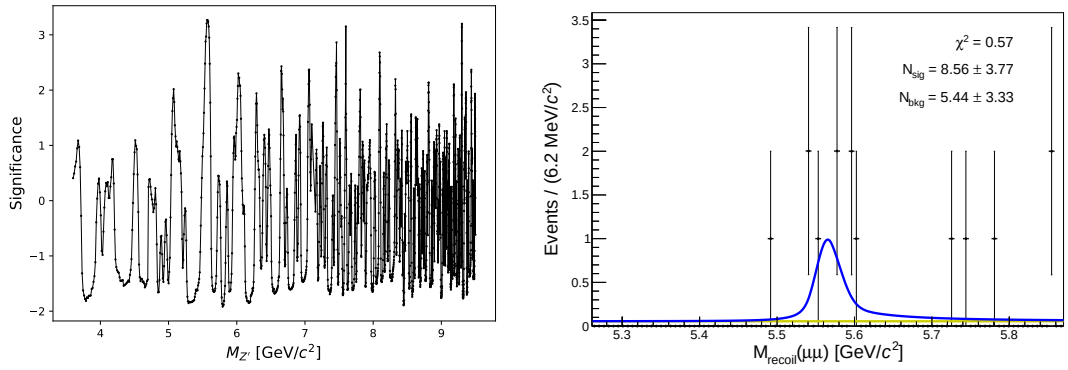

Figure 6.12 Left: Significance as function of the Z' mass obtained from the fit, obtained using 5.47 fb^{-1} of unhided data. Right: Fit of the mass point of 5.5655 GeV/c^2 for the highest significance observed of 3.26 from the fit scan.

We estimate the sensitivity to the coupling constant g' expected for different luminosity by rescaling the result obtained from simulation assuming 80 fb^1 of data: we degrade the result obtained from simulation by a factor $1/sqrt[4]2$, because we observed from data that the background expected in data is a factor ~ 2 higher than MC, and we rescale it by $\sqrt[4]{\mathscr{L}}$. It gives a realistic idea of where *Belle II* can go with this analysis with the current dataset. However, it is possible that the scaling factor for g' is something in between $\sqrt{\mathscr{L}}$ and $\sqrt[4]{\mathscr{L}}$, or it goes more like $\sqrt{\mathscr{L}}$ in some regions of the recoil mass spectrum (where background is very low) and $\sqrt[4]{\mathscr{L}}$ in others (where background is higher). the plot in Figure 6.13 shows several elements, so let has briefly list them here:

- Excluded region by previous measurement: 90% *CL* exclusion region from $Z' \to$ *inv.* analysis performed by *Belle II* with 0.276 fb^{-1} [57], 90% *CL* exclusion region from $Z' \to \mu\mu$ performed by *BABAR* with 514 fb^{-1} [59], *Belle* with 643 fb^{-1} and constraints estimated from Trident production [110];
- preliminary 90% *CL* sensitivity estimated from simulation using 80 fb^{-1} with the analysis discussed in this thesis (see Chapter 6 and Figure 6.4)
- preliminary 90% *CL* upper limits measured with 5.47 fb^{-1};
- 90% *CL* upper limits estimated with 80 fb^{-1} from simulation rescaled to 267 fb^{-1}, which correspond to the current full dataset of *Belle II*;
- the parameter space $(g', M_{Z'})$ that can explain the $(g-2)_\mu$.

We observe that using the full dataset collected with *Belle II* up to now (267 fb^{-1}) we will obtain the best results for this search but we still do not reach the upper limits on g' of the $L_\mu - L_\tau$ model set by *BABAR*, that used almost double the statistic, and *Belle*, that used 2.4 times the statistic.

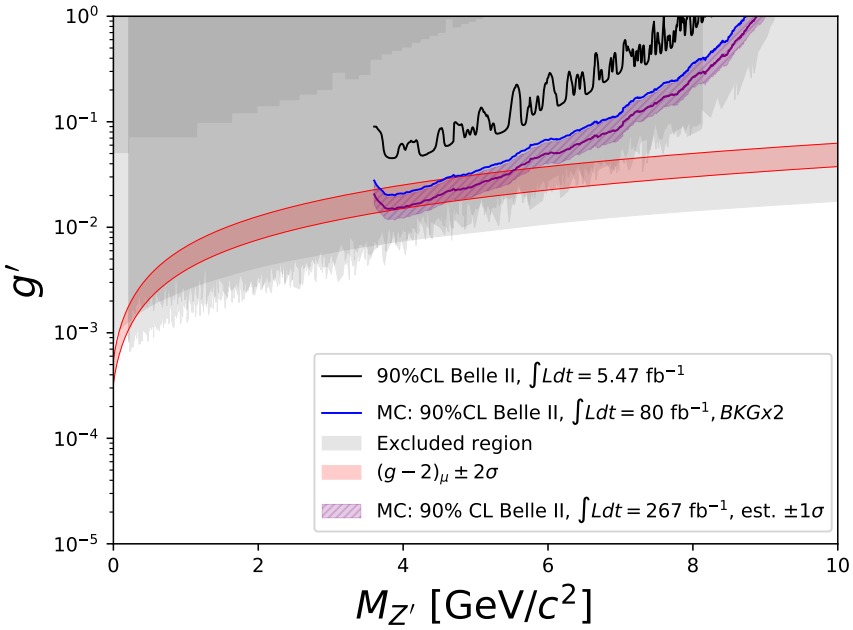

Figure 6.13 Preliminary 90% *CL* upper limits on g' for the $L_\mu - L_\tau$ model observed with 5.47 fb^{-1} at *Belle II* (black solid line) and estimated from simulation assuming 80 fb^{-1}, taking into account that in data we might have two times the background expected from simulation. The sensitivity estimated from simulation is rescaled at 267 fb^{-1} $\pm 1\sigma$ (purple band). In grey the excluded region from *BABAR* [59], *Belle* [60] ($Z' \to \mu\mu$), *Belle II* [57] ($Z' \to$ *inv.*) and the constraints from Trident production [110] is shown. The red band shows the phase space that can explain the $(g-2)_\mu$.

Conclusions and future prospects

In this thesis work, the analysis performed to search for a light dark mediator Z' decaying to a $\tau\tau$-pair in the process $e^+e^- \to \mu^+\mu^- Z', Z' \to \tau^+\tau^-$ has been presented. The analysis is based on Monte Carlo (MC) simulation to estimate the sensitivity to the coupling constant of Z' to leptons, g', as a function of the Z' mass, $M_{Z'}$, for a given integrated luminosity at *Belle II*.

At the time of writing this thesis, the analysis is meant to be performed on 54.7 fb^{-1} collected at $\Upsilon(4S)$ resonance at *Belle II* in the first half of 2020 (2020a-b, see Table 2.4). The original plan was to use the dataset collected at $\Upsilon(4S)$ in 2019 and throughout 2020 on $\Upsilon(4S)$, corresponding to $\sim$80 fb^{-1} in total. However, we do not include data collected in 2019 ($\sim$ 8.6 fb^{-1}), to avoid possible additional discrepancies mainly due to trigger lines used in the analysis that were not fully available in the 2019 dataset, and data collected at the end of 2020 ($\sim$ 16.4 fb^{-1} collected in 2020c), that have been processed with a different software release with respect to the one used to produce the official MC that we use (the only available during most of the period of the analysis). Moreover, we do not use data collected off-resonance because we can not validate the analysis on them (MC does not exist for off-resonance).
The analysis has yet to be approved internally by the *Belle II* collaboration, so we presented a preliminary 90% confidence level (*CL*) upper limits on g' measured using 10% data unhided, corresponding to 5.47 fb^{-1}. The result shown has not yet been approved and it can be shown only within this thesis work.
The Z' discussed in the thesis is introduced in the $L_\mu - L_\tau$ model, which is a theoretically and experimentally well motivated model that extends the Standard Model with an additional symmetry that preserves the difference between the leptonic number of the muon and tauon, therefore it is a theory free of gauge anomalies and renormalizable. Z' boson couples only with muons and tauons through a coupling constant with leptons, g', and it could explain the dark matter relic abundance in the Universe as well the $(g-2)_\mu$ anomaly for a coupling constant $g' \sim 10^{-4} - 10^{-3}$ and for a Z' mass in the range MeV/c^2-GeV/c^2 [21]. Furthermore, recent experimental results, already mentioned in the thesis, showed the phenomenology introduced by this model as a possible explanation for some tensions between the measurements obtained and the Standard Model prediction.
As discussed in the thesis, main motivations for this search include:

- currently, no experimental results for the search for a $Z' \to \tau\tau$ resonance recoiling against a muon pair in $\mu\mu\tau\tau$ final state exist;
- it can be considered a benchmark model with the possibility to reinterpret the results found for the Z' boson of the $L_\mu - L_\tau$ in other models, and in particular those with $\tau\tau$ resonance in a $\mu\mu\tau\tau$ final state (like axion-like particles and leptophilic dark scalars).

About the analysis, we presented:

- an extensive study of the background reduction based on neural network, the Multi-Layer Perceptron (MLP) method of the Multivariate Analysis (MVA). The MLP

uses 14 discriminating variables, deeply presented in the thesis. The selection criteria have been optimized, based on the Punzi figure of merit (Punzi-FOM) variable, for each 1 GeV-wide bin of $M_{Z'}$ used in the training of the MVA. The signal efficiency after the MLP selection ranges from 2.5%, at $M_{Z'} = 10$ GeV/c^2 to 13%, at $M_{Z'} = 3.6$ GeV/c^2, with at maximum efficiency of 15% at $M_{Z'}$ around 5.5 GeV/c^2;

- the signal modeling as the weighted sum of two Crystal Ball distributions and the signal yield extraction through a fit procedure have been tested. In particular, the strategy consists of performing a fit scan of 2385 with steps of half Z' mass resolution, σ_{peak}, over the recoil mass distribution calculated with respect to the recoil $\mu\mu$-pair;

- the data validation performed using two control samples, the $\pi^+\pi^-\tau^+\tau^-$ (CS1) and the $\mu^+\mu^-\tau^+\tau^-$ with $M_{recoil} < 3.4$ GeV/c^2 (CS2). In the thesis, particularly, we presented the study performed with CS1, while the study performed with CS2 is discussed in the Appendix A. For the analysis we use the logical OR between *fff* and CDCKLM trigger lines: to perform data validation we use the CDCKLM trigger efficiency study performed internally at *Belle II*, while we measure the *fff* trigger efficiency, since the trigger simulation is not available in MC. The study on *fff* trigger line is fully presented in the thesis. In general we observe a reasonable agreement between data and MC. Some differences could be explained by the missing model in MC, rather than the simulation itself.

- the studies on systematic uncertainties. The main sources are: MLP selection, particle ID selection, fit procedure and trigger selection. Systematics depend a little on Z' mass, and in general they amount at $\mathcal{O}(10\%)$;

- the expected 90% *CL* upper limits estimated from simulation assuming 80 fb^{-1}, with systematic uncertainties included, using CL_s frequentist technique;

- preliminary 10% data unhiding.

From simulation, we estimate that with 80 fb^{-1} of data we are sensitive up to $\sigma_{90\%CL} \sim 0.4$ fb and $g' \sim 1.67 \times 10^{-2}$. From the measurement performed with 5.47 fb^{-1}, we exclude the region above to $\sigma_{90\%CL} \sim 2.72$ fb and $g' \sim 4.5 \times 10^{-2}$. The result on the $L_\mu - L_\tau$ obtained with the dataset considered is not competitive with the existing constraints to the model. However, the analysis would be interesting because it is a first time search that can open the possibility to reinterpret the results in different theoretical models with a similar phenomenology. In fact, as already discussed, we will be sensitive also to different models with $\tau\tau$ resonances in $\mu\mu\tau\tau$ final state.
For what concerns the publication of the analysis, currently there are two viable ways under discussion inside the collaboration:

1) publish the analysis with $\sim$200 fb^{-1} collected up to mid 2021 (2019, 2020a-b-c, 2021a-b, see Table 2.4);

2) publish the analysis adding data collected in 2019 to the dataset presented in this thesis, reaching $\sim$63 fb^{-1} in total. This opens the possibility to produce an update

of the analysis with the full dataset collected up to Summer 2022 (almost 400 fb^{-1} in total) during the long shutdown in 2023 (see Section 2.4);

To include 2019 data, it is necessary to check carefully the efficiency of the trigger lines used in the analysis, for those data, that can introduce larger discrepancies. It requires few additional checks on data-MC comparison and systematic uncertainties.
To include data collected in 2020c and 2021a-b, it is necessary to move the analysis on the new software release. It requires to:

- run the analysis on the new official MC campaign based on the new software release used to process data until 2021a-b: it requires also to re-train the MVA using the new MC;
- produce the CDCKLM and *fff* trigger efficiencies using the full dataset.

For the sake of completeness, in order to use data collected at the end of 2021 (2021c) it is necessary to wait for the reprocessing of data and the next official MC campaign that will be both produced with the software release used to collect data in 2021c.
For what concerns a possible update of the analysis with the full dataset collected up to Summer 2022, the advantages regard the possibility to produce the best possible results for this analysis in a relatively short time (in 2023), and to be more sensitive in the case of an existing new $\tau^+\tau^-$ resonance still undiscovered. Moreover, there is still margin of improvement due to the presence of $e^+e^- \to \mu^+\mu^-\tau^+\tau^-$, $e^+e^- \to e^+e^-\tau^+\tau^-$ and $e^+e^- \to \mu^+\mu^-\mu^+\mu^-$ background components that could be rejected introducing them in the MVA training, that could be considered for the update.

In conclusion, in this thesis we presented the search for a light Z' boson of the $L_\mu - L_\tau$ model through the process $e^+e^- \to \mu^+\mu^- Z', Z' \to \tau^+\tau^-$. If no signal will be observed, the analysis will allow to measure the 90% *CL* upper limits on the cross section of the process and to constrain the $L_\mu - L_\tau$ model. The process analyzed has never been studied before in other experiments, and the analysis presented, based on 54.7 fb^{-1}, is currently under internal review. Although, with the dataset considered, we are not competitive with the existing limits for what concerns the $L_\mu - L_\tau$ model, the result would be very interesting both because it is a first time search and because there is the possibility to extend the result to different models that foresee a $\tau\tau$ resonance in $\mu\mu\tau\tau$ final state.
For this thesis work we finalized the analysis procedure and estimated the sensitivity for this search on simulation, assuming 80 fb^{-1} of data. We also performed the measurement using 5.47 fb^{-1}, yet to be approved by the collaboration, for this thesis only.

Appendices

A. Data-MC comparison: supplementary plots

In this appendix we present some additional plots about data-MC comparison for both control sample described in Chapter 5. In particular, we show the comparison for discriminant variables used in the MVA that are described in Chapter 3.

A.1 Control sample $\pi^+\pi^-\tau^+\tau^-$

We require *fff* trigger on data and we rescale MC using the *fff* trigger efficiencies. As a reminder of what described in Chapter 5, we apply the following selection:

- $\pi ID > 0.5$ for the two tagging pions;
- $\mu ID > 0.5$ OR $eID > 0.5$ OR $(1 - \mu ID - eID) > 0.5$ for the other two tracks in the event (also named τ-daughters);
- $M < 9.5$ GeV/c^2, the standard pre-selection;
- $M_{\pi\pi} > 2$ GeV/c^2. This selection proved to be necessary to remove a large part of hadronic structures, which dominate and are not reproduced (or are completely missing) in MC.

We used 54.7 fb^{-1} of data collected at the $\Upsilon(4S)$ resonance, and 100/fb of MC.
Figures A.1 shows the data/MC comparison for the dipion mass and the invariant mass of the four tracks in the event, respectively. The main contributions are $q\bar{q}$ and $\tau\tau$ processes, while other contributions are negligible.

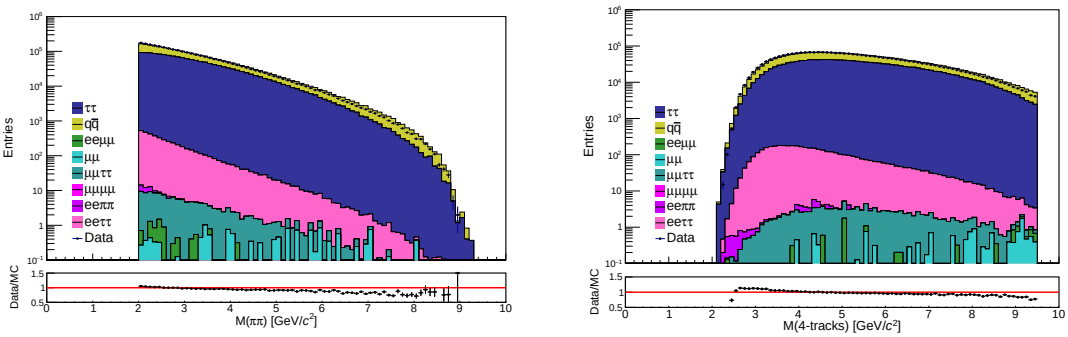

Figure A.1 Data/MC comparison for the invariant mass of the dipion (left) and the invariant mass of the four tracks in the event (right).

Figures A.2-A.4 show the comparison data-MC for the control sample $\pi^+\pi^-\tau^+\tau^-$ for the discriminant variables sensitive to the presence of a resonance in the recoil system.
Figures A.5-A.8 show the comparison data-MC for the same control sample for the discriminant variables sensitive to the presence of a $\tau\tau$-pair in the recoil system.

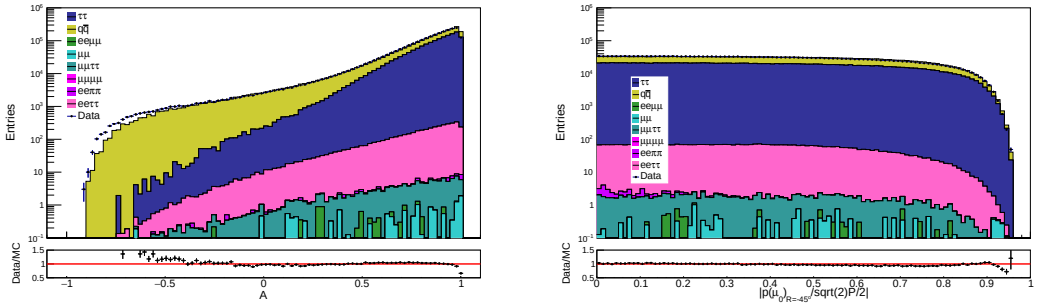

Figure A.2 Data/MC for the discriminant variable A (left) and $p(\mu_0)_{R=45^o}(\sqrt{2}/2 \cdot P)|$ (right).

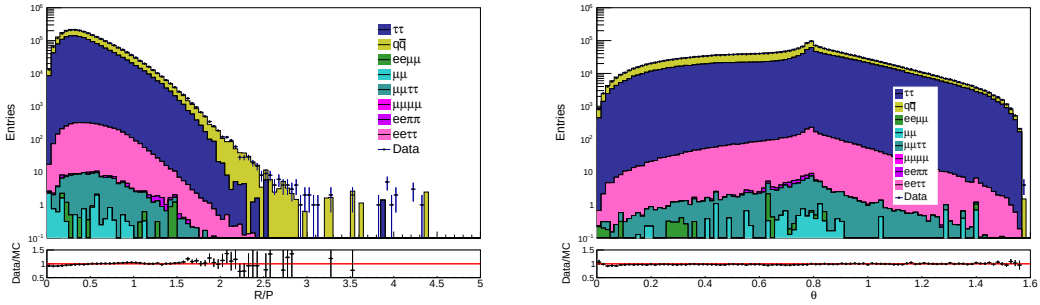

Figure A.3 Data/MC for the discriminant variable R/P (left) and θ (right).

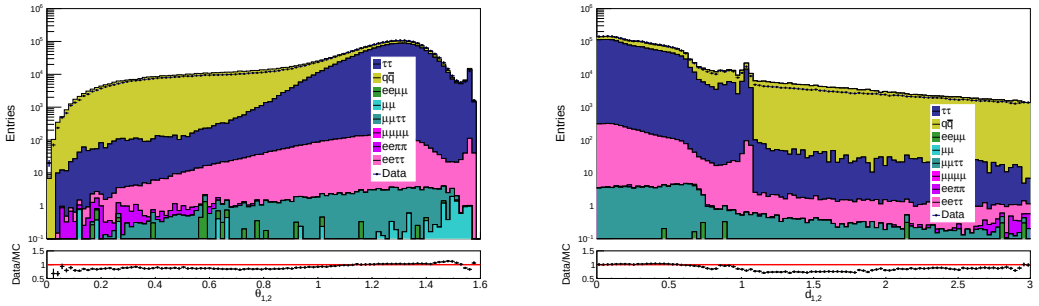

Figure A.4 Data/MC for the discriminant variable $\theta_{1,2}$ (left) and $d12_{1,2}$ (right).

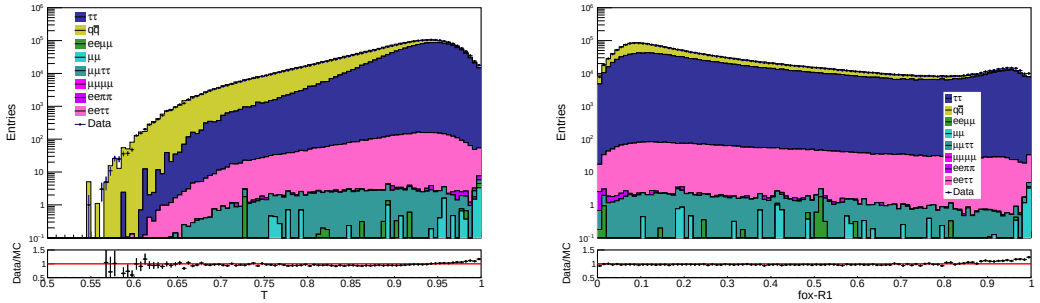

Figure A.5 Data/MC for the thrust T (left) and fox-R1 (right).

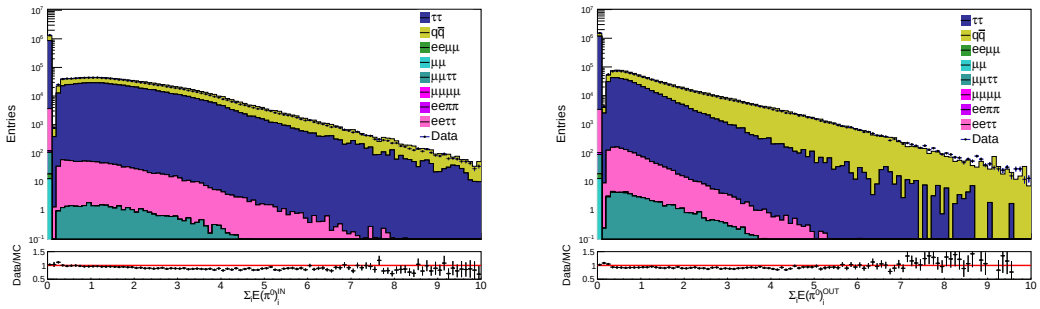

Figure A.6 Data/MC for the discriminant variable $\Sigma_{i=0}^{n_{\pi^0}} E_i(\pi^0)_{IN}^{CMS}$ (left) and $\Sigma_{i=0}^{n_{\pi^0}} E_i(\pi^0)_{OUT}^{CMS}$ (right).

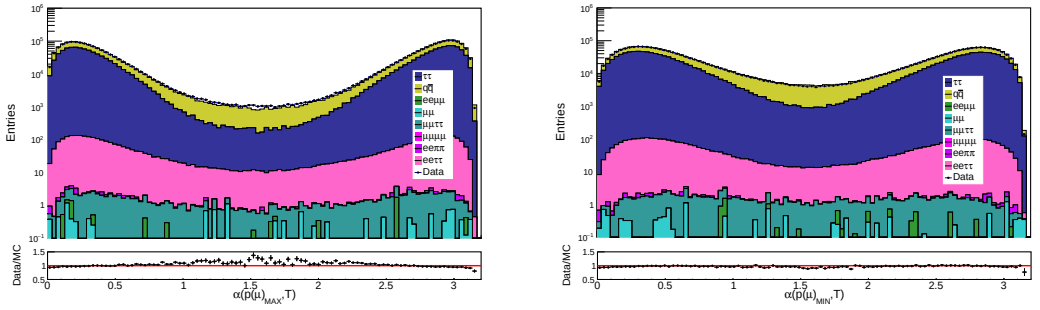

Figure A.7 Data/MC for the discriminant variable $\alpha(p(\mu)_{max}, \overrightarrow{n}_T)$ (left) and $\alpha(p(\mu)_{min}, \overrightarrow{n}_T)$ (right).

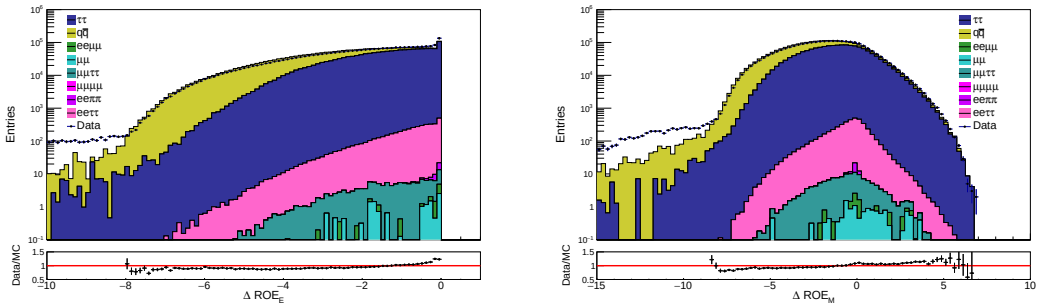

Figure A.8 Data/MC for the discriminant variable ΔROE_E (left) and ΔROE_M (right).

A.2 Control sample $\mu^+\mu^-\tau^+\tau^-$, with $M_{recoil} < 3.4$ GeV/c^2

The data/MC comparison is here limited to a small region of the recoil mass distribution. Moreover, with this control sample we are outside the signal region and consequently outside the region of application of the MLPs, since the first training range starts at 3.6 GeV/c^2, so it does not make sense to check the performance of the MLPs with this control sample.
We require *fff*-OR-CDCKLM trigger on data and we rescale MC using the *fff*-OR-CDCKLM trigger efficiencies. In this case the CDKLM trigger efficiencies are reliable because there are the two tagging muons. We apply the following selection:

- $\mu ID > 0.5$ for the two tagging muons;
- $\mu ID > 0.5$ OR $eID > 0.5$ OR $(1 - \mu ID - eID) > 0.5$ for the other two tracks in the event (also named τ-daughters);
- $M < 9.5$ GeV/c^2, the standard pre-selection;
- $M_{\mu\mu} > 2$ GeV/c^2. This selection proved to be necessary to remove a large part of hadronic structures, which dominate and are not reproduced (or are completely missing) in MC.

For this study we used 54.7 fb^{-1} of data collected at the $\Upsilon(4S)$ resonance, and 500 fb^{-1} of MC13a for all background components.
Figure A.9 shows the data/MC comparison respectively for the $\mu\mu$-pair invariant mass (up-left), the recoil mass distribution (up-right) and the invariant mass of the four tracks (down-left). The discrepancies observed are reasonably due to some missing components in MC: for example, in Figure A.9 up-left is possible to observe the presence of the J/ψ resonance, and in Figure A.9 down-left the presence of the $\psi(2S)$ resonance (not included in MC in both cases). Moreover, the $ee\mu\mu$ and $\mu\mu\mu\mu$ processes are generated without ISR contribution. The radiative tail of $\mu\mu\mu\mu$ events, for example, is not simulated, and causes an excess of MC at the $\Upsilon(4S)$, removed by the preselection $M < 9.5$ GeV/c^2, and an excess of data just below this cut, which is in fact observed in Figure A.9 down-left.

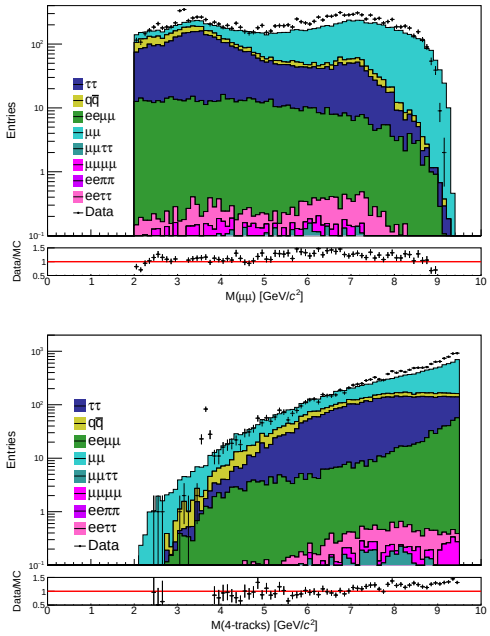

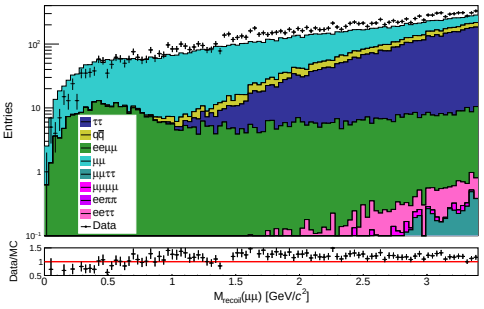

Figure A.9 Data/MC comparison for the invariant mass of the dimuon (up-left), for the recoil mass calculated with respect to the dimuon (up-right) and for the invariant mass of the four tracks in the event (down-left).

Additionally, other missing components are $\mu\mu\pi\pi$ and, at the moment. Figures A.10-A.12 show the comparison data-MC for the control sample $\pi^+\pi^-\tau^+\tau^-$ for the discriminant variables sensitive to the presence of a resonance in the recoil system. Figures A.13-A.16

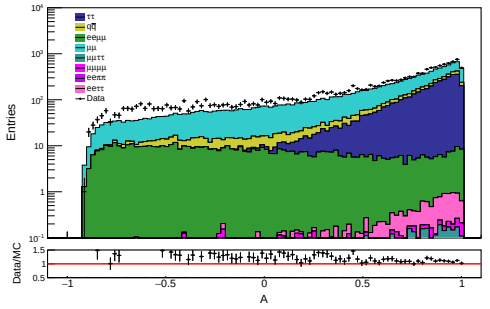

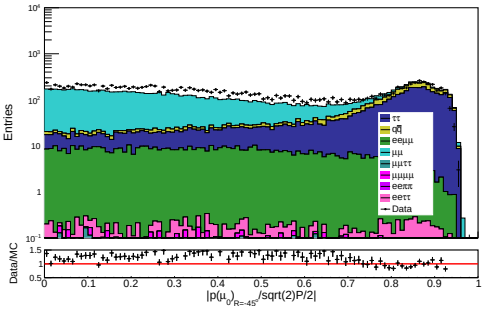

Figure A.10 Data/MC for the discriminant variable A (left) and $p(\mu_0)_{R=45^o}(\sqrt{2}/2 \cdot P)|$ (right).

show the comparison data-MC for the same control sample for the discriminant variables sensitive to the presence of a $\tau\tau$-pair in the recoil system.

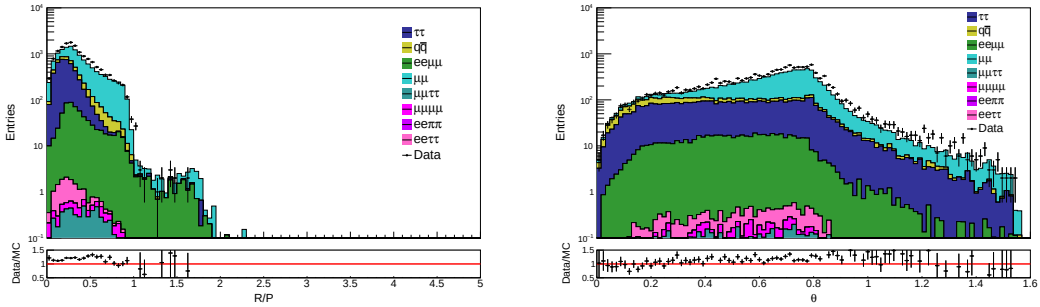

Figure A.11 Data/MC for the discriminant variable R/P (left) and θ (right).

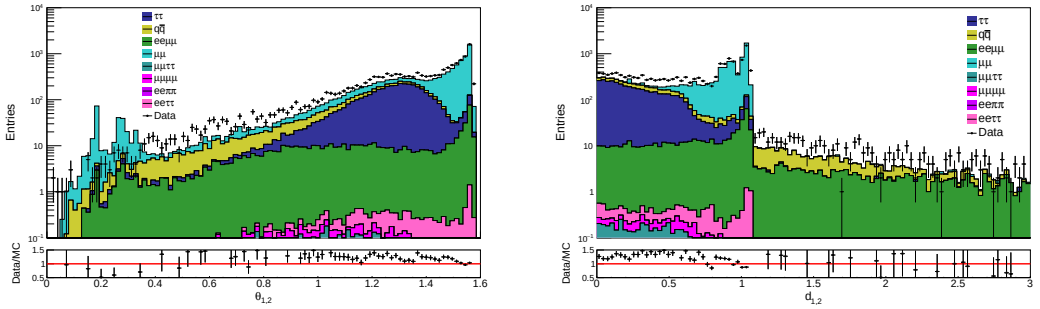

Figure A.12 Data/MC for the discriminant variable $\theta_{1,2}$ (left) and $d_{1,2}$ (right).

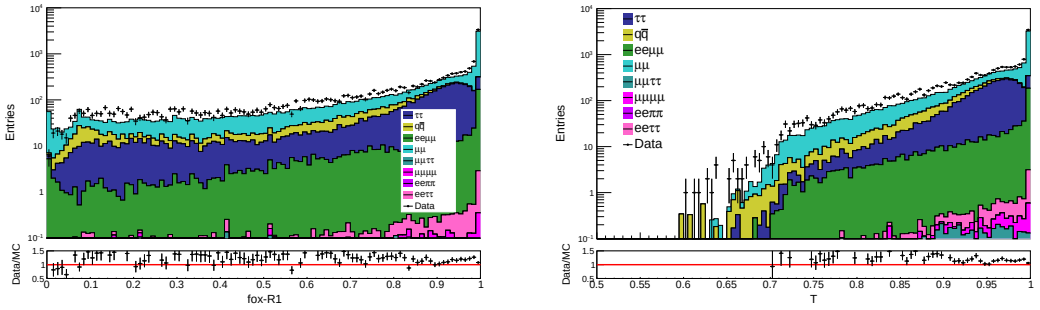

Figure A.13 Data/MC for the thrust T (left) and fox-R1 (right).

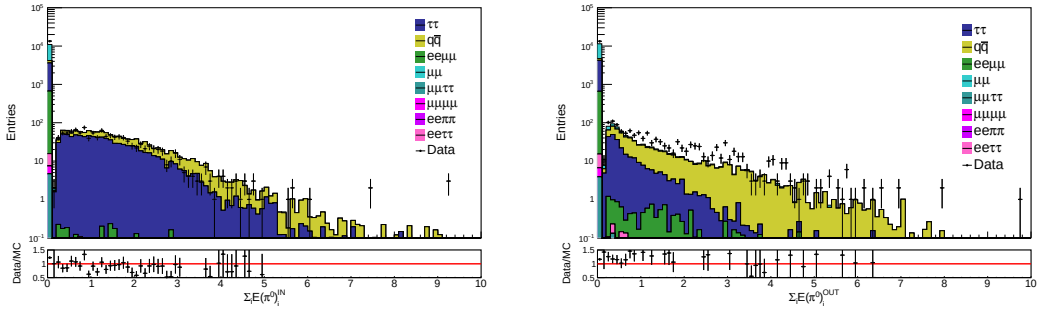

Figure A.14 Data/MC for the discriminant variable $\Sigma_{i=0}^{n_{\pi^0}} E_i(\pi^0)_{IN}^{CMS}$ (left) and $\Sigma_{i=0}^{n_{\pi^0}} E_i(\pi^0)_{OUT}^{CMS}$ (right).

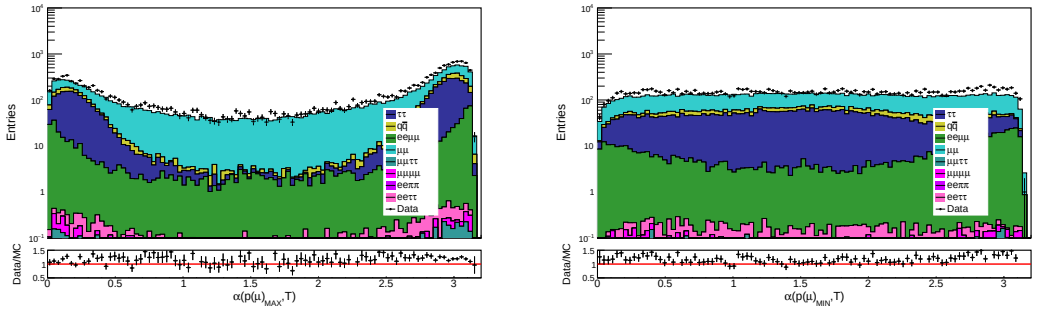

Figure A.15 Data/MC for the discriminant variable $\alpha(p(\mu)_{max}, \overrightarrow{n}_T)$ (left) and $\alpha(p(\mu)_{min}, \overrightarrow{n}_T)$ (right).

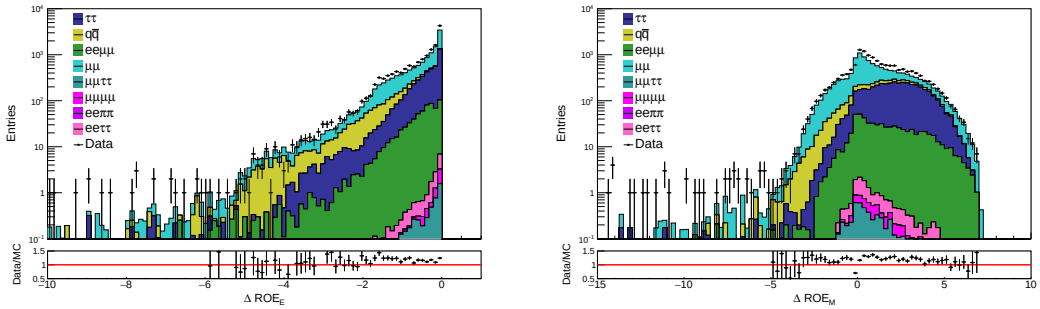

Figure A.16 Data/MC for the discriminant variable ΔROE_E (left) and ΔROE_M (right).

A.3 10% data unhiding

We require *fff*-OR-CDCKLM trigger on data and we rescale MC using the *fff*-OR-CDCKLM trigger efficiencies. Just as a reminder, we apply the following selection:

- $\mu ID > 0.5$ for the two tagging muons;
- $\mu ID > 0.5$ OR $eID > 0.5$ OR $(1 - \mu ID - eID) > 0.5$ for the other two tracks in the event (also named τ-daughters);
- $M < 9.5$ GeV/c^2, the standard pre-selection;
- $M_{\mu\mu} > 2$ GeV/c^2. This selection proved to be necessary to remove a large part of hadronic structures, which dominate and are not reproduced (or are completely missing) in MC.

For this study we used 5.47 fb^{-1} of data collected at the $\Upsilon(4S)$ resonance, and 500 fb^{-1} of MC for all background components.
Figure A.17 shows the data-MC comparison for the invariant mass of the $\mu\mu$-pair and for the invariant mass of the four tracks in the events. Figures A.18-A.20 show the comparison

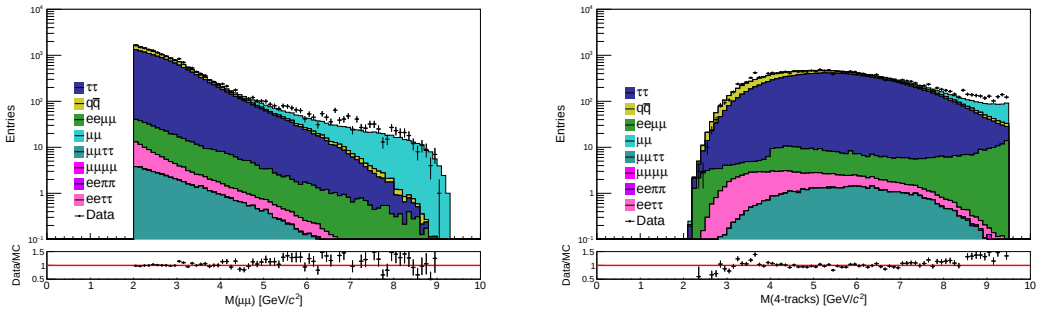

Figure A.17 Data/MC comparison for the invariant mass of the dimuon (left) and for the invariant mass of the four tracks in the event.

data-MC for the discriminant variables sensitive to the presence of a resonance in the recoil system.
Figures A.21-A.24 show the comparison data-MC for the discriminant variables sensitive to the presence of a $\tau\tau$-pair in the recoil system.

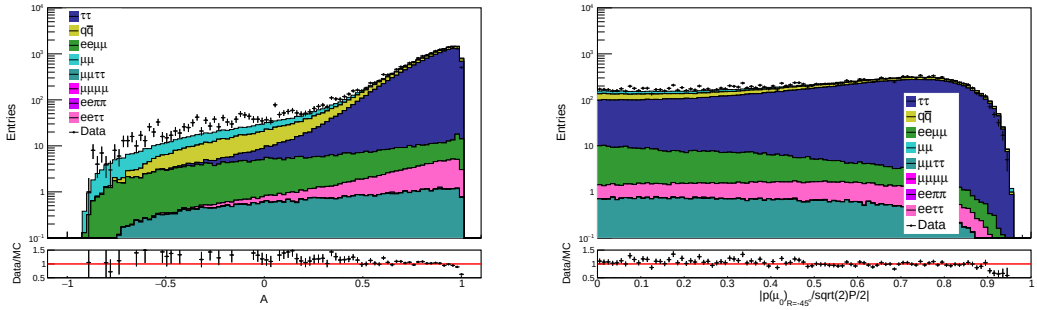

Figure A.18 Data/MC for the discriminant variable A (left) and $p(\mu_0)_{R=45^o}(\sqrt{2}/2 \cdot P)|$ (right).

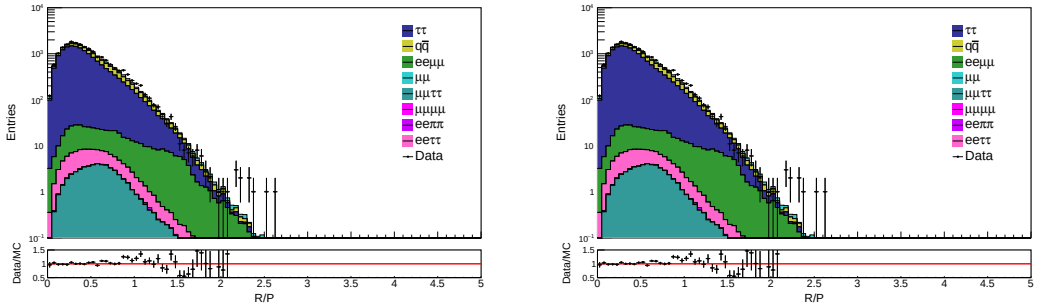

Figure A.19 Data/MC for the discriminant variable R/P (left) and θ (right).

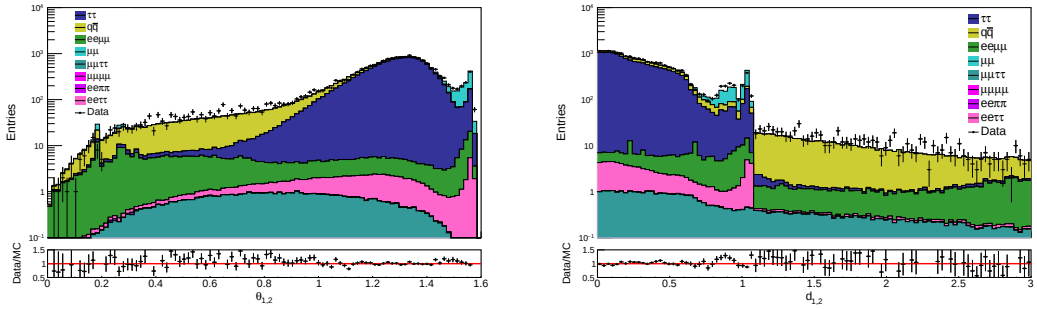

Figure A.20 Data/MC for the discriminant variable $\theta_{1,2}$ (left) and $d_{1,2}$ (right).

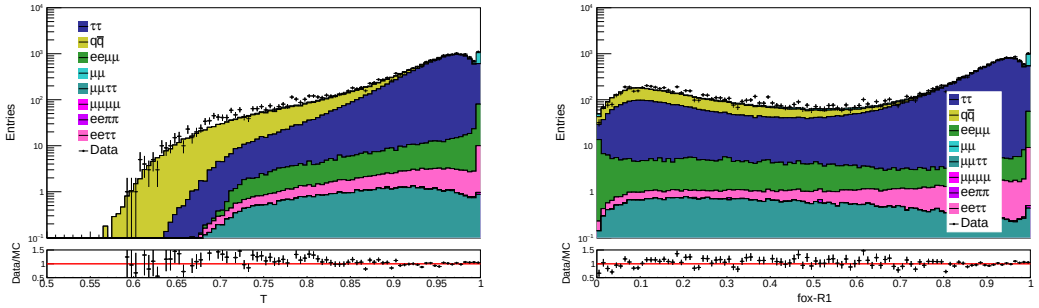

Figure A.21 Data/MC for the thrust T (left) and fox-R1 (right).

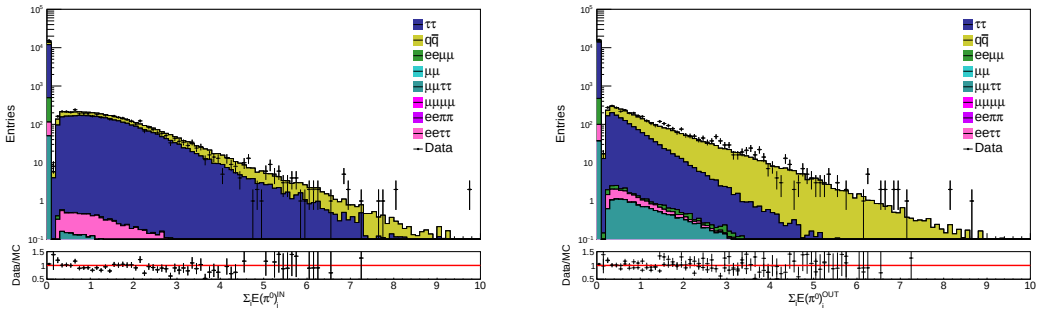

Figure A.22 Data/MC for the discriminant variable $\Sigma_{i=0}^{n_{\pi^0}} E_i(\pi^0)_{IN}^{CMS}$ (left) and $\Sigma_{i=0}^{n_{\pi^0}} E_i(\pi^0)_{OUT}^{CMS}$ (right).

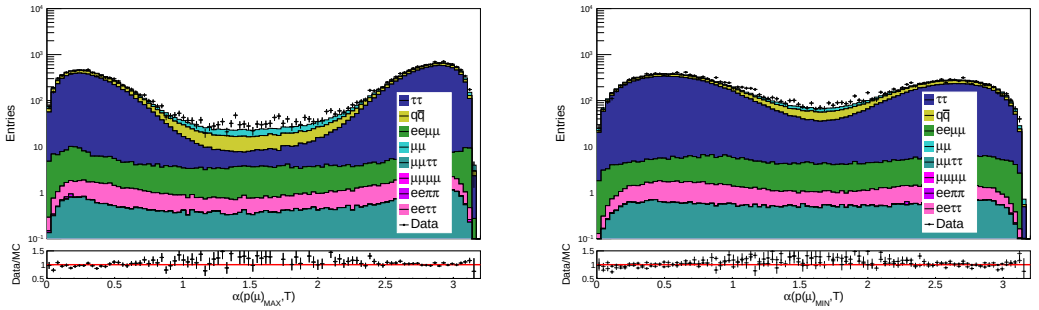

Figure A.23 Data/MC for the discriminant variable $\alpha(p(\mu)_{max}, \overrightarrow{n}_T)$ (left) and $\alpha(p(\mu)_{min}, \overrightarrow{n}_T)$ (right).

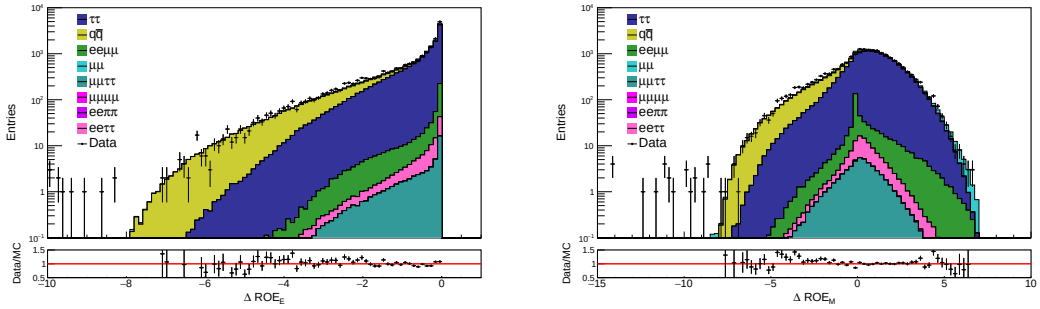

Figure A.24 Data/MC for the discriminant variable ΔROE_E (left) and ΔROE_M (right).

B. MVA supplementary plots and PID studies

In the first paragraph of this appendix we show some additional plots from MVA studies, while some additional studies concerning the MVA background efficiency and selection applied using the particle identification variables are shown in the second and third paragraphs.
For more details on MVA implementation see Chapter 3.

B.1 Supplementary plots from MVA

Figures B.1 and B.2 shows the linear correlation matrix of the discriminant variables for 1 GeV-wide training ranges 6 and 11, that correspond respectively to the training performed on intermediate and high recoil masses: $[8.1, 7.1]$ GeV/c^2 and $[9.1, 7.1]$ GeV/c^2. We observe that correlations between most of variables are different for signal and background. However, as the recoil mass increases, the correlations become more and more similar reducing the performance of MVA. Figures B.3 and B.4 show the ROC curves for

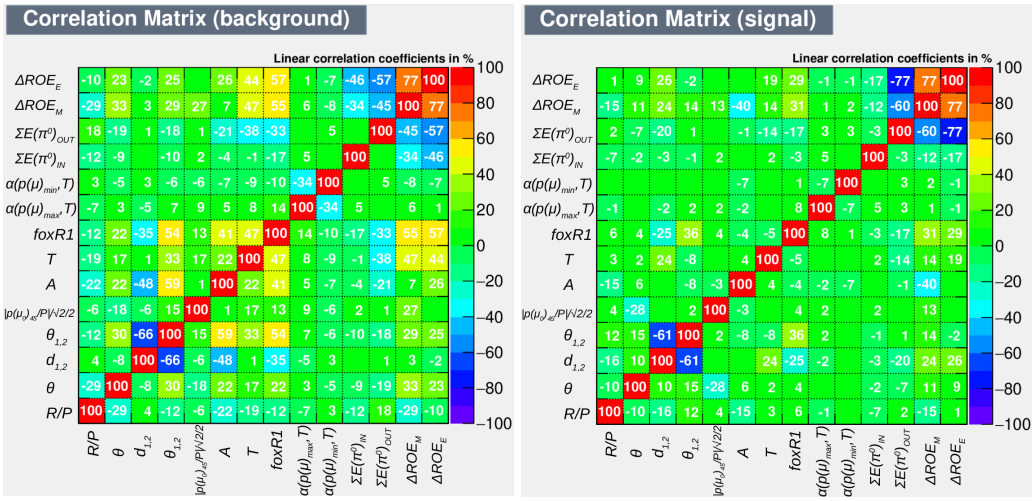

Figure B.1 Linear correlation coefficients for signal (right) and background (left) of the discriminant variables used in the MLP training for the sixth training range: $M_{Z'} = [6.1, 7.1]$ GeV/c^2.

the 1 GeV-wide ranges, where also the two different MVA methods (MLP and BDT) are compared. The plots shown are for training ranges from 5 to 12. For the first four training ranges see Chapter 3.
Figures B.5-B.7 shows the MLP convergence test for the first four 1 GeV-wide ranges. The plots show the convergence of the MLP error function as a function of the number of training cycles (epochs). The distributions reach a plateau and stops to decrease. They give indication that there is no over-training.
Finally, Figures B.8 and B.9 shows the MLP neuron output for the MLP 1 GeV-wide ranges. Again, the training and testing sample are statistically compatible so no sensible

over-training seems to be in force. Plots are for training ranges from 5 to 12, while the first four are shown in Chapter 3.

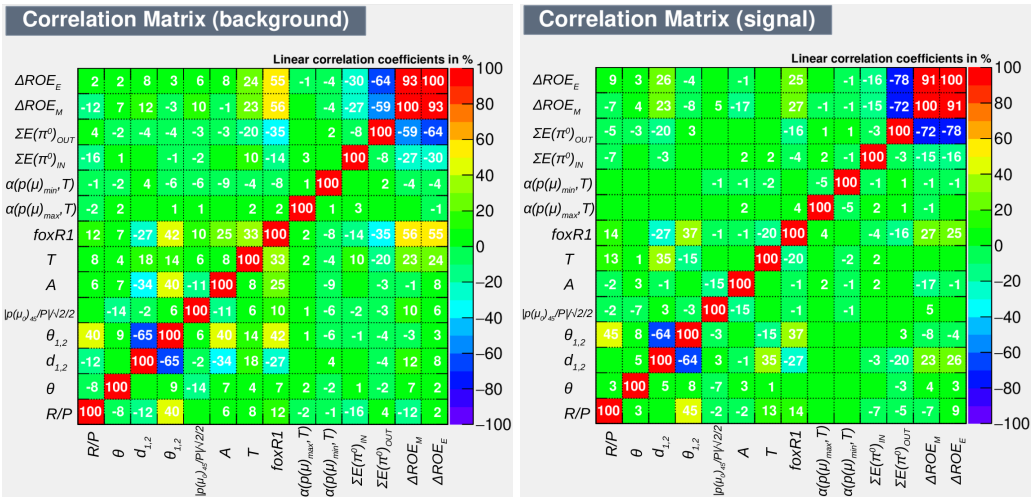

Figure B.2 Linear correlation coefficients for signal (right) and background (left) of the discriminant variables used in the MLP training for the eleventh training range: $M_{Z'} = [8.6, 9.6]$ GeV/c^2.

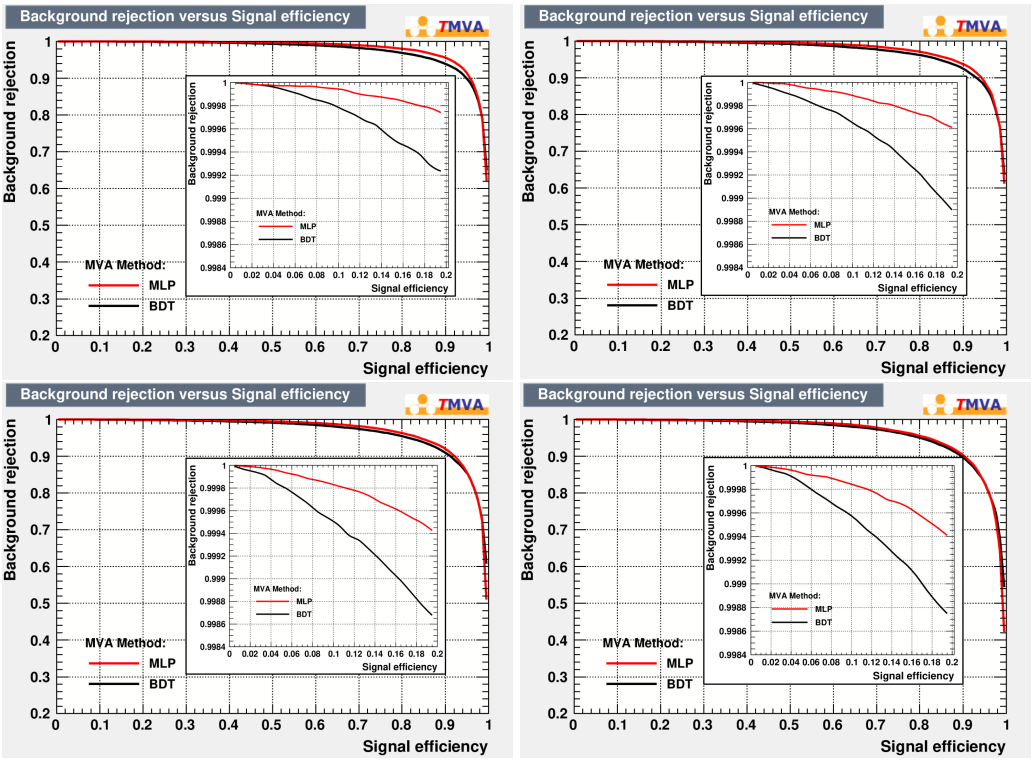

Figure B.3 ROC curves for 1GeV-range 5, 6, 7, 8.

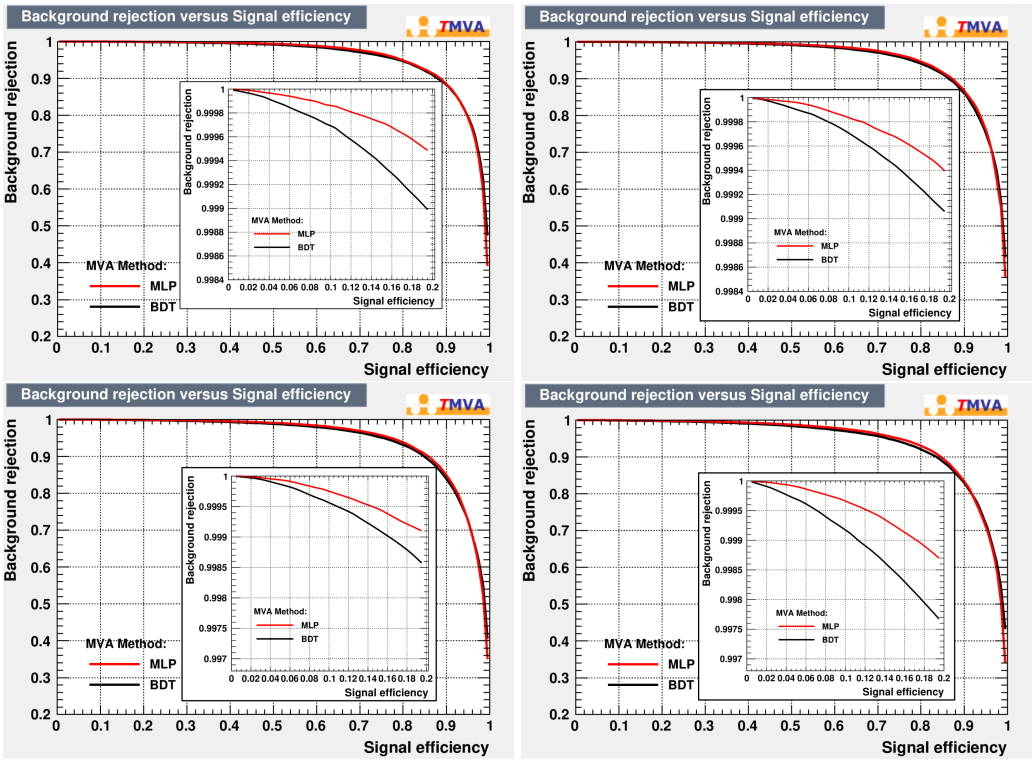

Figure B.4 ROC curves for 1GeV-range 9, 10, 11, 12. MLP is a bit better than BDT.

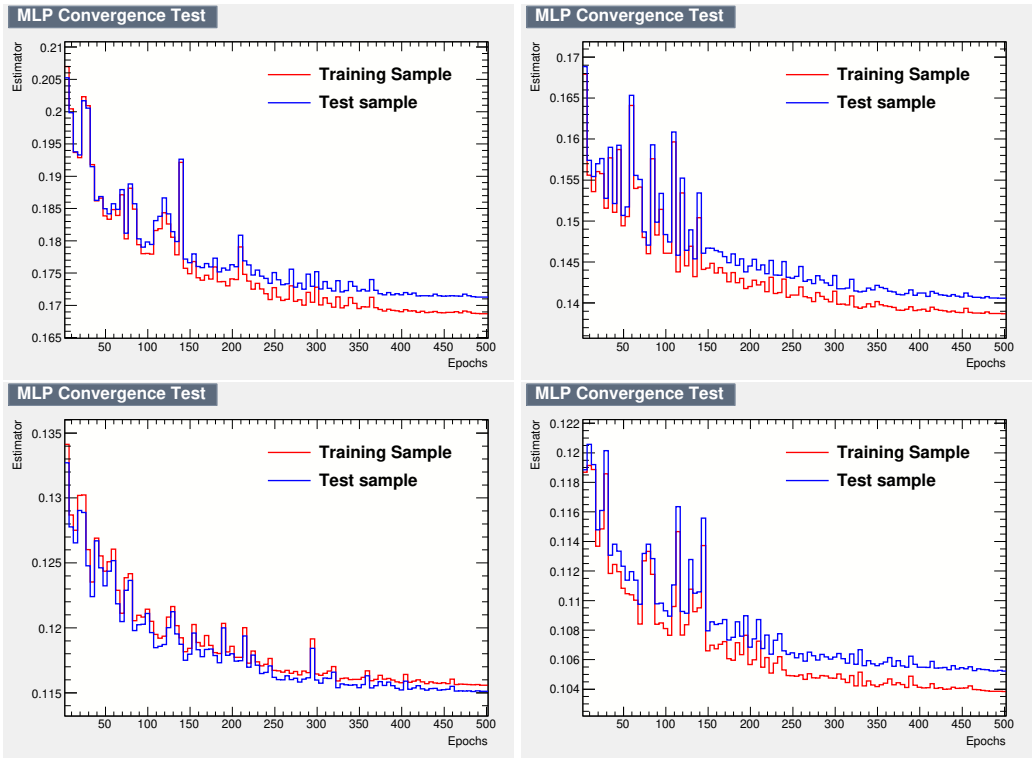

Figure B.5 MLP convergence tests for the first our 1GeV-ranges.

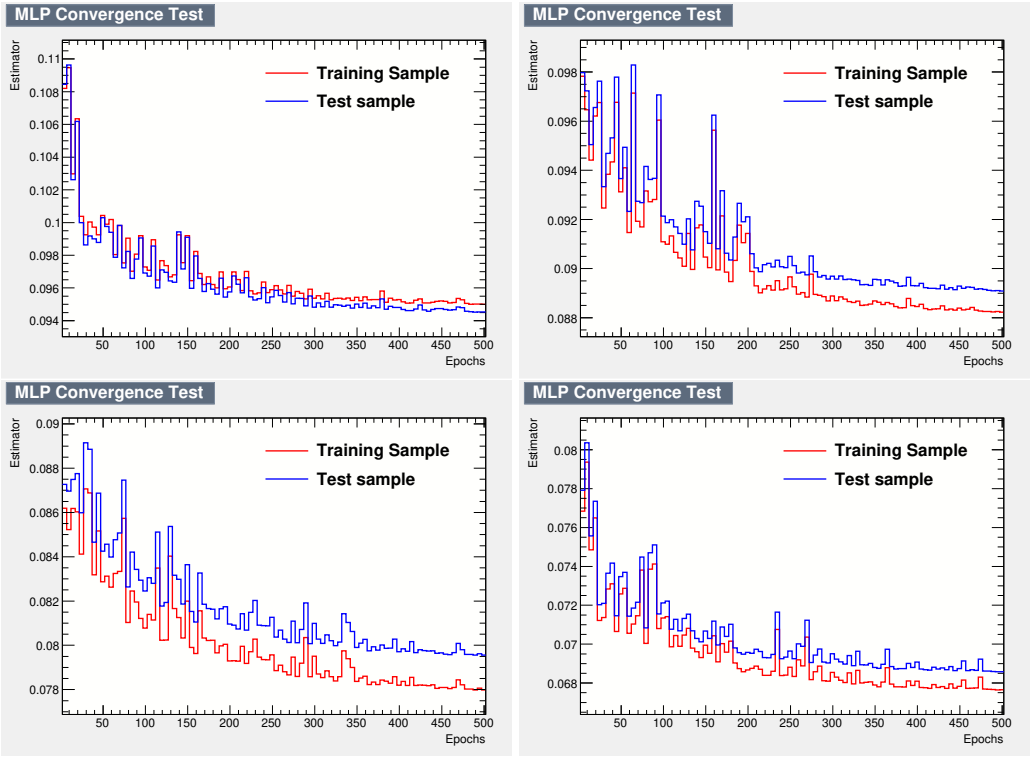

Figure B.6 MLP convergence tests for 1GeV-range 5, 6, 7 and 8.

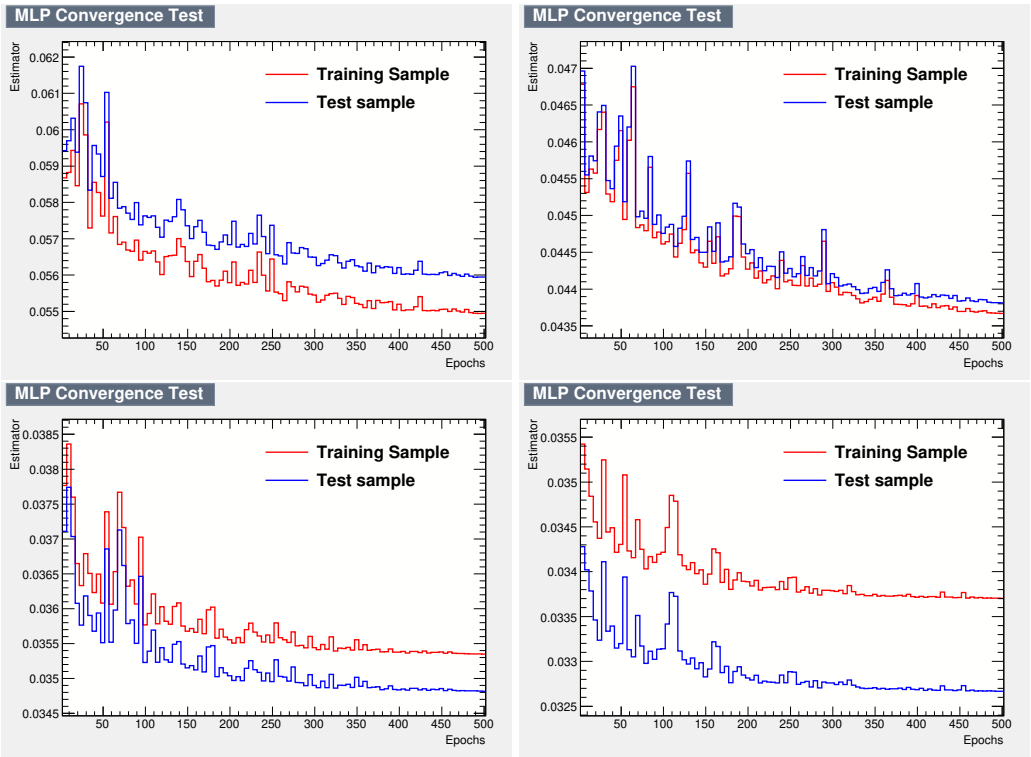

Figure B.7 MLP convergence tests for 1GeV-range 9, 10, 11 and 12.

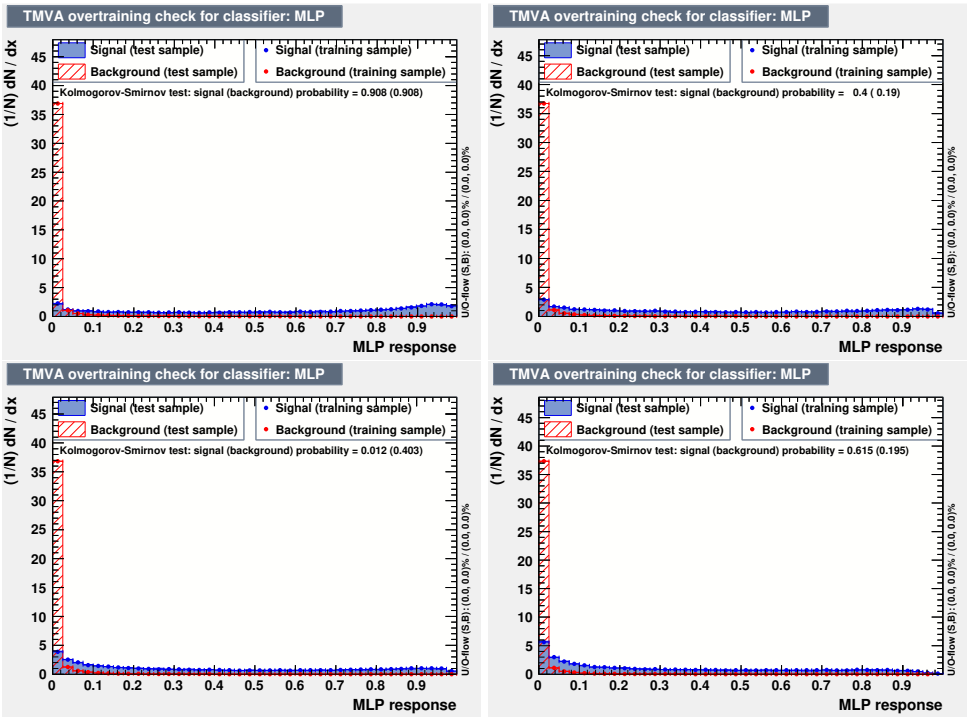

Figure B.8 MLP output neuron for 1GeV-range 5, 6, 7 and 8.

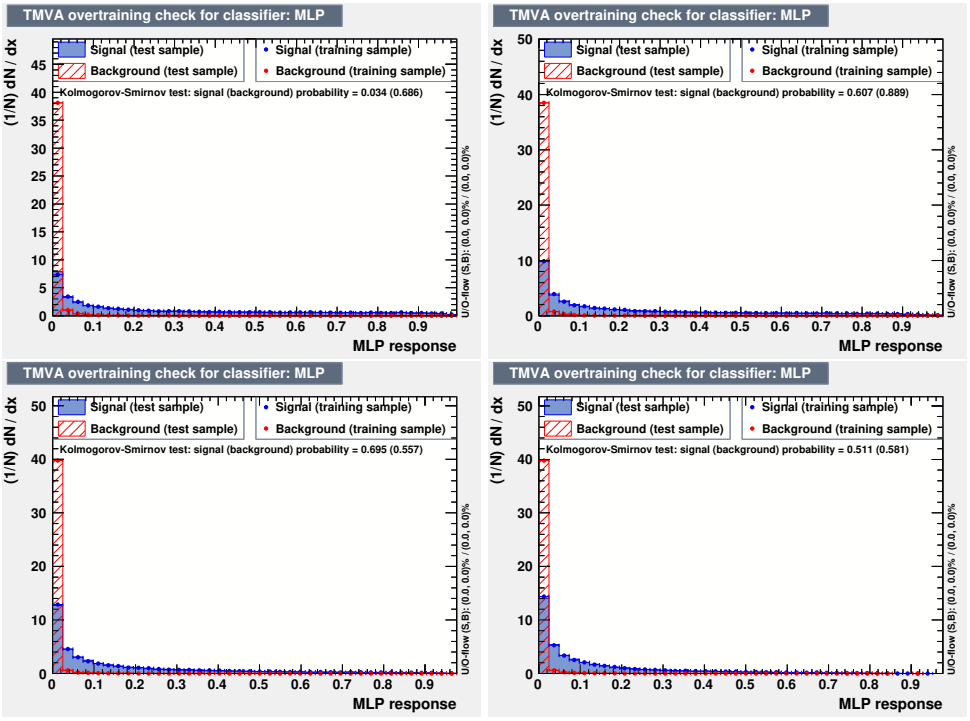

Figure B.9 MLP output neuron for 1GeV-range 9, 10, 11 and 12.

B.2 Additional checks on MVA effects

It can be useful to check if a specific event type contribute more to background than to signal in particular regions of the recoil mass to exploit this information to reject background. The type of the events are classified depending on the identification of the two $\tau - daughters$ tracks using the following selection based on PID variables:

- if $\mu ID > 0.5$ the track is considered as a muon;
- if $eID > 0.5$ the track is considered as an electron;
- if $(1 - \mu ID - eID) > 0.5$ the track is considered as a hadron.

So, for example, if we have one $\tau - daughter$ classified as a muon and the other classified as a hadron, the event type is classified as *eh*.
Figure B.10 shows the contribution of the different type of events to the recoil mass distribution, respectively for background (left) and a signal flat in the recoil mass distribution (right): there is no particular type of event that contributes more in a specific region in the background than in the signal.
Figure B.11 shows the background efficiency of the 1-GeV wide MLPs applied on different background components. The efficiency is different for the different background components.

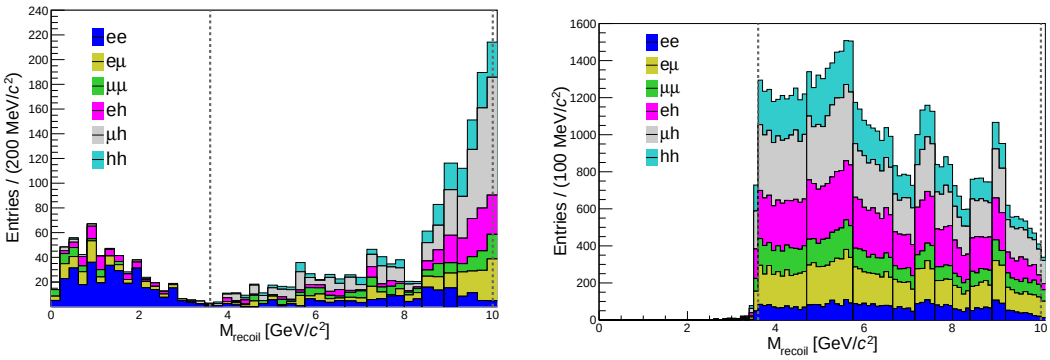

Figure B.10 Recoil mass distribution of background assuming 80 fb^{-1} of luminosity (left) and of a signal flat in the recoil mass distribution (right). The colours represent the different type of events.

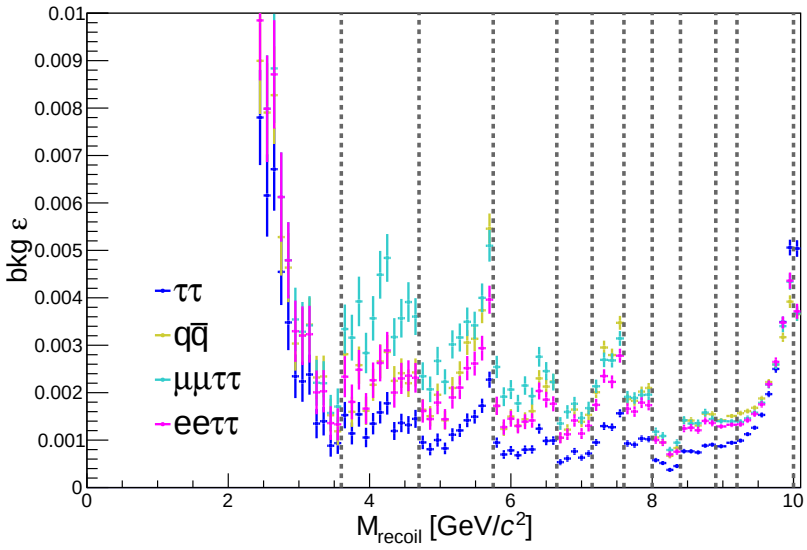

Figure B.11 Background efficiency for the 1-GeV wide MLPs. The grey dashed lines delimit the MLP application ranges. The colours indicate the different background processes considered.

B.3 PID selection checks

It is also interesting to check how the analysis performance changes selecting the two tagging muons with $\mu ID > 0.9$ rather than $\mu ID > 0.5$.
To check the analysis performance, the Punzi-FOM has been used, after the application of the MLP selection for different signal masses and assuming 80 fb^{-1} of background.
The number of background events used in definition of the Punzi-FOM has been evaluated counting the number of background events within $\pm 20\sigma$ from the nominal Z' mass and estimating the number of background events within $\pm 5\sigma$ from the nominal Z' mass dividing by 4. The results of this procedure should mimic the result we will get from the fit procedure.
Figure B.12 shows the Punzi-FOM after the application of the MLP selections for some signal samples and assuming a background of 80 fb^{-1} selecting the tagging muons with $\mu ID > 0.9$ and $\mu ID > 0.5$. We do not observe a significant difference in the two cases, because the loss of signal efficiency compensates the lower background expected cutting tighter on the μID.

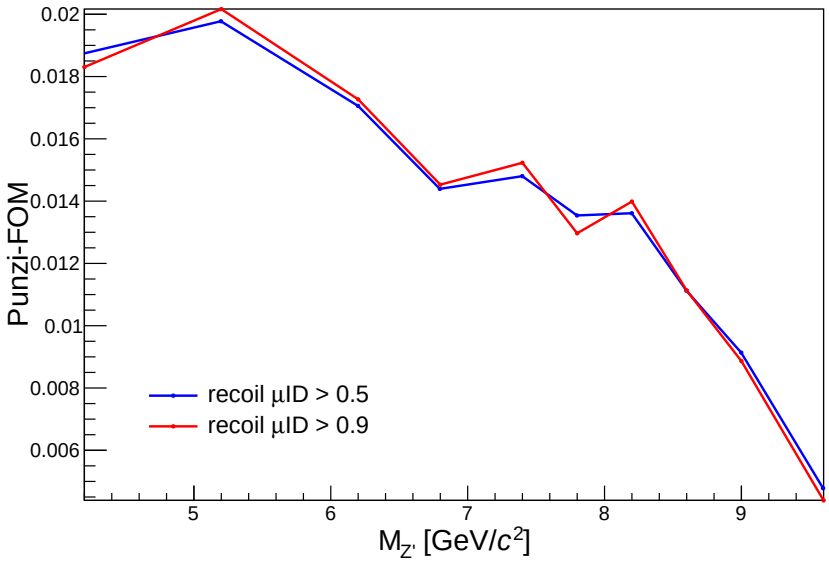

Figure B.12 Punzi-FOM after the application of the MLP selections for some signal samples and assuming a background of 80 fb^{-1} selecting the tagging muons with $\mu ID > 0.9$ and $\mu ID > 0.5$.

C. Fit procedure: supplementary plots

Figures C.1-C.8 show the pull distributions for signal and background for the different number of signal events injected (0, 10, 30 and 50) for the all Z' mass hypothesis used to produce the plots in Figures 4.17 and 4.18.

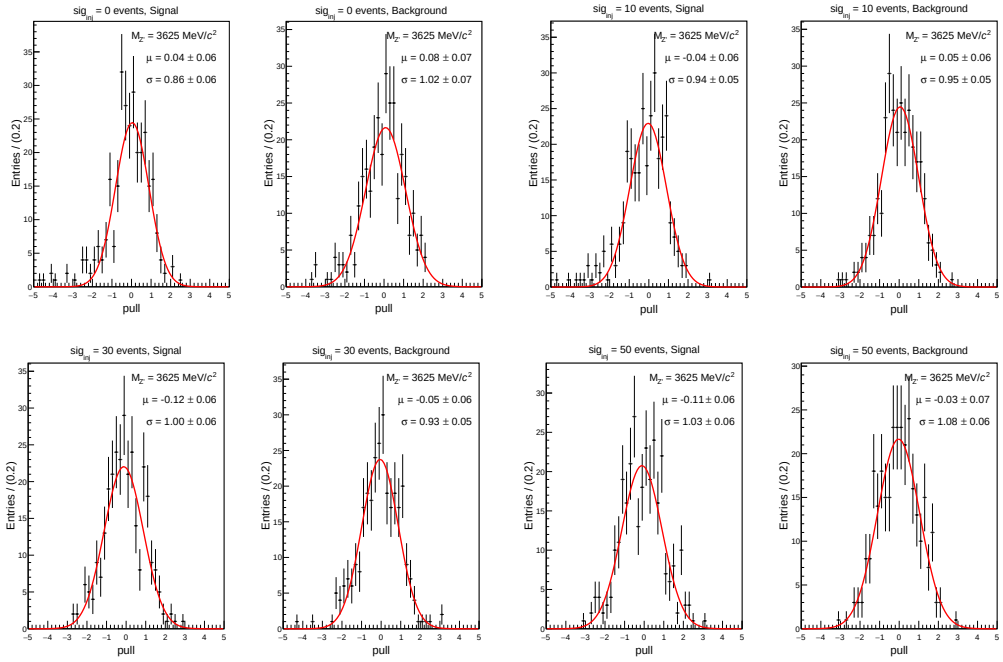

Figure C.1 Pull distributions for signal and background for the different number of signal events injected, for Z' = 3.625 GeV/c^2.

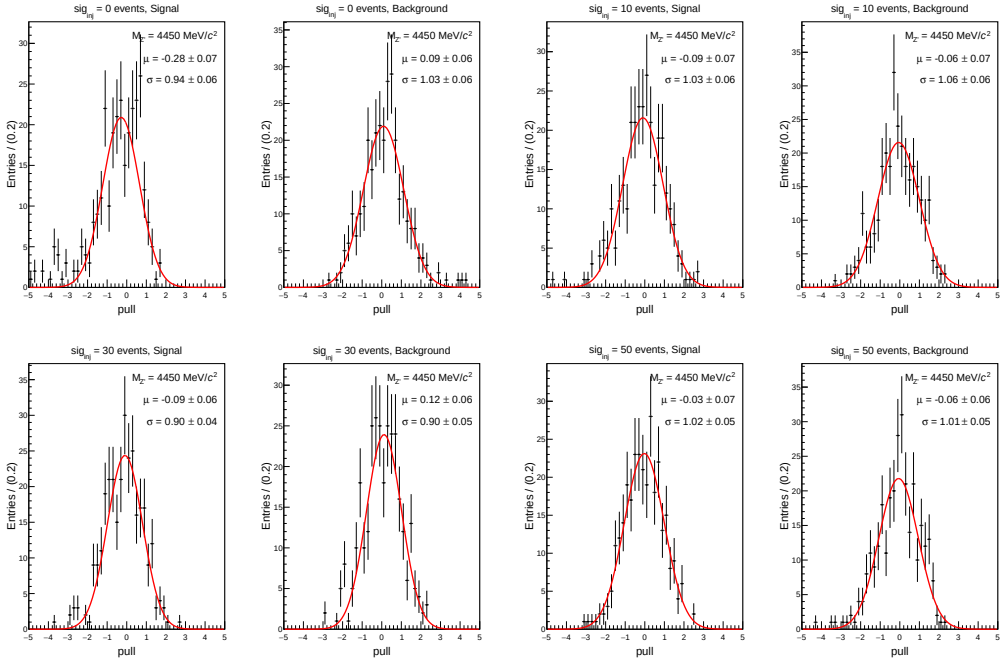

Figure C.2 Pull distributions for signal and background for the different number of signal events injected, for $Z' = 4.450$ GeV/c^2.

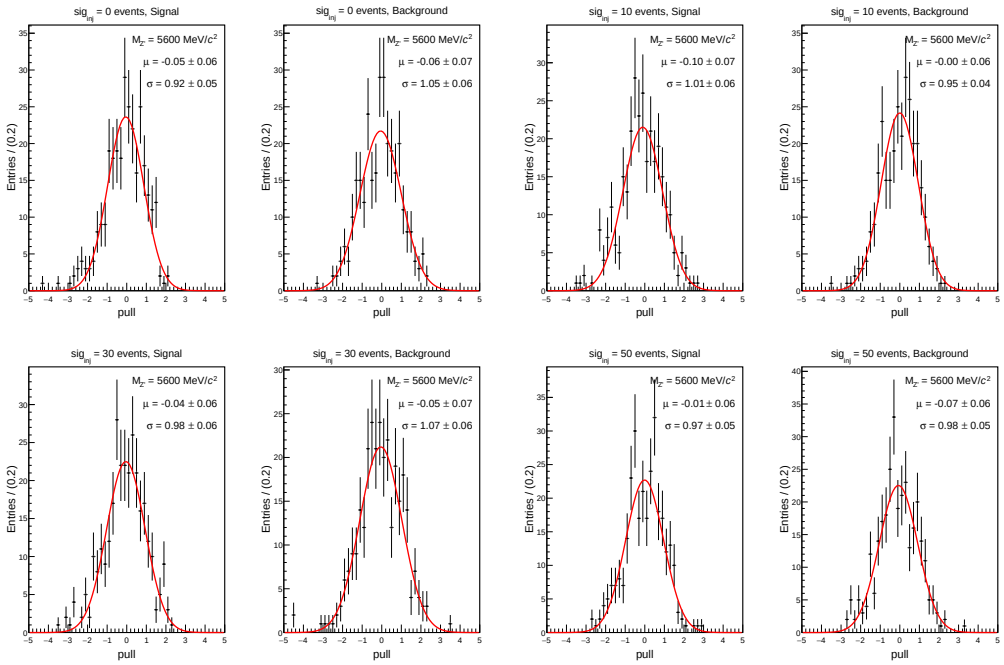

Figure C.3 Pull distributions for signal and background for the different number of signal events injected, for $Z' = 5.600$ GeV/c^2.

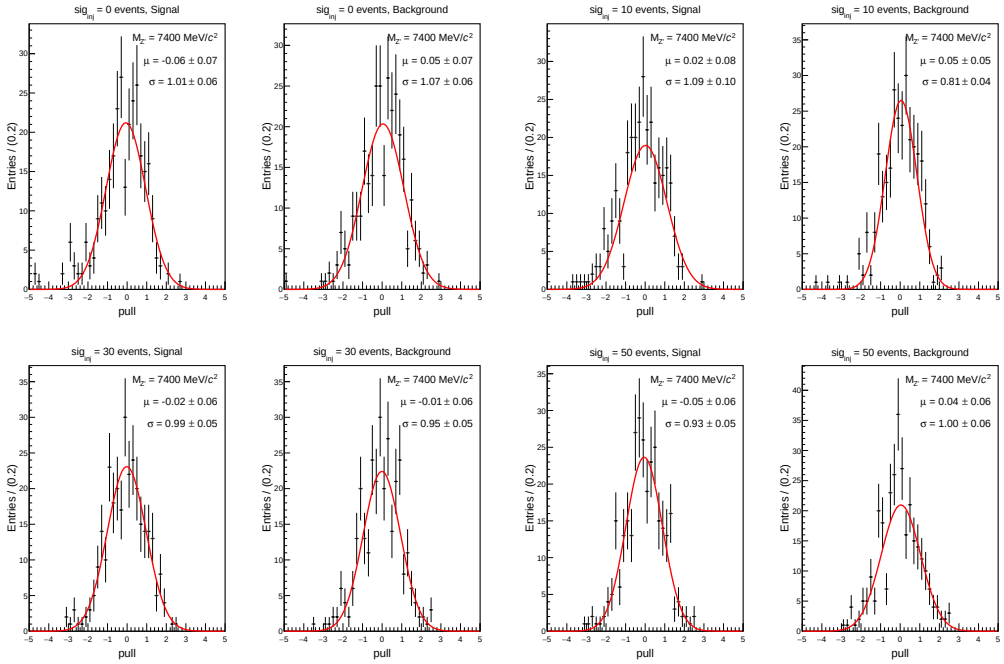

Figure C.4 Pull distributions for signal and background for the different number of signal events injected, for $Z' = 7.400\ \text{GeV}/c^2$.

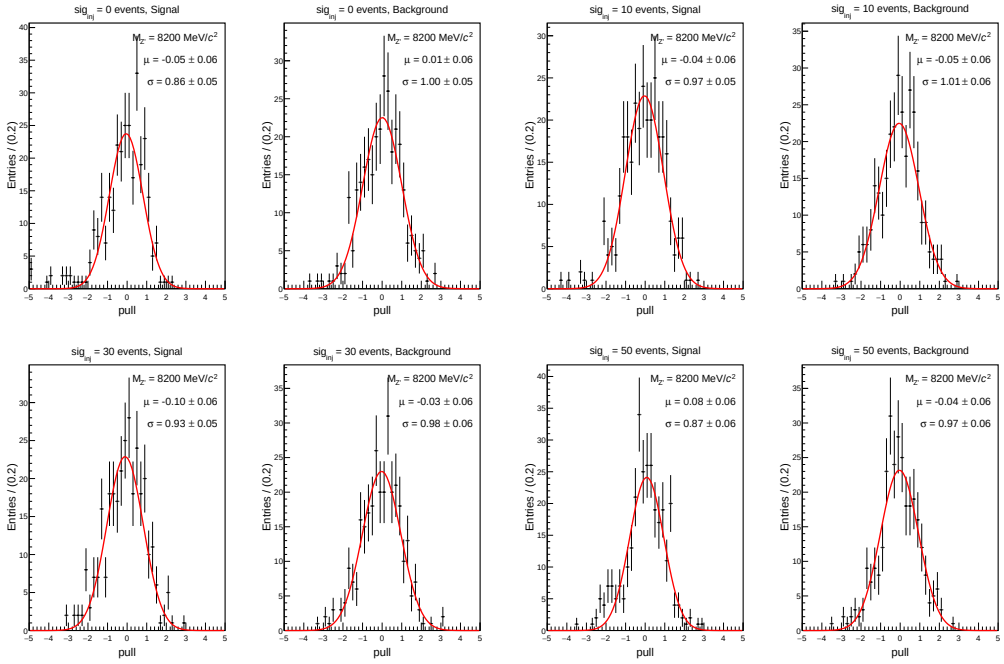

Figure C.5 Pull distributions for signal and background for the different number of signal events injected, for $Z' = 8.200\ \text{GeV}/c^2$.

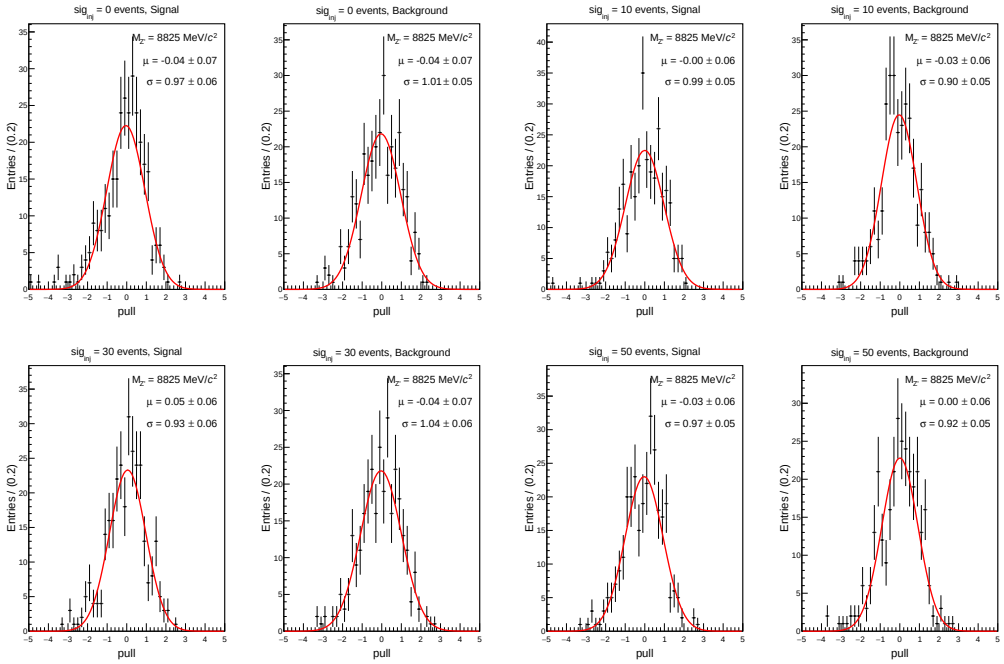

Figure C.6 Pull distributions for signal and background for the different number of signal events injected, for $Z' = 8.825$ GeV/c^2.

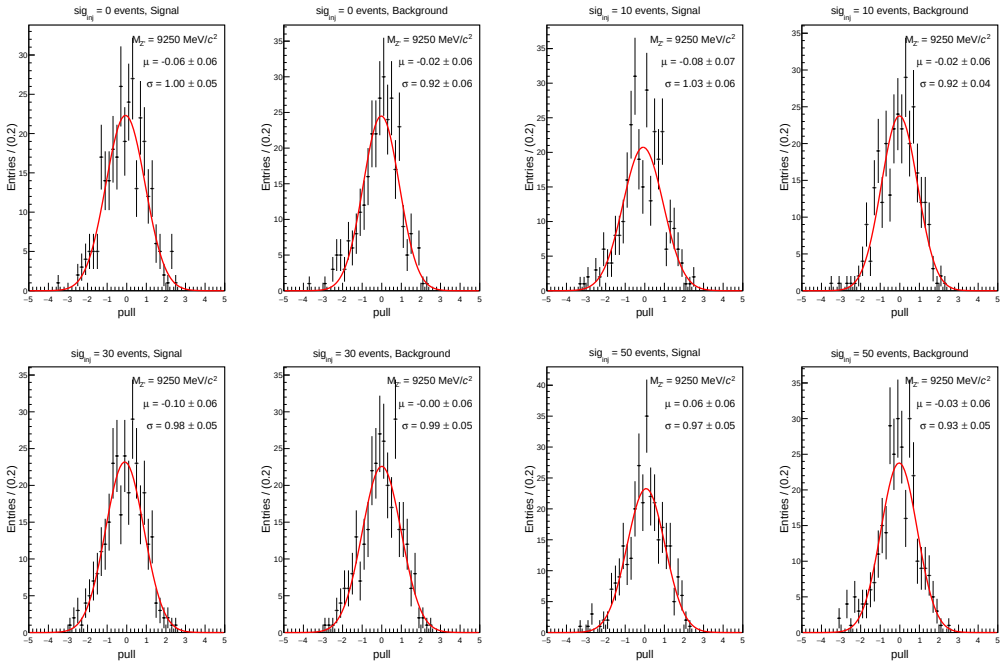

Figure C.7 Pull distributions for signal and background for the different number of signal events injected, for $Z' = 9.250$ GeV/c^2.

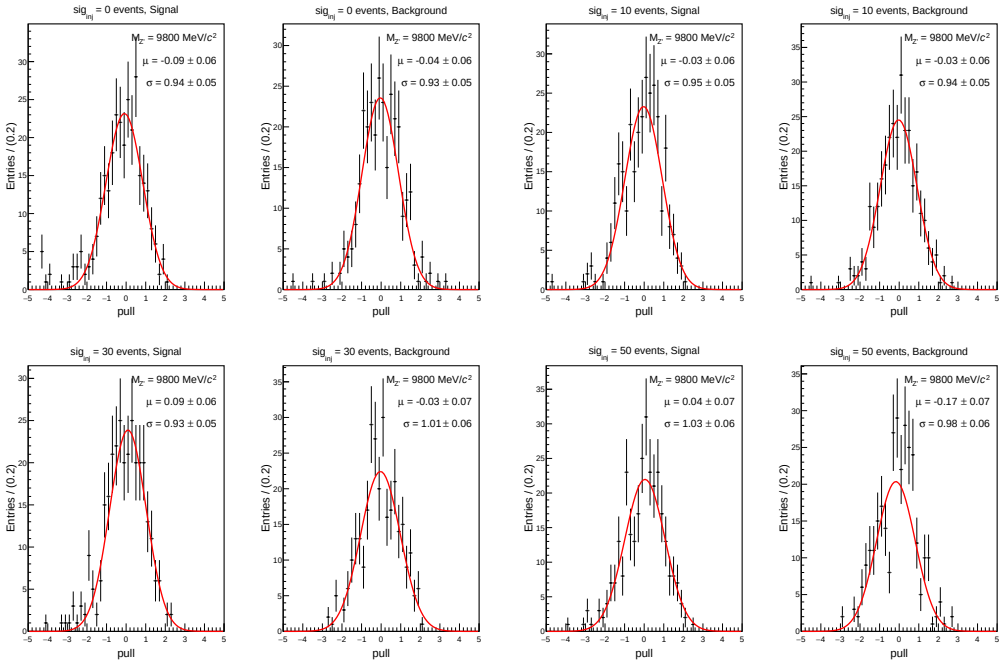

Figure C.8 Pull distributions for signal and background for the different number of signal events injected, for $Z' = 9.800$ GeV/c^2.

D. Upper limit calculation

The 90% confidence level upper limits to the measured Z' signal cross section has been computed within the RooStats framework [107], using the asymptotic calculator tool [108], with the following assumptions:

- the likelihood of the observed number of events is assumed to be Poissonian;
- all systematic uncertainties, including effect on signal efficiency due trigger efficiency, tracking efficiency, particle ID selection, luminosity determination, MLP selection, fit procedure, are modeled with a Gaussian function, with a width equal to the estimated size of the effect (see Table 5.1);
- the expected background number of events is assumed to be Poissonian.

In particular, upper limits have been calculated using a NLL [109] approach, using the CL_s method [105, 106].
The model implemented for the fit is

$$\begin{aligned} &N_{bkg} \cdot f_{\mathrm{BKG}(x)} + N_{sig} \cdot f_{\mathrm{SIG}(x)} \\ &N_{sig} = \sigma_{Z'} \cdot \varepsilon_S \cdot \mathscr{L} \end{aligned} \tag{D.1}$$

Where N_{bkg} and N_{sig} are respectively the number of background events and the signal yield returned from the fit, while $f_{BKG}(x)$ and $f_{SIG}(x)$ are the *p.d.fs* of signal and background of the observable x. The signal yield is defined as the product of the cross section of the process, $\sigma_{Z'}$, the signal efficiency, ε_S, and the luminosity $\mathscr{L}$ considered. So the number of observed events is

$$N_{obs} = \sigma_{Z'} \cdot \varepsilon_S \cdot \mathscr{L} + N_{bkg} \tag{D.2}$$

The calculation has been worked out by using for N_{obs} a Poissonian distribution convoluted with a Gaussian that summarizes the effects of all systematic uncertainties.
The procedure implemented in RooStats allow to directly obtain the upper limits on $\sigma_{Z'}$.

D.1 CL_s technique

A not exhaustive description of the CL_s technique is presented in this Section. However, the interested reader can find more details in Reference [112]. The CL_s method consists in normalizing the confidence level observed for the signal+background hypothesis, CL_{s+b}, to the confidence level observed for the background-only hypothesis, CL_b:

$$CL_s \equiv \frac{CL_{s+b}}{CL_b} = \frac{p_{s+b}}{1 - p_b} \tag{D.3}$$

where, $CL_{s+b} = p_{s+b}$ is the tested p-value, while $CL_b = 1 - p_b$ is the probability to get an observation which is less background-like than the observed one. In general, this method is performed in order to obtain conservative limits on the signal hypothesis.

With CL_s method the signal hypothesis will be considered excluded at the confidence level CL when $1-CL_s \leq CL$. By definition, CL_s is not a true confidence level, so the hypothetical false exclusion rate is generally less than the nominal rate of $1-CL$. Thus the use of CL_s increases the "coverage" of the analysis, but it also avoids that, considering two experiments with the same small expected signal rate but with different backgrounds, the experiment with the larger background may have a better expected performance, as it may happen considering CL_{s+b} only.
The following list specifies the general procedure.

1) Likelihood function $L(data|\sigma_{Z'},\theta)$

$$L(data|\mu,\theta) = P(data|\sigma_{Z'} \cdot N_{sig}^{exp}(\theta) + N_{bkg}^{exp}(\theta)) \cdot p(\tilde{\theta}|\theta) \tag{D.4}$$

where *data* can be real data, simulation, or pseudo-data briefly discussed later. In our case, the parameter of interest is $\sigma_{Z'}$, the cross section of the process, N_{sig}^{exp} and N_{bkg}^{exp} are the number of expected signal and background events. Multiple uncertainties can affect the predictions for both signal and background yields and they are handled by introducing nuisance parameters θ: in our case the width of the Gaussian that summarizes the effects of all systematic uncertainties and the number of expected background events itself. $\tilde{\theta}$ represents the default value of the nuisance parameters, so $p(\tilde{\theta}|\theta)$ is the *p.d.f* constraining the likelihood of the main measurement.
Considering an unbinned likelihood over n events in the data sample, $P(data|\sigma_{Z'}s+b)$ stands for

$$\frac{1}{n}\Pi_i(\sigma_{Z'}Sf_{SIG}(x_i) + Bf_{BKG}(x_i)) \cdot e^{-(\sigma_{Z'}S+B)} \tag{D.5}$$

where x_i is the set of observables, S and B are total event rates expected for signal and background.

2) To compare the compatibility of data with background-only and signal+background hypotheses, the test statistic used $\tilde{q}_{\sigma_{Z'}}$ is based on the profile likelihood ratio

$$\tilde{q}_{\sigma_{Z'}} = -2ln\frac{L(data|\sigma_{Z'},\widehat{\theta}_{\sigma_{Z'}})}{L(data|\widehat{\sigma}_{Z'},\widehat{\theta})} \tag{D.6}$$

where $\widehat{\theta}_{\mu}$ refers to the conditional maximum likelihood estimators of θ, given data and $\sigma_{Z'}$, while $(\widehat{\sigma}_{Z'},\widehat{\theta})$ is the pair of parameters that correspond to the global maximum of the likelihood.

3) The observed value of the test statistic for the particular $\sigma_{Z'}$ tested is found $\tilde{q}_{\sigma_{Z'}}^{obs}$.

4) The asymptotic calculator creates a set of Asimov datasets, that are pseudo-datasets for the background-only hypothesis. A Asimov dataset is generated for a particular set of model parameters such that the maximum likelihood best-fit value of all expected background events and the nuisance parameters are equal to the nominal ones. In this condition, asymptotic formulae for *p.d.f* $f(\tilde{q}_{\sigma_{Z'}}|\sigma_{Z'}=0,\widehat{\theta}_0^{obs})$, where $\widehat{\theta}^{obs}$ are obtained from fitting the observed data, from which one can derive the median expected limits and their bands, using the Asimov dataset.

5) Having constructed the two $f(\tilde{q}_{\sigma_{Z'}}|\sigma_{Z'}=0,\widehat{\theta}_0^{obs})$ and $f(\tilde{q}_{\sigma_{Z'}}|\sigma_{Z'},\widehat{\theta}_{\sigma_{Z'}}^{obs})$ distributions, the two p-values associated with the observations for the signal+background and background-only hypotheses, p_{s+b} and p_b are defined as

$$\begin{aligned} p_{s+b} &= P(\tilde{q}_{\sigma_{Z'}} \geq \tilde{q}_{\sigma_{Z'}}^{obs}|sig+bkg) = \int_{\tilde{q}_{\sigma_{Z'}}^{obs}}^{\infty} f(\tilde{q}_{\sigma_{Z'}}|\sigma_{Z'},\widehat{\theta}_{\sigma_{Z'}}^{obs})d\tilde{q}_{\sigma_{Z'}} \\ 1-p_b &= P(\tilde{q}_{\sigma_{Z'}} \geq \tilde{q}_{\sigma_{Z'}}^{obs}|bkg-only) = \int_{\tilde{q}_0^{obs}}^{\infty} f(\tilde{q}_0|0,\widehat{\theta}_0^{obs})d\tilde{q}_{\sigma_{Z'}} \end{aligned} \tag{D.7}$$

CL_s is defined in Equation D.3. For further details see also Reference [112]. Figure D.1 shows the result of the asymptotic calculator for the extraction of the 90$ CL upper limit for the mass $M_{Z'} = 5.655$ GeV/c^2 with the CL_s method, on simulation. The plot shows the p-value as a function of the tested cross section $\sigma_{Z'}$. The red line at 0.1 represents the significance, α, corresponding to 90% CL. The value extracted from the plot are the intersections between the red line ($\alpha = 0.1$) and the curves indicated in the legend of the plot.

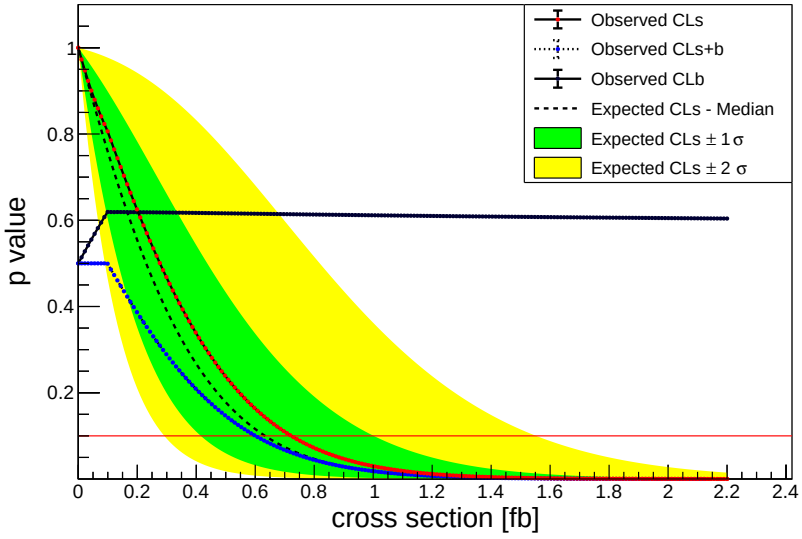

Figure D.1 Result of the asymptotic calculator for the calculation of the 90% CL upper limit for $M_{Z'} = 5.655$ GeV/c^2 using the CL_s method, on simulation.

Glossary and achronims

SM: Standard Model.

MC: Monte Carlo.

DM: dark matter.

CMBR: Cosmic Microwave Background Radiation.

WIMP: weakly interacting massive particle.

DS: dark sector.

VXD: Vertex Detector.

PXD: Pixel Detector.

DEPFET: Depleted Field Effect Transistor.

SVD: Silicon Vertex Detector.

DSSD: Double-Sided Silicon Strip Detector.

ASIC: application specific integrated circuit.

APV25: SVD front-end readout ASIC.

CDC: Central Drift Chamber.

ECL: Electromagnetic Calorimeter.

BECL: Barrel Electromagnetic Calorimeter.

ARICH: Aerogel Ring Imaging Cherenkov counter.

TOP: Time-of-propagation counter.

MCP-PMT: micro-channel plate photo-multiplier.

KLM: K_L and μ detector.

RPC: resistive plate chambers.

L1: hardware-based Level 1 trigger.

FPGA: Field Programmable Gate Array.

GRL: Global Reconstruction Logic.

GDL: Global Decision Logic.

HLT: software-based High Level Trigger.

basf2: Belle Analysis Framework 2.

DAQ: Data Acquisition System.

ISR: Initial State Radiation.

FSR: Final State Radiation.

MVA: Multi-Variate Analysis.

MLP: Multi-Layer Perceptron. One of the MVA methods.

BDT: Boosted Decision Tree. One of the MVA methods.

ANN: artificial neural network.

FOM: figure of merit.

ROC: receiver operating characteristic.

CL: confidence level.

UL: upper limits.

LEE: The look-elsewhere effect is a phenomenon in the statistical analysis where an apparently statistically significant observation may have actually arisen by chance.

Tagging muons (pions): the name we gave to the two muons (pions) not coming from the Z' decay in $\mu\mu Z', Z' \to \tau\tau$ (control sample: $\pi\pi Z', Z' \to \tau\tau$).

τ-daughters: the name we gave to the two tracks reconstract ar products from the decay of the τs from the Z' decay in $\mu\mu Z', Z' \to \tau\tau$ (control sample: $\pi\pi Z', Z' \to \tau\tau$).

Recoil mass: the mass of the system recoiling against two well identified opposite charge muons.

fff trigger line: requires at least three tracks reconstructed inside the *Belle II* detector.

CDCKLM*n* trigger lines: requires that the number of matched CDC tracks and KLM hits is n, where $n = 1, 2, 3, 4$.

CDCKLM trigger: the logical OR of CDCKLM*n* trigger lines.

CS1: indicate the control sample number 1, which is $\pi^+\pi^-\tau^+\tau^-$ for us. In this control sample we have two charged tracks, with opposite charge, identified as pions and two additional tracks that can be muons, electrons or pions.

CS2: indicate the control sample number 2, which is $\mu^+\mu^-\tau^+\tau^-$ with $M_{recoil} < 3.3$ GeV/c^2 for us. In this control sample we have two charged tracks, with opposite charge, identified as muons and two additional tracks that can be muons, electrons or pions.

CL_s method: a statistical method for setting upper limits on model parameters.

Crystaball distribution: it consists of a Gaussian core portion and a power-law low-end tail, below a certain threshold, and it commonly used to model various lossy processes in high-energy physics.

NDF: number of degrees of freedom.

List of figures

Figure of appendices are not listed here.

3.5: distributions for signal and background of $p(\mu_1)$ vs $p(\mu_0)$, p_T^{max} vs p_T^{min} and $p(\tau_{D,0}+\tau_{D,1})$ vs $M(\tau_{D,0},\tau_{D,1})$ for $M_{Z'} = 6.6$ GeV/c^2.

3.6: distributions for signal and background of $p(\mu_1)$ vs $p(\mu_0)$, p_T^{max} vs p_T^{min} and $p(\tau_{D,0}+\tau_{D,1})$ vs $M(\tau_{D,0},\tau_{D,1})$ for $M_{Z'} = 9.6$ GeV/c^2.

3.7: distributions of the discriminant variables A and $|p(\mu_0)_{R=45^o}/(\sqrt{2}/2 \cdot P)|$ for $M_{Z'} = 3.6$ GeV/c^2.

3.8: distributions of the discriminant variables A and $|p(\mu_0)_{R=45^o}/(\sqrt{2}/2 \cdot P)|$ for $M_{Z'} = 6.6$ GeV/c^2.

3.9: distributions of the discriminant variables A and $|p(\mu_0)_{R=45^o}/(\sqrt{2}/2 \cdot P)|$ for $M_{Z'} = 9.6$ GeV/c^2.

3.10: distributions of the discriminant variables R/P and θ for $M_{Z'} = 3.6$ GeV/c^2.

3.11: distributions of the discriminant variables R/P and θ for $M_{Z'} = 6.6$ GeV/c^2.

3.12: distributions of the discriminant variables R/P and θ for $M_{Z'} = 9.6$ GeV/c^2.

3.13: distributions of the discriminant variables $\theta_{1,2}$ and $d_{1,2}$ for $M_{Z'} = 3.6$ GeV/c^2.

3.14: distributions of the discriminant variables $\theta_{1,2}$ and $d_{1,2}$ for $M_{Z'} = 6.6$ GeV/c^2.

3.15: distributions of the discriminant variables $\theta_{1,2}$ and $d_{1,2}$ for $M_{Z'} = 9.6$ GeV/c^2.

3.16: invariant mass of photon pairs compatible with the hypothesis of π^0, for signal, $\tau\tau$ and $q\bar{q}$ events.

3.17: $\alpha(\pi^0, p(\mu)_{max})$, $\alpha(\pi^0, \mu_{p,min})$, $\alpha(\pi^0, p(\mu)_{max})$ vs $\alpha(\pi^0, p(\mu)_{min}$ for $M_{Z'} = 3.6$ GeV/c^2 and main background components.

3.18: discriminant variables $\Sigma_{i=0}^{n_{\pi^0}} E_i(\pi^0)_{IN}^{CMS}$), $\Sigma_{i=0}^{n_{\pi^0}} E_i(\pi^0)_{OUT}^{CMS}$ for $M_{Z'} = 3.6$ GeV/c^2.

3.19: thrust, T distribution for signal and background for $M_{Z'} = 3.6$ GeV/c^2, $M_{Z'} = 6.6$ GeV/c^2 and $M_{Z'} = 9.6$ GeV/c^2.

3.20: $foxR1$ distribution for signal and background for $M_{Z'} = 3.6$ GeV/c^2, $M_{Z'} = 6.6$ GeV/c^2 and $M_{Z'} = 9.6$ GeV/c^2.

3.21: $\alpha(p(\mu)_{max}, T)$ distribution for signal and background for $M_{Z'} = 3.6$ GeV/c^2, $M_{Z'} = 6.6$ GeV/c^2 and $M_{Z'} = 9.6$ GeV/c^2.

3.22: $\alpha(p(\mu)_{min}, T)$ distribution for signal and background for $M_{Z'} = 3.6$ GeV/c^2, $M_{Z'} = 6.6$ GeV/c^2 and $M_{Z'} = 9.6$ GeV/c^2.

3.23: ΔROE_M distribution for signal and background for $M_{Z'} = 3.6$ GeV/c^2, $M_{Z'} = 6.6$ GeV/c^2 and $M_{Z'} = 9.6$ GeV/c^2.

3.24: ΔROE_E distribution for signal and background for $M_{Z'} = 3.6$ GeV/c^2, $M_{Z'} = 6.6$ GeV/c^2 and $M_{Z'} = 9.6$ GeV/c^2.

3.25: Multi-Layer Perceptron with one hidden layer

4.8: c. The red line is the modeling, obtained from the average functions.

4.9: σ_{CB2} vs Z' mass for all the fit ranges shown in the legend and the σ_{CB1} vs Z' mass for all the fit ranges shown in the legend.

4.10: Final modeling of α_{CB1}, n_{CB1}, α_{CB2} and n_{CB2} as a function of Z' mass.

4.11: fit to the recoil mass distribution for the MC signal samples respectively for a generated Z' mass of 3.6, 4.6, 7.6, 8.6 GeV/c^2. The fit was performed keeping fixed all the CB parameters except N_{sig} in the signal *p.d.f.*

4.12: comparison of χ^2/NDF vs Z' for different fit ranges, for a toy-MC. and σ_{peak} vs Z' mass obtained from the fit with all CB parameters free and fixed.

4.13: fit to the recoil mass distribution for the MC signal samples respectively for a generated Z' mass of 3.6, 4.6, 7.6, 8.6 GeV/c^2. The fit was performed keeping fixed all the CB parameters except N_{sig} in the signal *p.d.f*, after the MLP selection.

4.14: Number of fitted signal events as a function of the number of generated signal events for $M_{Z'} = 3.6$ GeV/c^2.

4.15: the fit signal+background to the recoil mass distribution for the MC signal samples for Z' mass of 3.6, 4.6, 7.6, 8.6 GeV/c^2.

4.16: χ^2/NDF vs Z' for different fit ranges, for a toy-MC.

4.17: mean and RMS from Gauss fit of pull distribution obtained from signal fit from toy-MC.

4.18: mean and RMS from Gauss fit of pull distribution obtained from background fit from toy-MC.

4.19: pull distributions for signal and background for the different number of signal events injected, for $Z' = 6.375$ GeV/c^2.

4.20: Average reduce χ^2 for different fit ranges and different number of signal events injected.

5.1: signal events for different Z' mass do not peak at the nominal values of the Z' mass.

5.2: 90% confidence level upper limit on the cross section and g' coupling constant for the control sample $\pi^+\pi^-\tau^+\tau^-$ (CS1) estimated applying a cut and count strategy.

5.3: *fff* trigger efficiency as a function of the two minimum transverse momenta for events with less than 2 tracks in the barrel, and efficiency errors.

5.4: *fff* trigger efficiency as a function of the two minimum transverse momenta for events with 2 tracks in the barrel, and efficiency errors.

5.5: *fff* trigger efficiency as a function of the two minimum transverse momenta for events with 3 tracks in the barrel, and efficiency errors.

5.6: *fff* trigger efficiency as a function of the two minimum transverse momenta for events with 4

tracks in the barrel, and efficiency errors.

5.7: Signal efficiency requiring *fff*-OR-CDCKLM trigger, only *fff* trigger and only CDCKLM trigger.

5.8: Data/MC comparison for the recoil mass calculated with respect to the dipion.

5.9: Thrust distribution for $\tau\tau$ and $q\bar{q}$ events.

5.10: Data/MC comparison for the recoil mass calculated with respect to the dipion, for events with a thrust higher than 0.92, enriched in $\tau\tau$-like events, and lower than 0.87, enriched in $q\bar{q}$-like events.

5.11: Data/MC comparison for the recoil mass calculated with respect to the dipion, showing the MC $\pm 1\sigma$ band.

5.12: signal efficiency as a function of the Z' mass for different configuration of the *fff*-OR-CDCKLM triggers.

5.13: distribution of the highest difference between all the configuration of *fff*-OR-CDCKLM tested for each Z' mass point.

5.14: systematic uncertainties associated to the CDCKLM trigger as a function of the Z'.

5.15: PID systematics as a function of the Z' mass.

5.16: Data/MC comparison of the MLP efficiency on background, evaluated using control sample $\pi^+\pi^-\tau^+\tau^-$, for four different MLPs (MLPs from 1 to 4).

5.17: Data/MC comparison of the MLP efficiency on background, evaluated using control sample $\pi^+\pi^-\tau^+\tau^-$, for four different MLPs (MLPs from 5 to 8).

5.18: 0^{th}-order polynomial fit to the ratio $\varepsilon_{Data}/\varepsilon_{MC}$ in the full range covered by the $\pi^+\pi^-\tau^+\tau^-$ control sample. The uncertainty of the fit is considered as systematic.

5.19: distribution of the difference of the means, μ, returned by the Gaussian fit of the pulls from 0 for each mass point, evaluated as $(0-\mu)$. The signal yield is underestimated of 6.7% on average.

5.20: $\sigma(p_t)/p_t$ resolution in bins of p_t for slow pions (MC) and cosmics and $\sigma(p_t^*)/p_t^*$ resolution in bins of p_t^* for a dimuon sample, for MC13 and data.

5.21: modeling of systematic uncertainties as a function of the Z' mass.

6.1: cross section of the process estimated from the MadGraph5NLO generator assuming $g' = 0.01$, and linearly interpolated. The cross section is expressed in pb.

6.2: preliminary estimate at 90% *CL* expected sensitivity to the cross section of the process and to g' model, with trigger efficiency and preliminary systematic uncertainties included.

6.3: preliminary estimate at 90% *CL* expected sensitivity to the cross section of the process with vertical lines showing where the different MLP ranges of application end.

6.4: 90% *CL* sensitivity to the cross section of the process: The green/yellow bands indicate $\pm 1\sigma$ and $\pm 1\sigma$ intervals for the expected limits under the background-only hypothesis. The median expectation is shown with the dashed line, while black dots are the observed upper limits measured in simulation. And 90% *CL* sensitivity to g' with Brazilian band compared with the existing exclusion region from other experiments.

6.5: comparison of the sensitivity to the cross section and to g' evaluated with and without systematic uncertainties included.

6.6: ratio of the sensitivity to the cross section and to g' evaluated with and without systematic uncertainties included.

6.7: significance obtained allowing negative and only positive signal yields.

6.8: distribution of the upcrossings considering $Z_{test} = 1$.

6.9: data/MC comparison for the recoil mass calculated with respect to the dimuon.

6.10: recoil mass distribution for 10% data unhided compared with the different MC components.

6.11: 90% *CL* upper limits on the cross section of the process and g' measured on 5.47 fb^{-1} of unhided data, with Brazilian band.

6.12: Significance as function of the Z' mass obtained from the fit, obtained using 5.47 fb^{-1} of unhided data. Fit of the mass point of 5.5655 GeV/c^2 for the highest significance observed of 3.26 from the fit scan is also shown.

6.13: preliminary 90% *CL* upper limits on g' observed with 5.47 fb^{-1} at *Belle II*, and estimated $\pm 1\sigma$ rescaling at 80 fb^{-1} and 200 fb^{-1}, compared with the existing excluded region.

List of tables

Acknowledgement

This thesis work it would not have been possible without the support and guidance that I received from many people, that I like to mention here.

Firstly, I would like to express my sincere gratitude to my supervisor Prof. Francesco Forti for the continuous support that began with the master's thesis and has never stopped, for his patience, motivation, and immense knowledge. His guidance helped me in all the time of research.

I would like to acknowledge my co-supervisor Dr. Katsuro Nakamura for his support and for spending his precious time helping me with his knowledge and experience during my stay in KEK.

Thanks to all the Pisa group: Giulia, Giuliana, Stefano, Eugenio, Antonio. The passion they put in everything they do is a great motivation for me to always give the best. But above all, they showed me what it means to work as a team. I greatly appreciate the support received from all of them.

Thanks to Prof. Enrico Graziani and Giacomo who shared the analysis effort and supported me during the thesis work with their expertise, immense patience and knowledge.

I would like to express my gratitude to the *Belle II* collaboration, and in particular to the Dark Sector Working Group for the helpful discussions about the analysis and to the SVD group for their support in the SVD-related work.

I would like to thank the JENNIFER2 PhD secondment programme for supporting my PhD work under the EU grant n.822070.

Finally, I must express my very profound gratitude to my loved ones, especially my Mum, my Dad and Eleonora for always believing in me and encouraging me to follow my dreams. I will be grateful forever for your love.

Sic parvis magna

Bibliography

[1] Michael E. Peskin and Daniel V. Schroeder. *An Introduction to quantum field theory*. Reading, USA: Addison-Wesley, 1995. ISBN: 978-0-201-50397-5.

[2] Particle Data Group et al. "Review of Particle Physics". In: *Progress of Theoretical and Experimental Physics* 2020.8 (Aug. 2020). 083C01. ISSN: 2050-3911. DOI: 10.1093/ptep/ptaa104. eprint: https://academic.oup.com/ptep/article-pdf/2020/8/083C01/34673722/ptaa104.pdf. URL: https://doi.org/10.1093/ptep/ptaa104.

[3] Nicola Cabibbo. "Unitary Symmetry and Leptonic Decays". In: *Phys. Rev. Lett.* 10 (12 June 1963), pp. 531–533. DOI: 10.1103/PhysRevLett.10.531. URL: https://link.aps.org/doi/10.1103/PhysRevLett.10.531.

[4] *Updates and numerical results on the CKMfitter group*. URL: http://ckmfitter.in2p3.fr/.

[5] Gianfranco Bertone, Dan Hooper, and Joseph Silk. "Particle dark matter: evidence, candidates and constraints". In: *Physics Reports* 405.5-6 (Jan. 2005), pp. 279–390. ISSN: 0370-1573. DOI: 10.1016/j.physrep.2004.08.031. URL: http://dx.doi.org/10.1016/j.physrep.2004.08.031.

[6] E. V. Karukes, P. Salucci, and G. Gentile. "The dark matter distribution in the spiral NGC 3198 out to 0.22Rvir". In: *Astronomy & Astrophysics* 578 (May 2015), A13. ISSN: 1432-0746. DOI: 10.1051/0004-6361/201425339. URL: http://dx.doi.org/10.1051/0004-6361/201425339.

[7] Lars Bergström and Ariel Goobar. *Cosmology and Particle Astrophysics, 2° Ed.* Springer, Praxis Publishing, 2006.

[8] Monique Signore and Denis Puy. "Cosmic microwave background and first molecules in the early universe". In: *European Physical Journal C* 59 (Jan. 2009), pp. 117–172. DOI: 10.1140/epjc/s10052-008-0807-z.

[9] John McDonald. *Generation of WIMP Miracle-like Densities of Baryons and Dark Matter*. 2012. arXiv: 1201.3124 [hep-ph].

[10] R. Essig et al. *Dark Sectors and New, Light, Weakly-Coupled Particles*. 2013. arXiv: 1311.0029 [hep-ph].

[11] M. Cassé and P. Fayet. "Light Dark Matter". In: *EAS Publications Series* 20 (2006), pp. 201–208. ISSN: 1638-1963. DOI: 10.1051/eas:2006072. URL: http://dx.doi.org/10.1051/eas:2006072.

[12] John F. Beacom, Nicole F. Bell, and Gianfranco Bertone. "Gamma-Ray Constraint on Galactic Positron Production by MeV Dark Matter". In: *Physical Review Letters* 94.17 (May 2005). ISSN: 1079-7114. DOI: 10.1103/physrevlett.94.171301. URL: http://dx.doi.org/10.1103/PhysRevLett.94.171301.

[13] C. Bœhm, P. Fayet, and J. Silk. "Light and heavy dark matter particles". In: *Physical Review D* 69.10 (May 2004). ISSN: 1550-2368. DOI: 10.1103/physrevd.69.101302. URL: http://dx.doi.org/10.1103/PhysRevD.69.101302.

[14] C. BIRD, R. KOWALEWSKI, and M. POSPELOV. "DARK MATTER PAIR-PRODUCTION IN b $\rightarrow$ s TRANSITIONS". In: *Modern Physics Letters A* 21.06 (Feb. 2006), pp. 457–478. ISSN: 1793-6632. DOI: 10.1142/s0217732306019852. URL: http://dx.doi.org/10.1142/S0217732306019852.

[15] E. Aprile et al. "Dark Matter Search Results from a One Ton-Year Exposure of XENON1T". In: *Physical Review Letters* 121.11 (Sept. 2018). ISSN: 1079-7114. DOI: 10.1103/physrevlett.121.111302. URL: http://dx.doi.org/10.1103/PhysRevLett.121.111302.

[16] D. S. Akerib et al. "Results from a Search for Dark Matter in the Complete LUX Exposure". In: *Phys. Rev. Lett.* 118 (2 Jan. 2017), p. 021303. DOI: 10.1103/PhysRevLett.118.021303. URL: https://link.aps.org/doi/10.1103/PhysRevLett.118.021303.

[17] Xiangyi Cui et al. "Dark Matter Results from 54-Ton-Day Exposure of PandaX-II Experiment". In: *Physical Review Letters* 119.18 (Oct. 2017). ISSN: 1079-7114. DOI: 10.1103/physrevlett.119.181302. URL: http://dx.doi.org/10.1103/PhysRevLett.119.181302.

[18] Jim Alexander et al. *Dark Sectors 2016 Workshop: Community Report*. 2016. arXiv: 1608.08632 [hep-ph]. URL: http://lss.fnal.gov/archive/2016/conf/fermilab-conf-16-421.pdf.

[19] Biswajoy Brahmachari and Amitava Raychaudhuri. "Kinetic mixing and symmetry breaking dependent interactions of the dark photon". In: *Nuclear Physics B* 887 (Oct. 2014), pp. 441–455. ISSN: 0550-3213. DOI: 10.1016/j.nuclphysb.2014.08.015. URL: http://dx.doi.org/10.1016/j.nuclphysb.2014.08.015.

[20] Bob Holdom. "Two U(1)'s and Epsilon Charge Shifts". In: *Phys. Lett.* 166B (1986), pp. 196–198. DOI: 10.1016/0370-2693(86)91377-8.

[21] Julian Heeck and Werner Rodejohann. "Gauged $L_\mu - L_\tau$ Symmetry at the Electroweak Scale". In: *Phys. Rev.* D84 (2011), p. 075007. DOI: 10.1103/PhysRevD.84.075007. arXiv: 1107.5238 [hep-ph]. URL: https://arxiv.org/abs/1107.5238.

[22] Julian Heeck and Anil Thapa. *Explaining lepton-flavor non-universality and self-interacting dark matter with $L_\mu - L_\tau$*. 2022. DOI: 10.48550/ARXIV.2202.08854. URL: https://arxiv.org/abs/2202.08854.

[23] B. Abi et al. "Measurement of the Positive Muon Anomalous Magnetic Moment to 0.46 ppm". In: *Phys. Rev. Lett.* 126 (14 Apr. 2021), p. 141801. DOI: 10.1103/PhysRevLett.126.141801. URL: https://link.aps.org/doi/10.1103/PhysRevLett.126.141801.

[24] Takeshi Araki et al. “Detecting the $L_\mu - L_\tau$ gauge boson at Belle II”. In: *Physical Review D* 95.5 (Mar. 2017). ISSN: 2470-0029. DOI: 10.1103/physrevd.95.055006. URL: http://dx.doi.org/10.1103/PhysRevD.95.055006.

[25] Sz Borsanyi et al. “Leading hadronic contribution to the muon magnetic moment from lattice QCD”. In: *Nature* 593.7857 (2021), pp. 51–55.

[26] R. Aaij, B. Adeva, et al. “Test of lepton universality with $B^0 \to K^{*0} l^+ l^-$ decays”. In: *Journal of High Energy Physics* 2017.8 (Aug. 2017). DOI: 10.1007/jhep08(2017)055. URL: https://doi.org/10.1007%2Fjhep08%282017%29055.

[27] R. Aaij et al. “Search for Lepton-Universality Violation in $B^+ \to K^+ \ell^+ \ell^-$ Decays”. In: *Phys. Rev. Lett.* 122 (19 May 2019), p. 191801. DOI: 10.1103/PhysRevLett.122.191801. URL: https://link.aps.org/doi/10.1103/PhysRevLett.122.191801.

[28] S. Wehle et al. “Test of Lepton-Flavor Universality in $B \to K^* \ell^+ \ell^-$ Decays at Belle”. In: *Phys. Rev. Lett.* 126 (16 Apr. 2021), p. 161801. DOI: 10.1103/PhysRevLett.126.161801. URL: https://link.aps.org/doi/10.1103/PhysRevLett.126.161801.

[29] Wolfgang Altmannshofer et al. “Quark flavor transitions in $L_\mu - L_\tau$ models”. In: *Physical Review D* 89.9 (May 2014). ISSN: 1550-2368. DOI: 10.1103/physrevd.89.095033. URL: http://dx.doi.org/10.1103/PhysRevD.89.095033.

[30] R. Aaij et al. “Measurement of the Ratio of the $B^0 \to D^{*-} \tau^+ \nu_\tau$ and $B^0 \to D^{*-} \mu^+ \nu_\mu$ Branching Fractions Using Three-Prong τ-Lepton Decays”. In: *Phys. Rev. Lett.* 120 (17 Apr. 2018), p. 171802. DOI: 10.1103/PhysRevLett.120.171802. URL: https://link.aps.org/doi/10.1103/PhysRevLett.120.171802.

[31] A. Abdesselam et al. “Measurement of the branching ratio of $\bar{B}^0 \to D^{*+} \tau^- \bar{\nu}_\tau$ relative to $\bar{B}^0 \to D^{*+} \ell^- \bar{\nu}_\ell$ decays with a semileptonic tagging method”. In: *51st Rencontres de Moriond on EW Interactions and Unified Theories*. Mar. 2016. arXiv: 1603.06711 [hep-ex].

[32] Brian Shuve and Itay Yavin. “Dark matter progenitor: Light vector boson decay into sterile neutrinos”. In: *Phys. Rev. D* 89 (11 2014), p. 113004. DOI: 10.1103/PhysRevD.89.113004.

[33] The BABAR Collaboration. *Search for a Dark Leptophilic Scalar at BABAR*. 2020. arXiv: 2005.01885 [hep-ex]. URL: https://arxiv.org/abs/2005.01885.

[34] Brian Batell et al. “Muon anomalous magnetic moment through the leptonic Higgs portal”. In: *Physical Review D* 95.7 (2017), p. 075003.

[35] Chien-Yi Chen et al. “Implications of a light “dark Higgs” solution to the g μ- 2 discrepancy”. In: *Physical Review D* 93.3 (2016), p. 035006.

[36] Jia Liu et al. “A light scalar explanation of (g- 2) μ and the KOTO anomaly”. In: *Journal of High Energy Physics* 2020.4 (2020), pp. 1–25.

[37] Martin Bauer, Matthias Neubert, and Andrea Thamm. “Collider probes of axion-like particles”. In: *Journal of High Energy Physics* 2017.12 (Dec. 2017). DOI: 10.1007/jhep12(2017)044. URL: https://doi.org/10.1007%2Fjhep12%282017%29044.

[38] Martin Bauer et al. *Flavor probes of axion-like particles*. 2021. DOI: 10.48550/ARXIV.2110.10698. URL: https://arxiv.org/abs/2110.10698.

[39] R. Bernaber et al. *Dama Results*. 2003. URL: https://arxiv.org/abs/astro-ph/0305542v2.

[40] O. Adriani et al. “An anomalous positron abundance in cosmic rays with energies 1.5–100 GeV”. In: *Nature* 458.7238 (Apr. 2009), pp. 607–609. ISSN: 1476-4687. DOI: 10.1038/nature07942. URL: http://dx.doi.org/10.1038/nature07942.

[41] A. U. Abeysekara et al. “Extended gamma-ray sources around pulsars constrain the origin of the positron flux at Earth”. In: *Science* 358.6365 (Nov. 2017), pp. 911–914. ISSN: 1095-9203. DOI: 10.1126/science.aan4880. URL: http://dx.doi.org/10.1126/science.aan4880.

[42] M. Ackermann et al. “Measurement of Separate Cosmic-Ray Electron and Positron Spectra with the Fermi Large Area Telescope”. In: *Physical Review Letters* 108.1 (Jan. 2012). ISSN: 1079-7114. DOI: 10.1103/physrevlett.108.011103. URL: http://dx.doi.org/10.1103/PhysRevLett.108.011103.

[43] Sami Caroff. *High Statistics Measurement of the Positron Fraction in Primary Cosmic Rays with the Alpha Magnetic Spectrometer on the International Space Station*. 2016. arXiv: 1612.09579 [astro-ph.HE].

[44] S. N. Gninenko, N. V. Krasnikov, and V. A. Matveev. “Search for Dark Sector Physics with NA64”. In: *Physics of Particles and Nuclei* 51.5 (Sept. 2020), pp. 829–858. ISSN: 1531-8559. DOI: 10.1134/s1063779620050044. URL: http://dx.doi.org/10.1134/S1063779620050044.

[45] N. V. Krasnikov. “The Search for Light Dark Matter at NA64 Experiment”. In: *Physics of Particles and Nuclei* 51.4 (July 2020), pp. 697–702. ISSN: 1531-8559. DOI: 10.1134/S1063779620040449. URL: https://doi.org/10.1134/S1063779620040449.

[46] D. Banerjee et al. “Dark Matter Search in Missing Energy Events with NA64”. In: *Phys. Rev. Lett.* 123 (12 Sept. 2019), p. 121801. DOI: 10.1103/PhysRevLett.123.121801. URL: https://link.aps.org/doi/10.1103/PhysRevLett.123.121801.

[47] Torsten Åkesson et al. *Light Dark Matter eXperiment (LDMX)*. 2018. arXiv: 1808.05219 [hep-ex].

[48] V. Kozhuharov et al. “PADME: Searching for dark mediator at the Frascati BTF”. In: *Nuovo Cim. C* 40.5 (2017), p. 192. DOI: 10.1393/ncc/i2017-17192-4.

[49] CMS Collaboration. “Search for a very light NMSSM Higgs boson produced in decays of the 125 GeV scalar boson and decaying into tau leptons in pp collisions at $\sqrt{s} = 8$ TeV”. In: (2016). URL: https://arxiv.org/abs/1510.06534.

[50] ATLAS Collaboration. “Search for Higgs bosons decaying to aa in the $\mu\mu\tau\tau$ final state in pp collisions at $\sqrt{s} = 8$ TeV with the ATLAS experiment”. In: (2015). URL: https://arxiv.org/abs/1505.01609.

[51] LHCb Collaboration. “Search for hidden-sector bosons in $B^0 \to K^{0*}\mu^+\mu^-$ decays”. In: (2015). URL: https://arxiv.org/abs/1508.04094.

[52] LHCb Collaboration. “Search for Majorana neutrinos in $B^- \to \pi^+\mu^-\mu^-$ decays”. In: (2014). URL: https://arxiv.org/abs/1401.5361.

[53] LHCb Collaboration. “Search for long-lived particles decaying to jet pairs”. In: (2015). URL: https://arxiv.org/abs/1412.3021.

[54] Asmaa Abada et al. “Inclusive Displaced Vertex Searches for Heavy Neutral Leptons at the LHC”. In: (2018). URL: https://arxiv.org/pdf/1807.10024.pdf.

[55] J. P. Lees et al. “Search for Invisible Decays of a Dark Photon Produced in e+e- Collisions at BaBar”. In: *Physical Review Letters* 119.13 (Sept. 2017). ISSN: 1079-7114. DOI: 10.1103/physrevlett.119.131804. URL: http://dx.doi.org/10.1103/PhysRevLett.119.131804.

[56] E Kou et al. “The Belle II Physics Book”. In: *Progress of Theoretical and Experimental Physics* 2019.12 (Dec. 2019). ISSN: 2050-3911. DOI: 10.1093/ptep/ptz106. URL: http://dx.doi.org/10.1093/ptep/ptz106.

[57] I. Adachi et al. “Search for an invisibly decaying Z' boson at Belle II in $e^+e^- \to \mu^+\mu^-(e^\pm\mu^\mp)$ plus missing energy final states”. In: *Physical Review Letters* 124.14 (Apr. 2020). ISSN: 1079-7114. DOI: 10.1103/physrevlett.124.141801. URL: http://dx.doi.org/10.1103/PhysRevLett.124.141801.

[58] F. Abudinén et al. “Search for Axion-Like Particles Produced in e^+e^- Collisions at Belle II”. In: *Physical Review Letters* 125.16 (Oct. 2020). ISSN: 1079-7114. DOI: 10.1103/physrevlett.125.161806. URL: http://dx.doi.org/10.1103/PhysRevLett.125.161806.

[59] J. P. Lees et al. “Search for a muonic dark force at BaBar”. In: *Physical Review D* 94.1 (July 2016). ISSN: 2470-0029. DOI: 10.1103/physrevd.94.011102. URL: http://dx.doi.org/10.1103/PhysRevD.94.011102.

[60] T. Czank et al. *Search for $Z' \to \mu^+\mu^-$ in the $L_\mu - L_\tau$ gauge-symmetric model at Belle*. 2021. arXiv: 2109.08596 [hep-ex].

[61] Andrea Caputo et al. “Dark photon limits: A handbook”. In: *Physical Review D* 104.9 (Nov. 2021). ISSN: 2470-0029. DOI: 10.1103/physrevd.104.095029. URL: http://dx.doi.org/10.1103/PhysRevD.104.095029.

[62] Manuel A. Buen-Abad et al. *Cosmological Constraints on Dark Matter Interactions with Ordinary Matter*. 2021. arXiv: 2107.12377 [astro-ph.CO].

[63] Paul Frederik Depta, Marco Hufnagel, and Kai Schmidt-Hoberg. "Robust cosmological constraints on axion-like particles". In: *Journal of Cosmology and Astroparticle Physics* 2020.05 (May 2020), pp. 009–009. ISSN: 1475-7516. DOI: 10.1088/1475-7516/2020/05/009. URL: http://dx.doi.org/10.1088/1475-7516/2020/05/009.

[64] David d'Enterria. *Collider constraints on axion-like particles*. 2021. arXiv: 2102.08971 [hep-ex].

[65] The BABAR Collaboration. *Search for an Axion-Like Particle in B Meson Decays*. 2021. DOI: 10.48550/ARXIV.2111.01800. URL: https://arxiv.org/abs/2111.01800.

[66] R. Aaij et al. "Search for $A' \to \mu^+\mu^-$ Decays". In: *Physical Review Letters* 124.4 (Jan. 2020). ISSN: 1079-7114. DOI: 10.1103/physrevlett.124.041801. URL: http://dx.doi.org/10.1103/PhysRevLett.124.041801.

[67] Martin Bauer, Matthias Neubert, and Andrea Thamm. "Collider probes of axion-like particles". In: *Journal of High Energy Physics* 2017.12 (Dec. 2017). ISSN: 1029-8479. DOI: 10.1007/jhep12(2017)044. URL: http://dx.doi.org/10.1007/JHEP12(2017)044.

[68] SuperB Collaboration. *SuperB: A High-Luminosity Asymmetric e+ e- Super Flavor Factory. Conceptual Design Report*. 2007. DOI: 10.48550/ARXIV.0709.0451. URL: https://arxiv.org/abs/0709.0451.

[69] J. H. Christenson et al. "Evidence for the 2π Decay of the K_2^0 Meson". In: *Phys. Rev. Lett.* 13 (4 July 1964), pp. 138–140. DOI: 10.1103/PhysRevLett.13.138. URL: https://link.aps.org/doi/10.1103/PhysRevLett.13.138.

[70] A. J. Bevan et al. "The Physics of the B Factories". In: *The European Physical Journal C* 74.11 (Nov. 2014). ISSN: 1434-6052. DOI: 10.1140/epjc/s10052-014-3026-9. URL: http://dx.doi.org/10.1140/epjc/s10052-014-3026-9.

[71] D. Boutigny et al. *The BABAR Physics Book: Physics at an Asymmetric B Factory*. 1995.

[72] Honscheid K. *CESR and CLEO*. URL: https://www.slac.stanford.edu/econf/C990809/docs/honscheid.pdf.

[73] T. Abe et al. *Belle II Technical Design Report*. 2010. arXiv: 1011.0352 [physics.ins-det]. URL: https://arxiv.org/abs/1011.0352.

[74] N. Ohuchi et al. "SuperKEKB beam final focus superconducting magnet system". In: *Nuclear Instruments and Methods in Physics Research Section A: Accelerators, Spectrometers, Detectors and Associated Equipment* 1021 (2022), p. 165930. ISSN: 0168-9002. DOI: https://doi.org/10.1016/j.nima.2021.165930. URL: https://www.sciencedirect.com/science/article/pii/S0168900221008949.

[75] T. Hara, T. Kuhr, and Y. Ushiroda. *Belle II Coordinate System and Guideline of Belle II Numbering Scheme*. 2011. URL: https://indico.mpp.mpg.de/event/2308/material/0/1?contribId=0.

[76] I. Adachi et al. "Detectors for extreme luminosity: Belle II". In: *Nuclear Instruments and Methods in Physics Research Section A: Accelerators, Spectrometers, Detectors and Associated Equipment* 907 (2018). Advances in Instrumentation and Experimental Methods (Special Issue in Honour of Kai Siegbahn), pp. 46–59. ISSN: 0168-9002. DOI: https://doi.org/10.1016/j.nima.2018.03.068. URL: https://www.sciencedirect.com/science/article/pii/S0168900218304200.

[77] S. Bacher et al. "Performance of the diamond-based beam-loss monitor system of Belle II". In: *Nucl. Instrum. Meth. A* 997 (2021), p. 165157. DOI: 10.1016/j.nima.2021.165157. arXiv: 2102.04800 [physics.ins-det].

[78] P. Wieduwilt et al. "Performance of production modules of the Belle II pixel detector in a high-energy particle beam". In: *Nuclear Instruments and Methods in Physics Research Section A: Accelerators, Spectrometers, Detectors and Associated Equipment* 991 (Mar. 2021), p. 164978. ISSN: 0168-9002. DOI: 10.1016/j.nima.2020.164978. URL: http://dx.doi.org/10.1016/j.nima.2020.164978.

[79] K. Adamczyk et al. "The Design, Construction, Operation and Performance of the Belle II Silicon Vertex Detector". In: (Jan. 2022). arXiv: 2201.09824 [physics.ins-det].

[80] M. J. French et al. "Design and results from the APV25, a deep sub-micron CMOS front-end chip for the CMS tracker". In: *Nucl. Instrum. Meth. A* 466 (2001). Ed. by T. Ohsugi et al., pp. 359–365. DOI: 10.1016/S0168-9002(01)00589-7.

[81] K. Adamczyk et al. "The Belle II silicon vertex detector assembly and mechanics". In: *Nucl. Instrum. Meth. A* 845 (2017). Ed. by G. Badurek et al., pp. 38–42. DOI: 10.1016/j.nima.2016.03.100.

[82] M. Starič. "Pattern recognition for the time-of-propagation counter". In: *Nuclear Instruments and Methods in Physics Research Section A: Accelerators, Spectrometers, Detectors and Associated Equipment* 639.1 (2011). Proceedings of the Seventh International Workshop on Ring Imaging Cherenkov Detectors, pp. 252–255. ISSN: 0168-9002. DOI: https://doi.org/10.1016/j.nima.2010.09.176. URL: https://www.sciencedirect.com/science/article/pii/S0168900210022473.

[83] T. Kuhr et al. "The Belle II Core Software". In: *Computing and Software for Big Science* 3.1 (Nov. 2018). ISSN: 2510-2044. DOI: 10.1007/s41781-018-0017-9. URL: http://dx.doi.org/10.1007/s41781-018-0017-9.

[84] Anders Ryd et al. "EvtGen: A Monte Carlo Generator for B-Physics". In: (May 2005).

[85] Torbjörn Sjöstrand et al. “An introduction to PYTHIA 8.2”. In: *Computer Physics Communications* 191 (June 2015), pp. 159–177. ISSN: 0010-4655. DOI: 10.1016/j.cpc.2015.01.024. URL: http://dx.doi.org/10.1016/j.cpc.2015.01.024.

[86] S. Agostinelli et al. “GEANT4–a simulation toolkit”. In: *Nucl. Instrum. Meth. A* 506 (2003), pp. 250–303. DOI: 10.1016/S0168-9002(03)01368-8.

[87] *ROOT - homepage*. URL: https://root.cern.ch/.

[88] Frits A Berends, PH Daverveldt, and R Kleiss. “Complete lowest-order calculations for four-lepton final states in electron-positron collisions”. In: *Nuclear Physics B* 253 (1985), pp. 441–463.

[89] Sadaharu Uehara. “TREPS: A Monte-Carlo Event Generator for Two-photon Processes at e^+e^- Colliders using an Equivalent Photon Approximation”. In: (2013). arXiv: 1310.0157 [hep-ph].

[90] Stanisław Jadach, BFL Ward, and Zbignev Was. “The precision Monte Carlo event generator KK for two-fermion final states in e^+e^- collisions”. In: *Computer Physics Communications* 130.3 (2000), pp. 260–325.

[91] *TAUOLA - homepage*. URL: http://tauolapp.web.cern.ch/tauolapp/.

[92] Torbjörn Sjöstrand et al. “An introduction to PYTHIA 8.2”. In: *Computer Physics Communications* 191 (June 2015), pp. 159–177. DOI: 10.1016/j.cpc.2015.01.024. URL: https://doi.org/10.1016%2Fj.cpc.2015.01.024.

[93] Anders Ryd et al. “EvtGen: A Monte Carlo Generator for B-Physics”. In: (May 2005).

[94] Geoffrey C. Fox and Stephen Wolfram. “Observables for the Analysis of Event Shapes in e^+e^- Annihilation and Other Processes”. In: *Phys. Rev. Lett.* 41 (23 Dec. 1978), pp. 1581–1585. DOI: 10.1103/PhysRevLett.41.1581. URL: https://link.aps.org/doi/10.1103/PhysRevLett.41.1581.

[95] A. Hoecker et al. *TMVA - Toolkit for Multivariate Data Analysis*. 2009. arXiv: physics/0703039 [physics.data-an].

[96] Giovanni Punzi. “Sensitivity of searches for new signals and its optimization”. In: *eConf* C030908 (2003). Ed. by L. Lyons, R. P. Mount, and R. Reitmeyer, MODT002. arXiv: physics/0308063.

[97] William H Press and Saul A Teukolsky. “Savitzky-Golay smoothing filters”. In: *Computers in Physics* 4.6 (1990), pp. 669–672.

[98] John Erthal Gaiser. “Charmonium Spectroscopy From Radiative Decays of the J/ψ and ψ'”. Other thesis. Aug. 1982.

[99] Wouter Verkerke and David Kirkby. *The RooFit toolkit for data modeling*. 2003. arXiv: physics/0306116 [physics.data-an].

[100] Steve Baker and Robert D. Cousins. “Clarification of the use of CHI-square and likelihood functions in fits to histograms”. In: *Nuclear Instruments and Methods in Physics Research* 221.2 (1984), pp. 437–442. ISSN: 0167-5087. DOI: https://doi.org/10.1016/0167-5087(84)90016-4. URL: https://www.sciencedirect.com/science/article/pii/0167508784900164.

[101] M. Campajola and E. Graziani. *Measurement of the cdcklm1 trigger performances with Experiment 12 Data*. Internal note: BELLE2-NOTE-TE-2020-28. 2020.

[102] A. Glazov, P. Rados, and A. Rostomyan. *Measurement of the track reconstruction efficiency and fake rate with $e^+e^- \to \tau^+\tau^-$ events*. Internal note: BELLE2-NOTE-TE-2020-06. 2020.

[103] Belle II Collaboration. *Muon and electron identification efficiencies and hadron-lepton mis-identification probabilities*. Internal note: BELLE2-NOTE-TE-2020-27. 2020.

[104] R. Garg et al. *Track momentum resolution using dimuon sample in the phase 3 data*. Internal note: BELLE2-NOTE-TE-2020-59. 2020.

[105] A L Read. “Presentation of search results: the CLs technique”. In: *Journal of Physics G: Nuclear and Particle Physics* 28.10 (Sept. 2002), pp. 2693–2704. DOI: 10.1088/0954-3899/28/10/313. URL: https://doi.org/10.1088/0954-3899/28/10/313.

[106] Alexander L. Read. “Modified frequentist analysis of search results (The CL(s) method)”. In: *Workshop on Confidence Limits*. Aug. 2000, pp. 81–101.

[107] Lorenzo Moneta et al. “The RooStats Project”. In: *PoS* ACAT2010 (2010). Ed. by T. Speer et al., p. 057. DOI: 10.22323/1.093.0057. arXiv: 1009.1003 [physics.data-an].

[108] *AsymptoticCalculator Class Reference*. URL: https://root.cern/doc/master/classRooStats_1_1AsymptoticCalculator.html.

[109] In Jae Myung. “Tutorial on maximum likelihood estimation”. In: *Journal of Mathematical Psychology* 47.1 (2003), pp. 90–100. ISSN: 0022-2496. DOI: https://doi.org/10.1016/S0022-2496(02)00028-7. URL: https://www.sciencedirect.com/science/article/pii/S0022249602000287.

[110] Wolfgang Altmannshofer et al. “Neutrino Trident Production: A Powerful Probe of New Physics with Neutrino Beams”. In: *Phys. Rev. Lett.* 113 (9 Aug. 2014), p. 091801. DOI: 10.1103/PhysRevLett.113.091801. URL: https://link.aps.org/doi/10.1103/PhysRevLett.113.091801.

[111] Eilam Gross and Ofer Vitells. “Trial factors for the look elsewhere effect in high energy physics”. In: *The European Physical Journal C* 70 (2010), pp. 525–530. ISSN: 1434-6052. DOI: https://doi.org/10.1140/epjc/s10052-010-1470-8. URL: https://doi.org/10.1140/epjc/s10052-010-1470-8.

[112] The ATLAS Collaboration, The CMS Collaboration, The LHC Higgs Combination Group. *Procedure for the LHC Higgs boson search combination in Summer 2011*. Aug. 2011. URL: https://cds.cern.ch/record/1379837.